THOMAS GRAF

Modeling Coupled Thermohaline Flow and Reactive Solute Transport in Discretely-Fractured Porous Media

Thèse présentée
à la Faculté des études supérieures de l'Université Laval
dans le cadre du programme de doctorat en Sciences de la Terre
pour l'obtention du grade de Philosophiae Doctor (Ph.D.)

FACULTÉ DES SCIENCES ET DE GÉNIE
UNIVERSITÉ LAVAL
QUÉBEC

DÉCEMBRE 2005

The Université Laval requires the signatures of all persons using or photocopying this thesis. Please sign below, and give address and date.

Abstract

A three-dimensional numerical model is developed that couples the quartz-water chemical system with variable-density, variable-viscosity flow in fractured porous media. The new model also solves for heat transfer in fractured porous media, under the assumption of negligible thermal expansion of the rock. The fluid properties density and viscosity as well as chemistry constants (dissolution rate constant, equilibrium constant and activity coefficient) are calculated as a function of the concentrations of major ions and of temperature. Reaction and flow parameters, such as mineral surface area and permeability, are updated at the end of each time step with explicitly calculated reaction rates. The impact of porosity and aperture changes on specific storage is neglected. Adaptive time stepping is used to accelerate and slow down the simulation process in order to prevent physically unrealistic results. New time increments depend on maximum changes in matrix porosity and/or fracture aperture. Reaction rates at time level $L+1$ (implicit time weighting scheme) are used to renew all model parameters to ensure numerical stability. The model is verified against existing analytical, numerical and physical benchmark problems of variable-density flow, reactive solute transport and heat transfer in fractured porous media. The complexity of the model formulation allows chemical reactions and variable-density flow to be studied in a more realistic way than previously possible.

The present study first addresses the phenomenon of variable-density flow and transport in fractured porous media, where a single fracture of an arbitrary incline can occur. A general mathematical formulation of the body force vector is derived, which accounts for variable-density flow and transport in fractures of any orientation. Simulations of variable-density flow and solute transport are conducted for a single fracture, embedded in a porous matrix. The simulations show that density-driven flow in the fracture causes convective flow within the porous matrix and that the high-permeability fracture acts as a barrier for convection.

The new model was applied to simulate illustrative examples, such as the horizontal movement of a hot plume in a chemically reactive fractured medium. Thermohaline (double-diffusive) transport impacts both buoyancy-driven flow and chemical reactions. Free convective flow depends on the density contrast between the fluid (hot brine or

cool saltwater) and the reference fluid. In the example, density contrasts are generally small and fractures do not act like preferential pathways but contribute to transverse dispersion of the plume. Hot zones correspond to areas of quartz dissolution while in cooler zones, precipitation of imported silica prevails. The silica concentration is inversely proportional to salinity in high-salinity regions and directly proportional to temperature in low-salinity regions. The system is the most sensitive to temperature inaccuracy. This is because temperature impacts both the dissolution kinetics (Arrhenius equation) and the quartz solubility.

Résumé Français

Un modèle numérique tridimensionnel a été développé pour la simulation du système chimique quartz-eau couplé avec l'écoulement à densité et viscosité variable dans les milieux poreux discrètement fracturés. Le nouveau modèle simule aussi le transfert de chaleur dans les milieux poreux fracturés en supposant que l'expansion thermique du milieu est négligeable. Les propriétés du fluide, densité et viscosité, ainsi que les constantes chimiques (constant de taux de dissolution, constant d'équilibre, coefficient d'activité) sont calculées en fonction de la concentration des ions majeurs et de la température. Des paramètres de réaction et d'écoulement, comme la surface spécifique du minéral et la perméabilité sont mis jour à la fin de chaque pas de temps avec des taux de réaction explicitement calculés. Le modèle suppose que des changements de la porosite et des ouvertures de fractures n'ont pas d'impact sur l'emmagasinement spécifique. Des pas de temps adaptatifs sont utilisés pour accélérer et ralentir la simulation afin d'empêcher des résultats non physiques. Les nouveaux incréments de temps dépendent des changements maximum de la porosité et/ou de l'ouverture de fracture. Des taux de réaction au niveau temporel $L+1$ (schéma de pondération temporelle implicite) sont utilisés pour renouveler tous les paramètres du modèle afin de garantir la stabilité numérique. Le modèle a été vérifié avec des problèmes analytiques, numériques et physiques de l'écoulement à densité variable, transport réactif et transfert de chaleur dans les milieux poreux fracturés. La complexité de la formulation du modèle permet d'étudier des réactions chimiques et l'écoulement à densité variable d'une façon plus réaliste qu'auparavant possible.

En premier lieu, cette étude adresse le phénomène de l'écoulement et du transport à densité variable dans les milieux poreux fracturés avec une seule fracture à inclinaison arbitraire. Une formulation mathématique générale du terme de flottabilité est dérivée qui tient compte de l'écoulement et du transport à densité variable dans des fractures de toute orientation. Des simulations de l'écoulement et du transport à densité variable dans une seule fracture implanté dans une matrice poreuse ont été effectuées. Les simulations montrent que l'écoulement à densité variable dans une fracture cause la convection dans la matrice poreuse et que la fracture à perméabilité élevée agit comme barrière pour la convection.

Le nouveau modèle a été appliqué afin de simuler des exemples, comme le mouvement horizontal d'un panache de fluide chaud dans un milieu fracturé chimiquement réactif. Le transport thermohalin (double-diffusif) influence non seulement l'écoulement à densité variable mais aussi les réactions chimiques. L'écoulement à convection libre dépend du contraste de densité entre le fluide (panache chaud ou de l'eau salée froide) et le fluide de référence. Dans l'exemple, des contrastes de densité sont généralement faibles et des fractures n'agissent pas comme des chemins préférés mais contribuent à la dispersion transverse du panache. Des zones chaudes correspondent aux régions de dissolution de quartz tandis que dans les zones froides, la silice mobile précipite. La concentration de silice est inversement proportionnelle à la salinité dans les régions à salinité élevée et directement proportionnelle à la température dans les régions à salinité faible. Le système est le plus sensible aux inexactitudes de température. Ceci est parce que la température influence non seulement la cinétique de dissolution (équation d'Arrhenius), mais aussi la solubilité de quartz.

Acknowledgements

Firstly, a big thank you goes to my supervisor, René Therrien! He invited me over to Canada and wisely guided me through the course of this research. I am grateful for his constantly open door and ears and for always giving me thoughtful advice. I also deeply appreciated our attending conferences, teaching courses and visiting other researchers on both the national and international level. Merci beaucoup, René! Craig T. Simmons is thanked for giving very detailed comments on the thesis, for inspiring and fruitful discussions on variable-density flow and for inviting me over to Australia. I also thank the examiners Rob A. Schincariol and Alfonso Rivera for carefully reviewing the thesis.

I want to thank Young-Jin Park for constantly sharing his expertise on finite element modeling. I am also thankful to Ekkehard Holzbecher for immediately responding to my rare emails and for giving detailed explanations on a variety of topics. Rob McLaren is thanked for double-checking my model modifications and for implementing them in the official version of the numerical groundwater model. I also thank Patricia Dove for giving valuable information on quartz kinetics. John Molson and Thomas Wolery are thanked for providing diverse user's guides and modeling software. I am also grateful to Chris Neville for sending detailed analytical solutions on heat transfer.

Financial support for this project was provided by the Canadian Water Network (CWN) as well as by the Natural Sciences and Engineering Research Council of Canada (NSERC). I also wish to acknowledge both the International Council for Canadian Studies (ICCS) and the German Academic Exchange Service (DAAD) for providing a Postgraduate Scholarship stipend.

I thank my parents, Helga and Günter Graf, for their skillful channelization of my energy and for giving me patience and endurance. Vielen Dank!

I finally thank my wife, Mardi, for her breathless support, her never-ending optimism and her love, which were always my inspiration. Thank you for all that!

Dedication

To Mardi

For helping me cope with our new situation on another continent, for sharing ups and downs and for the daily smile on your lips!

To my brother, Hannes

For showing that persistence always pays off in the end.

To my high-school teachers, Gerhard Frohnmüller and Lothar Klimt

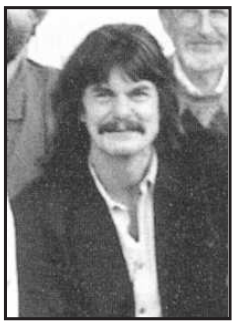

For opening my eyes to the scientific world and for teaching Earth Sciences in a very understandable yet highly sophisticated way.

Contents

List of Tables

List of Figures

Chapter 1

Introduction

Problem Definition

With time, manmade industrial waste has become increasingly hazardous. The production of radioactive waste during the last decades has created a new challenge for responsible waste treatment. Recycling nuclear waste or transmuting long-lived radionuclides into short-lived or even stable forms are not an option from an economical or technical standpoint (von Hippel, 2001). The logical consequence is to permanently isolate radioactive contaminants from the biosphere. The safe disposal of radionuclides is commonly regarded as feasible in low-permeability geological media at depths up to 1,000 m (Davison et al., 1994b).

At great depth, groundwater is a hot saline Na-Ca-Cl brine (Farvolden et al., 1988; Stober and Bucher, 2005). The temperature of the ambient rock as well as that of the water follow the geothermal gradient. In addition, radioactive waste is known to release large amounts of thermal energy. As a consequence, deep-fluid properties such as viscosity and density can not be assumed to be uniform. Variations of fluid density play an important role in contaminant migration within various geological media. Seemingly insignificant fluid density differences create flow gradients that are equivalent to typical hydraulic head gradients (Simmons, 2005). If, for example, a fluid of high density overlies a less dense fluid, the system is potentially unstable and density-driven flow

may take place to level out the density stratification and to eventually stabilize the system. Additionally, if the flow is transient, there are temporal changes of density.

Critical safety questions arise due to the presence of fractures in the rock formation. Fractures have a great impact on mass transport because they represent preferential pathways where accidentally released radionuclides migrate at velocities that are several orders of magnitude faster than within the rock matrix itself. Simulating solute transport in fractured media is typically difficult because the network geometry, especially the fracture network connectivity and fracture apertures, are almost impossible to measure accurately.

Significant increases in temperature cause rock-fluid interactions such as mineral dissolution and precipitation. Chemical reactions can have a major impact on fluid flow. Physical flow properties, such as matrix permeability and fracture aperture are modified if chemical rock-fluid interactions occur. This can be significant because the Cubic Law states that the discharge through a fracture is proportional to the cube of its aperture. As an example, an increase of the fracture aperture by 26% doubles the discharge through this fracture. The high number of conceivable feedback scenarios between variable-density flow and reactive solute transport demonstrates that the two processes are strongly coupled. This is especially the case in discretely-fractured media where high groundwater flow velocities enable rapid transport of reactive species to the location of the chemical reaction and away from it. The temporal change of material properties is slow and yet it is likely to play an important role because radioactive waste needs to be reliably isolated during an extremely long time, up to 10,000 years (Davison et al., 1994b). Clearly, the ability to predict the transport behavior of hazardous chemicals leaked to the geosphere is essential. It is important to understand the chemically reactive transport of radioactive contaminants in fractured media under the influence of fluctuating fluid density.

Field experiments are one means to explore the spatial and temporal distribution of contaminants in the subsurface. They are fundamental to the comprehension of flow and transport processes but are also time-consuming and expensive. Also, pure field data represents only a snapshot and is not useful to forecast solute transport. Another problem with conducting experiments in fractured media is the sampling technique. As

soon as a well is drilled into fractured rock to take a sample, the hydraulic properties of the aquifer are modified and the flow field is disturbed. Thus, the act of measuring has an impact on the variable that has to be determined and makes accurate measuring impossible. This is an illustrative example of Heisenberg's principle of uncertainty, which was initially formulated for elementary particles whose position and momentum can never be determined precisely at the same time (Heisenberg, 1927). In fact, it is not easy to study complex processes, such as density-driven flow and reactive transport in fractured rock formations in the real world. As an alternative, physical and numerical models are very helpful tools for studying and predicting long-term effects in complex systems.

Prior Studies on Variable-Density Flow

In the last century, the foundations for modeling density-driven flow and transport were laid by Rayleigh (1916). He mathematically formulated the principles that govern the onset of instabilities caused by thermally induced fluid density variations in porous media. Variable-density flow and solute transport in porous media has been investigated experimentally and numerically for half a century, beginning with the experimental studies by Taylor (1954). Taylor (1954) investigated Rayleigh instability in a vertical capillary tube. He filled the tube with freshwater and connected the top of it with a dyed liquid of higher density in order to observe convective flow of the two miscible fluids. While Taylor (1954) focused on the impact of salinity on fluid density, Elder (1965) conducted experiments where the fluid temperature plays the key role. Meanwhile, still lacking powerful computer facilities, Wooding (1957) first presented a manual finite difference solution of steady state thermal convection in porous media. Nevertheless, neither Taylor nor Elder nor Wooding were able to reproduce and verify the experimentally or manually obtained results with those from a computer.

Numerically simulating variable-density flow became much more efficient in the early 1960's, when the first computers were available for research. Back then, computers had to be installed arduously at a fixed location. Of importance were the IBM 650 in Wellington, New Zealand (Weir, 2003), and the CDC-3600 in San Diego, USA, which was the first computer that had double-precision floating-point arithmetics (Cody,

1964). With this new technology, Wooding (1962) could reproduce Taylor's (1954) results with satisfactory agreement using the IBM, whereas Elder (1966) was able to numerically simulate his own laboratory experiments (Elder, 1965) on the CDC. Improvements in computer performance have enabled increasingly precise and complex simulations of variable-density flow, predominantly in porous media (Figures 1.1a and 1.1b).

In homogeneous porous media (Figure 1.1a), variable-density flow has recently been studied in experimental and numerical simulations in the fields of (i) convection beneath salt lakes (Simmons and Narayan, 1997; Wooding et al., 1997b; Simmons et al., 1999), (ii) seawater intrusion in coastal aquifers (Huyakorn et al., 1987; Xue et al., 1995), (iii) infiltration of leachates from waste disposal sites (Frind, 1982) and (iv) the analysis of instability development (Leijnse and Oostrom, 1994; Schincariol et al., 1994; Wooding et al., 1997a).

In heterogeneous porous media (Figure 1.1b), Schincariol and Schwartz (1990) were the pioneers in experimentally investigating density dependent flow and transport in layered and lenticular media. They found that (i) the transport pattern in the layers is greatly sensitive to hydraulic conductivity and (ii) the heterogeneities in the lenticular medium create relatively large dispersion that tends to dissipate instabilities. Thus, Schincariol et al. (1997) and Schincariol (1998) inferred that heterogeneities play opposite roles in the generation and subsequent growth of instabilities. On one hand, heterogeneities initially perturb a plume while on the other hand, once instabilities are generated, heterogeneities dampen their growth on probably all spatial scales. Simmons et al. (2001) showed that the style of heterogeneity in a porous medium will greatly influence the propagation of dense plumes, with disorganized heterogeneity tending to dissipate convection by mixing and thus reducing plume instabilities. Prasad and Simmons (2003) confirmed this observation. They carried out numerical variable-density transport simulations in a heterogeneous porous media. Prasad and Simmons (2003) used a modified form of the Elder (1967) problem, where the permeability was randomly distributed to study the effects of heterogeneity on solute transport. Holzbecher (1998) and Diersch and Kolditz (2002) provide an excellent overview of prior modeling work in porous media, clearly showing that there is currently a lack of models that take into account the crucial influence of fractures.

As opposed to the study of variable-density flow in porous media, laboratory experiments in fractured media have not yet been carried out. Studies by Murphy (1979), Malkovsky and Pek (1997; 2004) and Shi (2005) showed that two-dimensional convective flow with rotation axis normal to the fracture plane can occur within vertical fractures. These studies, however, did not represent fractures as discrete planes but as vertical high-permeability fault zones. Shikaze et al. (1998) numerically simulated variable-density flow and transport in discretely-fractured media. They found that vertical fractures with an aperture as small as 50 μm significantly increase contaminant migration relative to the case where fractures are absent. Interestingly, it was also shown that dense solute plumes may develop in a highly irregular fashion and are extremely difficult to predict. However, Shikaze et al. (1998) represented discrete fractures by one-dimensional segments. This assumption reduces the spatial fracture dimension to 1D, inhibiting convection within the fracture. Also, Shikaze et al. (1998) limited their studies to a regular fracture network consisting of only vertical and horizontal fractures, embedded in a porous matrix (Figure 1.1c). Thus, it still remains unclear how instabilities grow in a complex nonorthogonal fracture network, where fractures of any incline can occur (Figure 1.1d). A network of fractures having irregular orientations will exhibit a different style of heterogeneity, as opposed to a regular fracture distribution. It is also unknown if this different mode of heterogeneity affects dense plume migration as suggested by Simmons et al. (2001).

Processes, which affect the fluid properties on one hand and induce reactions on the other hand, are elevated temperatures or high salt contents. Numerical models that couple variable-density flow with reactive transport are rare and "the development of these codes has only just begun" (Post, 2005). Already available models vary greatly in their coupling method and in model sophistication (Post, 2005).

Prior Studies on Reactive Solute Transport

Reactive transport models are typically specialized to the chemical system being investigated. There is a large body of studies where the chemistry is highly complex, with a large number of mobile species involved in the reactions (Sanford and Konikow, 1989; Yeh and Tripathi, 1989; Steefel and Lasaga, 1994; Walter et al., 1994; Zysset et al., 1994;

Schäfer and Therrien, 1995; Bolton et al., 1996; Steefel and MacQuarrie, 1996; Steefel and Lichtner, 1998b; Schäfer et al., 1998; Ghogomu and Therrien, 2000; Saaltink et al., 2001; Geiger et al., 2002; Freedman and Ibaraki, 2002; Mayer et al., 2002; Freedman and Ibaraki, 2003; Spycher et al., 2003). Other models consider reactions with aqueous silica (H_4SiO_4) as the only mobile reactive component (Johnson et al., 1998; Steefel and Lichtner, 1998a; White and Mroczek, 1998). In this case, the reactive transport equation remains linear and complicated iterative solvers as described by Steefel and MacQuarrie (1996) do not need to be applied.

In the past, many authors examined reactive solute transport in porous media assuming constant fluid density (e.g. Steefel and MacQuarrie, 1996; Steefel and Yabusaki, 1996). However, Bolton et al. (1996) and Freedman and Ibaraki (2002) investigated the impact of density-driven flow on chemical reactions. Freedman and Ibaraki (2002) numerically studied the horizontal migration of a dense plume in an unfractured porous medium where density varies only with salinity and not with temperature. The results were compared with simulations where chemical reactions are ignored. The most important outcome of Freedman and Ibaraki's (2002) studies was that chemical reactions do not significantly impact density-driven flow in porous media. However, Freedman and Ibaraki (2002) focused on the small spatiotemporal scale and did not study long-term effects at the field scale. They also ignored the influence of temperature and salinity on both the solubility of solutes and on the reaction kinetics. Nonetheless, Bolton et al. (1996) studied coupled thermal convection and quartz dissolution/precipitation at a large spatiotemporal scale. They found that long-term changes of porosity and permeability can either increase the flow velocities and the degree of subsaturation (in regions of dissolution) or they inhibit flow rates and the degree of supersaturation (in regions of precipitation). However, Bolton et al. (1996) did not account for the salinity dependency of the kinetic rate law nor for the salinity effect on fluid density and viscosity.

Simulations of reactive transport in fractured systems have previously been carried out by a number of authors (Steefel and Lasaga, 1994; Steefel and Lichtner, 1998b; Ghogomu and Therrien, 2000; Geiger et al., 2002). Not all of the studies addressed the question of how dissolution/precipitation reactions will alter fracture aperture and matrix permeability and, thus, impact the flow field. Modifications of flow parame-

ters were either not considered (Ghogomu and Therrien, 2000) or only applied to the permeability of the porous matrix (Geiger et al., 2002). However, other investigations have shown that chemical reactions within open fractures trigger complex reaction-flow feedback scenarios (Steefel and Lasaga, 1994; Steefel and Lichtner, 1998b) and that fracture aperture may no longer be assumed as constant.

Steefel and Lichtner (1998b) studied the infiltration of a hyper-alkaline fluid along a discrete fracture. They observed that within tens of years, the permeability feedback between reaction and transport is significant. It was also found that fluid flow through the fracture is likely to collapse due to self-sealing if reaction rates in the fracture are only one order of magnitude larger than in the adjacent matrix. On the other hand, if the rates are of the same order of magnitude, the porous matrix will be cemented first.

While most studies ignored density variations when investigating reactive transport in fractured media (Steefel and Lichtner, 1998b; Ghogomu and Therrien, 2000; Geiger et al., 2002), Steefel and Lasaga (1994) fully accounted for thermal density-driven flow. According to Steefel and Lasaga (1994), geothermal convection cells in reactive fractured media are never stable. This is because upwelling fluids cool and the resulting precipitation of minerals significantly reduces permeability leading to highly dispersive plumes. On the other hand, if fluids move downwards to a zone of higher temperature, dissolution reactions locally increase permeability leading to channelling of flow. However, Steefel and Lasaga (1994) did not account for the impact of salinity on both the reaction kinetics and on fluid properties. Nevertheless, other studies suggested that the rate-enhancing effect of salt is significant (Dove, 1999) and that fluid salinity also impacts both the quartz solubility (Marshall and Chen, 1982; Langmuir, 1997) and the fluid properties density and viscosity (Holzbecher, 1998).

Table 1.1 summarizes previous modeling efforts of coupled variable-density flow and reactive transport. It highlights subtle differences between the model assumptions made by various authors. The studies are not listed chronologically but according to increasing complexity of the model used. The model developed in the present study continues the series of increasing model complexity and provides simulation capacities previously lacking.

Table 1.1: Previous studies of reactive solute transport in porous and fractured porous media. If density is a function of salinity and/or temperature, the model couples reactions with variable-density flow.

Simulated processes →	Reactive transport		Heat transfer		Density from		Viscosity from		Reaction kinetics from		Reactive species solubility from	
↓ Authors	in PM[a]	in FM[b]	in PM	in FM	salinity	temperature	salinity	temperature	salinity	temperature	salinity	temperature
Steefel and MacQuarrie (1996)	$\surd^{c}$	–	–	–	–	–	–	–	–	–	–	–
Johnson et al. (1998)	$\surd^{\phi,A}$	–	–	–	–	–	–	–	–	√	–	√
Steefel and Yabusaki (1996)	$\surd^{\phi,A}$	–	–	–	–	–	–	–	–	√	√	√
Freedman and Ibaraki (2001)	$\surd^{\phi,\kappa,A}$	–	–	–	√	–	√	–	–	–	–	–
White and Mroczek (1998)	$\surd^{\phi,\kappa,A}$	–	–	–	–	–	–	–	√	√	√	√
Bolton et al. (1996)	$\surd^{\phi,\kappa,A}$	–	√	–	√	√	–	√	–	√	–	√
Ghogomu and Therrien (2000)	$\surd^{c}$	$\surd^{c}$	–	–	–	–	–	–	–	–	–	–
Geiger et al. (2002)	$\surd^{\kappa}$	$\surd^{c}$	–	–	–	–	–	–	–	–	–	–
Steefel and Lichtner (1998b)	$\surd^{\phi,A}$	$\surd^{(2b),A}$	–	–	–	–	–	–	√	–	–	–
Steefel and Lasaga (1994)	$\surd^{\phi,A}$	$\surd^{(2b),A}$	√	√	–	√	–	√	–	√	–	√
present study	$\surd^{\phi,\kappa,A}$	$\surd^{(2b),A}$	√	√	√	√	√	√	√	√	√	√

[a] Porous media

[b] Fractured media

[c] No change of simulation parameters considered

$^{\phi}$ Change of matrix porosity considered

$^{\kappa}$ Change of matrix permeability considered

$^{(2b)}$ Change of fracture aperture considered

^{A} Change of specific mineral surface area considered

Contribution of this Study

The principal goal of this study is to develop a numerical model to simulate dense plume migration in a chemically reactive fractured environment. The new model is based on the existing FRAC3DVS model, which solves variable-saturated and multi-component transport in discretely-fractured porous media (Therrien and Sudicky, 1996). The model developed in this study solves for variable-density, variable-viscosity flow and kinetically controlled reactive solute transport in fractured porous media. Aqueous silica is the single reactive species considered. Silicate minerals are the most abundant minerals in nature, making up 90% of the earth's crust (Krauskopf and Bird, 1995). The focus will be put on α-quartz, the most common SiO_2 polymorph in the upper crust. The equilibrium thermodynamic behavior of quartz and its hydrolyzed form silica as a function of temperature are known very accurately (Rimstidt, 1997). Additionally, in numerous experiments, the quartz dissolution rate constant in pure water and in electrolyte solutions has been correlated with temperature (Dove, 1999). Relationships exist that describe the quartz dissolution rate constant over a wide range of conditions. In the developed model, both the quartz solubility and the reaction kinetics as well as physical fluid properties are calculated from temperature and from the dissolved species concentration. The low-temperature range 0°C to 300°C and a wide range of salinity are considered. Simulations are carried out in low-temperature hydrothermal fields where instantaneous equilibrium can not be assumed. The temperature distribution in space and time is obtained from the transient convective-conductive-dispersive heat transfer equation.

The model includes first-order kinetic reaction between solid quartz and aqueous silica. Therefore, the reactive transport equation is linear and solved in one step. The transport and the variable-density, variable-viscosity flow equations are linked through an iterative Picard approach. The absolute change of hydraulic head, temperature and concentration of nonreactive species have to satisfy the convergence criteria for the iteration. The solute transport equations of the reactive silica species is solved outside the Picard Iteration to save CPU time. Material properties are also updated at the end of a time step because their change is minor relative to the change of solute concentration. Recalculating material properties outside the Picard Iteration is called quasi-stationary state approximation and has first been introduced by Lichtner (1988).

Reaction rates at time level $L+1$ (implicit time weighting scheme) are used to renew all model parameters. The choice of an implicit scheme ensures numerical stability of the simulation procedure (Steefel and Lasaga, 1994). An adaptive time stepping scheme is applied to accelerate or slow down the simulation process. New time step sizes depend on the change of porosity and/or fracture aperture during the previous time interval.

Chapters 1, 3.1, 3.2, 4.1, 4.2, 4.3, 4.4, 5.1, 6.1, 8 and Appendices B, C, E of this work are written as an article and published in a scientific journal. The reference of the article is:

[1] Graf T and Therrien R, 2005. Variable-density groundwater flow and solute transport in porous media containing nonuniform discrete fractures. *Advances in Water Resources* **28** (12): 1351-1367.

Articles containing other selected subjects of this work are in preparation and will be submitted shortly. Their reference and the included chapters/appendices are listed below.

[2] Graf T and Therrien R. Variable-density groundwater flow and solute transport in complex fracture networks. Chapters 1, 2.1, 3.1, 3.2, 4.1, 6.2, 6.3, 7.1, 8 and Appendix E.

[3] Graf T and Therrien R. Coupled thermohaline groundwater flow and reactive solute transport in fractured porous media: 1. Model development and verification. Chapters 1, 2.2, 2.3, 3.3, 3.4, 4.2, 4.5, 4.6, 5.2, 5.3 and Appendices A, D, E.

[4] Graf T and Therrien R. Coupled thermohaline groundwater flow and reactive solute transport in fractured porous media: 2. Illustrative examples and sensitivity analysis. Chapters 1, 6.4, 6.5, 7.2, 8 and Appendix E.

[5] Graf T, Therrien R and Simmons CT. Numerical aspects of variable-density flow: A systematic analysis of the Elder (1967) convection problem. Not included in this thesis.

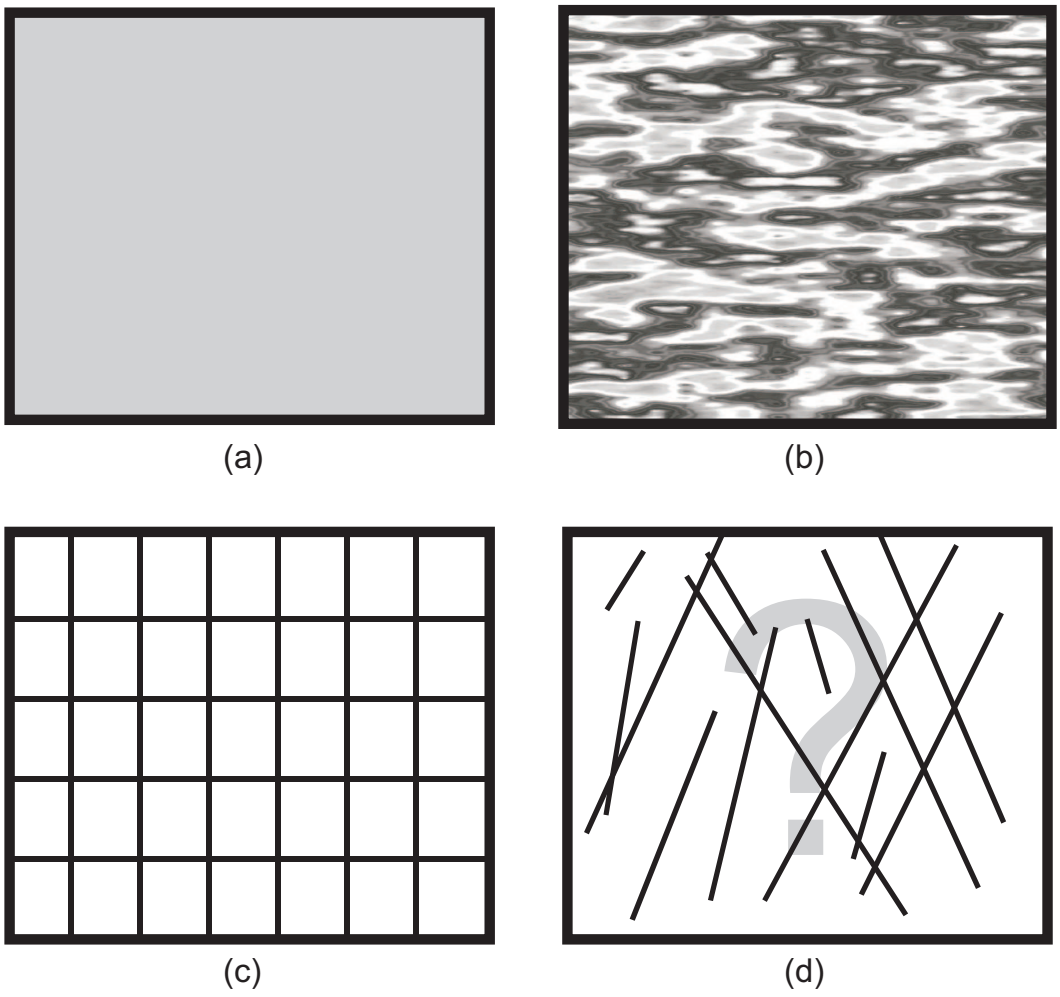

Figure 1.1: Different styles of geological media: (a) homogeneous porous medium, (b) heterogeneous porous medium, (c) fractured medium consisting of regular orthogonal fractures and (d) fractured geological medium with nonuniform fracture aperture, trace and orientation. In (a) and (b), the shades of grey represent hydraulic conductivity (Figure modified from Simmons et al. (2001)).

Chapter 2

Physicochemical System

The system to be modeled consists of transient convective flow and reactive silica transport within an irregular fracture network. Section 2.1 briefly explains the geostatistical laws that dictate how irregular networks are randomly generated. Unstable variable-density flow and transport in the networks generated will be examined in Section 6.3. The following Section 2.2 illustrates the simulated quartz-water system and how the reaction parameters are quantified from thermohaline conditions. In Section 2.3, variable-density flow phenomena (stable-unstable flow, free-forced-mixed convection) are described and the onset conditions for free convection are presented. The formulae used to calculate fluid properties as well as the equations which are used to update the physicochemical simulation parameters (matrix porosity, matrix permeability, fracture aperture and specific mineral surface area) using reaction rates are also shown.

2.1 Fracture Networks

The generation of realistic three-dimensional fracture networks for numerical simulations is extremely challenging. Fractures can be scanned from photos of outcrops, which gives a detailed 2D view but which is a very time-consuming method. Random fracture generators are more common, faster and can reach a high degree of sophistication.

However, 3D random fracture generators have the disadvantage that the space of the porous matrix between the fractures is hard to discretize once the fractures have been generated. This becomes even more challenging when fractures are considered as discs, polygons or non-planar 2D objects.

In this study, a 2D random fracture generator was developed. Complex 2D fracture networks can be randomly produced where fractures are two-dimensional rectangular planes. Fracture orientation, trace and aperture follow geostatistical distributions. Thus, fracture networks that are different and yet statistically equivalent can be produced. The discrete fractures are assumed to be of tectonic origin, leading to a conjugated system of two fracture families (Figure 2.1). Thus, fracture orientations, φ, follow a double-peak Gaussian distribution with the peaks at -30^{o} and +30^{o}.

It is assumed that fracture traces are distributed log-normally (Mathab et al., 1995) while fracture apertures obey an exponential distribution. The aperture is constant within each fracture. Furthermore, it is assumed that fracture traces and apertures correlate. Thus, few fractures of large trace and aperture exist while numerous fractures of small trace also have small apertures.

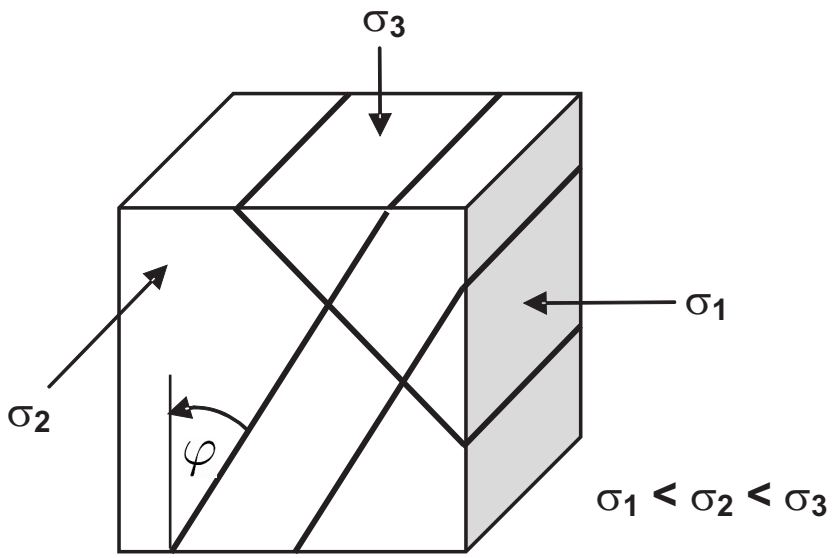

Figure 2.1: Conjugated system of two fracture families. Shown are the principal directions of normal stress, σ_i [M L^{-1} T^{-2}].

2.2 Chemical System

Rimstidt and Barnes (1980) experimentally studied the quartz-water system, which can be described by the following reaction

$$\mathrm{SiO_{2(s)}} \; + \; 2\,\mathrm{H_2O_{(aq)}} \; \underset{r_-}{\overset{r_+}{\rightleftharpoons}} \; \mathrm{H_4SiO_{4(aq)}} \tag{2.1}$$

where r_+ and r_- [both MOL $\mathrm{M^{-1}}$ $\mathrm{T^{-1}}$] are the dissolution and precipitation rates of quartz ($\mathrm{SiO_2}$), respectively. Note that $\mathrm{H_4SiO_4}$ and $\mathrm{Si(OH)_4}$ are regarded as chemically and physically identical (Tester et al., 1994). Upon applying the law of mass action to reaction (2.1), the rate of the forward reaction (dissolution), r_+, can be written as (Rimstidt and Barnes, 1980; Dove and Crerar, 1990; Dove and Nix, 1997; Dove, 1999; Ganor et al., 2005)

$$r_+ = \left(\frac{\partial m_{\mathrm{H_4SiO_4}}}{\partial t}\right)_{dissolution} = k_+^0 \; \frac{A_s}{M_w} \; a_{\mathrm{SiO_2}} \; a_{\mathrm{H_2O}}^2 \tag{2.2}$$

where $m_{\mathrm{H_4SiO_4}}$ [MOL $\mathrm{M^{-1}}$] is the molal concentration of silica, k_+^0 [MOL $\mathrm{L^{-2}}$ $\mathrm{T^{-1}}$] is the quartz dissolution rate constant in deionized water, A_s [$\mathrm{L^2}$] is the active surface area of quartz, M_w [M] is the mass of water and a_σ [here dimensionless] is the activity of species σ. It is assumed that pure solids and pure liquids (i.e. $\mathrm{SiO_2}$ and $\mathrm{H_2O}$) have activities equal to unity, such that $a_{\mathrm{SiO_2}} = a_{\mathrm{H_2O}} = 1$ (Krauskopf and Bird, 1995). The precipitation rate of reaction (2.1), r_-, describes a kinetic reaction of first order and can be evaluated with (Rimstidt and Barnes, 1980; Dove and Crerar, 1990; Dove and Nix, 1997; Dove, 1999; Ganor et al., 2005)

$$r_- = \left(\frac{\partial m_{\mathrm{H_4SiO_4}}}{\partial t}\right)_{precipitation} = -k_- \; \frac{A_s}{M_w} \; a_{\mathrm{H_4SiO_4}} \tag{2.3}$$

where k_- [M $\mathrm{L^{-2}}$ $\mathrm{T^{-1}}$] is the precipitation rate constant. The net production rate of dissolved silica, r_{net} [MOL $\mathrm{M^{-1}}$ $\mathrm{T^{-1}}$], is the sum of the dissolution rate (2.2) and the precipitation rate (2.3):

$$\left(\frac{\partial m_{\mathrm{H_4SiO_4}}}{\partial t}\right)_{net} = \left(\frac{\partial m_{\mathrm{H_4SiO_4}}}{\partial t}\right)_{dissolution} + \left(\frac{\partial m_{\mathrm{H_4SiO_4}}}{\partial t}\right)_{precipitation} \tag{2.4}$$

or

$$r_{net} = k_+^0 \; \frac{A_s}{M_w} - k_- \; \frac{A_s}{M_w} \; a_{\mathrm{H_4SiO_4}} \tag{2.5}$$

where the activity of silica, $a_{H_4SiO_4}$ [MOL M^{-1}], is the product of the activity coefficient $\gamma_{H_4SiO_4}$ [–] and the molal concentration $m_{H_4SiO_4}$ [MOL M^{-1}] of silica:

$$a_{H_4SiO_4} = \gamma_{H_4SiO_4} \cdot m_{H_4SiO_4} \tag{2.6}$$

At equilibrium, the amount of dissolved silica does not change with time and, thus, the left hand side of Equation (2.5) vanishes. Under this equilibrium condition, silica activity can be written as

$$a_{H_4SiO_4}^{equilibrium} = \frac{k_+^0}{k_-} = K_{eq} \tag{2.7}$$

where K_{eq} [MOL M^{-1}] is the quartz solubility or equilibrium constant of reaction (2.1). With (2.6), (2.7) and $k_+^0 = k_+^{corr}$, the quartz dissolution rate constant, corrected for salt water, the net rate of silica production in the porous matrix can finally be written as

$$r_{net} = \phi_{qz}\ k_+^{corr}\ A_{qz}\ \left(1 - \frac{\gamma_{H_4SiO_4}}{K_{eq}}\ m_{H_4SiO_4}\right) \tag{2.8}$$

and in a discrete fracture as

$$r_{net}^{fr} = \phi_{qz}^{fr}\ k_+^{corr}\ A_{qz}^{fr}\ \left(1 - \frac{\gamma_{H_4SiO_4}}{K_{eq}}\ m_{H_4SiO_4}^{fr}\right) \tag{2.9}$$

where $A_{qz} = A_s/M_w$ and $A_{qz}^{fr} = A_s^{fr}/M_w^{fr}$ [both L^2 M^{-1}] are the specific quartz surface areas in the porous matrix and in the fracture, respectively. The sign of the reaction rate indicates in which direction reaction (2.1) proceeds:

$$r_{net},\ r_{net}^{fr} \quad \begin{cases} < 0 & \text{system is supersaturated} \quad \rightarrow \text{precipitation of quartz} \\ = 0 & \text{system is equilibrated} \quad \rightarrow \text{no reaction} \\ > 0 & \text{system is subsaturated} \quad \rightarrow \text{dissolution of quartz} \end{cases}$$

This chemical model is based on the transition state theory and simulates reactive transport with a chemical kinetic reaction of mixed zeroth/first order. It is essentially the same as used by Rimstidt and Barnes (1980) and by White and Mroczek (1998), except that the rate law is also a function of the quartz volume fraction, ϕ_{qz}, as proposed by Johnson et al. (1998). The following paragraphs explain how the developed model quantifies parameters k_+^{corr}, $\gamma_{H_4SiO_4}$ and K_{eq}. All three functions are illustrated graphically in Figure D.1 in Appendix D.

Corrected Dissolution Rate Constant, k_+^{corr}

The quartz dissolution rate constant in deionized water, k_+^0, is commonly calculated using the Arrhenius equation (e.g. Lasaga, 1984; Steefel and Yabusaki, 1996):

$$k_+^0 = k_{25}^0 \exp\left[\frac{-E_a}{R^*}\left(\frac{1}{T} - \frac{1}{298.15}\right)\right] \tag{2.10}$$

where k_{25}^0 [MOL L^{-2} T^{-1}] is the known quartz dissolution rate constant in deionized water at 25°C, E_a [MOL^{-1} M L^2 T^{-2}] is the activation energy, necessary to overcome the potential energy maximum of the transition state and T [ϑ] is the absolute temperature. The universal gas constant, R^* [MOL^{-1} M L^2 T^{-2} ϑ^{-1}], and the constant k_{25}^0 are given in Rimstidt and Barnes (1980) as 8.3144 mol^{-1} kg m^2 sec^{-2} K^{-1} and 4.3×10^{-14} mol m^{-2} sec^{-1}, respectively. The values of E_a for quartz dissolution found in other studies range between 36 and 96 kJ mol^{-1}. The value 75.0 kJ mol^{-1} is applied as proposed by Rimstidt and Barnes (1980) and used in Steefel and Lasaga (1994) as well as in the software packages OS3D and GIMRT (Steefel and Yabusaki, 1996).

Equation (2.10) is valid for deionized water. However, Dove and Crerar (1990) have shown that the presence of electrolytes in the fluid can increase the reaction rate by 1.5 orders of magnitude. If solute concentrations are high, adsorbed cations give the quartz surface structure a form similar to that shown in Figure 2.2 (Dove and Crerar, 1990). Clearly, the bond angle, α, opens up if salt is present relative to silica dissolution in deionized water (Figure 2.2 below). Thus, the siloxane bond, indicated by a grey arrow in Figure 2.2, becomes more vulnerable to attacks by water dipoles. As a consequence, dissolution progresses faster in electrolyte solutions.

The concentration of the bivalent (IIA) cations (Mg^{2+}, Ca^{2+}) dominates the dissolution rate while the effect of monovalent (IA) cations (Na^+, K^+) is minor due to their less effective adsorption at low concentrations (Dove, 2004, personal communication). Dove (1999) demonstrated that the fraction of adsorption sites occupied by species Na^+, Mg^{2+} and Ca^{2+} can be expressed by a Langmuir model for equilibrium adsorption (Rimstidt and Dove, 1986; Blum and Lasaga, 1988; Dove and Crerar, 1990) as

$$\theta_{Na^+} = \frac{K_{ad}^{Na^+}\ m_{Na^+}}{1 + K_{ad}^{Na^+}\ m_{Na^+} + K_{ad}^{Mg^{2+}}\ m_{Mg^{2+}} + K_{ad}^{Ca^{2+}}\ m_{Ca^{2+}}} \tag{2.11}$$

$$\theta_{\mathrm{Mg^{2+}}} = \frac{K_{ad}^{\mathrm{Mg^{2+}}}\ m_{\mathrm{Mg^{2+}}}}{1 + K_{ad}^{\mathrm{Na^{+}}}\ m_{\mathrm{Na^{+}}} + K_{ad}^{\mathrm{Mg^{2+}}}\ m_{\mathrm{Mg^{2+}}} + K_{ad}^{\mathrm{Ca^{2+}}}\ m_{\mathrm{Ca^{2+}}}} \tag{2.12}$$

$$\theta_{\mathrm{Ca^{2+}}} = \frac{K_{ad}^{\mathrm{Ca^{2+}}}\ m_{\mathrm{Ca^{2+}}}}{1 + K_{ad}^{\mathrm{Na^{+}}}\ m_{\mathrm{Na^{+}}} + K_{ad}^{\mathrm{Mg^{2+}}}\ m_{\mathrm{Mg^{2+}}} + K_{ad}^{\mathrm{Ca^{2+}}}\ m_{\mathrm{Ca^{2+}}}} \tag{2.13}$$

where θ_σ [–] is the fraction of adsorption sites occupied by cation σ and where m_σ [MOL M^{-1}] and K_{ad}^{σ} [MOL^{-1} M] are the molal concentration and the equilibrium adsorption coefficient of σ, respectively. The quantity K_{ad}^{σ} does not vary significantly with temperature (Dove, 2004, personal communication) and can be taken for sodium, magnesium and calcium as $10^{1.78}$, $10^{3.7}$ and $10^{3.35}$ mol^{-1} kg, respectively (Dove, 1999). The developed model computes the constant k_{+}^{σ} from a fit to experimental data published by Dove (1999), who measured the dependence of quartz dissolution rates on different electrolyte concentrations at 200°C of sodium chloride, magnesium chloride and calcium chloride. Thus, the logarithm of the dissolution rate constant for $\mathrm{Na^{+}}$ can be written as

$$\log k_{200}^{\mathrm{Na^{+}}} = -\frac{2.8 \times 10^{-4}}{m_{\mathrm{Na^{+}}}} - 6.35 \tag{2.14}$$

and for $\mathrm{Mg^{2+}}$ and $\mathrm{Ca^{2+}}$ as

$$\log k_{200}^{\mathrm{Mg^{2+}}} = -\frac{2.2 \times 10^{-4}}{m_{\mathrm{Mg^{2+}}}} - 6.80 \tag{2.15}$$

and

$$\log k_{200}^{\mathrm{Ca^{2+}}} = -\frac{1.3 \times 10^{-6}}{(m_{\mathrm{Ca^{2+}}})^2} - 6.35 \tag{2.16}$$

where log denotes the decadic logarithm $\log_{10}$. With the help of the Arrhenius equation (2.10) and with Equations (2.14) to (2.16), the dissolution rate constant of species σ at any concentration and temperature can be formulated as

$$k_{+}^{\sigma} = k_{200}^{\sigma}\ \exp\left[\frac{-E_a}{R^*}\left(\frac{1}{T} - \frac{1}{473.15}\right)\right] \tag{2.17}$$

Using Equations (2.11) to (2.17), the corrected dissolution rate constant, k_{+}^{corr}, is defined here as

$$\begin{aligned} k_{+}^{corr} = {} & k_{+}^{\mathrm{Na^{+}}}\ \theta_{\mathrm{Na^{+}}} + k_{+}^{\mathrm{Mg^{2+}}}\ \theta_{\mathrm{Mg^{2+}}} + k_{+}^{\mathrm{Ca^{2+}}}\ \theta_{\mathrm{Ca^{2+}}} \\ & + k_{+}^{0}\Big[1 - (\theta_{\mathrm{Na^{+}}} + \theta_{\mathrm{Mg^{2+}}} + \theta_{\mathrm{Ca^{2+}}})\Big] \end{aligned} \tag{2.18}$$

where Dove's (1999) idea of competitive adsorption is adapted in order to account for protons "adsorbed" on the remaining sites (Figure 2.2), expressed by the last term in (2.18). This last term does not occur in Dove's (1999) original formulation of the dissolution rate constant in a mixed electrolyte solution. However, the term is necessary to obtain a correct rate constant in water of very low salinity, where $m_\sigma \rightarrow 0$, thus $\theta_\sigma \rightarrow 0$ and therefore $k_+^{corr} \rightarrow k_+^0$.

Electrolyte concentration and fluid temperature are the main factors that affect the quartz dissolution rate constant. However, it has been reported in the scientific literature that quartz dissolution is also a function of pH. In the past, this functionality has been investigated by various authors with very similar results. Brady and Walther (1989) found that between the pH of zero surface charge of quartz ($\mathrm{pH}_{zpc} = 2.4$) and pH 7, the dissolution rate constant in deionized water remains nearly constant. However, between pH 8 and pH 12, they observed that the rate increases by about 0.3 log rate units per increasing pH unit. Bennett et al. (1988) and Bennett (1991) only investigated the case of pH less than 7 and quantified the pH dependence as 0.1 and 0.1-0.2 log rate units per pH unit, respectively. These quantities should be regarded with care, though, because their determination is based on very few data points and, therefore, an accurate relationship at pH < 7 is "not definable" (Bennett, 1991). Since H_4SiO_4 is a weak acid, the pH of the system investigated in this study is expected to be in the range slightly below pH 7. In this range, the changes of the dissolution rate constant are "small [...] and difficult to interpret" (Bennett, 1991). Therefore, the pH dependency of quartz dissolution rates is neglected in this study.

Activity Coefficient, $\gamma_{\mathbf{H_4SiO_4}}$

The magnitude of γ_σ relative to 1.0 indicates in which way the solubility of species σ changes relative to its solubility in deionized water:

$$\gamma_\sigma \begin{cases} < 1 & \text{higher solubility of species } \sigma \\ = 1 & \text{no change in solubility} \\ > 1 & \text{lower solubility of species } \sigma \end{cases}$$

In an electrolyte solution, the solubility of a neutral species, such as H_4SiO_4, is a function of the amount of dissolved salt and temperature. Marshall and Chen (1982) have proposed a modified form of the Setchenow equation to calculate the activity coefficient of H_4SiO_4 in a mixed electrolyte solution at any given temperature:

$$\log \gamma_{H_4SiO_4} = \sum_{\sigma} D_\sigma m_\sigma \tag{2.19}$$

where D_σ is the dimensionless, temperature dependent Marshall-Chen coefficient of ion σ and m_σ is the molal concentration [MOL M^{-1}] of σ. Marshall and Chen (1982) give values of D_σ for species Na^+, Mg^{2+}, Cl^- and SO_4^{2-} in the temperature range 25°C to 300°C. Due to the physicochemical similarity of magnesium and calcium, their Marshall-Chen coefficients are assumed to be identical, such that $D_{Ca^{2+}} = D_{Mg^{2+}}$. A further assumption is made here that the D_σ can be extrapolated beyond the 25°C to 300°C temperature range down to 0°C.

Equilibrium Constant, K_{eq}

In the developed model, the equilibrium constant, K_{eq}, is expressed as a function of absolute temperature, T, over the temperature range 0°C to 300°C (Rimstidt, 1997):

$$\log K_{eq} = -\frac{1107.12}{T} - 0.0254 \tag{2.20}$$

Other models use an apparent solubility, which also accounts for the impact of salinity (Fournier, 1983; von Damm et al, 1991; Shibue, 1994; Mroczek and Christenson, 2000). However, the present model takes ion activity into consideration by calculating nonzero Marshall-Chen coefficients in Equation (2.19) and by, thus, employing silica activity coefficients that are greater than or equal to one. In the calculation of quartz solubility, two more assumptions are made. Krauskopf and Bird (1995) showed that below pH 9, there is no influence of pH on quartz solubility. In addition, White and Mroczek (1998) demonstrated that the pressure effect on quartz solubility is insignificant within the temperature range considered in this study.

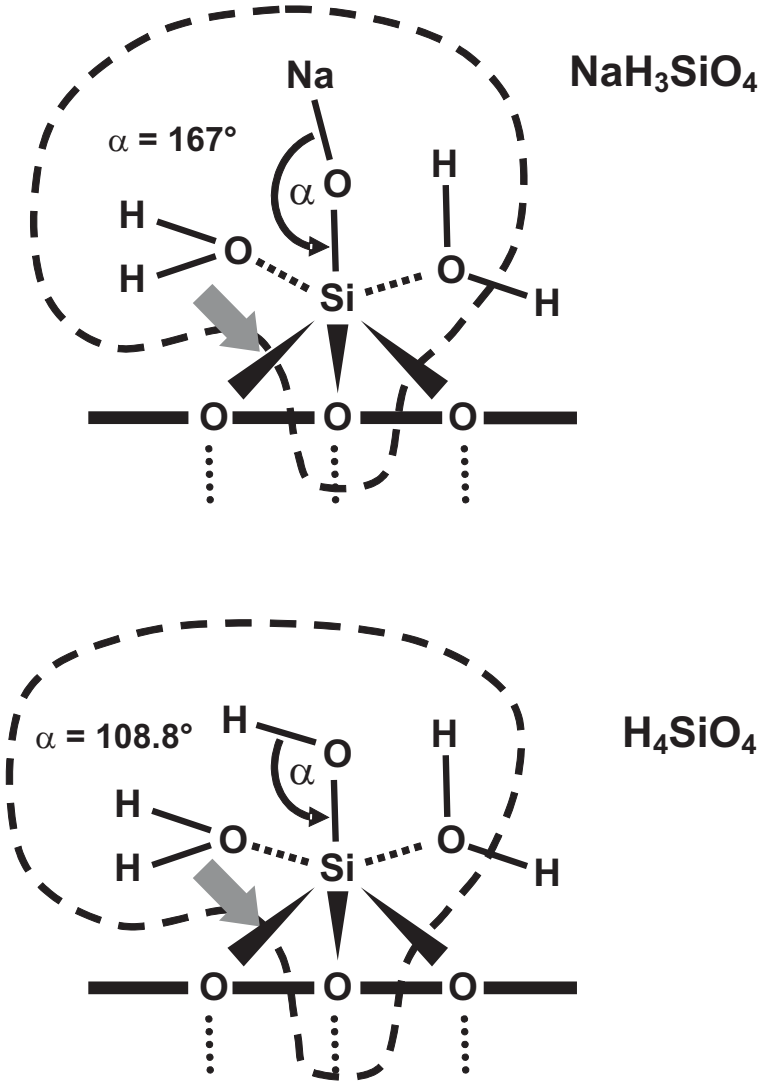

Figure 2.2: Dissolution of silica in deionized water (below) and in an electrolyte solution (above). The grey arrow indicates one of the two siloxane bonds, which have to be broken. This bond is less accessible to water dipoles in deionized water. Thus, dissolution rates are higher in saline solutions (Dove and Crerar, 1990).

2.3 Physical System

Convection Phenomena

In flow fields where a non-zero hydraulic gradient is created by externally applied forces and where density effects are neglected, fluid flow is purely hydraulically driven. This phenomenon is called forced convection. In contrast, if the hydraulic gradient is uniquely created by spatial density differences, the occurring displacement of fluid mass is buoyancy-driven. This second flow phenomenon is called free convection. However, if spatiotemporal density differences are observed, the flow is not necessarily density-driven. Density differences may be too small to induce movement of fluid and the system remains stable. In this case, solutes are only transported by molecular diffusion. On the other hand, larger density differences may provoke free convective flow, resulting in regional downwards movement of dense fluid (fingering), which is counterbalanced by upwards flow in upwelling regions. Such flow regimes are unstable and solutes are transported by molecular diffusion and advection.

Flow regimes where the fluid flow is both hydraulically and buoyancy-driven are referred to as mixed convective flow systems. Shikaze et al. (1998) demonstrated that the magnitude of the imposed hydraulic gradient controls whether forced or free convection is the dominant flow mechanism in mixed convective fractured systems. Thermal convection occurs when temperature differences cause a density gradient, whereas solute or haline convection is due to salinity differences. If both temperature and salinity impact fluid density, the convective flow is termed thermohaline. More details on convective flow phenomena in porous media can be found in Holzbecher (1998) and in Nield and Bejan (1999).

In numerical simulations, spatial dimensionality is a key factor that influences the pattern of free convection within the finite element grid. In nature, free convection in wells and fractures is physically possible. However, representing an open borehole or a discrete fracture by one-dimensional segments completely inhibits numerically simulating convection within such 1D elements (Shikaze et al., 1998). In vertical two-dimensional representations of the flow domain, convection cells with rotation axes

normal to the 2D grid, can be numerically simulated. In this case, the 2D domain can represent a vertical porous layer (Horton and Rogers, 1945; Lapwood, 1948; Caltagirone, 1975; Elder, 1967; Weatherill et al., 2004), a tilted porous layer (Bories and Combarnous, 1973; Weatherill et al., 2004), a highly permeable fault zone (Murphy, 1979; Shi, 2005) or a discrete fracture. A fully three-dimensional representation of the model domain allows free convection to occur in multiple ways. This has been studied in aqueous systems (Bénard, 1900), highly permeable fault zones (Malkovsky and Pek, 1997; 2004) and porous media (Davis, 1967; Beck, 1972; Diersch and Kolditz, 1998).

Onset Condition of Free Convection

In homogeneous isotropic media, the onset of free convection can be determined by the value of the dimensionless Rayleigh number, Ra (Rayleigh, 1916). The Rayleigh number is the ratio between buoyancy forces driving free convective flow and dispersive/viscous forces tending to dissipate unstable flow by enhanced mixing. If density gradients are caused by differences in salt content, the haline Rayleigh number is defined as (Wooding, 1997a; Simmons et al., 2001; Weatherill et al., 2004):

$$Ra = \frac{\rho_0 g \alpha^{salt} \kappa (\Delta c) \ell_z}{\phi \mu_0 D_0} \tag{2.21}$$

where Δc [–] is the concentration difference between top and bottom boundaries and where ℓ_z [L] is the height of the domain. If concentration differences are small and/or if dispersion caused by molecular diffusion is large, Ra is small indicating that the system is stable. On the other hand, a large concentration difference and/or less diffusion may cause unstable, density-driven flow. In this case, the Rayleigh number exceeds the threshold value Ra_c, which is the critical Rayleigh number.

In an infinitely extended 3D horizontal layer, the value of Ra_c depends on the boundary conditions for flow and transport. If all domain boundaries are impermeable for flow, top and bottom boundaries are assigned constant concentrations and all other boundaries are assigned zero-dispersive flux conditions, Ra_c has the value $4\pi^2$ (Nield and Bejan, 1999). In a system where $Ra > 4\pi^2$, square convection cells of width ℓ_z form. If a second threshold, Ra_{c2}, is exceeded, the convection cells are unstable with time. Values of Ra_{c2} are in the range of 240-280 according to Nield and Bejan (1999)

or in the range of 240-300 according to Diersch and Kolditz (2002).

In a 3D horizontal layer of finite length, the value of Ra_c also depends on how well convection cells "fit" in the domain. The ability of cells to fit in the domain depends on the two aspect ratios A and B (Horton and Rogers, 1945; Lapwood, 1948):

$$\mathrm{A} = \frac{\ell_x}{\ell_z} \qquad\qquad \mathrm{B} = \frac{\ell_y}{\ell_z} \tag{2.22}$$

Caltagirone (1982) accounted for the dependence of Ra_c on aspect ratios. He presented an analytically derived critical Rayleigh number for a three-dimensional bounded layer:

$$Ra_c = \min_{\mathrm{i,j}} \frac{\pi^2 \left(\frac{\mathrm{i}^2}{\mathrm{A}^2} + \frac{\mathrm{j}^2}{\mathrm{B}^2} + \mathrm{k}^2\right) \left(\mathrm{A}^2\mathrm{i}^2\mathrm{k}^2 + \mathrm{B}^2\mathrm{j}^2\mathrm{k}^2 + \left(\mathrm{i}^2 + \mathrm{j}^2\right)^2\right)}{\left(\mathrm{i}^2 + \mathrm{j}^2\right)^2} \tag{2.23}$$

where i, j and k are integers. The 2D solution to (2.23) is achieved by setting $\mathrm{j} = 0$. In this case, the critical Rayleigh number is only a function of aspect ratio A:

$$Ra_c = \min_{\mathrm{i}} \frac{\pi^2 \left(\frac{\mathrm{i}^2}{\mathrm{A}} + \mathrm{k}^2\mathrm{A}\right)^2}{\mathrm{i}^2} \tag{2.24}$$

If and only if the aspect ratio A is an integer, the critical 2D Rayleigh number Ra_c reaches the minimum value $4\pi^2$. In this case, all convection cells form undistorted perfect circles. If A is not an integer, Ra_c exceeds the minimum value $4\pi^2$ because convection cells can not form in their preferred circular shape. For $\mathrm{A} < 1$, Ra_c can be several orders of magnitude larger than its minimum.

If the normal of a homogeneous isotropic layer is inclined by the angle φ, the Rayleigh number and its critical threshold can be calculated as (Caltagirone, 1982; Weatherill, 2004):

$$Ra^* = \frac{Ra}{\cos\varphi} \qquad\qquad Ra_c^* = \frac{Ra_c}{\cos\varphi} \tag{2.25}$$

The dimensionless Sherwood number, Sh, describes unstable flow in time. The Sherwood number defines the ratio between total solute mass flux and diffusive mass flux through a surface:

$$Sh = \frac{J_{total}}{J_{diffusion}} = \frac{J_{advection} + J_{dispersion} + J_{diffusion}}{J_{diffusion}} \tag{2.26}$$

A system is stable if all velocities are zero. In that case, diffusion is the only transport mechanism and $Sh = 1$, which is the minimum value of Sh. Unstable systems are characterized by $Sh > 1$, indicating solute transport by advection and dispersion in addition to that caused by diffusion alone. For unstable flow through the upper boundary of a model domain, Sh is defined here as

$$Sh = \frac{J_{total}}{\phi\tau D_d \left(\Delta C/\ell_z\right) \ell_x \ell_y} \tag{2.27}$$

where ΔC [M L^{-3}] is the maximum concentration difference across the model domain that is of size $\ell_x \times \ell_y \times \ell_z$. The Sherwood number is similar to the Nusselt number Nu, which is the ratio between total heat transfer and conductive heat transfer (Nusselt, 1944; Holzbecher, 1998). While Nu is a stability criterion for thermal convection, Sh is the mass-transfer equivalent for haline convection (Kreith, 1965).

Fluid Properties

In thermohaline convection problems, both fluid properties, density and viscosity, are a function of temperature and salinity, while the effect of pressure can be ignored (Bolton et al., 1996). In the developed model, both fluid quantities are first calculated as a function of temperature alone (ρ_T^0, μ_T^0) and then modified to account for salinity. The following paragraphs explain how the model quantifies the fluid properties ρ and μ and how solid phase properties are updated. The density and viscosity functions are illustrated graphically in Figure D.1 in Appendix D.

Under isobaric conditions, the fluid density is calculated as a function of temperature (ρ_T^0) for different temperature ranges (Holzbecher (1998) and references therein):

$$\rho_T^0 = \begin{cases} 1000 \cdot \Big(1 - \big([T_C - 3.98]^2/503570\big) \cdot \big([T_C + 283]/[T_C + 67.26]\big)\Big) \\ \qquad\qquad \text{for } 0^{\text{o}}\text{C} \leq T_C \leq 20^{\text{o}}\text{C} \\ 996.9 \cdot \Big(1 - 3.17 \times 10^{-4}\ [T - 298.15] - 2.56 \times 10^{-6}\ [T - 298.15]^2\ \Big) \\ \qquad\qquad \text{for } 20^{\text{o}}\text{C} < T_C \leq 175^{\text{o}}\text{C} \\ 1758.4 + 1000 \cdot T\ \Big(- 4.8434 \times 10^{-3} + T\ \Big(1.0907 \times 10^{-5} \\ \qquad -T \cdot 9.8467 \times 10^{-9}\Big)\Big) \qquad \text{for } 175^{\text{o}}\text{C} < T_C \leq 300^{\text{o}}\text{C} \end{cases} \tag{2.28}$$

where T_C $[\vartheta]$ and T $[\vartheta]$ are the temperatures in Celsius and Kelvin, respectively. In a second step, the fluid density at any given salinity and temperature is evaluated using the freshwater density at temperature T, ρ_T^0, and from the sum of all species concentrations using the following empirical relation

$$\rho = \rho_T^0 + \alpha^{salt} \cdot \sum_\sigma C_\sigma \tag{2.29}$$

where α^{salt} $[\text{M}^{-1}\ \text{L}^3]$ is the solutal expansion coefficient. The impact of dissolved silica on fluid density is not significant below 350°C (Fournier, 1983; Mroczek and Christenson, 2000) and, therefore, ignored in Equation (2.29). The developed model calculates density from the concentration of eight major ions found in natural waters: Na^+, K^+, Ca^{2+}, Mg^{2+}, Cl^-, SO_4^{2-}, CO_3^{2-} and HCO_3^-. The empirical law (2.29) is calibrated using Pitzer's ion interaction model (Monnin, 1989; 1994), which calculates fluid density from the partial electrolyte volumes. The Monnin model is more precise than Equation (2.29) but also very time-consuming because it iterates between fluid density and species molality. The Monnin model was used here to derive an empirical expression for α^{salt} as a function of the groundwater chemistry in the Canadian Shield given by Farvolden et al. (1988) in the form

$$\alpha^{salt} = -0.0829 \cdot \ln\left(\sum_\sigma C_\sigma\right) + 1.1415 \tag{2.30}$$

where C_σ $[\text{M}\ \text{L}^{-3}]$ must be given in mg l^{-1}.

Although the fluid viscosity is assumed constant in some studies of thermohaline transport (Turner, 1979; Tyvand, 1980; Evans and Nunn, 1989; Yoshida et al., 1995), it

is recommended to relate viscosity to both temperature (Bolton et al., 1996) and salinity (Freedman and Ibaraki, 2002) because it can increase by a factor of two between pure water and a dense brine (Oldenburg and Pruess, 1998). Different relations to calculate fluid viscosity from temperature are used that cover different temperature ranges:

$$\mu_T^0 = \begin{cases} 1.787 \times 10^{-3} \cdot \exp\Big(\big(-0.03288 + 1.962 \times 10^{-4} \cdot T_C \big) \cdot T_C \Big) \\ \qquad\qquad\qquad\qquad\qquad\qquad \text{for } 0^{\circ}\text{C} \leq T_C \leq 40^{\circ}\text{C} \\ 10^{-3} \cdot \Big(1 + 0.015512 \cdot [T_C - 20]\Big)^{-1.572} \qquad \text{for } 40^{\circ}\text{C} < T_C \leq 100^{\circ}\text{C} \\ 0.2414 \cdot 10\hat{}\Big(247.8/[T_C + 133.15]\Big) \qquad \text{for } 100^{\circ}\text{C} < T_C \leq 300^{\circ}\text{C} \end{cases} \tag{2.31}$$

The relationship between $0^{\circ}\text{C} \leq T_C \leq 40^{\circ}\text{C}$ is used by Molson et al. (1992), the other two relations are given by Holzbecher (1998) and references therein. Finally, viscosity is expressed as a function of salinity and temperature by substituting the temperature-dependent freshwater viscosity, μ_T^0, in the the Jones-Dole equation:

$$\mu = \mu_T^0 \cdot \left(1 + \sum_{\sigma} B_\sigma M_\sigma\right) \tag{2.32}$$

where M_σ is the molar concentration of species σ. Marcus (1985) gives values of the $B-$coefficients [L^3 MOL^{-1}] for each species.

Solid Phase Properties

Chemical reactions have a significant impact on a number of physical flow and transport properties. In the developed model, the quartz volume fraction, ϕ_{qz} [–], is recalculated using (Steefel and Yabusaki, 1996; Steefel and Lasaga, 1994):

$$\frac{\partial \phi_{qz}}{\partial t} = -V_{qz}\ r_M^{L+1} \tag{2.33}$$

where V_{qz} [MOL^{-1} L^3] is the molar volume of quartz and r_M^{L+1} [MOL L^{-3} T^{-1}] is the molar reaction rate at time level $L+1$. In finite difference form, this equation becomes

$$\phi_{qz}^{L+1} = \phi_{qz}^{L} - \Delta t\ V_{qz}\ r_M^{L+1} \tag{2.34}$$

where $\Delta t = t^{L+1} - t^L$ [T] is the time step size. The molar volume of a mineral is the ratio of its molecular weight to its density (Langmuir, 1997). The model updates porosity from the sum of all mineral volume fractions:

$$\phi^{L+1} = 1 - \sum_{\sigma} \phi_{\sigma}^{L+1} \tag{2.35}$$

where it is assumed that quartz is the only reactive solid species, thus $\phi_\sigma = constant$ for $\sigma \neq$ quartz. The specific surface area in the porous matrix is recalculated by means of the two-thirds power relation given by Steefel and Yabusaki (1996) as

$$A_{qz}^{L+1} = A_{qz}^{init} \begin{cases} \left[\left(\phi^{L+1}/\phi^{init}\right) \cdot \left(\phi_{qz}^{L+1}/\phi_{qz}^{init}\right)\right]^{2/3} & \text{dissolution of quartz} \\ \\ \left(\phi^{L+1}/\phi^{init}\right)^{2/3} & \text{precipitation of quartz} \end{cases} \tag{2.36}$$

where A_{qz}^{init} [L^2 M^{-1}] is the initial specific surface area in the matrix and where ϕ^{init} [–] and ϕ_{qz}^{init} [–] are the initial matrix porosity and quartz fraction, respectively.

The matrix permeability, κ_{ij} [L^2], is calculated from porosity for the special case of dissolution and precipitation of quartz as given by Weir and White (1996):

$$\kappa_{ij}^{L+1} = \kappa_{ij}^{init} \cdot \left\{ 1 - \left[1 - \left(\frac{\phi^{L+1} - \phi_c}{\phi^{init} - \phi_c} \right)^{1.58} \right]^{0.46} \right\} \tag{2.37}$$

where κ_{ij}^{init} is the initial permeability and ϕ_c is the critical porosity at which $\kappa_{ij} = 0$. This relation is obtained from theoretical considerations of deposition and dissolution of quartz grains, arranged in a rhombohedral array of uniform spheres (Weir and White, 1996). Similar to matrix porosity, fracture apertures are recalculated from (Steefel and Lichtner, 1998ab):

$$(2b)^{L+1} = (2b)^L \cdot \left(1 + \Delta t \; V_{qz} \; r_M^{L+1}\right) \tag{2.38}$$

and, finally, the specific surface area in the fracture is updated using (Steefel and Lichtner, 1998a):

$$A_{qz}^{fr,L+1} = A_{qz}^{fr,init} \cdot \left(\frac{(2b)^{L+1}}{(2b)^{init}} \right) \tag{2.39}$$

where $A_{qz}^{fr,init}$ [L^2 M^{-1}] is the initial specific surface area in the fracture and where $(2b)^{init}$ [L] is the initial fracture aperture. The initial surface area in a two-dimensional

rectangular fracture element is the ratio between active surface area, given by $A_s = 2\omega\ L_x L_z$, and the mass of water stored in the 2D element, $M_w = \rho \cdot (2b)\ L_x L_z$, where ω [–] is the fracture roughness coefficient (Figure 2.3). Thus, a fluid moving through a large fracture will encounter less mineral surface area per unit fluid mass than will a fluid moving through a narrow fracture, expressed by the following relation for the initial specific surface area:

$$A_{qz}^{fr,init} = \frac{\omega}{\rho\ b} \tag{2.40}$$

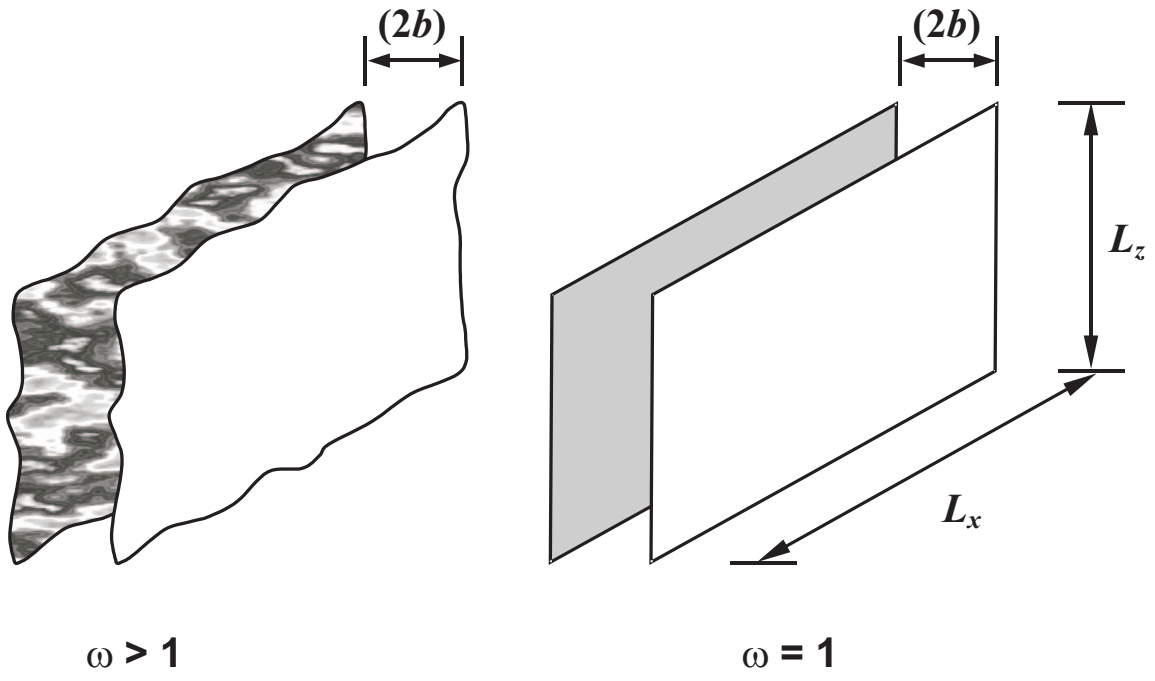

Figure 2.3: Fracture roughness coefficient for rough-walled (left) and smooth fractures.

Chapter 3

Governing Equations

The purpose of this chapter is to present the equations that govern the physicochemical system described in the previous chapter. Usually the continuum approach mathematically describes the fundamental processes of flow and transport. As both flow and transport vary in space, a sufficiently small volume is chosen for which both mass and flow quantities can be quantified. The physically exact treatment of flow and transport at the microscopic level is not possible due to the naturally high degree of complexity of geological media. Therefore, physical properties are averaged over a greater spatial scale, the macroscopic level. Flow and transport are balanced over the smallest volume possible that is large enough to justify parameter averaging. This volume is called representative elementary volume (REV [L^3]) and its size is $\Delta x \cdot \Delta y \cdot \Delta z$. Characteristic of the continuum approach is the formulation of a balance for both fluid mass and solute mass conservation over an REV. The results are two continuity equations, one for flow (coming from the fluid mass balance) and one for transport (coming from the solute mass balance).

Continuity is achieved if the net (fluid or solute) mass flux rate $\Delta\hat{j} = \hat{j}_{in} - \hat{j}_{out}$ [M T^{-1}] through the REV equals the temporal change of mass within the REV, $\partial M/\partial t$. In its most general form, the continuity equation is

$$\Delta\hat{j} \ \pm \ \Gamma_m \cdot \mathrm{REV} = \frac{\partial M}{\partial t} \tag{3.1}$$

where Γ_m [M L^{-3} T^{-1}] represents sources and sinks and where t [T] is time. This

general law can be used to derive the governing equations for both fluid flow and solute transport.

3.1 Constitutive Equations

The model uses the equivalent freshwater head h_0 [L], defined by Frind (1982) as

$$h_0 = \frac{P}{\rho_0 g} + z \tag{3.2}$$

where P [M L^{-1} T^{-2}] is the dynamic fluid pressure, ρ_0 [M L^{-3}] is the reference fluid density, g [L T^{-2}] is the gravitational acceleration and z [L] is the elevation above datum. The transport variable is the dimensionless relative concentration, c, which varies between 0 and 1. It is linked with density through the linear relationship

$$\rho_r = \gamma c \tag{3.3}$$

where ρ_r is the dimensionless relative density, defined in Frind (1982) as

$$\rho_r = \frac{\rho}{\rho_0} - 1 \tag{3.4}$$

where ρ [M L^{-3}] is the fluid density. The dimensionless constant γ is the maximum relative density given by

$$\gamma = \frac{\rho_{max}}{\rho_0} - 1 \tag{3.5}$$

where the assumption is made that the solute concentration of a fluid with the density $\rho = \rho_{max}$ is $c_{max} = 1$. It is also assumed that the impact of salinity on fluid viscosity is negligible.

Another transport variable is the solute concentration, expressed as volumetric mass, C [M L^{-3}]. If this variable is used, relative density is not calculated from the relative concentration as in (3.3) but directly from the fluid density as in (3.4), which is a function of the individual species concentrations and temperature (2.29). The fluid viscosity, μ [M L^{-1} T^{-1}], may also be nonuniform and related to the concentrations of all mobile components.

Under variable-density flow conditions, the Darcy flux, $q_i = \phi v_i$ [L T^{-1}], is a function of both the physical flow variable, h_0, and the chemical property, ρ_r. The Darcy flux in porous media can be completely expressed in terms of freshwater properties (after Frind (1982)):

$$q_i = -K_{ij}^0 \frac{\mu_0}{\mu} \left(\frac{\partial h_0}{\partial x_j} + \rho_r \eta_j \right) \qquad i,j = 1,2,3 \tag{3.6}$$

where the assumption of a horizontal datum (i.e. $\partial z / \partial z = 1$) is made and where η_j [–] represents the direction of flow with $\eta_j = 0$ in the horizontal directions and $\eta_j = 1$ in the horizontal directions (Frind, 1982). Using the ratio between the reference fluid viscosity, μ_0, and the fluid viscosity, μ [both M L^{-1} T^{-1}], the hydraulic conductivity of the porous medium, K_{ij}^0 [L T^{-1}], is the freshwater property (Bear, 1988):

$$K_{ij}^0 = \frac{\kappa_{ij} \rho_0 g}{\mu_0} \tag{3.7}$$

A three-dimensional Cartesian coordinate system is assumed, where the axes are co-linear with the principal directions of anisotropy. With this assumption, cross terms (K_{ij}^0 where $i \neq j$) in the hydraulic conductivity tensor vanish.

The Darcy flux in differently oriented two-dimensional fracture faces is calculated using the following form of the Darcy equation, presented by Bear (1988) for an inclined one-dimensional tube

$$q_s = -\frac{\kappa}{\mu} \left(\frac{\partial P}{\partial s} + \rho g \frac{\partial z}{\partial s} \right) \tag{3.8}$$

where s [L] is the axis along the tube and where κ [L^2] is the permeability of the porous material in the tube. The fluid pressure in (3.8) can be written in terms of equivalent freshwater head using relation (3.2). With relation (3.7) and because $\partial z / \partial s$ is the cosine of the slope, the Darcy flux in a fracture element can be written as

$$q_i^{fr} = -K_0^{fr} \frac{\mu_0}{\mu^{fr}} \left(\frac{\partial h_0^{fr}}{\partial x_j} + \rho_r^{fr} \eta_j \cos\varphi \right) \qquad i,j = 1,2 \tag{3.9}$$

where η_j is 0 in the horizontal direction and 1 along the fracture incline. The incline of a fracture face is given by φ with $\varphi = 0^o$ for a vertical face and $\varphi = 90^o$ for a horizontal face. In the case of flow within fractures, a local two-dimensional Cartesian coordinate system is assumed. The freshwater hydraulic conductivity of the fracture, K_0^{fr} [L T^{-1}], is derived from the parallel plate model as

$$K_0^{fr} = \frac{(2b)^2 \rho_0 g}{12 \mu_0} \tag{3.10}$$

where $(2b)$ [L] is the fracture aperture. The application of Darcy's law in fractures (3.9) requires that the Reynolds number be smaller than 1 (Bear and Verruijt, 1987).

Both Darcy equations, (3.6) and (3.9), embody the effects of both forced and free convection. The former is controlled by the magnitude and sign of the hydraulic head gradient, $\partial h_0/\partial x_i$, while the latter is represented by the buoyancy term, $\rho_r \eta_j$. The relative density is positive if salinity is high, reducing the Darcy flux in the vertical direction. In fracture elements, using the cosine-weighted buoyancy term, $\rho_r^{fr} \eta_j \cos\varphi$, allows computing the Darcy flux in fracture elements of any incline φ. In a vertical face ($\varphi = 0^o$), the contribution of buoyancy to the Darcy flux has a maximum because $\cos\varphi$ becomes 1 while in a horizontal face ($\varphi = 90^o$), density effects do not contribute to the Darcy flux because $\cos\varphi$ vanishes.

3.2 Variable-Density Flow

The fluid mass balance equation can be derived from Equation (3.1) by assuming 1D flow in x-direction for the moment. Then, $\hat{j}$ [M T^{-1}] is equal to $Q_x \cdot \Delta y\ \Delta z$, where $Q_x = \phi \rho v_x$ [M L^{-2} T^{-1}] is the flow rate of fluid mass along the x-axis. Upon writing the fluid mass that is stored in the REV as $M = \phi\rho \cdot \Delta x\ \Delta y\ \Delta z$ [M] and with the assumption that both fluid and matrix are compressible, the three-dimensional flow continuity equation is commonly written in vector form as

$$-\nabla \bullet (\phi\rho\ \mathbf{v}) \pm \Gamma_m = \frac{\partial(\phi\rho)}{\partial t} \tag{3.11}$$

where ϕ is the dimensionless porosity, ∇ [L^{-1}] is the divergence operator and $\mathbf{v}$ [L T^{-1}] is the average fluid velocity vector. A single Newtonian fluid is assumed, where the dynamic viscosity is constant at all shear rates under isothermal and isobaric conditions.

Omitting sources and sinks and upon applying the product rule, the left hand side of (3.11) can be written as $-\rho\ \nabla \bullet (\phi\mathbf{v}) - (\phi\mathbf{v}) \bullet \nabla\rho$. A usual simplification of (3.11) is the application of the Oberbeck-Boussinesq (OB) approximation (Oberbeck, 1879; Boussinesq, 1903). The OB assumption reflects to what degree density variations are accounted for. It is common to consider density effects only in the buoyancy term of the momentum equations (3.6) and (3.9), and to neglect density in the fluid and

solute mass conservation equations. This first level of the OB assumption is generally correct because spatial density variations, $\nabla\rho$, are commonly minor, relative to density, ρ. Thus, the left hand side of (3.11) simplifies to $-\rho\ \nabla\bullet(\phi\mathbf{v})$ and the fluid mass balance equation becomes

$$-\nabla\bullet(\phi\mathbf{v}) = \frac{1}{\rho}\ \frac{\partial(\phi\rho)}{\partial t} \tag{3.12}$$

The term $(\phi\mathbf{v})$ on the left of (3.12) can now be replaced by the Darcy flux, $\mathbf{q}$, given in scalar form by (3.6) and (3.9). The right hand side of (3.12) represents the compressibility of both the medium and the fluid. For flow in porous media, the compressiblity is commonly expressed as $S_S \cdot \partial h_0/\partial t$, where S_S [L^{-1}] is the specific storage of the porous matrix, given as (Bear, 1988; Domenico and Schwartz, 1998)

$$S_S = \rho_0 g(\alpha_m + \phi\alpha_{fl}) \tag{3.13}$$

where α_m [M^{-1} L T^2] and α_{fl} [M^{-1} L T^2] are the matrix and fluid compressibility, respectively. Because matrix compressibility is two orders of magnitude greater than fluid compressibility, it is assumed here that changes in porosity do not impact specific storage in the porous matrix. Thus, the equation that governs saturated variable-density, variable-viscosity flow in porous media has the following parabolic scalar form in three dimensions

$$\frac{\partial}{\partial x_i}\left[K_{ij}^0\frac{\mu_0}{\mu}\left(\frac{\partial h_0}{\partial x_j} + \rho_r\eta_j\right)\right] = S_S\frac{\partial h_0}{\partial t} \qquad\qquad i,j = 1,2,3 \tag{3.14}$$

The specific storage in an open fracture, S_S^{fr} [L^{-1}], can be derived from (3.13) by assuming that the fracture is essentially incompressible, such that $\alpha_m = 0$, and by setting its porosity to 1. It is also assumed that changes in fracture aperture have no impact on specific storage in fractures:

$$S_S^{fr} = \rho_0 g\alpha_{fl} \tag{3.15}$$

Flow in an open discrete fracture takes place in two dimensions. Therefore, the corresponding governing equation is defined in a local 2D coordinate system. The governing variable-density flow equation in fractured media is similar to that presented by several authors (Berkowitz et al., 1988; Sudicky and McLaren, 1992; Shikaze et al.,

1998; Therrien et al., 2004):

$$(2b)\left\{\frac{\partial}{\partial x_i}\left[K_0^{fr}\frac{\mu_0}{\mu^{fr}}\left(\frac{\partial h_0^{fr}}{\partial x_j}+\rho_r^{fr}\eta_j\cos\varphi\right)\right]-S_S^{fr}\,\frac{\partial h_0^{fr}}{\partial t}\right\}+q_{n|I^+}-q_{n|I^-}=0$$

$$i,j=1,2 \qquad (3.16)$$

where the last two terms represent normal components of fluid flux across the boundary interfaces (I^+ and I^-) that separate the fracture and the porous matrix. In the conceptual model, fractures are idealized as two-dimensional parallel plates. Therefore, both the total head, h_0^{fr}, and the relative density, ρ_r^{fr}, are uniform across the fracture width.

The boundary conditions for Equations (3.14) and (3.16) can be of first-, second- or third-type as defined by Frind (1982) or by Istok (1989).

3.3 Reactive Solute Transport

The governing equation for reactive solute transport can also be derived from Equation (3.1). In this case, the solute mass stored in the REV is $M=\phi C\cdot\Delta x\ \Delta y\ \Delta z$ [M]. Let the mass flux rate, $\hat{j}$ [M T^{-1}], be the solute flux rate in x-direction, $\hat{j}=J_x\cdot\Delta y\ \Delta z$, where J_x [M L^{-2} T^{-1}] is the sum of advective flux, $J_x^{advection}=q_xC$, and dispersive-diffusive Fickian flux, $J_x^{dispersion}+J_x^{diffusion}=-\phi D_{xx}\ (\partial C/\partial x)$. Then, for a sorptive species, the governing transport equation in porous media has the three-dimensional scalar parabolic-hyperbolic form (Bear, 1988)

$$\frac{\partial}{\partial x_i}\left(\phi D_{ij}\frac{\partial C}{\partial x_j}-q_iC\right)+\Gamma_m=\frac{\partial(\phi RC)}{\partial t} \qquad i,j=1,2,3 \qquad (3.17)$$

where ϕ [–] is matrix porosity and C [M L^{-3}] is solute concentration. In this form of the transport equation, the assumptions of fluid incompressibility and constant fluid density are made. The coefficients of the hydrodynamic dispersion tensor, D_{ij} [L^2 T^{-1}], are given by Bear (1988) as

$$\phi D_{ij}=(\alpha_l-\alpha_t)\frac{q_iq_j}{|q|}+\alpha_t|q|\delta_{ij}+\phi\tau D_d\delta_{ij} \qquad i,j=1,2,3 \qquad (3.18)$$

where α_l [L] and α_t [L] are the longitudinal and transverse dispersivity, respectively, τ [–] is matrix tortuosity, D_d [L^2 T^{-1}] is the free-solution diffusion coefficient and δ_{ij} [–] is the Kronecker delta function, defined by

$$\delta_{ij} = \begin{cases} 1 & \text{if } i = j \\ 0 & \text{if } i \neq j \end{cases} \tag{3.19}$$

The dimensionless retardation factor, R, is given by Freeze and Cherry (1979) as

$$R = 1 + \frac{\rho_b}{\phi} K_d \tag{3.20}$$

where ρ_b [M L^{-3}] is the bulk density of the porous medium and K_d [M^{-1} L^3] is the equilibrium distribution coefficient describing a linear Freundlich isotherm.

The source/sink term, Γ_m, is $-\phi\lambda RC$ for radioactive components with decay constant λ [T^{-1}]. For chemically reactive species (e.g. silica), the governing transport equation is obtained from (3.17) by replacing the concentration, C, by the silica molality, $m_{H_4SiO_4}$, and by setting the source/sink term, Γ_m [now MOL M^{-1} T^{-1}], equal to the net reaction rate, r_{net}, given by (2.8). Yeh and Tripathi (1989) argue that precipitation/dissolution reactions and sorption can not be simulated simultaneously if the aqueous component is the primary dependent species. Thus, the distribution coefficient of silica must be set to zero in Equation (3.20).

Therrien and Sudicky (1996) give the equation that governs solute transport in fractured media as:

$$(2b)\left\{\frac{\partial}{\partial x_i}\left(D_{ij}^{fr}\frac{\partial C^{fr}}{\partial x_j} - q_i^{fr}C^{fr}\right) + \Gamma_m^{fr} - R^{fr}\frac{\partial C^{fr}}{\partial t}\right\} + \Omega_{n|I^+} - \Omega_{n|I^-} = 0$$

$$i, j = 1, 2 \tag{3.21}$$

where D_{ij}^{fr} [L^2 T^{-1}] is the hydrodynamic dispersion coefficient of the fracture, calculated as

$$D_{ij}^{fr} = (\alpha_l^{fr} - \alpha_t^{fr})\frac{q_i^{fr}q_j^{fr}}{|q^{fr}|} + \alpha_t^{fr}|q^{fr}|\delta_{ij} + D_d\delta_{ij} \qquad i, j = 1, 2 \tag{3.22}$$

where α_l^{fr} and α_t^{fr} [both L] are the longitudinal and transverse fracture dispersivity, respectively. The dimensionless fracture retardation factor, R^{fr}, is given by (Freeze and

Cherry, 1979):

$$R^{fr} = 1 + \frac{2K_d^{fr}}{(2b)} \tag{3.23}$$

where K_d^{fr} [L] is the fracture-surface distribution coefficient. The last two terms in Equation (3.21) represent advective-dispersive-diffusive loss or gain of solute mass across the fracture-matrix interfaces I^+ and I^- (Sudicky and McLaren, 1992). Sources and sinks are represented by the term Γ_m^{fr}, which equals $-\lambda R^{fr} C^{fr}$ for radioactive chemicals. For the silica species, the transport equation in fractured media can be obtained from (3.21) by replacing the concentration, C^{fr}, by the silica molality, $m^{fr}_{\mathrm{H_4SiO_4}}$, by setting the source/sink term, Γ_m^{fr} [now MOL M^{-1} T^{-1}], equals to the net reaction rate, r_{net}^{fr}, given by (2.9), and by neglecting sorption reactions (Yeh and Tripathi, 1989).

The reactive source/sink term always consists of a first order reaction term representing the precipitation and a constant term of zeroth order describing the dissolution reaction. Thus, both reactive transport equations in porous and fractured media are linear, allowing a one-step solution. Therefore, neither an iterative operator splitting, two-step scheme nor a computationally demanding fully-coupled, one-step approach are required. Performing a Newton Iteration and formulating Jacobian matrix entries would have highly complicated the model development.

The boundary conditions for Equations (3.17) and (3.21) can be of first-, second- or third-type as defined by Frind (1982) or by Istok (1989).

3.4 Heat Transfer

Under transient flow conditions, heat is transported by convection, conduction, mechanical heat dispersion and radiation. In nature, the temperature of the solid phase and their contained fluids is different because heat transfer is a transient process. But physically speaking, both temperatures can be assumed identical because heat transfer between the phases is a fast process relative to other heat transfer mechanisms (Holzbecher, 1998).

Convection describes heat transfer by moving fluid mass. Conductive transport occurs without mass displacement but within the medium due to a temperature gradient alone. Conduction depends, therefore, on the thermodynamic properties of the medium. Mechanical heat dispersion results from heterogeneity of the medium at all spatial scales. If groundwater velocity is low, conduction is the dominant heat transfer mechanism while convection becomes more important in high-velocity environments. Radiation of heat can be understood as electromagnetic waves and is, therefore, entirely independent of both the temperature and the thermodynamic properties of the medium. As a consequence, the amount of thermal energy transferred by way of radiation can not be quantified at a given point in the medium (Planck, 1906) and, thus, radiation is commonly neglected in numerical heat transfer models. The analogous processes of convection, conduction and mechanical heat dispersion for the solute transport case are advection, molecular diffusion and mechanical dispersion, respectively. Thus, based on the similarity to Equation (3.17), the convective-conductive-dispersive heat transfer equation in porous media can be written in a form similar to that given by Molson et al. (1992) as

$$\frac{\partial}{\partial x_i}\left((k_b + \phi D_{ij}\ \rho_l \tilde{c}_l)\,\frac{\partial T}{\partial x_j} - q_i\ \rho_l \tilde{c}_l\ T\right) = \rho_b \tilde{c}_b\ \frac{\partial T}{\partial t} \qquad i,j = 1,2,3 \tag{3.24}$$

where k_b [M L T^{-3} ϑ^{-1}] is the bulk thermal conductivity, ρ [M L^{-3}] is density and $\tilde{c}$ [L^2 T^{-2} ϑ^{-1}] is specific heat. The absolute temperature, T [ϑ], is the average temperature between the solid and the liquid phase (Domenico and Schwartz, 1997). The subscripts "l" and "b" refer to the liquid and bulk phases, respectively. A gaseous phase is absent. In Equation (3.24), it is also assumed that external heat sinks and sources due to chemical reactions (dissolution/precipitation) are negligible. The heat capacity, $\rho\tilde{c}$ [M L^{-1} T^{-2} ϑ^{-1}], denotes the heat removed or gained from a unit volume for a unit change in temperature (Domenico and Schwartz, 1997). The bulk properties $\rho_b\tilde{c}_b$ and k_b can be quantified considering the volume fractions of the solid and the liquid phase according to Bolton et al. (1996)

$$\rho_b \tilde{c}_b = (1-\phi)\rho_s \tilde{c}_s + \phi \rho_l \tilde{c}_l \tag{3.25}$$

$$k_b = (1-\phi)k_s + \phi k_l \tag{3.26}$$

where the subscript "s" refers to the solid phase.

Heat transport in an open discrete fracture can be written using a two-dimensional equation similar to Equations (3.21) and (3.24) in the form

$$(2b)\left\{\frac{\partial}{\partial x_i}\left(\left(k_l + D_{ij}^{fr}\ \rho_l \tilde{c}_l\right)\frac{\partial T^{fr}}{\partial x_j} - q_i^{fr}\ \rho_l \tilde{c}_l\ T^{fr}\right) - \rho_l \tilde{c}_l\ \frac{\partial T^{fr}}{\partial t}\right\} + \Lambda_{n|I^+} - \Lambda_{n|I^-} = 0$$

$$i, j = 1, 2 \tag{3.27}$$

The last two terms represent convective-dispersive-conductive loss or gain of thermal energy across the fracture-matrix interfaces I^+ and I^-. The temperature is uniform across the fracture width. Furthermore, it is assumed that, along the fracture-matrix interface, the temperature in the fracture and the adjoining matrix are identical.

In the developed model, the boundary conditions for Equations (3.24) and (3.27) can be of first (Dirichlet) type of the form

$$T = T_0 \tag{3.28}$$

and

$$T^{fr} = T_0^{fr} \tag{3.29}$$

Chapter 4

Numerical Modeling

The purpose of this chapter is to present how the previously described governing equations are implemented in the FRAC3DVS model. First, the unmodified FRAC3DVS model is illustrated in Section 4.1, followed by a brief explanation of the finite element technique to discretize the governing equations in Section 4.2. Section 4.3 focuses on how inclined discrete fractures are implemented into the finite element grid. Section 4.4 describes the finite element formulation of the buoyancy part in the fracture flow equation while the last two sections (4.5 and 4.6) present the full finite element formulation of the solute transport and heat transfer equations.

4.1 The FRAC3DVS Model

FRAC3DVS is a 3D saturated-unsaturated numerical groundwater flow and multicomponent solute transport model (Therrien and Sudicky, 1996; Therrien et al., 2004). The governing equations for flow and transport are derived from the continuum approach. The flow equation is discretized in space by means of a control volume finite element approach, ensuring mass conservation at the elemental and global level. The transport equation is solved using a Galerkin finite element approach. The porous, low-permeability matrix is represented by regular three-dimensional blocks and fractures of high permeability are represented by two-dimensional rectangular planes. Using undis-

torted finite elements allows an analytical discretization of the governing equations by means of elemental influence coefficient matrices (Frind, 1982; Therrien and Sudicky, 1996). Thus, there is no need to numerically integrate. The solution takes into account advective flow and non-reactive transport, molecular diffusion, and mechanical dispersion in both the fractures and the matrix.

In FRAC3DVS, vertical and horizontal 2D fractures are incorporated into the 3D grid by superimposing two-dimensional face elements onto the three-dimensional grid, consisting of regular block elements. Two-dimensional faces represent the fracture whereas three-dimensional blocks denote the porous matrix. In order to fully couple the fracture with the porous matrix, faces and blocks share common nodes along the fracture walls. Thus, nodes at fracture locations receive contributions from both the block elements as well as from the fracture faces. Furthermore, for these mutual nodes, both hydraulic head and concentration at the fracture/matrix interface are assumed to be equal. Therefore, it is not necessary to explicitly calculate the exchange terms q_n, Ω_n and Λ_n in Equations (3.16), (3.21) and (3.27), respectively. This contrasts to the dual-continuum approach, where the governing equations of the fractures and the matrix are solved independently, linked through explicitely computed exchange terms. The discrete fracture approach has previously been applied by several authors (Sudicky and McLaren, 1992; Shikaze et al., 1994; Therrien and Sudicky, 1996; Shikaze et al., 1998) and its description is, therefore, not repeated here.

The model FRAC3DVS has been modified to incorporate inclined fractures to simulate variable-density flow and transport. The improved model also solves for heat transfer in discretely-fractured porous media. Both fluid properties, density and viscosity, are functions of salinity, temperature or both. In this study, FRAC3DVS has also been expanded to account for reactive silica transport. Chemical reactions are coupled with variable-density flow through a feedback between reactions and flow parameter updates. The reaction kinetics and the quartz solubility are functions of both salt concentration and temperature.

4.2 Solution Strategies

All governing equations for variable-density flow (3.14 and 3.16), reactive solute transport (3.17 and 3.21) and heat transfer (3.24 and 3.27) are partial differential equations of second order and are resolved numerically. Due to its flexibility, the method used is the finite element method (FEM). The basic principle of the FEM is to first define a differential operator $L(\xi)$ of the differential equation with the unknown ξ as

$$L(\xi) = 0 \tag{4.1}$$

Next, the unknown, ξ, is approximated by a linear combination of linear basis functions, w_J, in the way

$$\xi \simeq \hat{\xi} = \sum_{J=1}^{Nn} \xi_J \; w_J(x, y, z) \tag{4.2}$$

where Nn is the total number of nodes in the finite element grid. The elemental basis or approximation functions, w_J, are chosen such that $w_J(x_I, y_I, z_I) = \delta_{IJ}$ where (x_I, y_I, z_I) is the location of node I (Figure 4.1). This choice implies that

$$w_J = \begin{cases} 1 \text{ at node } J \\ 0 \text{ everywhere else in the domain} \end{cases} \tag{4.3}$$

Therefore, the sum of all basis functions on the grid node I is always one:

$$\sum_J w_J = 1 \qquad\qquad \forall \; I \tag{4.4}$$

In Equation (4.1), the unknown exact solution ξ is now replaced by the trial solution $\hat{\xi}$ such that the left hand side of (4.1) is the nonzero residual $L(\hat{\xi})$:

$$0 = L(\xi) \simeq L(\hat{\xi}) = L\left(\sum_J \xi_J \; w_J\right) \neq 0 \qquad\qquad \forall \; I \tag{4.5}$$

In a third step, the residual, $L(\hat{\xi})$, is multiplied by a weighting function, ν_I, and the global integral of the weighted residual is then forced to zero:

$$\int_\Omega L\left(\sum_J \xi_J \; w_J\right) \nu_I \; \mathrm{d}\Omega = 0 \qquad\qquad \forall \; I \tag{4.6}$$

where Ω is the model domain. The choice of the weighting function, ν_I, depends on the specific FEM. In the common Galerkin method, ν_I is set equal the approximation function, w_I. In the control volume finite element (CVFE) method, ν_I is chosen as 1, dividing the domain into subdomains or nodal control volumes. Thus, the CVFE method ensures mass conservation at both the elemental and the global level.

Lastly, the integration and the summation in (4.6) are treated as interchangeable operations. Breaking up the global integral of sums into a sum of elemental integrals finally yields the finite element formulation as

$$\sum_J \left\{ \sum_e \int_{V^e} \left(L\left(\xi_J \; w_J\right) \nu_I \right) \, \mathrm{d}V^e \right\} = 0 \qquad \forall \; I \tag{4.7}$$

where Σ_e refers to the summation over all elements that join node J and where V^e is the volume of element e. The integrals in (4.7) do not need to be solved numerically but can directly be replaced by elemental influence coefficient matrices if undistorted rectangular 2D fracture faces and regular hexahedral 3D matrix elements are used (Frind, 1982; Therrien and Sudicky, 1996). With a finite difference approach applied to the temporal derivative, Equation (4.7) can be brought in the standard matrix form

$$\mathbf{A} \bullet \xi = \mathbf{d} \tag{4.8}$$

where the global matrix, $\mathbf{A}$, is of dimension $Nn \times Nn$, while both the vector of unknowns, ξ, and the known vector, $\mathbf{d}$, are of size $Nn \times 1$. In the numerical model FRAC3DVS, Equation (4.8) is solved using the WATSIT iterative solver package for general sparse matrices (Clift et al., 1996) and a conjugate gradient stabilized (CGSTAB) acceleration technique (Rausch et al., 2005). A more detailed description of the FEM and its application in hydrogeology can be found in Istok (1989).

The processes of variable-density flow and reactive solute transport are naturally coupled. Density variations cause weak nonlinearities in the flow equation. In the developed model, they are treated by means of a sequential iterative approach (SIA), also called Picard Iteration, which links the two governing equations for flow and transport. This method alternately solves the two governing equations during each time step until convergence is attained (Figure 4.2).

Mineral dissolution/precipitation has a direct impact on a variety of physicochemical and material properties during the simulation process. A change of porosity and

fracture aperture affects the active surface areas, A_{qz} and A_{qz}^{fr}, which, in turn, change the net rate of reaction (2.1). The change of such parameters is naturally fully coupled with flow, heat transfer and solute transport. However, mineral volume fractions change much more slowly than do the solute concentrations in the fluid (Sanford and Konikow, 1989; Steefel and Lasaga, 1994; Steefel and Yabusaki, 1996; Saaltink et al., 2001). Therefore, in the present model, like in other common geochemical models, fluid properties are updated after each iteration of the Picard loop whereas material properties are updated after each time step rather than after each iteration (Figure 4.2). This procedure of recalculating material parameters at the end of each time step is called quasi-stationary state approximation and has first been introduced by Lichtner (1988). Using the reaction rate at time level L+1 (implicit time weighting scheme) to renew all model parameters ensures numerical stability (Steefel and Lasaga, 1994).

This decoupled, two step approach works well for relatively small time step sizes. However, if nonuniform time step sizes are used to accelerate the simulation, the time increment may become too large and, thus, high dissolution rates may lead to negative quartz volume fractions or to negative fracture apertures. An adaptive time stepping scheme was implemented to avoid unphysical results and to stabilize the simulation procedure. The time step sizes depend on the absolute change of porosity according to:

$$(\Delta t)^{L+1} = \frac{\phi^*}{\max|\phi^{L+1} - \phi^L|}\ (\Delta t)^L \tag{4.9}$$

where ϕ^* is the maximum absolute change in porosity allowed during a single time step. Therrien and Sudicky (1996) previously used adaptive time stepping in the simulation of variably-saturated flow. If the maximum change in porosity is greater than the allowed threshold, the fraction in relation (4.9) is less than 1 and the updated new time step size is smaller than the previous one. In this case, the old time step is repeated using the new reduced time increment, $(\Delta t)^L := (\Delta t)^{L+1}$, without updating the material properties. This method is different from that presented by Therrien and Sudicky (1996) where time steps are not repeated and where new time step sizes always apply for the following time step. However, too large time increments do not satisfactorily couple variable-density flow and reactive transport with parameter changes. In fractured systems, the adaptive time stepping can also be based on absolute changes in fracture aperture by using an expression identical to (4.9). If both time step size controllers (porosity control and aperture control) are employed, the new time step size is calculated from the material whose time step multiplier is smaller.

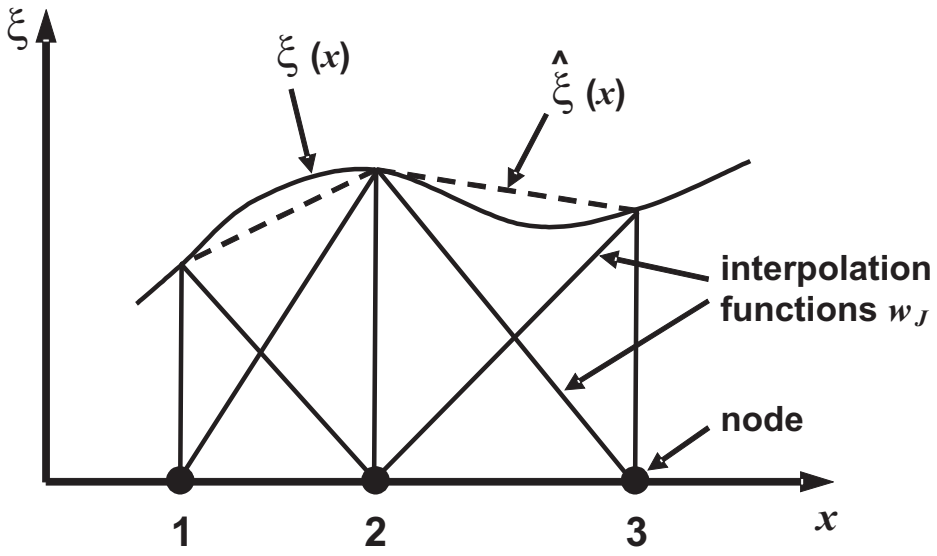

Figure 4.1: One-dimensional example of the trial solution, $\hat{\xi}$, and the unknown continuous solution, ξ (Steefel and MacQuarrie, 1996).

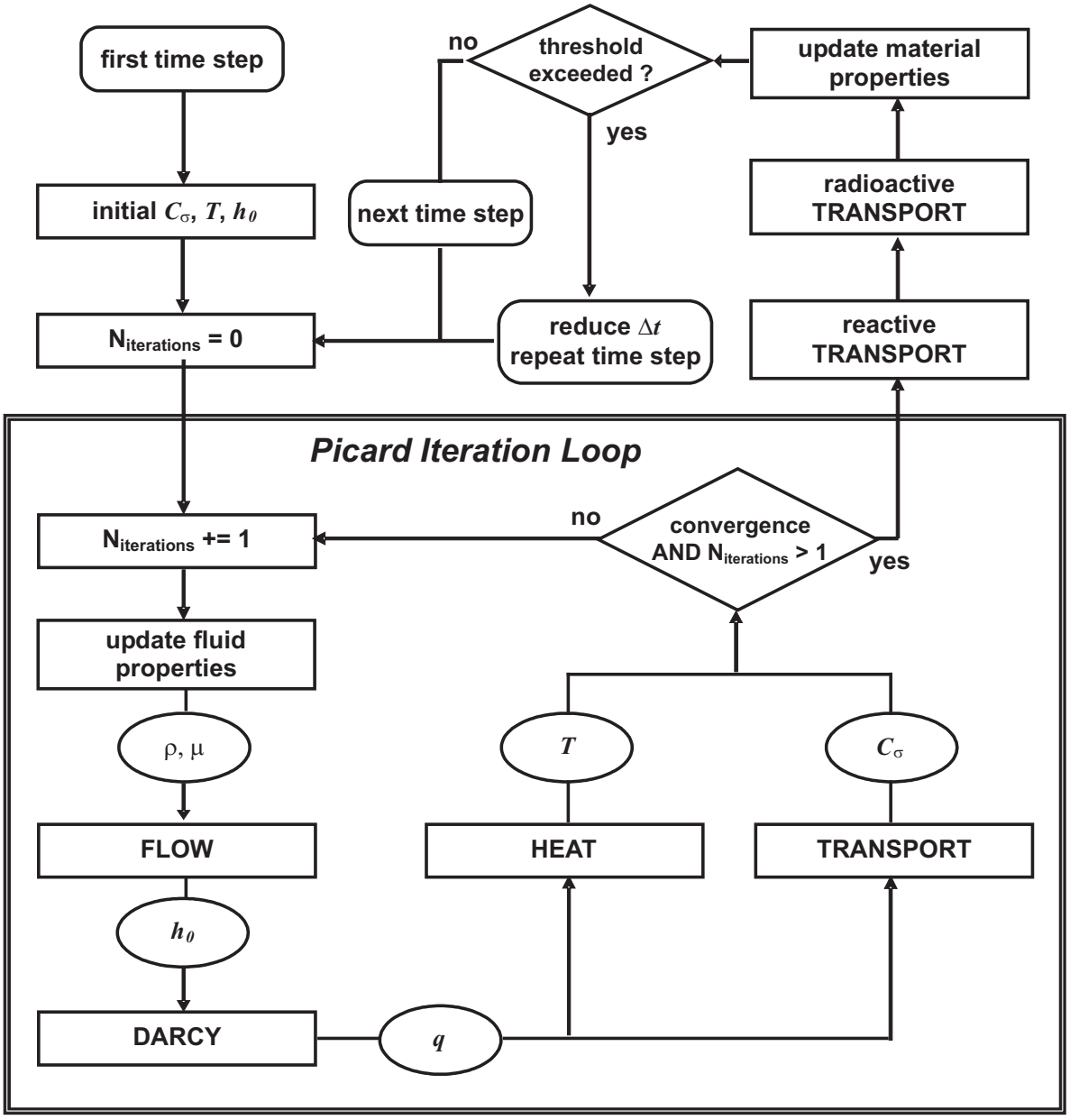

Figure 4.2: Flow chart of the Picard Iteration with chemistry loop to couple variable-density, variable-viscosity flow and solute transport with external chemical reactions and parameter updates.

4.3 Discretizing Inclined Fractures

The original version of FRAC3DVS offers discretizing horizontal and vertical fractures. The FRAC3DVS model was modified to also simulate variable-density flow and reactive solute transport in irregular fracture networks, where inclined fractures are likely to occur.

While the six faces on the outer surface of the block elements can be used for the discretization of regular fractures, for inclined fractures an additional six inclined faces inside the blocks are also available. Figure 4.3 exhibits the orientation of the six inclined faces. Note that the two faces in the block on the right of Figure 4.3 are not inclined but vertical. However, for convenience, they are considered as inclined as well because they do not correspond to a boundary face of the block. Furthermore, it can be seen that all available 6 element boundary faces and 6 inclined faces are rectangular and undistorted. Using the control volume finite element method, and assuming continuity of hydraulic head, concentration and temperature at the common fracture-matrix nodes, results in an unchanged connectivity pattern for the 3D porous medium elements, irrespective of the presence of fractures.

Similar to the integration of horizontal and vertical (i.e. regular) fractures, inclined fractures are incorporated in the finite element grid by superimposing 2D fracture faces onto the 3D block elements of the porous matrix. The 8 nodes of the 3D matrix element are labelled from 1 to 8 while the 4 nodes of the 2D fracture element are labelled from 1 to 4 (Figure 4.4). With the superposition, nodes 1 to 4 of an inclined 2D fracture element coincide with nodes 2, 3, 8 and 5 of the 3D matrix element.

In FRAC3DVS, the location of three-dimensional inclined fractures is defined by two points and by a coordinate axis parallel to the fracture. The fracture shown in Figure 4.5 is parallel to the y-axis and defined by the two points West (W) and East (E) that coincide with the beginning and the end of a fracture. The fracture nodes between W and E are selected using a simple least distance criterion: for every node P that defines the fracture, the distance of all three neighbor nodes of P to the undiscretized fracture is calculated. The neighbor node whose distance to the fracture is the smallest is selected as a fracture node and becomes point P for the next step. Initially, P is

identical to W. This process is repeated until the point P meets the end point E. Figure 4.5 is an example of how an inclined fracture is discretized in an irregular, relatively coarse grid. Note that the grid is 3D with a unit thickness. Thus, the fracture is 2D and defined by W and E and by its orientation (parallel to the y-axis).

Inclined fractures are a combination of inclined, horizontal and vertical faces. The mathematical formulation of density effects in each of these three types of fracture elements is described in the following section.

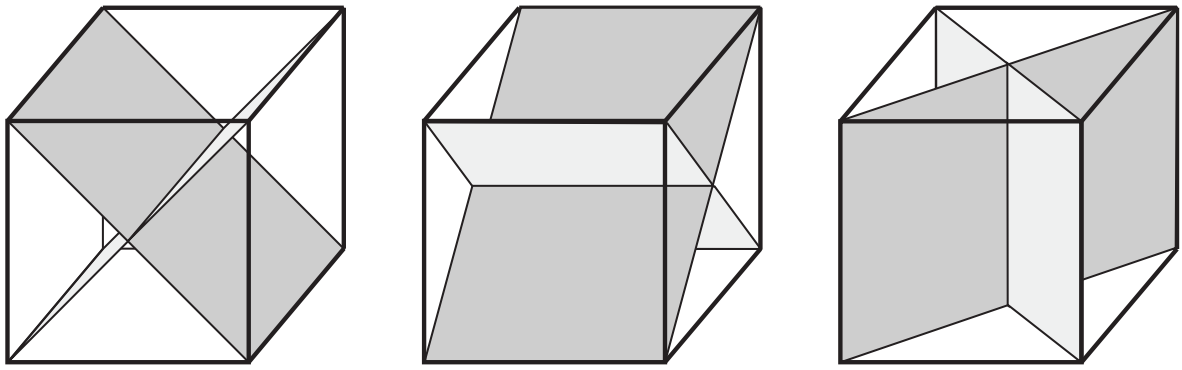

Figure 4.3: Inclined faces in three-dimensional block elements.

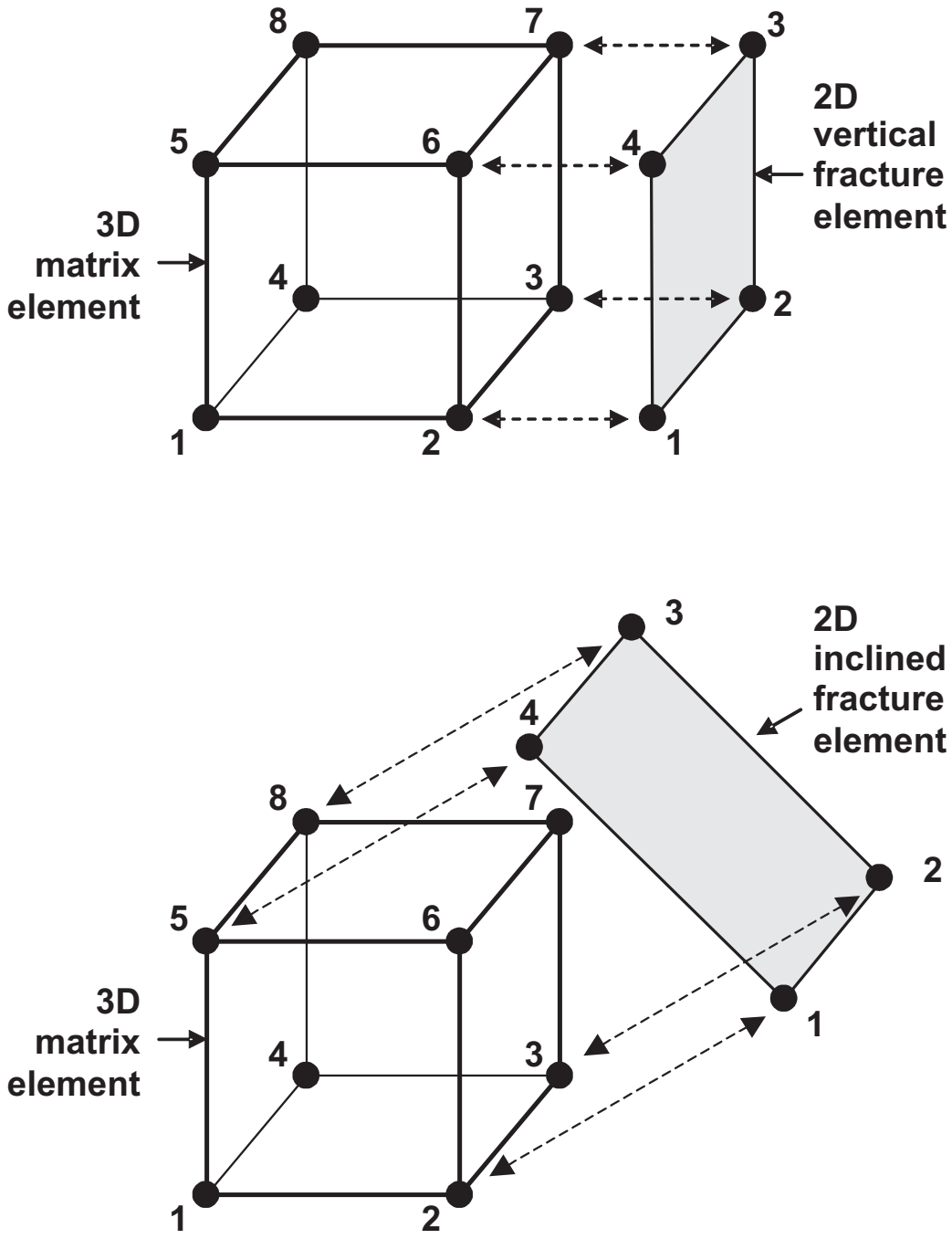

Figure 4.4: Superposition of 2D vertical and inclined fracture elements onto 3D matrix elements, where both continua share common grid nodes (modified from Rausch et al., 2005).

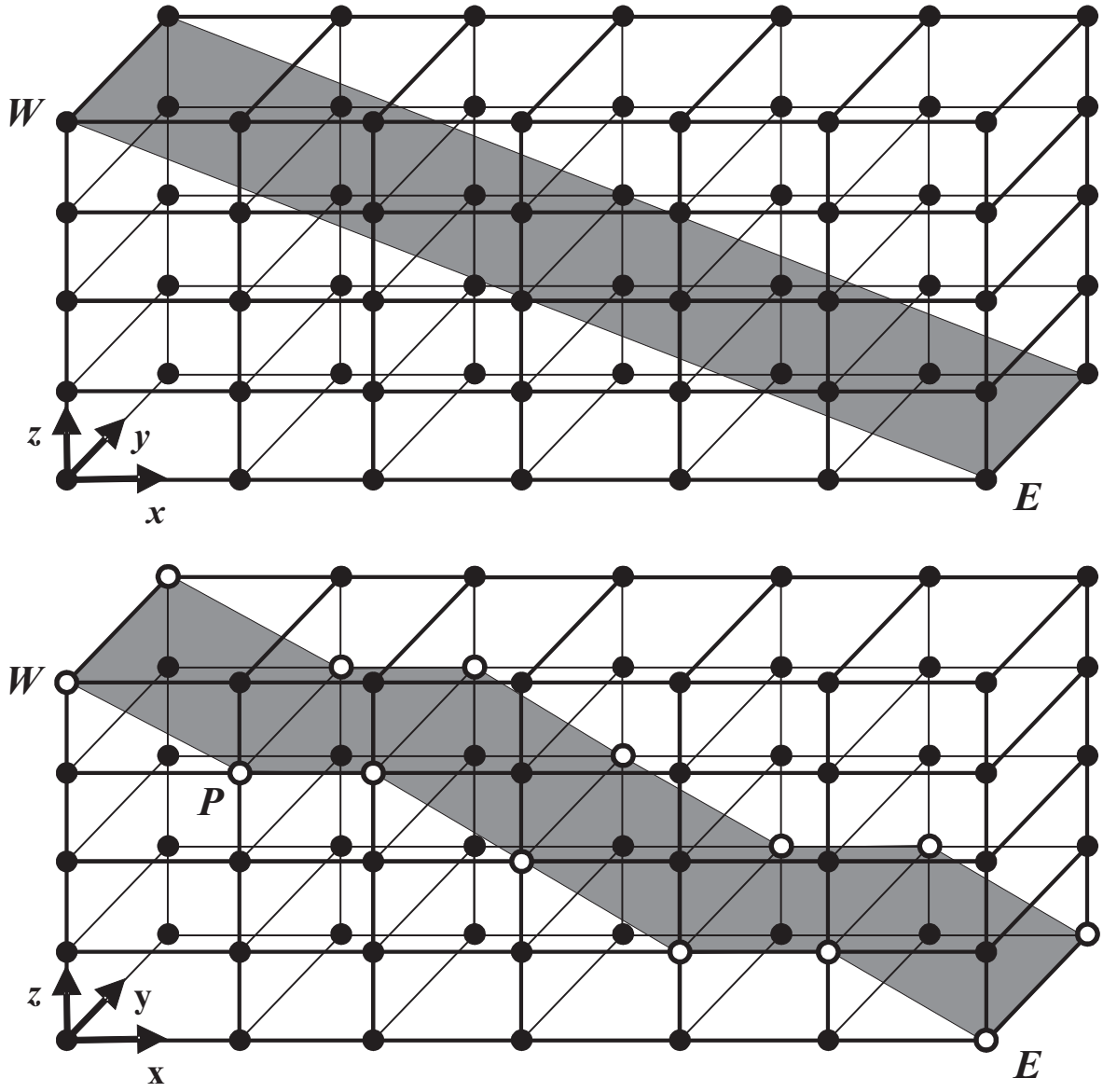

Figure 4.5: Selecting two-dimensional elements of an inclined fracture. The fracture in nature (above) is discretized by snapping to the closest nodes (below). Common fracture-matrix nodes are highlighted.

4.4 Variable-Density Flow

Therrien and Sudicky (1996) extensively discuss the finite element formulation as well as the numerical implementation of the no-density flow equations in porous and fractured media. Their derivation is not repeated here. This section focuses on the finite element formulation of the buoyancy term in fractures of any orientation.

Frind (1982) provides the finite element formulation of the 2D variable-density flow equation in porous media in the absence of fractures. The elements used in his study are two-dimensional vertical undistorted rectangles. However, if fractures are present and assuming the common node approach, the hydraulic head at the fracture/matrix interface is identical in both media such that the exchange terms $q_n|_{I^+}$ and $q_n|_{I^-}$ in Equation (3.16) vanish. In this case, the 2D flow equation in a porous matrix as given in Frind (1982) and the 2D flow equation in a discrete fracture given by (3.16) are mathematically identical. As a consequence, Frind's finite element formulation for variable-density flow in 2D matrix elements can also be used for density-driven flow in 2D fracture faces.

For clarity, the terms h_0 and ρ_r instead of h_0^{fr} and ρ_r^{fr} will be used below. Assuming constant viscosity for the moment, the differential operator $L(h_0)$ can be written as

$$L(h_0) = \frac{\partial}{\partial x_i}\left[K_0^{fr}\left(\frac{\partial h_0}{\partial x_j} + \rho_r \eta_j \cos\varphi\right)\right] - S_S^{fr}\,\frac{\partial h_0}{\partial t} = 0 \tag{4.10}$$

Next, the unknown exact solution, h_0, is approximated by a trial solution in the usual form

$$h_0 \simeq \hat{h}_0 = \sum_{J=1}^{Nn} h_0^J\; w_J(x,y,z) \tag{4.11}$$

such that the left hand side of (4.10) will be a nonzero residual. Following Frind's derivation, the finite element formulation of the balance equation (3.16) can be written as a semi-discrete global matrix system in the compact form

$$\mathbf{H} \bullet \mathbf{h_0} \;+\; \mathbf{S} \bullet \frac{\partial \mathbf{h_0}}{\partial t} \;+\; \mathbf{g} \;=\; \mathbf{f} \tag{4.12}$$

where superscript "fr" is dropped for clarity. In (4.12), $\mathbf{H}$ [L T^{-1}] is the conductance or stiffness matrix, $\mathbf{S}$ [L] is the fluid mass matrix, $\mathbf{g}$ [L^2 T^{-1}] is the body force vector

and $\mathbf{f}$ [L^2 T^{-1}] is the boundary flux vector. Vector $\mathbf{g}$ represents density effects and is, therefore, of special interest in this study. See Frind (1982) for details about how the other matrices and vectors are defined.

If 2D fracture faces are assumed, each of the four arrays in (4.12) can be written as the sum of all the Nfe elemental arrays, Nfe being the total number of fracture elements in the grid. Following this, the fracture body force vector, $\mathbf{g}$, can be expressed as

$$\mathbf{g} = \sum_{fe} \mathbf{g}^{fe} \tag{4.13}$$

where $\mathbf{g}^{fe}$ [L^2 T^{-1}] is the body force vector, written at the fracture elemental level. In a two-dimensional quadrilateral element, whose sides coincide with the local coordinate axes $\bar{x}$ and $\bar{z}$, the entries g_i^{fe} [L^2 T^{-1}] of vector $\mathbf{g}^{fe}$ are calculated after Frind (1982) as

$$g_i^{fe} = \iint_{A^{fe}} K_0^{fr}\ \overline{\rho}_r^{fe} \cos\varphi\ \frac{\partial w_i^{fe}}{\partial \bar{z}}\ \mathrm{d}\bar{x}\ \mathrm{d}\bar{z} \qquad\qquad i = 1, 2, 3, 4 \tag{4.14}$$

where $\overline{\rho}_r^{fe}$ is the average relative density in the fracture element (face) fe, w_i^{fe} [–] is the value of the 2D approximation function in face fe at node i and A^{fe} [L^2] is the surface area of fe. The double integral in (4.14) represents the general mathematical expression of buoyancy in a 2D fracture face of any three-dimensional orientation. However, the discretized inclined fracture can be a combination of horizontal, vertical and inclined two-dimensional elements. Integration of Equation (4.14) is required to obtain the finite formulation of density effects for fracture elements with arbitrary orientations, in order to fully account for density effects in the entire fracture.

The right side of (4.14) can be integrated in two different ways. First, the fracture weighting function is defined in terms of local coordinates in the usual way (e.g. for node 1) as $w_1^{fe} = (L_{\bar{x}} - \bar{x})(L_{\bar{z}} - \bar{z})/(L_{\bar{x}} \cdot L_{\bar{z}})$, where $L_{\bar{x}}$ [L] and $L_{\bar{z}}$ [L] are the element dimensions in the $\bar{x}$- and $\bar{z}$-direction, respectively (Figure 4.6). With the derivative of w_1^{fe}, the integration in (4.14) is identical to that presented by Frind (1982), resulting in the following coefficient for node 1:

$$g_1^{fe} = -K_0^{fr}\ \overline{\rho}_r^{fe} \cos\varphi\ \frac{L_{\bar{x}}}{2} \tag{4.15}$$

which can be obtained likewise for the other nodes 2, 3 and 4.

The second, more general method first assumes a vertical face, which will be rotated to match its real inclined position. In this case of a vertical face, the cosine in (4.14) is unity and the local coordinate axes of the face, $\bar{x}$ and $\bar{z}$, coincide with the global coordinates, x and z, (Figure 4.6) such that:

$$g_i^{fe} = \iint\limits_{A^{fe}} K_0^{fr}\ \overline{\rho}_r^{fe}\ \frac{\partial w_i^{fe}}{\partial z}\ \mathrm{d}x\ \mathrm{d}z \qquad\qquad i = 1, 2, 3, 4 \tag{4.16}$$

Unlike in the first method, the density term is now defined over a vertical fracture element. If the quasi-vertical face is rotated back to its original inclined position, the buoyancy term (4.14) has to be integrated over the entire 2D inclined element area for an arbitrary face orientation in 3D. However, the weighting function as well as its derivative are 2D functions that are defined over a surface defined in 3D space. Thus, a surface integral calculus problem has to be solved where the function $f(x, y, z) = K_0^{fr}\ \overline{\rho}_r^{fe}\ (\partial w_i^{fe}/\partial z)$ is defined over the surface S of the fracture face.

Following Thomas and Finney (1988), the integral of a function $f(x, y, z)$ over a surface S in space, described by the function $F(x, y, z) = constant$ (Figure 4.7), can be calculated by evaluating a closely related double integral over the vertical projection or shadow of S on a coordinate plane in the form

$$\iint\limits_S f(x, y, z)\ \mathrm{d}S = \iint\limits_R f(x, y, z)\ \frac{|\nabla F|}{|\nabla F \bullet \mathbf{p}|}\ \mathrm{d}A \tag{4.17}$$

where R is the shadow region on the ground plane beneath surface S and $\mathbf{p}$ is a vector normal to R. This surface integral can be directly evaluated only if a 1:1 mapping of S in the xy- or in the xz-plane exists. Then, R could be S_{xy} or S_{xz} because both projections yield the same result. The projection of S in the xz-plane is considered because a pseudo-vertical fracture element was assumed.

From Figure 4.6, equation $F(x, y, z) = constant$ of the surface S, which defines the plane of the two-dimensional fracture element, can easily be derived as $L_z y - L_y z = 0$. Thus, a 1:1 mapping of S in both coordinate planes exists and, as a consequence, the integral on the right hand side of (4.17) can be evaluated and we have

$$S: \quad F(x, y, z) = L_z\ y - L_y\ z \tag{4.18}$$

$$\nabla F = 0 \cdot \mathbf{i} + L_z \cdot \mathbf{j} - L_y \cdot \mathbf{k} \tag{4.19}$$

$$|\nabla F| = \sqrt{L_y^2 + L_z^2} \tag{4.20}$$

and with $\mathbf{p} = \mathbf{j}$, the unit vector in y-direction

$$|\nabla F \bullet \mathbf{p}| = |\nabla F \bullet \mathbf{j}| = L_z \tag{4.21}$$

Therefore, Equation (4.17) becomes

$$\iint\limits_{S} f(x,y,z)\ \mathrm{d}S = \iint\limits_{S_{xz}} f(x,y,z)\ \frac{\sqrt{L_y^2 + L_z^2}}{L_z}\ \mathrm{d}x\ \mathrm{d}z \tag{4.22}$$

where $\mathrm{d}A = \mathrm{d}x \cdot \mathrm{d}z$. With the function $f(x,y,z) = K_0^{fr}\ \overline{\rho}_r^{fe}\ (\partial w_i^{fe}/\partial z)$, which must be integrated, the entries of the elemental body force vector g_i^{fe} from Equation (4.14) are given in the form

$$g_i^{fe} = \int\limits_0^{L_z}\int\limits_0^{L_x} K_0^{fr}\ \overline{\rho}_r^{fe}\ \frac{\partial w_i^{fe}}{\partial z}\ \sqrt{1 + \frac{L_y^2}{L_z^2}}\ \mathrm{d}x\ \mathrm{d}z \qquad i = 1,2,3,4 \tag{4.23}$$

The elemental approximation function w_i^{fe} is always formulated as a function of local coordinates rather than global ones. Therefore, the integral in Equation (4.23) has to be evaluated in the local coordinates $\bar{\chi}$. The required coordinate transformation is a rotation around the x-axis by angle φ (see Figure 4.6) and can be written in the matrix form

$$\begin{bmatrix} 1 & 0 & 0 \\ 0 & \cos\varphi & -\sin\varphi \\ 0 & \sin\varphi & \cos\varphi \end{bmatrix} \bullet \begin{Bmatrix} x \\ y \\ z \end{Bmatrix} = \begin{Bmatrix} \bar{x} \\ \bar{y} \\ \bar{z} \end{Bmatrix} \tag{4.24}$$

Thus, we can write the derivatives

$$\frac{\partial \bar{z}}{\partial z} = \cos\varphi \tag{4.25}$$

$$\frac{\partial z}{\partial \bar{z}} = \cos\varphi \tag{4.26}$$

The integral of Equation (4.23) is rewritten in terms of local coordinates by first substituting the derivative by means of the chain rule, leading to

$$\frac{\partial w_i^{fe}}{\partial z} = \frac{\partial w_i^{fe}}{\partial \bar{z}} \cdot \frac{\partial \bar{z}}{\partial z} \tag{4.27}$$

and, second, by adjusting the elementary volume following

$$\mathrm{d}x\ \mathrm{d}z = \mathrm{det}\mathbf{J} \cdot \mathrm{d}\bar{x}\ \mathrm{d}\bar{z} \tag{4.28}$$

Here, the Jacobian matrix $\mathbf{J}$ [–] collapses to the simple 1×1 matrix

$$\mathbf{J} = \left[\frac{\partial z}{\partial \bar{z}}\right] \tag{4.29}$$

with determinant det$\mathbf{J}$ given by Equation (4.26). According to Figure 4.6, the approximation function for node 1 may be expressed in local coordinates as

$$w_1^{fe}(\bar{x}, \bar{z}) = \frac{1}{L_x H}(L_x - \bar{x})(H - \bar{z}) \tag{4.30}$$

with the spatial derivative

$$\frac{\partial w_1^{fe}}{\partial \bar{z}} = \frac{\bar{x} - L_x}{L_x H} \tag{4.31}$$

where H [L] is the hypotenuse of the occurring triangle in the yz-plane, given as $H = \sqrt{L_y^2 + L_z^2}$. Now use can be made of Equations (4.25), (4.26), (4.27), (4.28), (4.29) and (4.31) to rewrite Equation (4.23). The elemental body force vector entry g_1^{fe} can be written in local coordinates as

$$g_1^{fe} = \int_0^H \int_0^{L_x} \left(K_0^{fr}\ \overline{\rho}_r^{fe}\ \left[\frac{\bar{x} - L_x}{L_x\ H}\right]\ \cos^2\varphi\ \sqrt{1 + \frac{L_y^2}{L_z^2}}\ \right)\ \mathrm{d}\bar{x}\ \mathrm{d}\bar{z} \tag{4.32}$$

Finally, a two-dimensional integration in Equation (4.32) directly yields the solution for node 1:

$$g_1^{fe} = -K_0^{fr}\ \overline{\rho}_r^{fe}\ \frac{L^{\mathrm{TG}}}{2} \tag{4.33}$$

where the characteristic length L^{TG} [L] is a function of the element geometry such that

$$L^{\mathrm{TG}} = L_x \cdot \frac{L_z}{\sqrt{L_y^2 + L_z^2}} \tag{4.34}$$

Note that solution (4.33) is identical to (4.15) because $L_x = L_{\bar{x}}$ and because the second factor in (4.34) is the cosine of the fracture face incline, $\cos\varphi = L_z/\sqrt{L_y^2 + L_z^2}$. The repetition of steps (4.30) to (4.33) for nodes 2, 3 and 4 yields the following final

form of the elemental body force vector $\mathbf{g}^{fe}$ for arbitrarily inclined two-dimensional fracture elements.

$$\mathbf{g}^{fe} = K_0^{fr}\ \overline{\rho}_r^{fe}\ \frac{L^{\mathrm{TG}}}{2} \begin{Bmatrix} -1 \\ -1 \\ 1 \\ 1 \end{Bmatrix} \tag{4.35}$$

where L^{TG} is given by Equation (4.34). The characteristics of this length scale are:

[1] For a vertical fracture element, the calculated density effects reach a maximum. Solution (4.35) becomes identical to that in Frind (1982) because L^{TG} becomes L_x:

$$\lim_{L_y \to 0} L^{\mathrm{TG}} = L_x$$

[2] For a horizontal fracture element, no density effects occur and solution (4.35) becomes zero because L^{TG} vanishes:

$$\lim_{L_z \to 0} L^{\mathrm{TG}} = 0$$

[3] For every arbitrarily inclined fracture element, the magnitude of the density effect will exceed zero and will be smaller than the density effect in a vertical fracture element:

$$0 < L^{\mathrm{TG}} < L_x$$

[4] For an inclined fracture element, which is not parallel to the x-axis as shown in Figure 4.6, but to the y-axis as shown in Figure 4.5, the x- and y-dimensions in Equation (4.34) are simply switched:

$$L^{\mathrm{TG}} = L_y \cdot \frac{L_z}{\sqrt{L_x^2 + L_z^2}}$$

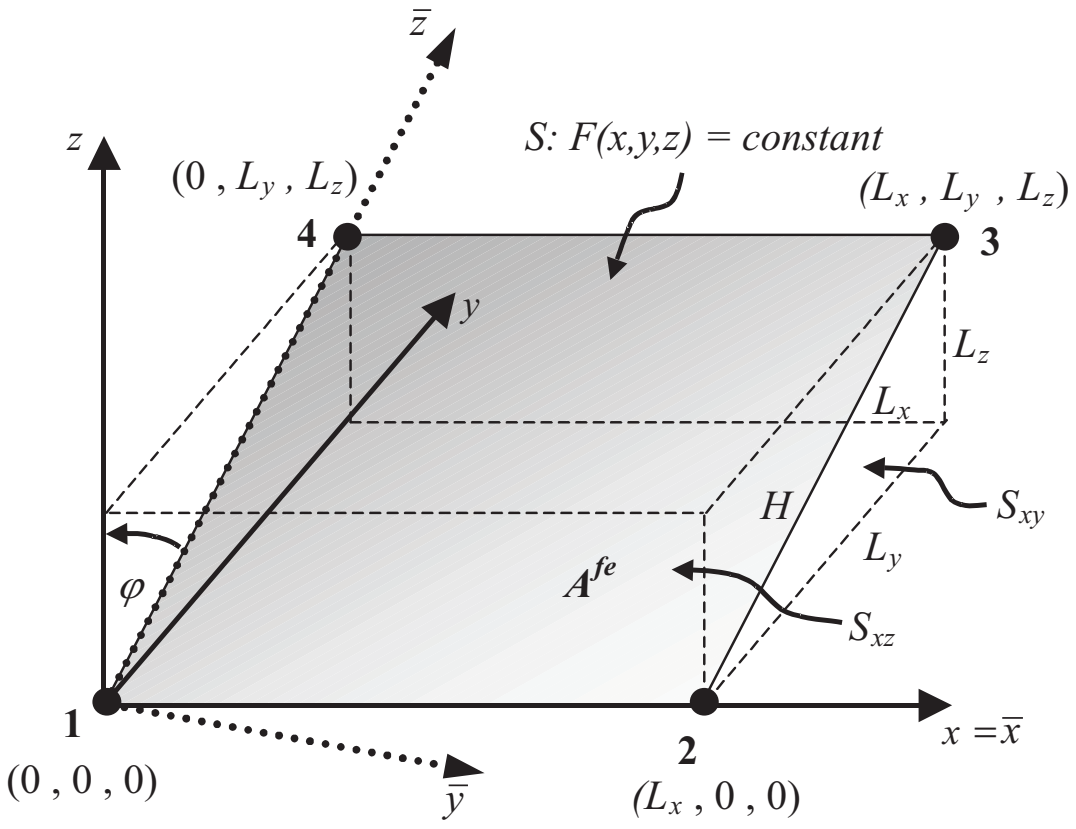

Figure 4.6: Geometry of an inclined 2D fracture element in three dimensions.

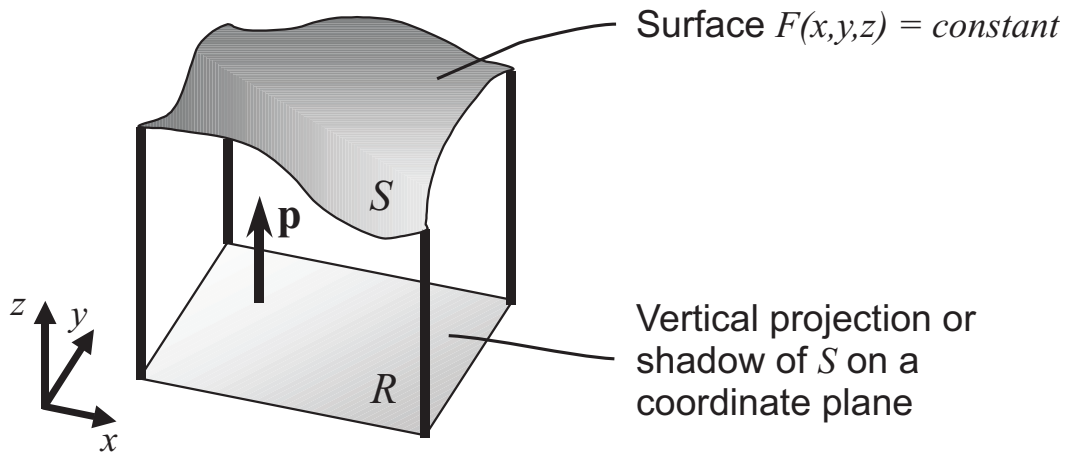

Figure 4.7: Projection of S on a coordinate plane (Thomas and Finney, 1988).

4.5 Reactive Solute Transport

Similar to the discretization of the variable-density flow equation, a differential operator $L(m)$ is defined for reactive solute transport. With (2.8) and (3.17), $L(m)$ has the following form for reactive solute transport in porous media

$$L(m) = \frac{\partial}{\partial x_i}\left(\phi D_{ij}\frac{\partial m}{\partial x_j} - q_i m\right) + \varepsilon - \frac{\varepsilon\ \gamma_{\mathrm{H_4SiO_4}}}{K_{eq}}\ m - \frac{\partial(\phi R m)}{\partial t} = 0$$

$$i, j = 1, 2, 3 \tag{4.36}$$

where $\varepsilon = \phi_{qz}\ k_{+}^{corr}\ A_{qz}$ and where m is the silica molality. The unknown, m, is approximated by a linear combination of linear basis functions w_J in the common way

$$m \simeq \hat{m} = \sum_{J=1}^{Nn} m_J\ w_J(x, y, z) \tag{4.37}$$

Substitution of the exact solution, m, by its approximation, $\hat{m}$, leads to the nonzero residual $L(\hat{m})$. As before, the global integral of the weighted residual is then forced to zero, yielding:

$$\int_{\Omega} L(\hat{m})\ \nu_I\ \mathrm{d}\Omega = 0 \qquad\qquad I = 1...Nn \tag{4.38}$$

The right hand side of (4.36) is now placed in (4.38), followed by a Galerkin approach, where $w_I = \nu_I$, and a final application of Green's theorem to the second derivative. The result is the following weak integral form of the differential equation

$$\begin{aligned}
&-\int_{\Omega}\left(\phi D_{ij}\ \frac{\partial \hat{m}}{\partial x_j}\ \frac{\partial w_I}{\partial x_i}\right)\ \mathrm{d}\Omega - \int_{\Omega}\left(q_i\ \frac{\partial \hat{m}}{\partial x_i}\ w_I\right)\ \mathrm{d}\Omega \\
&+\int_{\Omega}(\varepsilon\ w_I)\ \mathrm{d}\Omega - \int_{\Omega}\left(\frac{\varepsilon\ \gamma_{\mathrm{H_4SiO_4}}}{K_{eq}}\ \hat{m}\ w_I\right)\ \mathrm{d}\Omega - \int_{\Omega}\left(\phi R\ \frac{\partial \hat{m}}{\partial t}\ w_I\right)\ \mathrm{d}\Omega \\
&+\oint_{\Gamma}\left(\phi D_{ij}\ w_I\ \frac{\partial \hat{m}}{\partial x_j}\right)\ \mathrm{d}\Gamma = 0
\end{aligned}$$

$$i, j = 1, 2, 3 \qquad\qquad I = 1...Nn \tag{4.39}$$

The last term in (4.39) represents dispersive-diffusive mass flux at the domain boundary Γ. The integrals in the weak form (4.39) are then broken up to obtain the Nn

finite element equations for reactive transport. With the trial solution given by (4.37), treating the mass accumulation term in (4.39) with a lumped mass approach, and using the fact that summation and integration are interchangeable operations, one obtains the following rearranged set of Nn equations

$$\sum_{J=1}^{Nn} m_J \left\{ \sum_e \int_{V^e} \left(\phi D_{ij} \frac{\partial w_I}{\partial x_i} \frac{\partial w_J}{\partial x_j} + q_i \, w_I \frac{\partial w_J}{\partial x_i} + \frac{\varepsilon \, \gamma_{\mathrm{H_4SiO_4}}}{K_{eq}} \, w_I \, w_J \right) \mathrm{d}V^e + \right.$$

$$+ \sum_{J=1}^{Nn} \frac{\partial m_J}{\partial t} \left\{ \sum_e \int_{V^e} (\phi R \, w_I) \, \mathrm{d}V^e \right\} - \sum_e \int_{V^e} (\varepsilon \, w_I) \, \mathrm{d}V^e$$

$$= \sum_e \oint_{\Gamma^e} \left(\phi D_{ij} \, w_I \frac{\partial \hat{m}}{\partial n} \right) \mathrm{d}\Gamma^e$$

$$i, j = 1, 2, 3 \qquad I = 1...Nn \tag{4.40}$$

The steps (4.36) to (4.40) can be repeated for the discrete fractures using the governing transport equation (3.21) and relation (2.9) to obtain an integrated weak form of the fracture element contributions similar to (4.40). The technique of superimposing 2D fracture elements onto 3D porous matrix elements can then be applied such that each grid point J obtains contributions from all 2D and 3D elements that join node J. Computationally speaking, this corresponds to a loop over all Nn grid points, where integrated terms from all matrix elements e and all fracture elements fe are added up if the grid point J is a node of e and fe. Application of this procedure results in the following superimposed fracture-matrix system:

$$\sum_{J=1}^{Nn} m_J \left\{ \sum_e \int_{V^e} \left(\phi D_{ij} \frac{\partial w_I}{\partial x_i} \frac{\partial w_J}{\partial x_j} + q_i \, w_I \frac{\partial w_J}{\partial x_i} + \frac{\varepsilon \, \gamma_{\mathrm{H_4SiO_4}}}{K_{eq}} \, w_I \, w_J \right) \mathrm{d}V^e + \right.$$

$$\left. \sum_{fe} (2b) \int_{A^{fe}} \left(D^{fr}_{i'j'} \frac{\partial w^{fr}_I}{\partial x_{i'}} \frac{\partial w^{fr}_J}{\partial x_{j'}} + q^{fr}_{i'} \, w^{fr}_I \frac{\partial w^{fr}_J}{\partial x_{i'}} + \frac{\varepsilon^{fr} \, \gamma^{fr}_{\mathrm{H_4SiO_4}}}{K_{eq}} \, w^{fr}_I \, w^{fr}_J \right) \mathrm{d}A^{fe} \right\}$$

$$+ \sum_{J=1}^{Nn} \frac{\partial m_J}{\partial t} \left\{ \sum_e \int_{V^e} (\phi R \, w_I) \, \mathrm{d}V^e + \sum_{fe} (2b) \int_{A^{fe}} \left(R^{fr} \, w^{fr}_I \right) \mathrm{d}A^{fe} \right\}$$

$$- \sum_e \int_{V^e} (\varepsilon \, w_I) \, \mathrm{d}V^e - \sum_{fe} (2b) \int_{A^{fe}} \left(\varepsilon^{fr} \, w^{fr}_I \right) \mathrm{d}A^{fe}$$

$$= \sum_e \oint_{\Gamma^e} \left(\phi D_{ij} \, w_I \frac{\partial \hat{m}}{\partial n} \right) \mathrm{d}\Gamma^e + \sum_{fe} (2b) \oint_{\Gamma^{fe}} \left(D^{fr}_{i'j'} \, w^{fr}_I \frac{\partial \hat{m}}{\partial n} \right) \mathrm{d}\Gamma^{fe}$$

$$i, j = 1, 2, 3 \qquad i', j' = 1, 2 \qquad I = 1...Nn \tag{4.41}$$

where Σ_e and Σ_{fe} symbolize the summation over all porous matrix and fracture elements, respectively, that join node J. Equation (4.41) can be written in a compact semi-discrete matrix form similar to that given by Frind (1982):

$$\mathbf{R} \bullet \mathbf{m} \; + \; \mathbf{T} \bullet \frac{\partial \mathbf{m}}{\partial t} \; + \; \mathbf{u} \; = \; \mathbf{b} \tag{4.42}$$

where $\mathbf{R}$ [L^3 T^{-1}] is the advective-dispersive-reactive transport matrix, $\mathbf{T}$ [L^3] is the solute mass matrix, $\mathbf{u}$ [MOL M^{-1} L^3 T^{-1}] represents the constant quartz dissolution reaction rate, and $\mathbf{b}$ [MOL M^{-1} L^3 T^{-1}] contains the dispersive mass flux at the domain boundary Γ. The definitions of matrices $\mathbf{R}$ and $\mathbf{T}$ and vectors $\mathbf{u}$ and $\mathbf{b}$ are given in Appendix A. A standard finite difference approach is applied to (4.42) in order to discretize the temporal derivative of $\mathbf{m}$ such that

$$\frac{\partial \mathbf{m}}{\partial t} \; = \; (1-\alpha)\, \dot{\mathbf{m}}^L + \alpha\, \dot{\mathbf{m}}^{L+1} \; \simeq \; \frac{\mathbf{m}^{L+1} - \mathbf{m}^L}{\Delta t} \tag{4.43}$$

which gives a time-weighted form of (4.42) as

$$\left(\alpha \mathbf{R} + \frac{1}{\Delta t}\mathbf{T}\right) \bullet \mathbf{m}^{L+1} = \left(-(1-\alpha)\mathbf{R} + \frac{1}{\Delta t}\mathbf{T}\right) \bullet \mathbf{m}^L + \left((1-\alpha)\mathbf{b}^L + \alpha \mathbf{b}^{L+1} - \mathbf{u}\right)$$

$$0 < \alpha \leq 1 \tag{4.44}$$

where α [–] is a time-weighting factor. An implicit time-weighting scheme ($\alpha = 1$) usually gives results of highest numerical stability (Istok, 1989). In this case, Equation (4.44) becomes

$$\left(\mathbf{R} + \frac{1}{\Delta t}\mathbf{T}\right) \bullet \mathbf{m}^{L+1} = \left(\frac{1}{\Delta t}\mathbf{T}\right) \bullet \mathbf{m}^L + \left(\mathbf{b}^{L+1} - \mathbf{u}\right) \tag{4.45}$$

which can be written in the compact form

$$\mathbf{A} \bullet \mathbf{m} = \mathbf{d} \tag{4.46}$$

where the matrix $\mathbf{A}$ is the term in the brackets on the left hand side of (4.45), the vector $\mathbf{m}$ represents the unknown molalities at time level L+1, and the vector $\mathbf{d}$ embodies all known terms, summarized on the right hand side of relation (4.45).

4.6 Heat Transfer

The finite element formulation of the heat transfer equations (3.24) and (3.27) is similar to the solute transport problem. Repeating steps (4.36) to (4.40) in an analogous fashion, the semi-discrete form of the heat transfer equations obtained by assembling the porous matrix and the fracture zone is given by

$$\sum_{J=1}^{Nn} T_J \left\{ \sum_e \int_{V^e} \left((k_b + \phi D_{ij}\ \rho_l \tilde{c}_l)\ \frac{\partial w_I}{\partial x_i}\ \frac{\partial w_J}{\partial x_j}\ + (q_i\ \rho_l \tilde{c}_l)\ w_I\ \frac{\partial w_J}{\partial x_i} \right)\ \mathrm{d}V^e + \right.$$

$$\left. \sum_{fe} (2b) \int_{A^{fe}} \left(\left(k_l + D^{fr}_{i'j'}\ \rho_l \tilde{c}_l \right)\ \frac{\partial w^{fr}_I}{\partial x_{i'}}\ \frac{\partial w^{fr}_J}{\partial x_{j'}}\ + \left(q^{fr}_{i'}\ \rho_l \tilde{c}_l \right)\ w^{fr}_I\ \frac{\partial w^{fr}_J}{\partial x_{i'}} \right)\ \mathrm{d}A^{fe} \right\}$$

$$+ \sum_{J=1}^{Nn} \frac{\partial T_J}{\partial t} \left\{ \sum_e \int_{V^e} (\rho_b \tilde{c}_b\ w_I)\ \mathrm{d}V^e + \sum_{fe} (2b) \int_{A^{fe}} \left(\rho_l \tilde{c}_l\ w^{fr}_I \right)\ \mathrm{d}A^{fe} \right\}$$

$$= \sum_e \oint_{\Gamma^e} \left((k_b + \phi D_{ij}\ \rho_l \tilde{c}_l)\ w_I\ \frac{\partial \hat{T}}{\partial n} \right)\ \mathrm{d}\Gamma^e$$

$$+ \sum_{fe} (2b) \oint_{\Gamma^{fe}} \left(\left(k_l + D^{fr}_{i'j'}\ \rho_l \tilde{c}_l \right)\ w^{fr}_I\ \frac{\partial \hat{T}}{\partial n} \right)\ \mathrm{d}\Gamma^{fe}$$

$$i, j = 1, 2, 3 \qquad i', j' = 1, 2 \qquad I = 1...Nn \tag{4.47}$$

These Nn equations are further discretized with a finite difference scheme in time to finally obtain a matrix system similar to (4.46).

Chapter 5

Verification Problems

In this chapter, simulation results are presented to verify variable-density flow (Section 5.1), reactive solute transport (Section 5.2) and heat transfer (Section 5.3). The verification problems of reactive transport and heat transfer that imply a single fracture are identical to the fracture-matrix system used by Tang et al. (1981) shown in Figure 5.11. Tang et al. (1981) presented the analytical solution of solute transport along a single fracture embedded in a porous matrix.

The variable-density flow solution in porous media was compared with available numerical as well as laboratory results. These are the Elder (1967) 2D problem of free convection and the experimental 3D saltpool problem (Oswald and Kinzelbach, 2004). In the developed model, variable-density flow in a fracture takes place in vertical, horizontal and inclined faces. Density-driven flow in vertical fracture elements was tested using results from numerical simulations carried out by Shikaze et al. (1998). In horizontal faces, density effects naturally do not occur and the buoyancy term (4.14) vanishes. To date, density-driven flow in inclined fractures has not yet been investigated. Thus, numerical or experimental simulation results of this problem do not exist. Therefore, two simulations with a single 45°-inclined fracture were run with the present model. The first scenario represents the target case because the fracture was discretized by inclined 2D elements. In the second reference case, the fracture consisted of horizontal and vertical elements. The fracture velocities in this second staircase-fracture were multiplied by a correction factor to account for the longer path. Finally, variable-

density flow in a vertical and an inclined fracture was also verified by comparing the onset of unstable flow with the analytical solution for the critical Rayleigh number presented by Caltagirone (1982).

Reactive solute transport was verified using analytical solutions, where the solute source term was set equal the first order precipitation rate and where a constant term represents the forward dissolution reaction. Thus, the transport equation remains linear and is mathematically identical to a transport problem that implies first order radioactive decay and a constant term of zeroth order. The problem was completely linearized by assuming constant material properties and by neglecting the presence of electrolytes. Verification examples are presented for reactive solute transport in porous media, fractured media with an impermeable matrix and fractured porous media. The first two cases are 1D problems, where the fixed silica molality on the recharge boundary is zero. This causes a permanent dissolution reaction within the model domain with a maximum rate on the recharge boundary. The inflowing deionized water constantly dilutes the silicic water, leading to a steadily increasing silica molality along the flow axis. The third test case verifies 2D reactive transport in a fractured porous environment. The unknown silica molality of this problem was increased by the equilibrium constant, thus introducing a new transport variable. With the new variable, the constant dissolution reaction term vanishes, such that the transport problem is mathematically identical to the problem studied by Tang et al. (1981). Consequently, the solution becomes analogous to the Tang et al. (1981) analytical solution.

The heat transfer equation is a standard parabolic-hyperbolic partial differential equation of second order. It is mathematically identical to the pure advective-dispersive-diffusive transport equation. Four verification problems are presented to test the heat transfer equations. Conduction and convection are tested in both an unfractured porous medium (example *heat1*) and in a single fracture within an impermeable matrix (example *heat2*). The Ogata-Banks (1961) equation is used as the reference analytical solution. The third verification example tests heat flux in both the porous matrix and in the fracture. If heat conduction and mechanical dispersion in the fracture are neglected, an analytical solution in fractured porous media exists in a form analogous to that presented by Tang et al. (1981).

Yang and Edwards (2000) studied long-term variable-density, variable-viscosity thermal flow in a 2D anisotropic porous medium on the field scale. Their numerical simulation of heat transfer is used as a fourth test case. This last problem includes all heat transfer mechanisms in both continua with variable fluid properties. Therefore, the available solution is numerical.

5.1 Variable-Density Flow

Variable-Density Flow in Porous Media

Variable-density flow and transport in porous media was verified in two and three dimensions. All simulations used implicit transport time weighting, as is common in other variable-density simulations, and full upstream weighting as proposed by Frolkovič and De Schepper (2000).

First, the Elder (1967) salt convection problem was simulated to qualitatively test the model in two dimensions. Kolditz et al. (1998) point out that, for a coarse grid, the central transport direction is downwards, whereas a fine grid exhibits central upwelling. These observations were confirmed by Prasad and Simmons (2004) as well as in the present study using FRAC3DVS (Figure 5.1).

Another model verification consisted of comparing the Elder (1967) results presented by Frolkovič and De Schepper (2000) to those of FRAC3DVS. This verification is more trustworthy than that described in the previous paragraph because both numerical models (the Frolkovič and De Schepper (2000) model and FRAC3dVS) use the same numerical approach (control volume finite element method, CVFE) as well as the same flow variable (fluid pressure, P). The governing flow equation for this variable is given in Appendix B. Frolkovič and De Schepper (2000) carried out their numerical simulations in the half domain of the symmetric Elder problem. Interestingly, they found that an extremely fine grid (32,768 nodes in the half domain) again exhibits central downwelling, which was also discovered by Diersch and Kolditz (2002). Their results are in very good visual agreement with those from the FRAC3DVS model (Figure 5.2).

A new benchmark problem for variable-density transport in 3D has been presented by Oswald and Kinzelbach (2004). This problem is based on the three-dimensional variable-density flow and solute transport experiments in porous media conducted by Oswald (1999). In these experiments, a 0.2 m × 0.2 m × 0.2 m closed box initially contained saltwater from the bottom up to 8 cm, with the rest of the box filled with freshwater. A constant freshwater recharge through one upper corner of the box disturbed this stable layering of two miscible fluids. The concentration of the mixed fluid versus time was measured at the discharging open hole on the opposite side of the input location. Oswald (1999) used two different initial concentrations $c_{01} = 0.01$ (case 1) and $c_{02} = 0.1$ (case 2). The experimental results were numerically reproduced by Johannsen et al. (2002), who also present tabular data of the measured concentrations versus time.

The FRAC3DVS model output was compared in three dimensions with Oswald's (1999) experimental results, given in Johannsen et al. (2002). The physical parameters given by Oswald and Kinzelbach (2004) were used. The first problem of the lower initial concentration 0.01 (case 1) was used because Johannsen et al. (2002) showed that, in this case, grid convergence is achieved with a relatively coarse grid, whereas for case 2, the solution converged only for a very fine grid, consisting of at least 274,625 grid points (Johannsen et al., 2002). Good agreement between the experimental results from Oswald (1999), the numerical results from Diersch and Kolditz (2002) and the FRAC3DVS model was obtained (Figure 5.3). The long-term results of this low density case more closely resemble the experimental data than in Diersch and Kolditz (2002); however, differences remain.

Variable-Density Flow in Fractured Porous Media

Variable-density flow in vertical fractures was verified by reproducing the results presented by Shikaze et al. (1998). The trial which includes only vertical fractures was used as a test case. The external hydraulic heads on both aquifer top and bottom were set to zero because Shikaze et al. (1998) showed that density effects are best accounted for if the imposed head gradient vanishes. Otherwise, the effect of forced convection may suppress free convection. In the numerical simulations, the left and right boundaries

were assumed to be impermeable for flow. The top of the domain is assumed to be a salt lake with a constant concentration equal to 1.0. All other boundaries for transport are zero dispersive-flux boundaries. The physical parameters used are identical to those presented in Shikaze et al. (1998) and summarized in Table 5.1. The 3D domain is of size $\ell_x = 10$ m, $\ell_y = 1$ m and $\ell_z = 10$ m. The spatial discretization used was 0.025 m in both the x- and the z-direction and unity in the y-direction. Fracture spacings are nonuniform as shown in Figure 5.4. The figure shows excellent agreement between the concentration distributions calculated by the two numerical models.

Table 5.1: Model parameters used in fractured media studies. All parameters are identical to those used by Shikaze et al. (1998).

Parameter	Value
Free-solution diffusion coefficient (D_d)	5×10^{-9} m^2 sec^{-1}
Brine density (ρ_{max})	1200 kg m^{-3}
Reference density (ρ_0)	1000 kg m^{-3}
Fluid compressibility (α_{fl})	4.4×10^{-10} kg^{-1} m sec^2
Matrix compressibility (α_m)	1.0×10^{-8} kg^{-1} m sec^2
Fluid dynamic viscosity (μ)	1.1×10^{-3} kg m^{-1} sec^{-1}
Matrix permeability (κ_{ij})	10^{-15} m^2
Matrix longitudinal dispersivity (α_l)	0.1 m
Matrix transverse dispersivity (α_t)	0.005 m
Matrix porosity (ϕ)	0.35
Tortuosity (τ)	0.1
Fracture dispersivity (α^{fr})	0.1 m
Fracture aperture ($2b$)	50 μm

In horizontal fracture elements, the buoyancy term, g_i^e, becomes zero. This was tested by running two variable-density simulation trials using a square vertical slice. The first case is an unfractured porous medium whereas in the second case, a single horizontal fracture is running across the middle of the domain. External driving forces for fluid flow were not imposed. The fracture-matrix node in the center of the slice was assigned a constant concentration while the concentration on all other nodes was initially zero. In both cases, a plume develops, which migrates downwards. The observed results are identical, showing that there is no buoyancy effect in the horizontal fracture

additional to that in the porous matrix.

Variable-density flow in a fracture with incline $\varphi = 45^{o}$ was verified by comparing results from two different scenarios. In the scenario 1, an inclined fracture is discretized by only inclined faces (Figure 5.5a). In a second scenario, the inclined fracture consists of only vertical and horizontal faces (Figure 5.5b). Representing a discrete fracture by one layer of two-dimensional faces with only one 2D finite element in the horizontal y-direction, is essentially a 1D description of the discrete fracture. This representation inhibits numerically simulating convection within the fracture, both normal and perpendicular to the fracture plane. However, the entire fracture-matrix system is a 2D vertical slice, allowing convection with rotation axis normal to the slice.

Both trials were run with the developed model. The first scenario is the target simulation because inclined faces are used, for which model verification is required. Case 2 is the reference simulation because variable-density flow in vertical and horizontal fracture faces has already been verified. All simulations use a three-dimensional vertical slice with dimensions $\ell_x = 12$ m, $\ell_z = 10$ m as model domain. The left and right boundaries are assumed to be impermeable, whereas the top and bottom boundaries are specified as constant equivalent head boundaries with zero heads. The contaminant source of constant concentration, $c = c_L$, overlies groundwater of initial concentration, $c = c_0$, where $c_0 = 0.0 \ < \ c_L = 1.0$.

All simulations cover a time of 20 years. Time step sizes are kept constant at 0.2 years. The input parameters for the numerical simulations are shown in Table 6.3. These parameters were held constant throughout all simulations unless otherwise stated. It is assumed that the porous matrix is isotropic and homogeneous throughout and that the entire aquifer is completely saturated.

Grids of different discretization levels were generated to investigate the adequate grid line density. The method is called grid convergence study and it involves performing a simulation on successively finer grids. As the grid is refined, the spatial discretization errors should asymptotically approach zero, excluding computer round-off errors.

Here, the grid at the lth level ($l = 1,2...$) consists of $480l^2$ identical square elements,

which have the size $\Delta x = \Delta z = 1/2l$ m. Increasing grid levels correspond to finer grids. Several simulations of scenario 1 were performed at increasing grid levels and the tracer breakthrough was monitored at the observation point ($x = 6$ m, $z = 6$ m) in the fracture as shown in Figure 5.5. Grid convergence was achieved for the grid of level 5 (Figure 5.6), consisting of 12,000 square elements of size $\Delta x = \Delta z = 0.1$ m. With this grid, the grid Péclet number $\mathrm{Pe}_g = \Delta x/\alpha_l$ becomes 1.0, satisfying the widely accepted criteria for neglecting numerical dispersion, $\mathrm{Pe}_g \leq 2$, as well as oscillations, $\mathrm{Pe}_g \leq 4$.

It is remarkable that grid convergence was accomplished that easily, which is not obvious for two-dimensional free convective flow regimes. Common 2D convection studies are the Elder (1967) problem and the orthogonal fracture network simulations by Shikaze et al. (1998). Although both problems are physically very different, both cases demonstrate that 2D free convective flow depends on grid line density. For the former problem, grid convergence is practically never achieved because different qualitative results (i.e. central downwelling - upwelling - downwelling) are obtained with different spatial discretizations (i.e. coarse - fine - extremely fine). Strong dependency on spatial discretization was also observed for the latter problem. Shikaze et al. (1998) reached grid convergence by refining the grid until the resulting concentration plots appeared unchanged (Shikaze, 2004, personal communication). In the present case, the described grid convergence study was carried out up to the 10^{th} grid level to make sure that, at higher levels, the convective system does not completely change its behavior as is the case in the Elder problem.

With the appropriate grid level 5, simulations of scenario 1 and 2 were run. In order to account for the longer path in the fracture of scenario 2, the fracture velocities in this scenario were multiplied at each time step with a correction factor. The ratio of the lengths of the two fractures has to coincide with the ratio of their average flow velocities, represented by the maximum fracture velocity (see Figure 5.8e). In the present case of a 45^{o}-inclined fracture, this ratio is $\sqrt{2}$. The output of the two simulations is shown in Figure 5.7.

The model output from scenario 1 and 2 was objectively compared by means of quantitative indicators described by Prasad and Simmons (2004). The calculated indicators are shown in Figure 5.8. Quantitatively evaluating model results also accounts

for mass fluxes through the upper boundary (indicators shown in Figures 5.8a and b), penetration depth of the 60% concentration contour (c), maximum matrix and fracture velocities (d and e) and mass balance (f). This quantitative evaluation completes conventional comparison of isochlors and breakthrough curves (Figure 5.7 left and right, respectively). Figures 5.7 and 5.8 clearly show very good agreement between the two results, indicating that variable-density flow in inclined fractures is verified.

Figure 5.8e can also be used to verify the Reynolds number requirement, $Re = q^{fr}d/\nu < 1$, for Darcy's law in fractures (Equation 3.9). The figure shows that the Darcy flux in the fracture, q^{fr}, does not exceed 10,000 m yr^{-1}. If the fracture aperture is chosen as the representative microscopic length, $d = (2b)$, and with the kinematic viscosity given by $\nu = \mu/\rho_0$, the Reynolds number is 0.01495. Thus, laminar flow as well as a linear relationship between q_i^{fr} and $\partial h_0^{fr}/\partial x_j$ is ensured for all simulations presented in Figure 5.7 and Chapter 6.

The primary purpose of Figure 5.8 is to demonstrate that the model is verified. A more rigorous interpretation of the figure follows in Section 6.1 where results of scenario 1 and its variations are discussed in more detail.

Onset of Convection in Fractured Media

The analytical solution (2.24) for the onset condition of free convection in homogeneous isotropic media was used here to verify variable-density flow in a fracture. The onset of unstable flow was verified in both a vertical and an inclined fracture. Two series of simulations, one for a vertical and another for an inclined fracture, were carried out. Different Rayleigh numbers were obtained by changing the fracture aperture. In both series, the porous matrix was considered impermeable. Boundary conditions were imposed as outlined in Section 2.3.

The first series involves a single vertical fracture within an impermeable matrix. The fracture is of height $\ell_{\bar{z}} = 40$ m and of varying length $\ell_{\bar{x}} = 0.5\ \ell_{\bar{z}}$, $1.0\ \ell_{\bar{z}}$, $1.5\ \ell_{\bar{z}}$, $2.0\ \ell_{\bar{z}}$ and $3.0\ \ell_{\bar{z}}$. The spatial discretization of the discrete fracture is 1.0 m in both the local $\bar{x}$- and the $\bar{z}$-direction (Shi, 2005). As in Weatherill et al. (2004), the system was

perturbed by increasing the initial nodal concentration at ($\bar{x} = 0.5\ \ell_{\bar{x}}$, $\bar{z} = 0.5\ \ell_{\bar{z}}$) by 10%. According to theory, simulations with $Ra < Ra_c$ remain stable while systems with $Ra > Ra_c$ exhibit unstable variable-density flow with varying numbers of rolls. Figure 5.9 plots the stable/unstable flow behavior and shows that the analytical solution (2.24) correctly separates stable from unstable model results.

The second series involves a single inclined fracture, with incline $\varphi = 45^{\circ}$, within an impermeable matrix. The fracture plane is the diagonal of a cuboidal matrix block and is of height $\ell_{\bar{z}} = 56.5685$ m and its length varies akin to the vertical fracture case. The spatial discretization of the discrete fracture is 1.41421 m in both the $\bar{x}$- and the $\bar{z}$-direction. The system was initially perturbed as described in the previous paragraph. The Rayleigh number, Ra^*, as well as its critical threshold value, Ra_c^*, are now by the factor $1/\cos\varphi$ larger than in the vertical fracture case (Equation (2.25); Caltagirone, 1982; Weatherill, 2004). Figure 5.10 demonstrates that the analytical solution (2.25) correctly plots the simulation results in two half-areas.

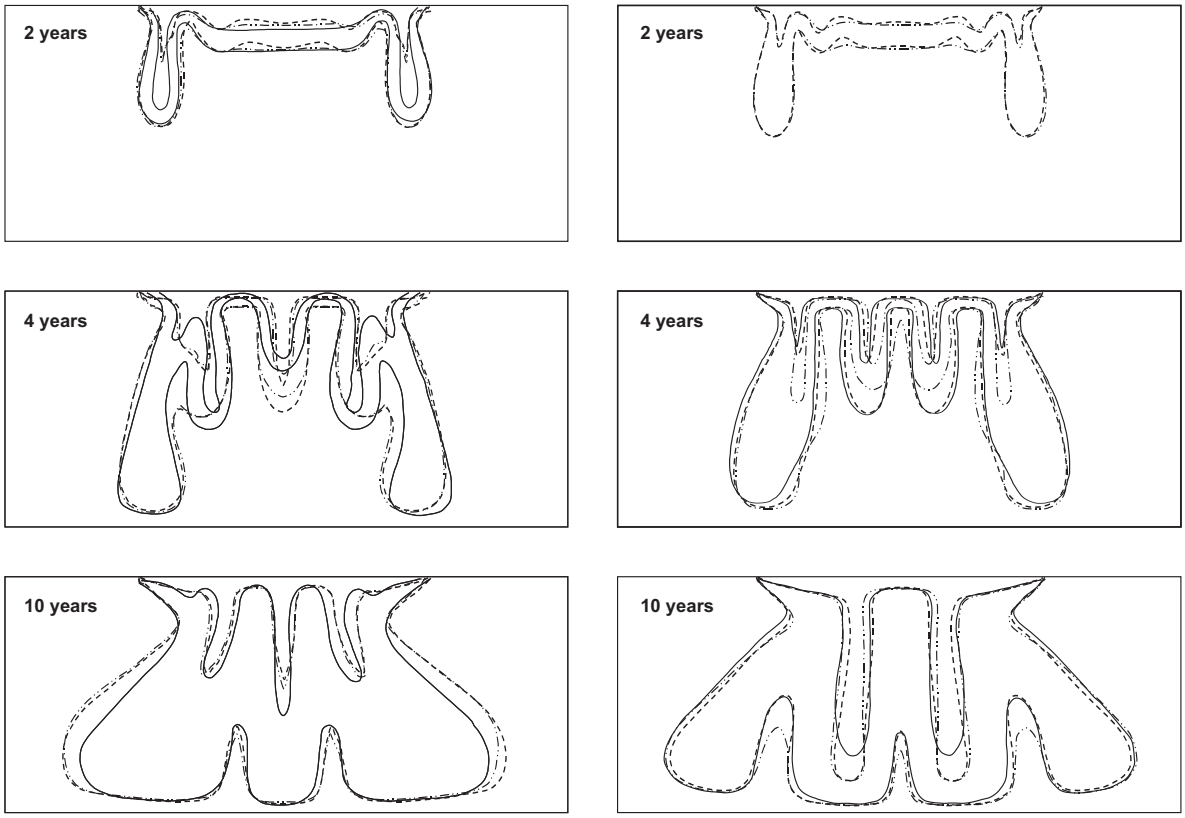

Figure 5.1: Results of the Elder problem for a coarse grid (left; 60 × 30 elements) and a fine grid (right; 120 × 40 elements) at 2, 4 and 10 years simulation time by Elder (1967) [— coarse grid], Kolditz et al. (1998) [— fine grid], Prasad and Simmons (2004) [- ·· -] and the present model [- -]. The domain size is 600 m × 150 m.

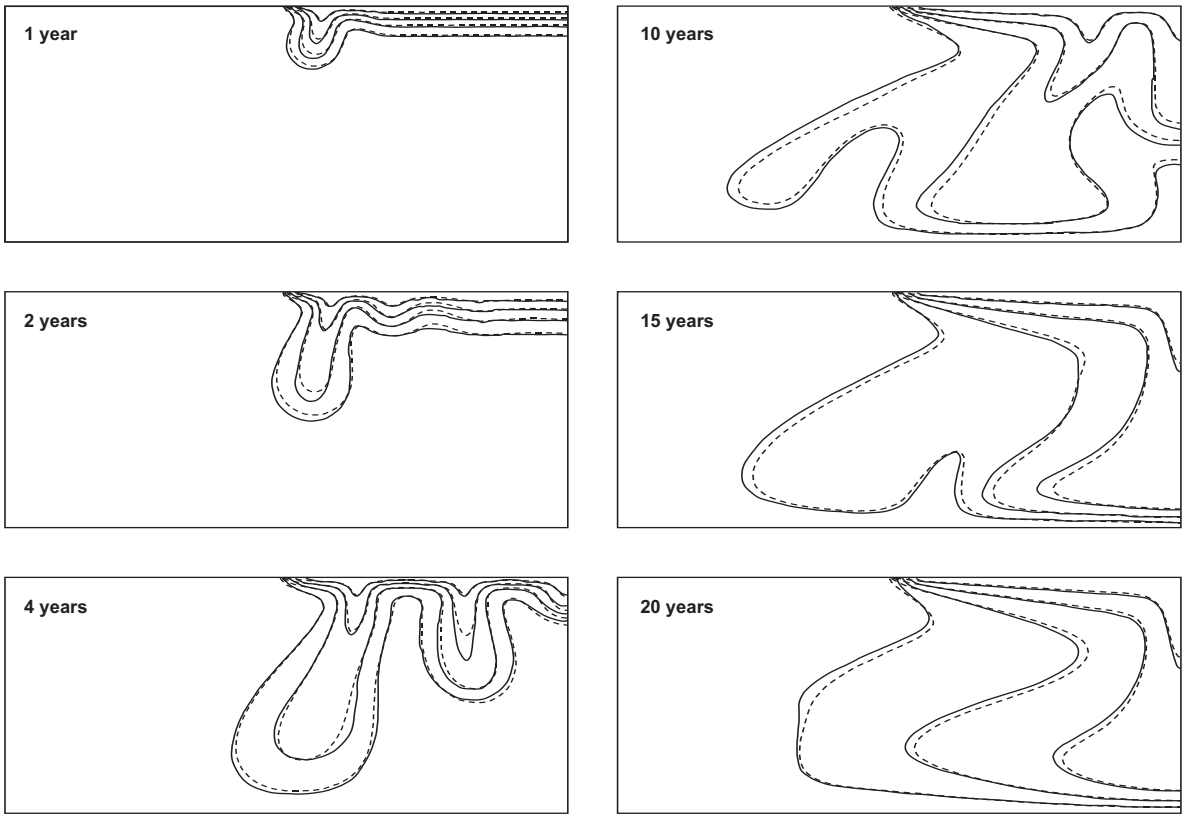

Figure 5.2: Results of the Elder problem for an extremely fine grid (256 × 128 elements in the half domain) at 1, 2, 4, 10, 15 and 20 years simulation time by Frolkovič and De Schepper (2000) [—] and the present model [- -]. Shown are the 20%, 40%, 60% and 80% contours. The half domain size is 300 m × 150 m.

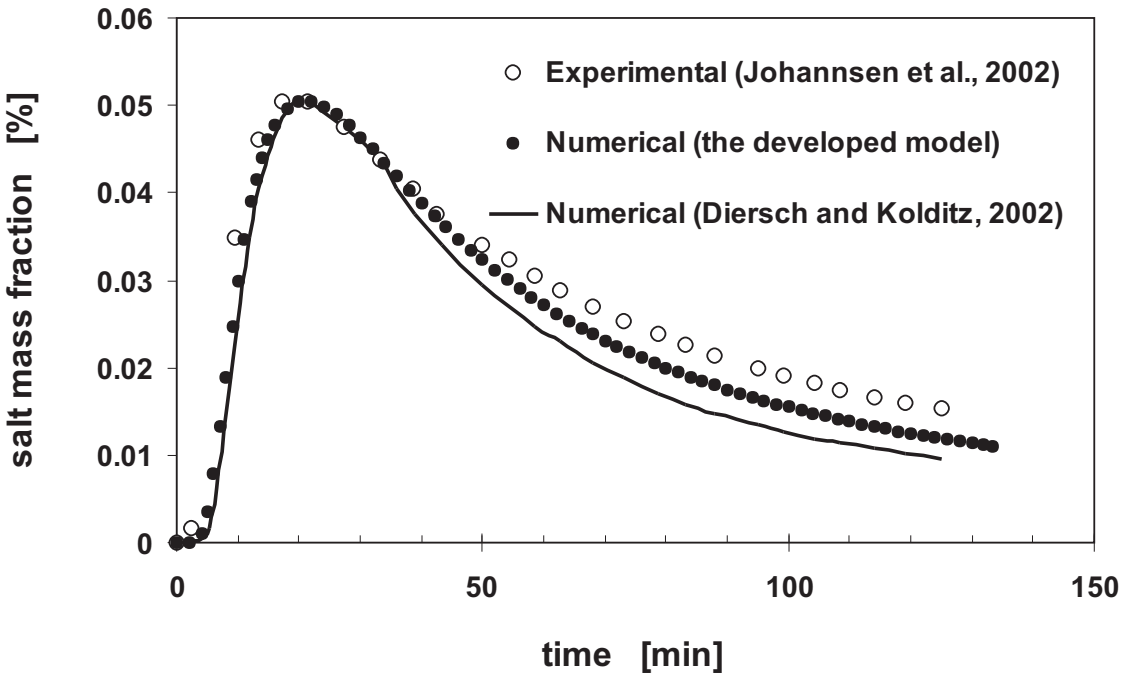

Figure 5.3: Results of three-dimensional variable-density transport simulations in porous media.

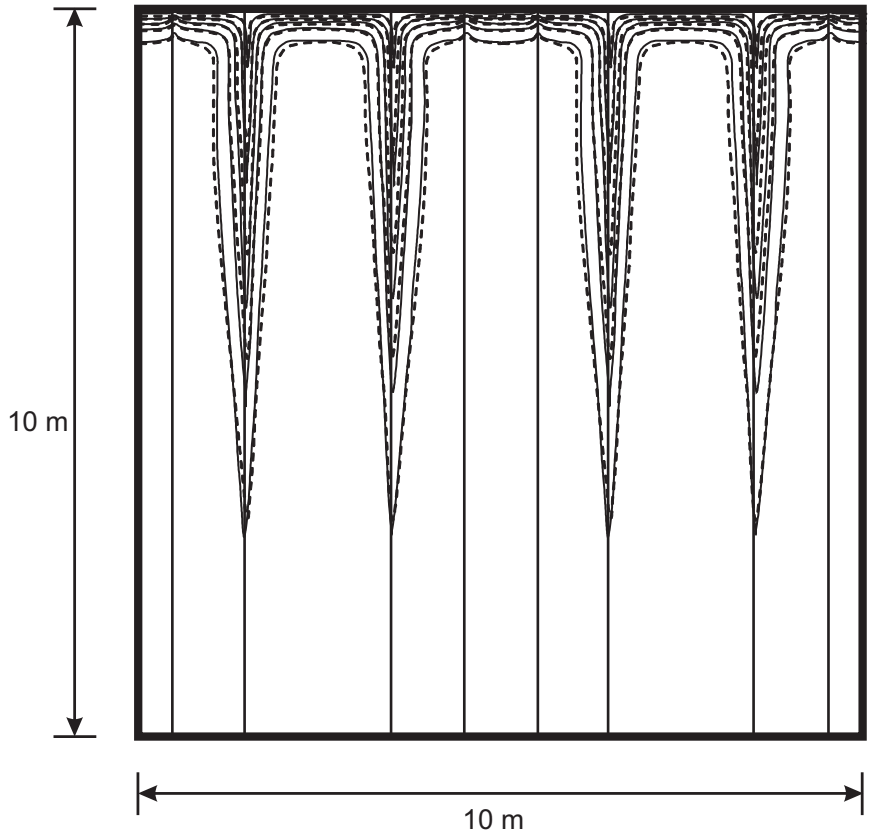

Figure 5.4: Variable-density flow in a set vertical fractures embedded in a porous matrix. Shown are the concentration contours from 0.1 to 0.9 with a contour interval of 0.2 at 2 years simulation time from Shikaze et al. (1998) [—] and from the present model [- -].

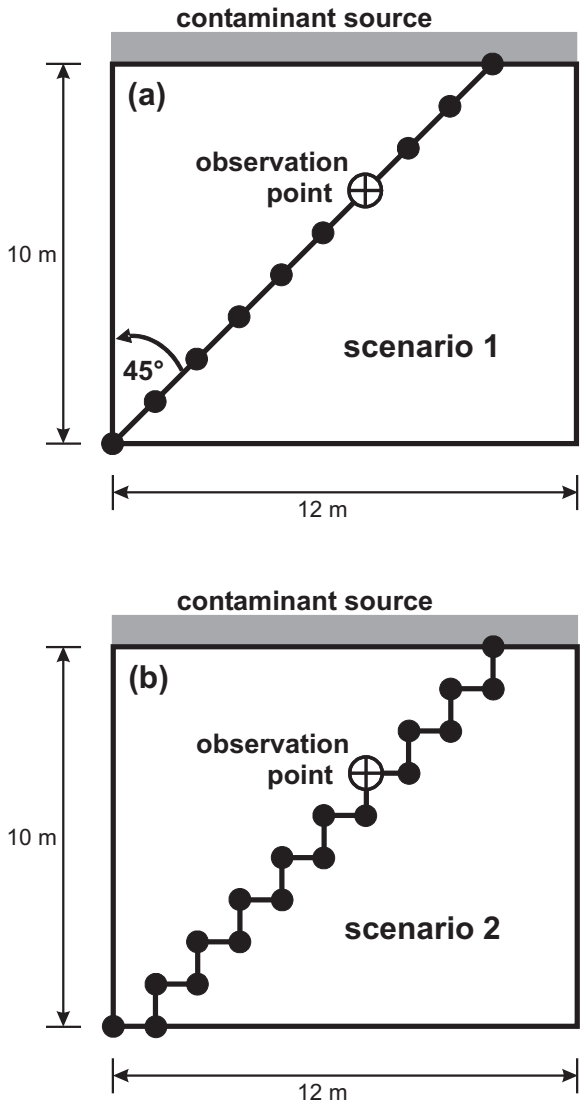

Figure 5.5: Different discretizations of an inclined fracture for verifying density-driven flow in inclined fractures. The second scenario uses corrected fracture velocities.

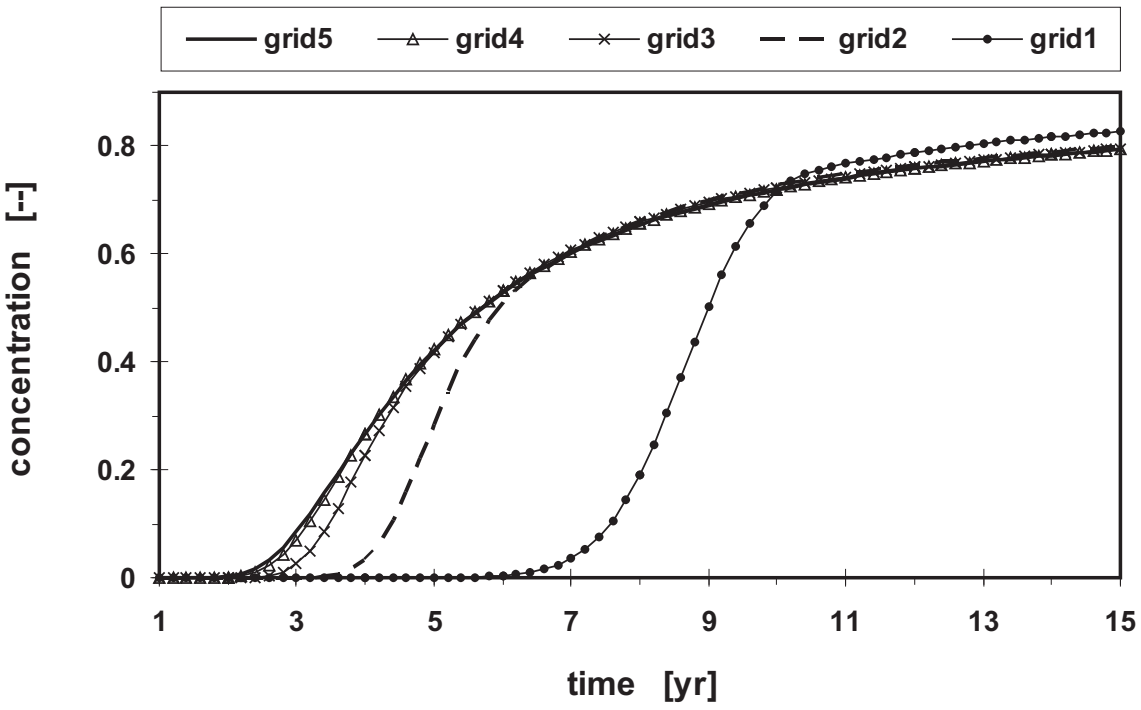

Figure 5.6: Grid convergence for the single inclined fracture case (scenario 1).

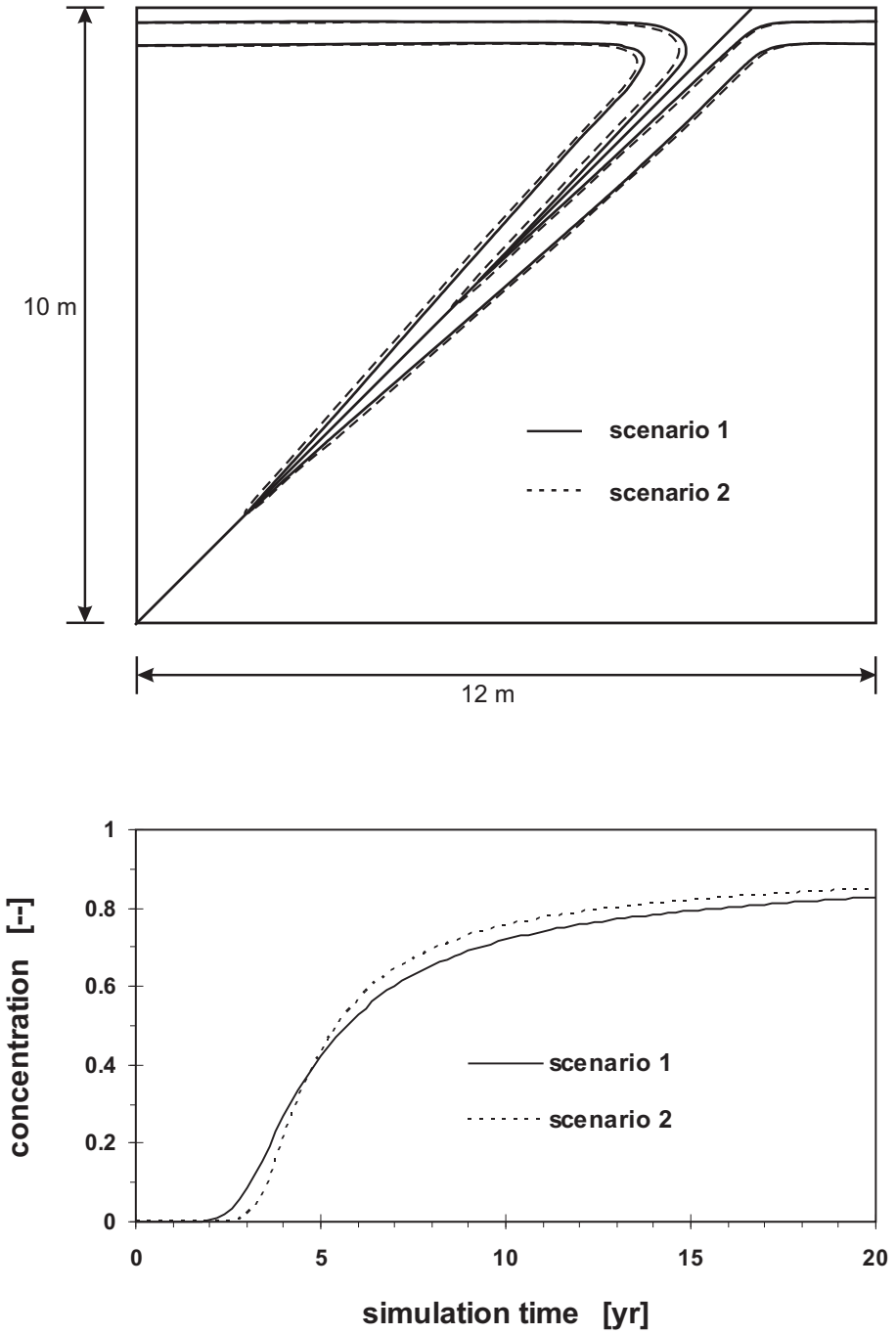

Figure 5.7: Results of the model verification for scenario 1 and 2: Concentration contours (20% and 60%) at 8 years simulation time and breakthrough curve at the observation point.

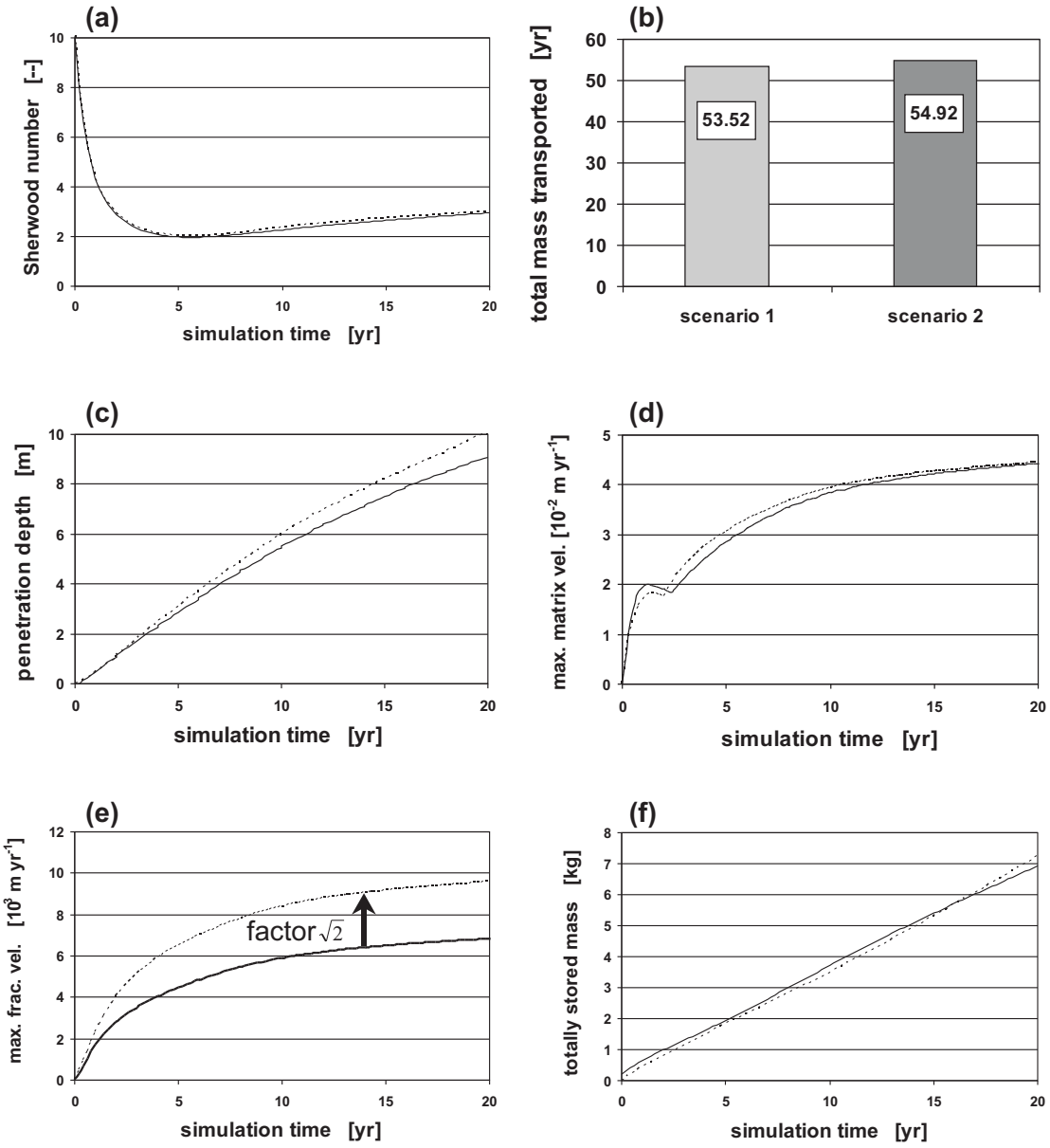

Figure 5.8: Results of the model verification with quantitative parameters (a) to (f), applied to scenario 1 [—] and 2 [- -].

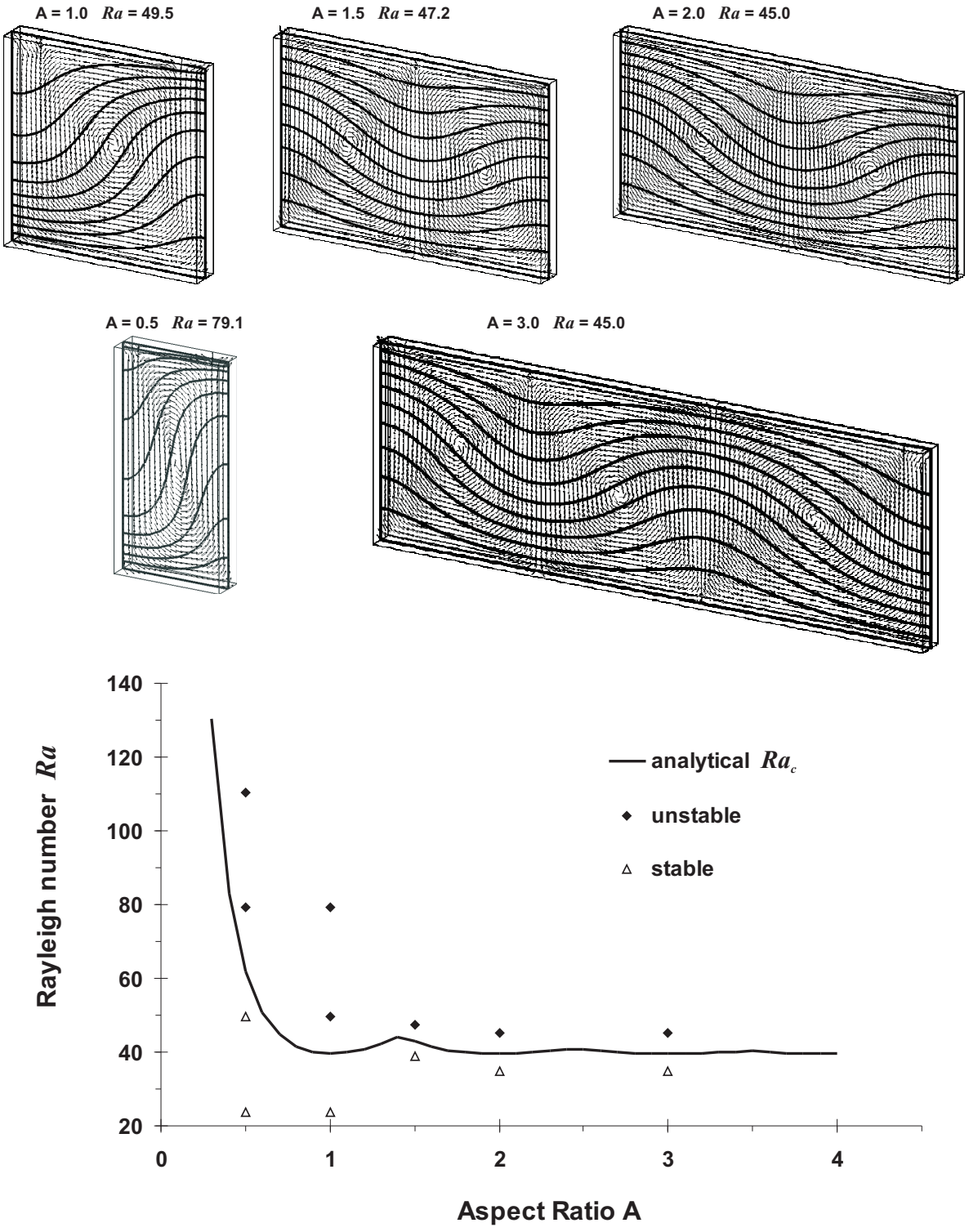

Figure 5.9: Stability plot showing two half-areas divided by the theoretically derived Ra_c as a function of aspect ratio A using a vertical fracture. Stable numerical FRAC3DVS simulations plot in the southern half-area while unstable cases as shown above plot in the northern half-area.

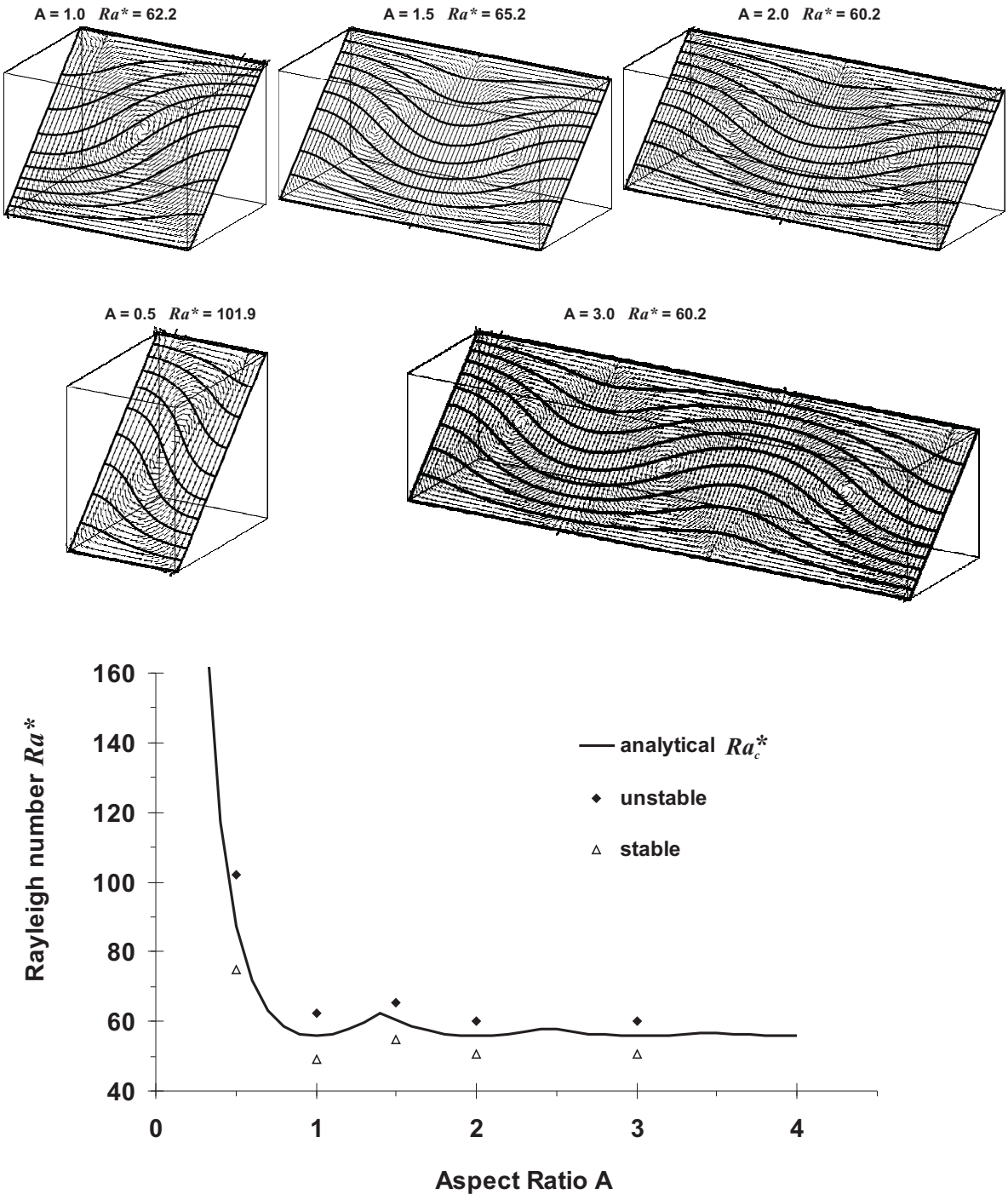

Figure 5.10: Stability plot showing two half-areas divided by the theoretically derived Ra_c^* as a function of aspect ratio A using an inclined fracture. Stable simulations plot in the southern half-area while unstable cases as shown above plot in the northern half-area.

5.2 Reactive Solute Transport

The three verification problems presented here test reactive transport in porous media, fractured media and fractured porous media, respectively. Table 5.2 summarizes which examples verifies reactive transport in what continuum.

Table 5.2: Overview of the verification problems that verify reactive solute transport in porous and fractured media.

Continuum being tested →	Reactive solute transport	
↓ Verification example	in PM[a]	in FM[b]
reac1	√	–
reac2	–	√
reac3	√	√

[a] Porous media
[b] Fractured media

In all verification examples for reactive transport, groundwater is assumed to be free of dissolved electrolytes, such that $k_+^{corr} = k_+^0$ and $\gamma_{H_4SiO_4} = 1$. For simplicity, the molal concentration of silica will be written as m.

Reactive Transport in Porous Media (*reac1*)

The first example verifies 1D advective-reactive transport in a porous medium where fractures are absent. In this case, governing equation (3.17) has the following form

$$\frac{\partial m}{\partial t} + v\frac{\partial m}{\partial x} + \frac{\phi_{qz} k_+^0 A_{qz}}{\phi}\left(\frac{m}{K_{eq}} - 1\right) = 0 \qquad 0 \leq x \leq \infty \tag{5.1}$$

A steady state flow solution yields the constant flow velocity, v. Assuming constant material and fluid properties, and further assuming a constant background temperature fully linearizes the transport problem. Fixing the boundary molality to zero and with the initial condition, $m(t = 0) = 0$, the analytical solution to (5.1) is given by Johnson

et al. (1998) in the transient form:

$$\frac{m}{K_{eq}} = \begin{cases} 1 - \exp[-\mathcal{A} \cdot (x/v)] & \text{for } x \leq v \cdot t \\ \\ 1 - \exp[-\mathcal{A} \cdot t] & \text{for } x > v \cdot t \end{cases} \tag{5.2}$$

where

$$\mathcal{A} = \frac{\phi_{qz} k_+^0 A_{qz}}{\phi K_{eq}} \tag{5.3}$$

The finite element domain used in the numerical simulations consists of 31 uniform blocks in the flow direction. Model parameters are given in Table 5.3 and the analytical as well as the numerical results at three different output times are shown in Figure 5.12. Verifying the net reaction rates (Figure 5.13) is important to ensure correct recalculations of material parameters. However, if material properties are assumed constant in time, explicitly calculating and comparing the reaction rates is pure postprocessing and does not verify the processor.

Reactive Transport in Fractured Media (*reac2*)

In the second verification problem, 1D advective-reactive transport in a single fracture within an impermeable matrix is tested. In this case, the governing transport equation in the fracture is

$$\frac{\partial m^{fr}}{\partial t} + v^{fr} \frac{\partial m^{fr}}{\partial z} + \phi_{qz}^{fr} k_+^0 A_{qz}^{fr} \left(\frac{m^{fr}}{K_{eq}} - 1 \right) = 0 \qquad 0 \leq z \leq \infty \tag{5.4}$$

With the same assumptions and initial/boundary conditions used in the previous example, the analytical solution of Equation (5.4) is analogous to (5.2) and given by

$$\frac{m^{fr}}{K_{eq}} = \begin{cases} 1 - \exp[-\mathcal{A}^{fr} \cdot (z/v^{fr})] & \text{for } z \leq v^{fr} \cdot t \\ \\ 1 - \exp[-\mathcal{A}^{fr} \cdot t] & \text{for } z > v^{fr} \cdot t \end{cases} \tag{5.5}$$

where

$$\mathcal{A}^{fr} = \frac{\phi_{qz}^{fr} k_+^0 A_{qz}^{fr}}{K_{eq}} \tag{5.6}$$

Table 5.3: Model parameters used in the verification example for 1D reactive silica transport in an unfractured porous matrix (*reac1*). All parameters are identical to those used by Johnson et al. (1998) unless otherwise stated.

Parameter	Value
Constant background temperature (T_C)	239°C
Matrix porosity (ϕ)	0.425
Quartz volume fraction[a] (ϕ_{qz})	0.575
Specific surface area in the matrix (A_{qz})	54.2 m^2 kg^{-1}
Groundwater velocity in the porous matrix[b] (v)	1.9727×10^{-5} m sec^{-1}
Dissolution rate constant[c] (k_+^0)	1.3298×10^{-8} mol m^{-2} sec^{-1}
Equilibrium constant[c] (K_{eq})	6.4996×10^{-3} mol kg^{-1}
Domain size (ℓ_x)	3.1 cm
Output times (t_1, t_2, t_3)	518.76 sec, 1021.8 sec and 1572.0 sec

[a] $1-\phi$
[b] q/ϕ
[c] Computed by this model for deionized water at $T_C = 239$°C

The spatial discretization and all model parameters are identical to those used in the previous example and given in Table 5.3. The specific surface area in the fracture is estimated as 10% of that previously used in the porous matrix. The results are shown in the Figures 5.14 and 5.15, which are qualitatively identical to Figures 5.12 and 5.13.

Reactive Transport in Fractured Porous Media (*reac3*)

The third verification problem examines 2D advective-reactive transport in a single fracture, embedded in a porous matrix where the solutes migrate due to molecular diffusion alone. Chemical reactions take place in both continua. Molecular diffusion and mechanical dispersion in the fracture are neglected, allowing an easier formulation of the analytical solution with no need to numerically integrate. Groundwater in the fracture migrates at a constant velocity. Heat transfer is not considered here, but a constant background temperature is imposed. The chemical interaction between the fluid and the

solid phase is represented by a kinetic reaction term of first order and a constant source term. Thus, the problem investigated is mathematically nearly identical to that given by Tang et al. (1981) where the solute sink is due to first order radioactive decay but where solute sources are not considered. It is further assumed that the material properties (i.e. matrix porosity, hydraulic conductivity, fracture aperture, mineral surface area) are constant in time. Different mineral surface areas in the porous matrix and in the fracture are used, resulting in two different net reaction rates. Mathematically speaking, this is in contrast to the assumption made by Tang et al. (1981) where the radioactive decay rates in fracture and matrix are identical.

Initially, the entire domain is in thermodynamic equilibrium. Silica-free deionized water enters the fracture at a constant rate during the entire simulation, diluting the silica-saturated fluid in the fracture. All boundaries, except the fracture inlet and outlet, are impermeable for flow and are assigned zero-dispersive transport rates. The drop of silica molality due to dilution creates a thermodynamic disequilibrium and triggers an immediate dissolution reaction. Eventually, the system reaches equilibrium between dilution and dissolution.

With $m = m' + K_{eq}$ and $m^{fr} = m^{fr'} + K_{eq}$, the governing equations of this problem using the new variables, m' and $m^{fr'}$, are given by Steefel and Lichtner (1998a) in the form:

$$\frac{\partial m'}{\partial t} - D_d \, \frac{\partial^2 m'}{\partial x^2} + \frac{\phi_{qz} k_+^0 A_{qz}}{\phi K_{eq}} \, m' = 0 \qquad\qquad b \leq x \leq \infty \tag{5.7}$$

and

$$\frac{\partial m^{fr'}}{\partial t} + v^{fr} \, \frac{\partial m^{fr'}}{\partial z} + \frac{\phi_{qz}^{fr} k_+^0 A_{qz}^{fr}}{K_{eq}} \, m^{fr'} - \frac{\phi D_d}{b} \, \frac{\partial m^{fr'}}{\partial x}\bigg|_{x=b} = 0$$

$$0 \leq z \leq \infty \tag{5.8}$$

for reactive transport in the porous matrix and in the discrete fracture, respectively. Using the new governing equations (5.7) and (5.8), both initial and boundary conditions are identical to those used in Tang et al. (1981). They are formulated mathematically by Steefel and Lichtner (1998a) who presented the steady state as well as the transient analytical solutions.

In the numerical simulation, the finite element domain is similar to that shown in Figure 5.11. It is spatially discretized in the x-direction using a gradually increasing Δx with factor 1.1 from $\Delta x = 0.005$ cm near the fracture to $\Delta x = 0.1$ cm at the domain boundary. In the flow direction, the Δz increases with factor 1.25 from $\Delta z = 0.001$ cm near the source to $\Delta z = 0.1$ cm at the domain boundary. All model parameters are summarized in Table 5.4.

Table 5.4: Model parameters used in the verification example for 2D reactive silica transport in fractured porous media (*reac3*).

Parameter	Value
Constant background temperature[a] (T_C)	239°C
Matrix porosity (ϕ)	0.35
Quartz volume fractions[b] (ϕ_{qz}, ϕ_{qz}^{fr})	0.65
Specific surface area in the matrix[a] (A_{qz})	54.2 m^2 kg^{-1}
Specific surface area in the fracture[c] (A_{qz}^{fr})	6.15 m^2 kg^{-1}
Free-solution diffusion coefficient[d] (D_d)	1.0×10^{-10} m^2 sec^{-1}
Fracture aperture[d] ($2b$)	200 μm
Groundwater velocity in the fracture[d] (v^{fr})	1.9727×10^{-5} m sec^{-1}
Dissolution rate constant[e] (k_+^0)	1.3298×10^{-8} mol m^{-2} sec^{-1}
Equilibrium constant[e] (K_{eq})	6.4996×10^{-3} mol kg^{-1}
Domain size[a] (ℓ_x, ℓ_z)	2.0 cm, 3.1 cm
Location of cross-sections (z_1, z_2)	0.1 ℓ_z, 0.5 ℓ_z
Output times (t_1, t_2, t_3, t_4)	500 sec, 1000 sec, 2000 sec and steady state

[a] Johnson et al. (1998)
[b] $1 - \phi$
[c] From Equation (2.40) with $\omega = 1.0$
[d] Steefel and Lichtner (1998a)
[e] Computed by this model for deionized water at $T_C = 239$°C

Figure 5.16 shows the concentration profile versus distance along the fracture for both the analytical and the numerical solution. Steefel and Lichtner (1998a) previously described the discrepancy at early times and interpreted this as numerical dispersion in upwind formulations of the advection term. However, as the simulation proceeds in time, this inconsistency diminishes and eventually vanishes after an infinitely long period of time. Note that the two steady state solutions in the Figures 5.14 and 5.16

coincide qualitatively but have been reached from different initial conditions. Perfect match between the analytical solution and the results from this model are obtained with the molal concentrations in the matrix. Figure 5.17 shows two cross-sections of the steady state simulation.

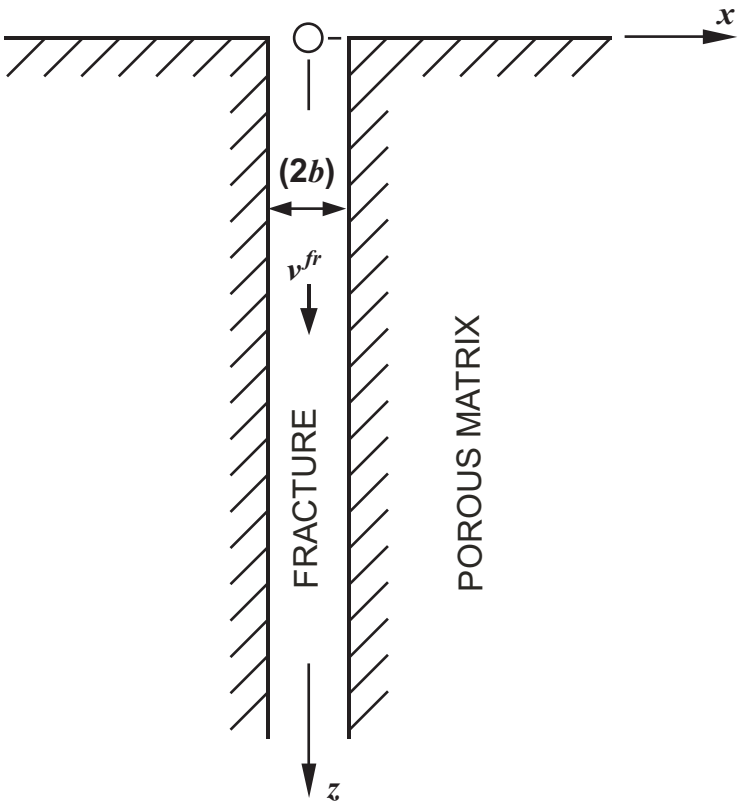

Figure 5.11: Fracture-matrix system used for model verification (Tang et al., 1981).

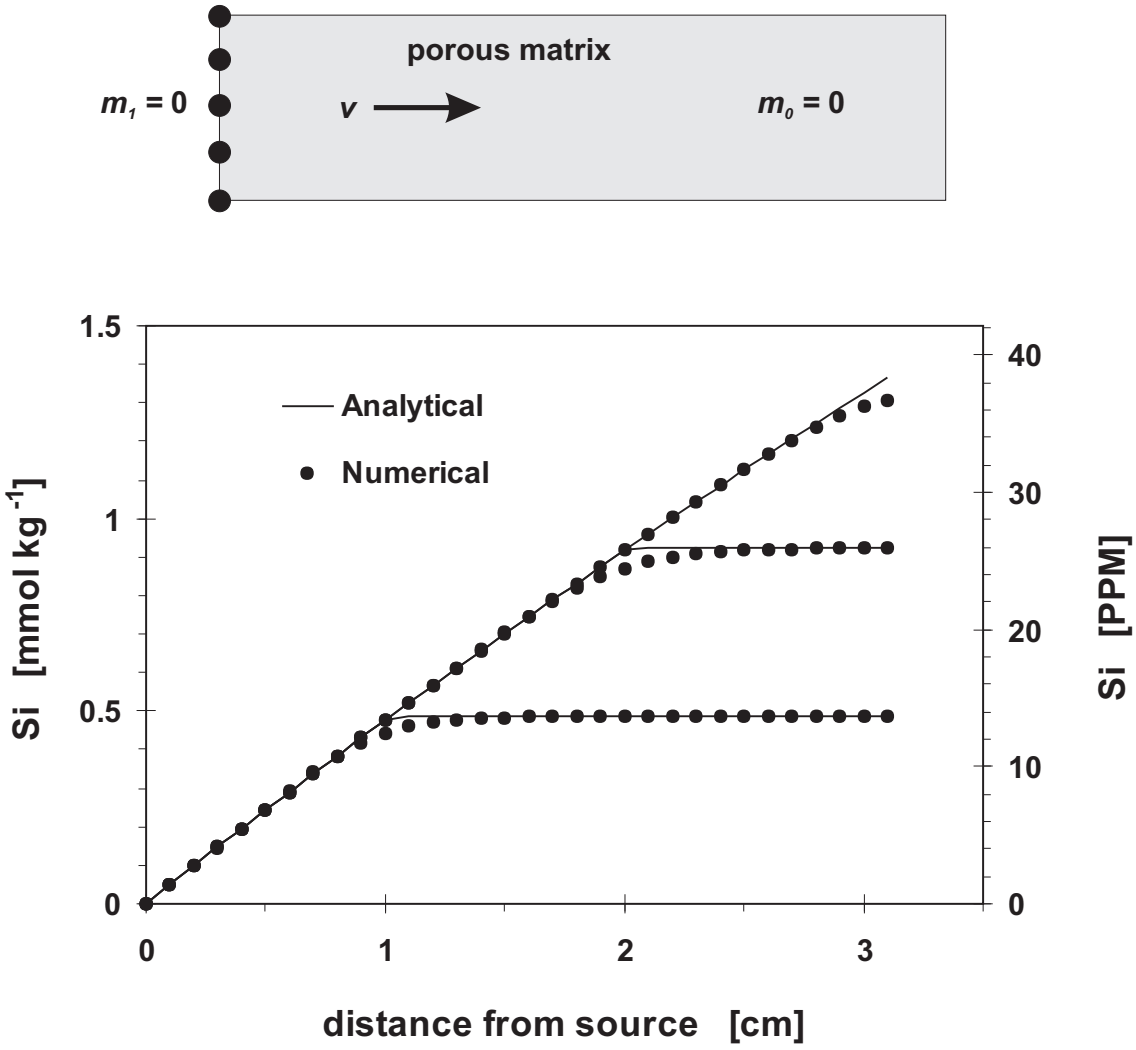

Figure 5.12: Concentration profiles of 1D reactive transport of silica in an unfractured porous matrix (*reac1*). Shown are the molal concentrations in the matrix at 518.76 (below), 1021.8 and 1572.0 seconds.

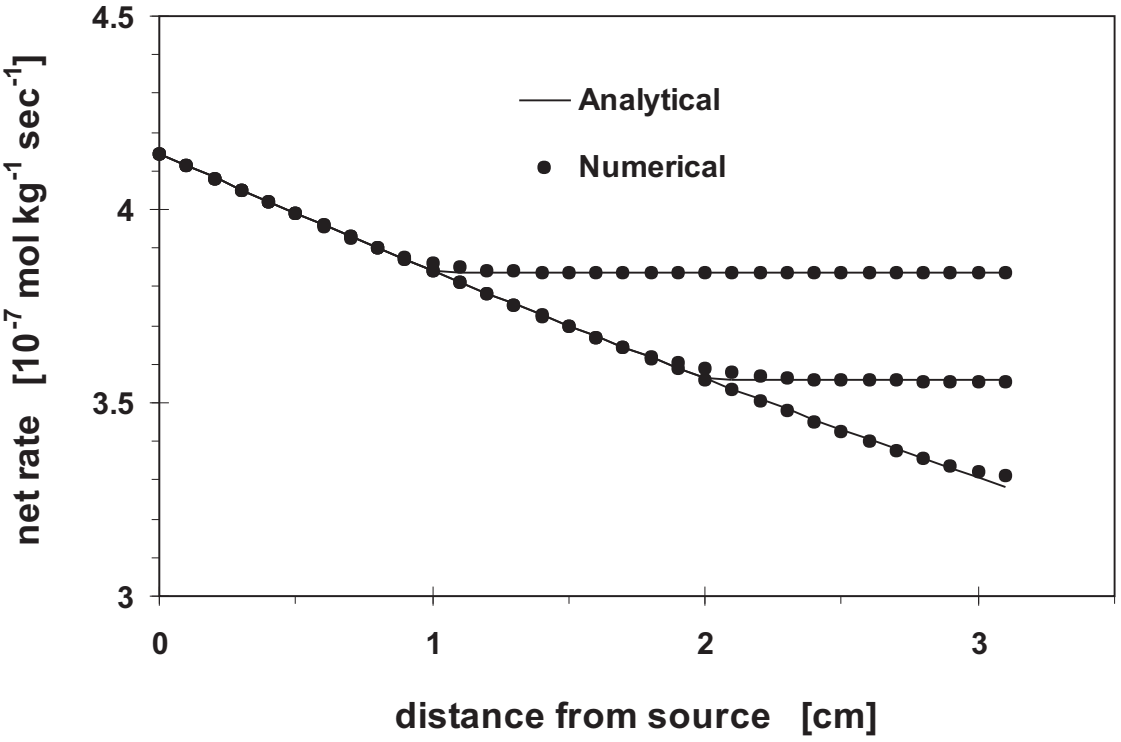

Figure 5.13: Net reaction rate profiles of 1D reactive transport of silica in an unfractured porous matrix (*reac1*). Shown are the rates in the matrix at 518.76 (above), 1021.8 and 1572.0 seconds.

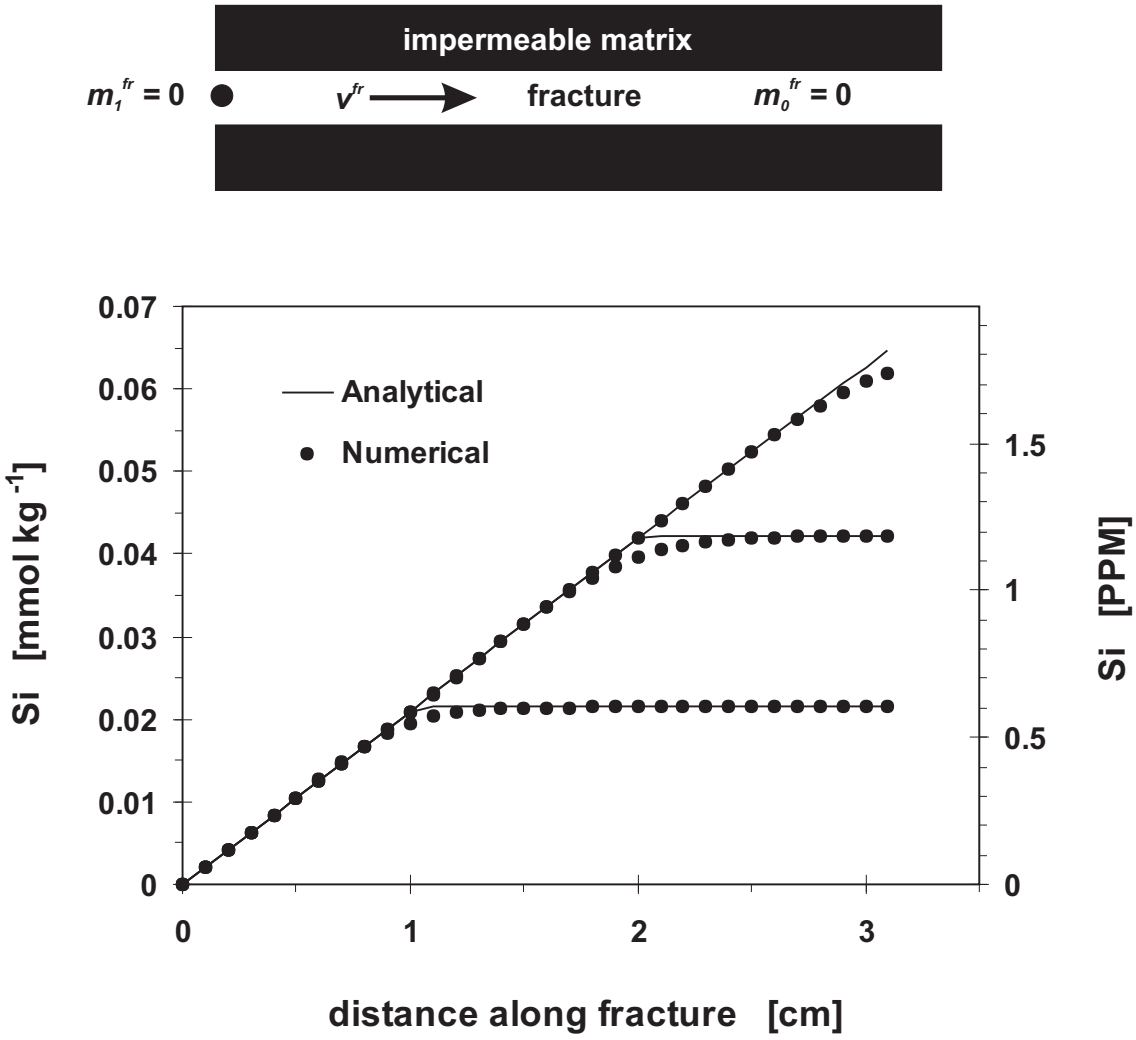

Figure 5.14: Concentration profiles of 1D reactive transport of silica in a single fracture embedded in an impermeable matrix (*reac2*). Shown are the molal concentrations in the fracture at 518.76 (below), 1021.8 and 1572.0 seconds.

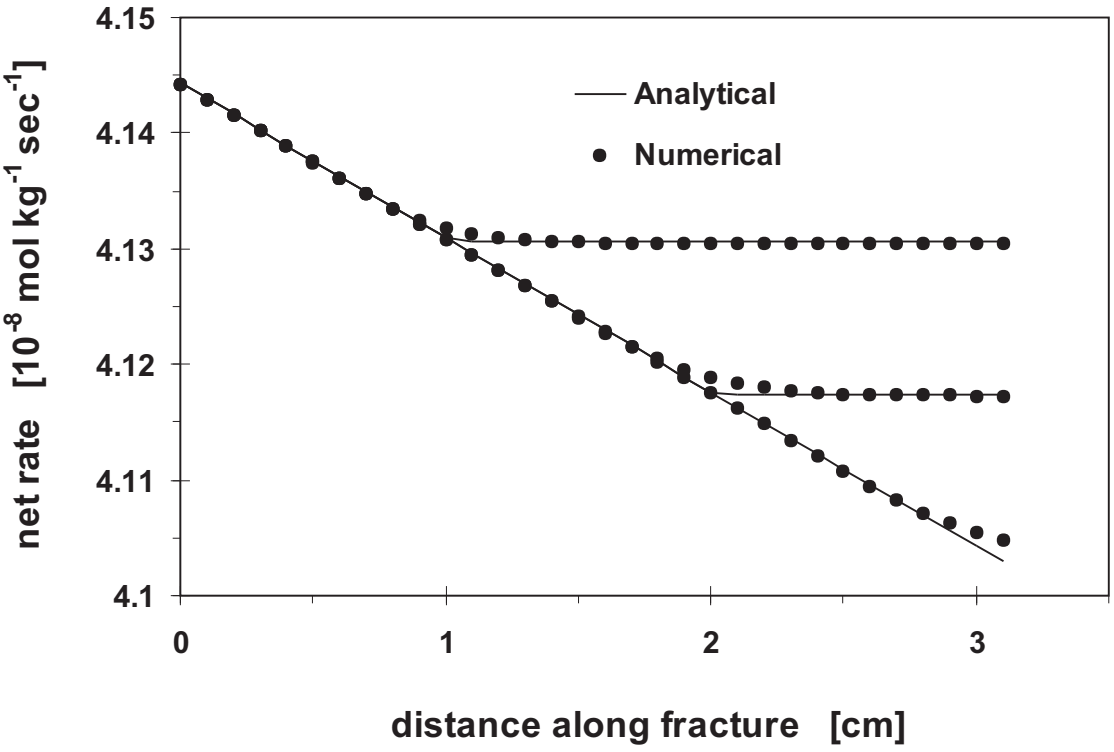

Figure 5.15: Net reaction rate profiles of 1D reactive transport of silica in a single fracture embedded in an impermeable matrix (*reac2*). Shown are the rates in the fracture at 518.76 (above), 1021.8 and 1572.0 seconds.

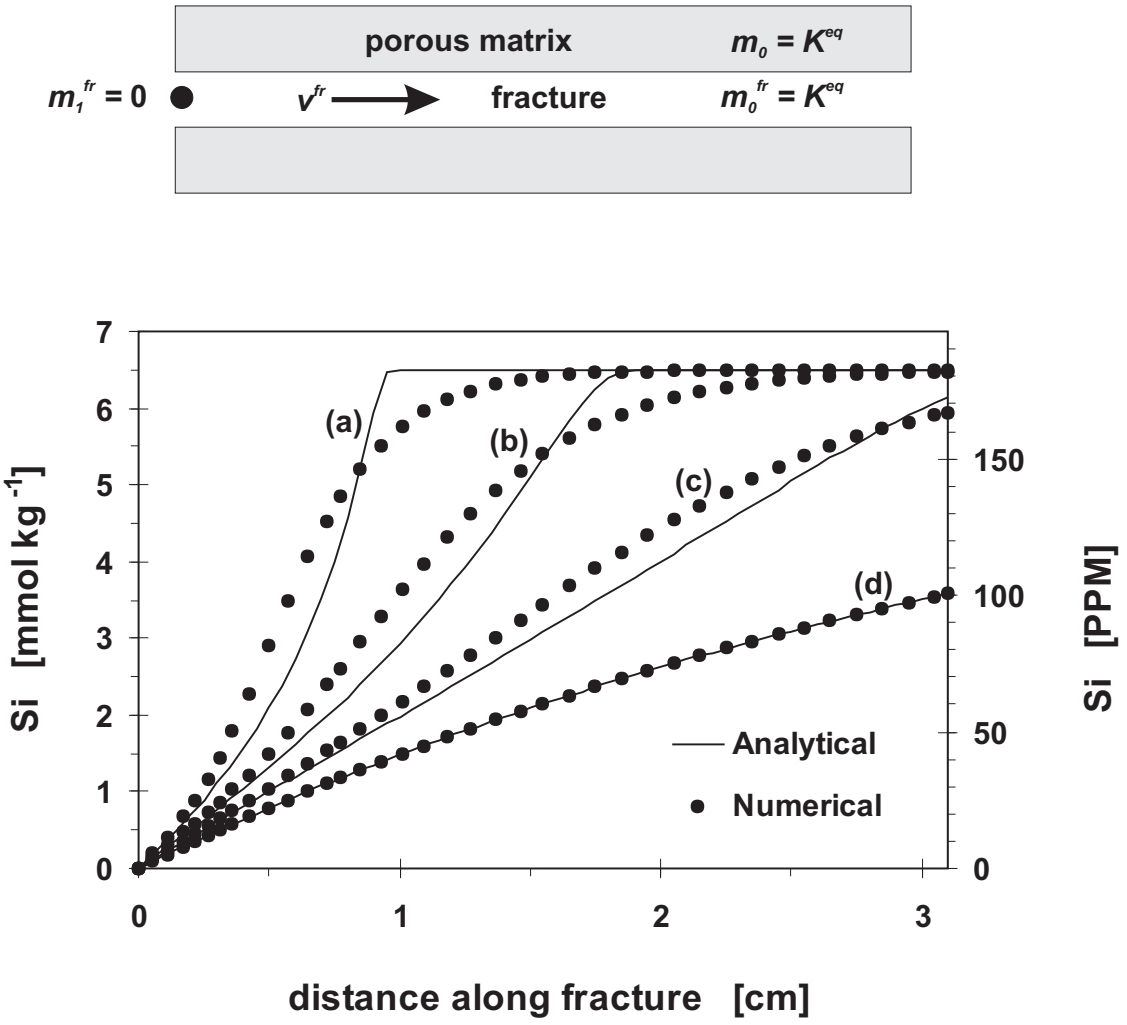

Figure 5.16: Concentration profiles of 2D reactive transport of silica in discretely-fractured porous media (*reac3*). Shown are the silica molalities in the fracture at (a) 500, (b) 1000 and (c) 2000 seconds and at (d) steady state.

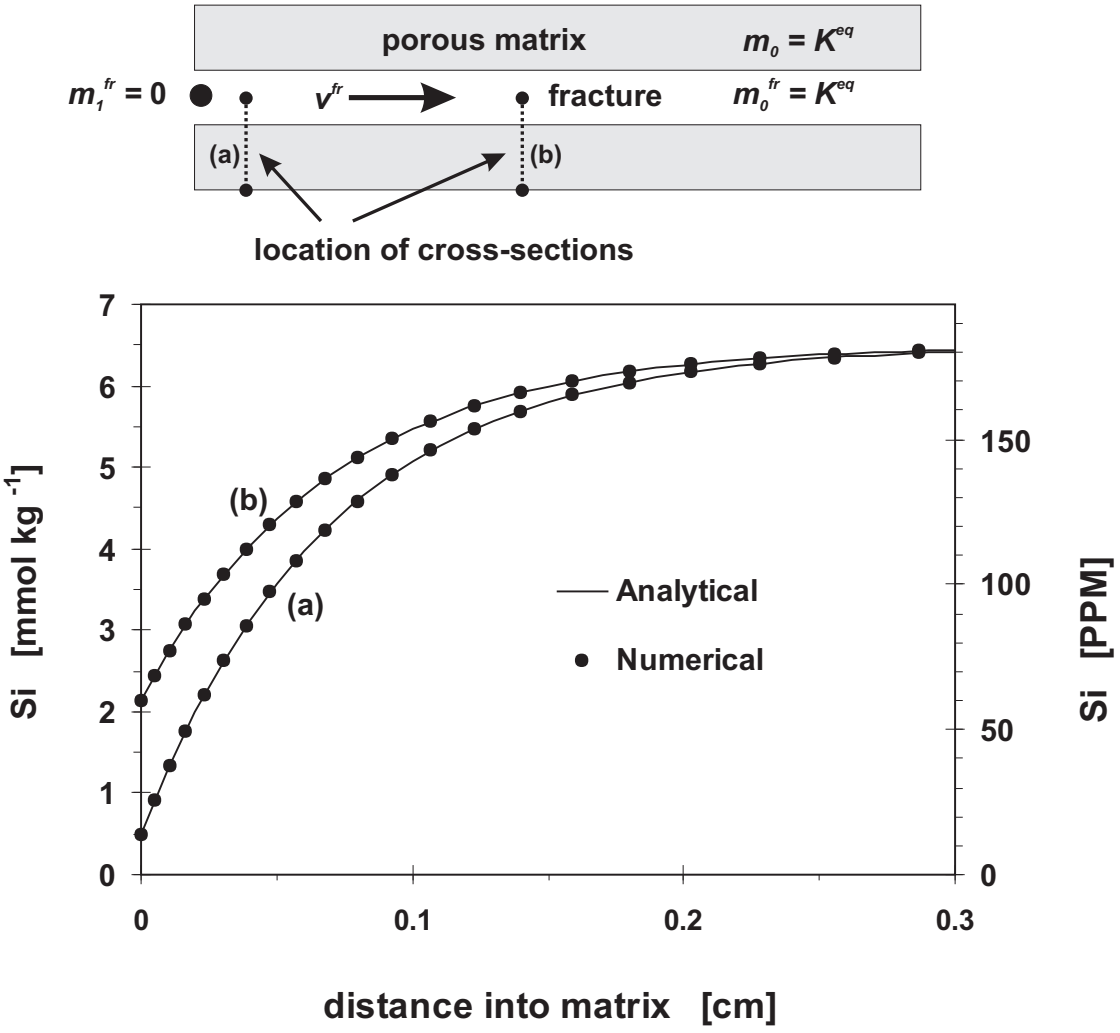

Figure 5.17: Concentration profiles of 2D reactive transport of silica in discretely-fractured porous media (*reac3*). Shown are the silica molalities in the matrix at steady state at the distances (a) 0.31 cm and (b) 1.55 cm from the fracture.

5.3 Heat Transfer

The first three verification problems test heat transfer in porous media, fractured media and fractured porous media, respectively. The fourth problem is a comparison with numerical simulation results (Yand and Edwards, 2000), including all heat transfer mechanisms in porous media. Table 5.5 summarizes which examples verifies what part of the governing heat transfer equations.

Table 5.5: Overview of the verification problems that verify different heat transfer mechanisms in porous and fractured media.

Heat transfer mechanism tested →	Conduction		Convection		Mechanical heat dispersion		Fracture - matrix
↓ Verification example	in PM[a]	in FM[b]	in PM	in FM	in PM	in FM	conduction
heat1	√	–	√	–	√	–	–
heat2	–	√	–	√	–	√	–
heat3	√	–	–	√	–	–	√
heat4	√	–	√	–	√	–	–

[a] Porous media
[b] Fractured media

Heat Transfer in Porous Media (*heat1*)

The first test case verifies 1D heat transfer in an unfractured porous matrix. A constant velocity along the flow axis is imposed. The impact of temperature on fluid properties is ignored, which linearizes the problem. Thermal energy is transported by way of conduction, advection and mechanical dispersion. In this case, the governing equation (3.24) can be rewritten in the form:

$$D_{th}\frac{\partial^2 T}{\partial x^2} - v_{th}\frac{\partial T}{\partial x} = \frac{\partial T}{\partial t} \tag{5.9}$$

where D_{th} [L^2 T^{-1}] is the thermal dispersion coefficient:

$$D_{th} = \frac{k_b + \phi D_{xx}\rho_l \tilde{c}_l}{\rho_b \tilde{c}_b} \tag{5.10}$$

and v_{th} [L T^{-1}] is the retarded velocity:

$$v_{th} = q \cdot \frac{\rho_l \tilde{c}_l}{\rho_b \tilde{c}_b} = q \cdot \frac{1}{\phi R_{th}} \tag{5.11}$$

with the thermal retardation coefficient R_{th} [–] (Molson et al., 1992):

$$R_{th} = 1 + \frac{(1-\phi)\rho_s \tilde{c}_s}{\phi \rho_l \tilde{c}_l} \tag{5.12}$$

Equation (5.9) has the standard parabolic-hyperbolic form of a 1D partial differential equation. Therefore, if (5.9) is subject to the Dirichlet boundary condition, $T = T_1$, the solution is the Ogata-Banks (1961) analytical solution:

$$\frac{T - T_0}{T_1 - T_0} = \frac{1}{2}\left[\operatorname{erfc}\left(\frac{x - v_{th}t}{2\sqrt{D_{th}t}}\right) + \exp\left(\frac{v_{th}x}{D_{th}}\right)\operatorname{erfc}\left(\frac{x + v_{th}t}{2\sqrt{D_{th}t}}\right)\right] \tag{5.13}$$

where T_0 is the initial temperature in the domain.

In the numerical simulation, the finite element domain was spatially discretized by using 20 uniform blocks in the flow direction. All simulation parameters are given by Table 5.6. The developed numerical model is compared with the analytical solution (5.13) as well as with numerical results presented by Ward et al. (1984) who used the model SWIFT. The results are depicted in Figure 5.18.

Heat Transfer in Fractured Media (*heat2*)

The second test case verifies advective-conductive-dispersive 1D heat transfer in a single fracture embedded in an impermeable matrix. As in the previous case, a constant flow velocity along the axis is imposed and fluid properties are kept constant in order to linearize the problem. Hence, the governing equation (3.27) simplifies to:

$$D_{th}^{fr}\frac{\partial^2 T^{fr}}{\partial z^2} - v^{fr}\frac{\partial T^{fr}}{\partial z} = \frac{\partial T^{fr}}{\partial t} \tag{5.14}$$

where D_{th}^{fr} [$\mathrm{L}^2\ \mathrm{T}^{-1}$] is the fracture thermal dispersion coefficient, given by:

$$D_{th}^{fr} = \frac{k_l}{\rho_l \tilde{c}_l} + D_{zz}^{fr} \tag{5.15}$$

and where v^{fr} is the constant groundwater flow velocity along the fracture. Equation (5.14) is a standard 1D parabolic-hyperbolic partial differential equation. If the Dirichlet boundary condition $T^{fr} = T_1^{fr}$ is imposed on the fracture inlet, the Ogata-Banks (1961) analytical solution is now:

$$\frac{T^{fr} - T_0^{fr}}{T_1^{fr} - T_0^{fr}} = \frac{1}{2}\left[\operatorname{erfc}\left(\frac{z - v^{fr}t}{2\sqrt{D_{th}^{fr}t}}\right) + \exp\left(\frac{v^{fr}z}{D_{th}^{fr}}\right)\operatorname{erfc}\left(\frac{z + v^{fr}t}{2\sqrt{D_{th}^{fr}t}}\right)\right] \tag{5.16}$$

Table 5.6: Model parameters used in the verification example for 1D heat transfer in an unfractured porous matrix (*heat1*). All parameters are identical to those used by Ward et al. (1984).

Parameter	Value
Bulk thermal conductivity (k_b)	2.16 kg m sec^{-3} K^{-1}
Heat capacity of solid ($\tilde{c}_s$)	1254.682 m^2 sec^{-2} K^{-1}
Solid density (ρ_s)	1602 kg m^{-3}
Heat capacity of water ($\tilde{c}_l$)	4185 m^2 sec^{-2} K^{-1}
Fluid density (ρ_l)	1000 kg m^{-3}
Matrix porosity (ϕ)	0.1
Longitudinal dispersivity (α_l)	14.4 m
Heat dispersion coefficient[a] (D_{th})	1.15×10^{-5} m^2 sec^{-1}
Thermal retardation coefficient[b] (R_{th})	5.323
Darcy flux (q)	3.53×10^{-7} m sec^{-1}
Retarded velocity[c] (v_{th})	6.63×10^{-7} m sec^{-1}
Initial temperature (T_0)	37.78°C
Boundary temperature (T_1)	93.33°C
Domain size (ℓ_x)	600 m
Output times (t_1, t_2)	2,148 d and 4,262 d

[a] from relation (5.10)
[b] from relation (5.12)
[c] $q/(\phi R^{th})$

where T_0^{fr} is the initial temperature in the fracture.

In the numerical simulation, the finite element domain was spatially discretized along the fracture by using element sizes that gradually increase by the factor 1.1 from $\Delta z = 0.1$ m near the elevated temperature to $\Delta z = 15$ m at the domain boundary. The groundwater velocity in the fracture was set to 7.0×10^{-7} m sec^{-1} and the fracture dispersivity used was 5.0 m, giving the fracture thermal dispersion coefficient as 3.62×10^{-6} m^2 sec^{-1}. All other parameters are identical to those used in the previous example and given in Table 5.6. The simulation results are depicted in Figure 5.19.

Heat Transfer in Fractured Porous Media (*heat3*)

The third test case verifies 2D heat transfer in a single fracture embedded in a porous matrix. This verification example is based on analytical results presented by Meyer (2004), who investigated advective transient heat transfer in a fracture while in the porous matrix, heat is transported due to conduction alone. Mechanical heat dispersion as well as conduction within the fracture are not considered, making numerical integration unnecessary. The groundwater flow velocity in the fracture is constant. Under these assumptions, the governing equations of this problem simplify from (3.24) and (3.27) to:

$$\rho_b \tilde{c}_b \, \frac{\partial T}{\partial t} - k_b \, \frac{\partial^2 T}{\partial x^2} = 0 \qquad\qquad b \le x \le \infty \tag{5.17}$$

and

$$\rho_l \tilde{c}_l \, \frac{\partial T^{fr}}{\partial t} + \rho_l \tilde{c}_l \; v^{fr} \, \frac{\partial T^{fr}}{\partial z} - \frac{k_b}{b} \, \frac{\partial T^{fr}}{\partial x}\bigg|_{x=b} = 0 \qquad 0 \le z \le \infty \tag{5.18}$$

for heat transport in the matrix and in the discrete fracture, respectively. The last term in (5.18) expresses conductive loss of heat from the fracture into the matrix on the fracture-matrix interface. Initially, the entire system has the uniform temperature, T_0. The fluid entering the fracture has the constant temperature, T_1. All boundaries, except the fracture inlet and outlet, are impermeable for groundwater flow and for heat exchange. According to Meyer (2004), the transient solution along the fracture is:

$$\frac{T^{fr} - T_0}{T_1 - T_0} = \operatorname{erfc}\left(\frac{z \, \sqrt{k_b \; \rho_b \tilde{c}_b}}{2 v^{fr} \rho_l \tilde{c}_l b \, \sqrt{(t - z/v^{fr})}} \right) \tag{5.19}$$

Using the analytical results presented by Tang et al. (1981), it can be shown that the transient solution along a cross-section from the fracture into the porous matrix is given by

$$\frac{T - T_0}{T_1 - T_0} = \text{erfc}\left(\frac{z\ \sqrt{k_b\ \rho_b \tilde{c}_b}}{2v^{fr}\rho_l \tilde{c}_l b\ \sqrt{(t - z/v^{fr})}} + \frac{\sqrt{\rho_b \tilde{c}_b}\ (x - b)}{2\sqrt{k_b}\ \sqrt{(t - z/v^{fr})}} \right) \tag{5.20}$$

The fracture-matrix system used is identical to that shown in Figure 5.11. The finite element domain was spatially discretized in the x-direction by gradually increasing Δx with constant factor 1.1 from $\Delta x = 0.01$ m near the fracture to $\Delta x = 0.1$ m at the domain boundary. In the flow direction, Δz also increases gradually from $\Delta z = 0.1$ m near the elevated temperature to $\Delta z = 0.5$ m at the domain boundary. All other parameters are presented in Table 5.7 and the simulation results are exhibited in the Figures 5.20 and 5.21.

Table 5.7: Model parameters used in the verification example for 2D heat transfer in a single fracture embedded in a porous matrix (*heat3*). All parameters are identical to those used by Meyer (2004).

Parameter	Value
Bulk thermal conductivity (k_b)	3.4 kg m sec^{-3} K^{-1}
Heat capacity of solid ($\tilde{c}_s$)	908 m^2 sec^{-2} K^{-1}
Solid density (ρ_s)	2550 kg m^{-3}
Heat capacity of water ($\tilde{c}_l$)	4192 m^2 sec^{-2} K^{-1}
Fluid density (ρ_l)	997 kg m^{-3}
Matrix porosity (ϕ)	0.2
Groundwater flow velocity in the fracture (v^{fr})	0.05 m sec^{-1}
Initial temperature (T_0)	10°C
Boundary temperature (T_1)	15°C
Domain size (ℓ_x, ℓ_z)	2 m, 10 m
Location of cross-sections (z_1, z_2)	0.1 m, 0.61 m
Output times (t_1, t_2)	5,000 sec and 10,000 sec

Heat Transfer in Anisotropic Porous Media (*heat4*)

The last verification problem for heat transfer is the 2D field scale example presented by Yang and Edwards (2000). This test case represents a realistic scenario of radioactive waste disposal in the low-permeability anisotropic granitic rock of the Canadian Shield (Davison et al., 1994a). Figure 5.22 shows the conceptual model, a vertical slice of dimensions 2,000 m × 1,000 m with a unit thickness. Radionuclides are disposed of in a 1,300 m long horizontal vault at a depth of 500 m below surface. The simulation domain consists of three anisotropic porous layers. The radioactive waste represents an exponentially decreasing heat source due to remaining radioactivity (Davison et al., 1994a). Thus, the term $\Gamma = 11.59$ kg m^{-1} sec^{-3} $\cdot$ exp(-5.5×10^{-10} sec^{-1} $\cdot$ t), as given by Yang and Edwards (2000), was added as heat source term to the left hand side of Equation (3.24). All boundaries are impermeable for flow. Top and bottom boundaries have constant temperatures to mimic a geothermal gradient of 11.5 K km^{-1}, which is natural in the study area. All other boundaries are impermeable for heat transfer. Initially, the geothermal field is undisturbed with horizontal isotherms.

In the numerical simulations carried out with the developed model, the temperature is assumed to have an impact on both fluid properties density and viscosity. This conforms with the assumption made by Yang and Edwards (2000). Chemical reactions are not considered. All model parameters are summarized in Table 5.8. The variable-density, variable-viscosity flow and heat transfer results are exhibited in Figure 5.23, which shows excellent agreement between the two numerical models compared.

Table 5.8: Model parameters used in the verification example for 2D variable-density thermal flow and heat transfer in anisotropic porous media (*heat4*). All parameters are identical to those used by Yang and Edwards (2000).

Parameter	Value
Bulk thermal conductivity (k_b)	2.0 kg m sec^{-3} K^{-1}
Heat capacity of solid ($\tilde{c}_s$)	800 m^2 sec^{-2} K^{-1}
Heat capacity of water ($\tilde{c}_l$)	4174 m^2 sec^{-2} K^{-1}
Solid density (ρ_s)	2630 kg m^{-3}
Matrix permeability (κ_{xx}, κ_{zz})	Layer 1: 1.0×10^{-15} m^2, 5.0×10^{-15} m^2
	Layer 2: 1.0×10^{-17} m^2, 5.0×10^{-17} m^2
	Layer 3: 1.0×10^{-19} m^2, 1.0×10^{-19} m^2
Matrix porosity (ϕ)	0.004
Domain size (ℓ_x, ℓ_z)	2000 m, 1000 m
Spatial discretization ($\Delta x, \Delta z$)	25 m, 25 m

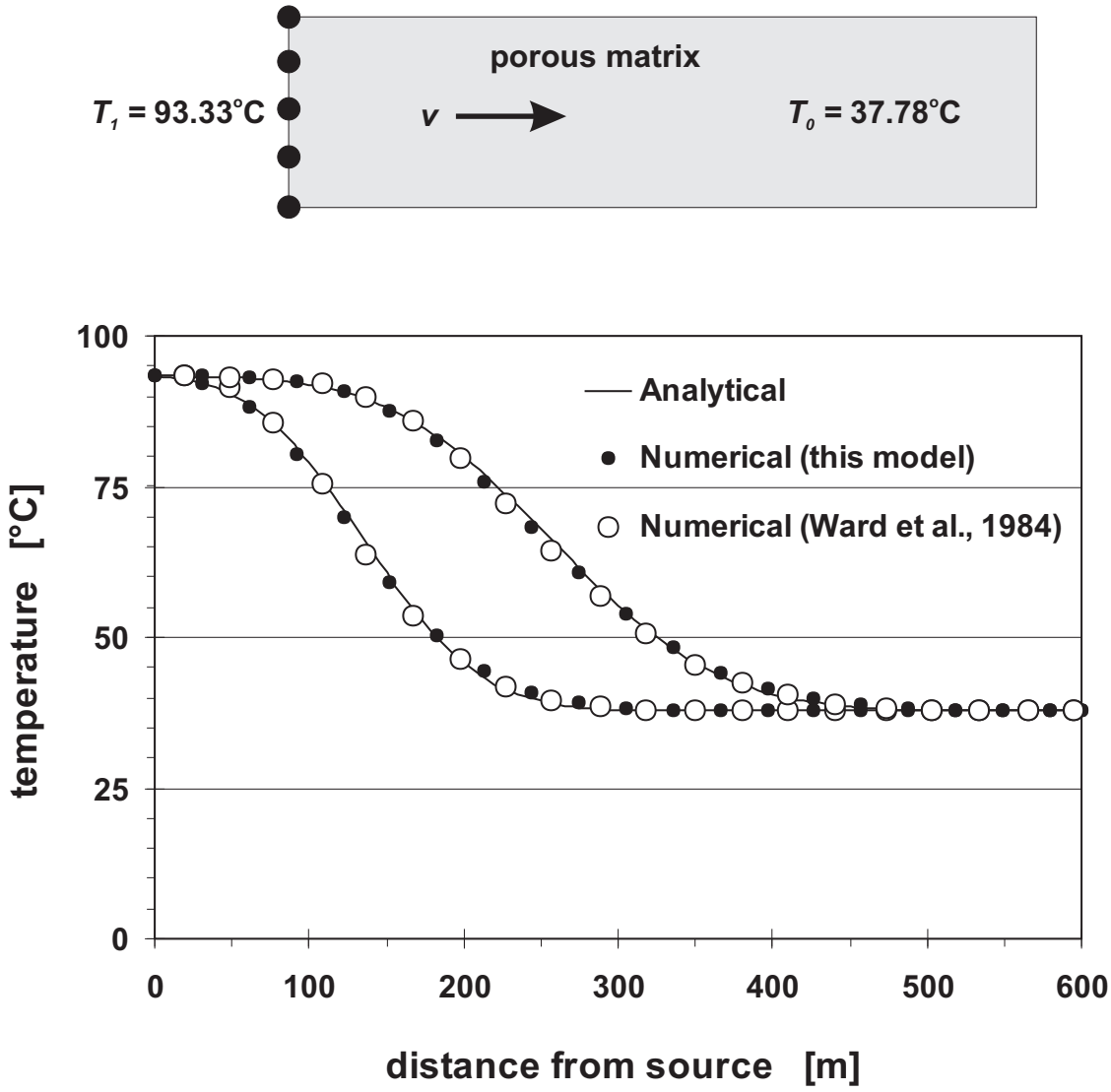

Figure 5.18: Temperature profiles of 1D heat transfer in an unfractured porous matrix (*heat1*). Shown are the temperatures in the matrix at 2,148 (left) and 4,262 (right) days.

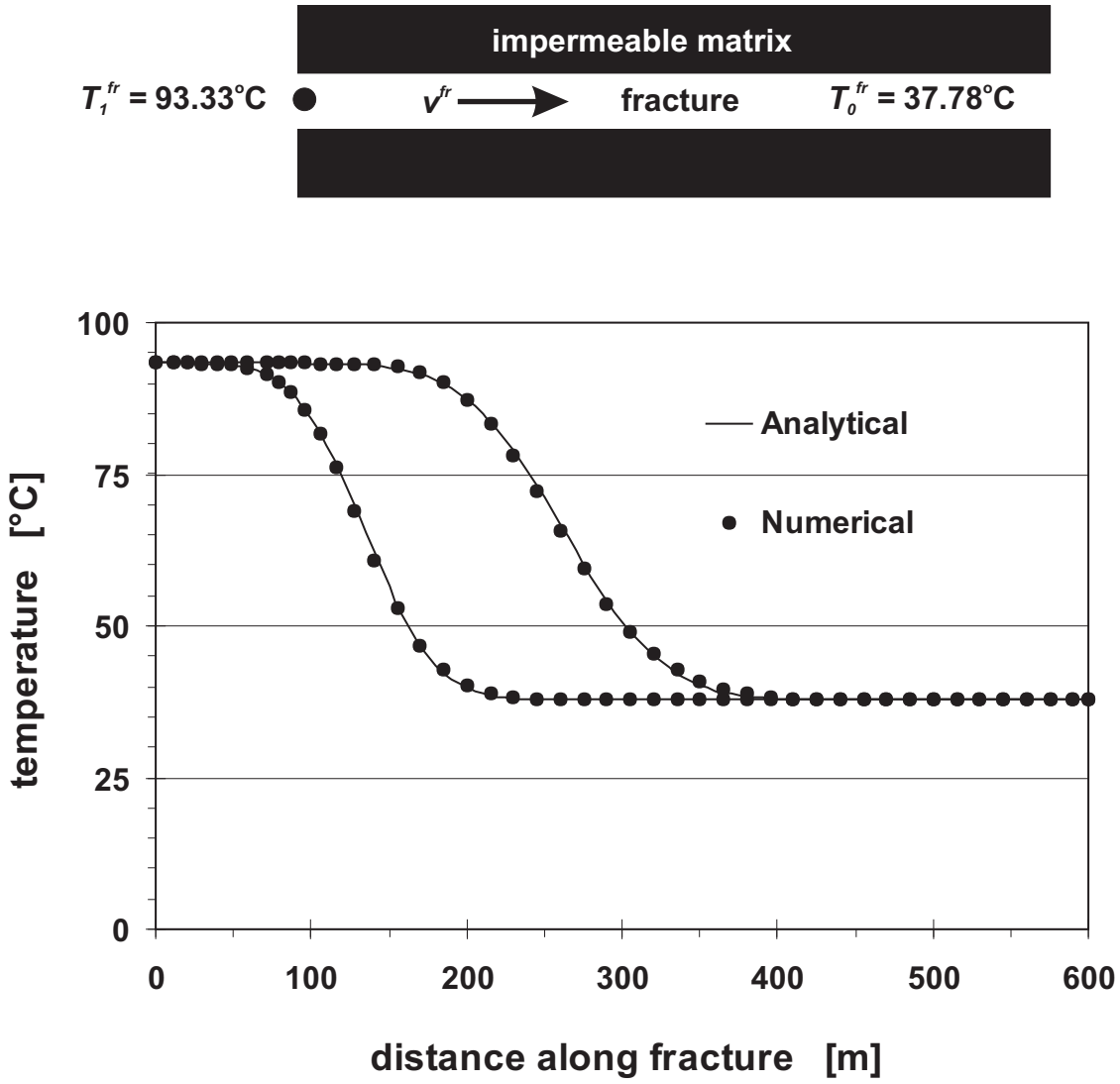

Figure 5.19: Temperature profiles of 1D heat transfer in a single fracture within an impermeable matrix (*heat2*). Shown are the temperatures in the fracture at 2,148 (left) and 4,262 (right) days.

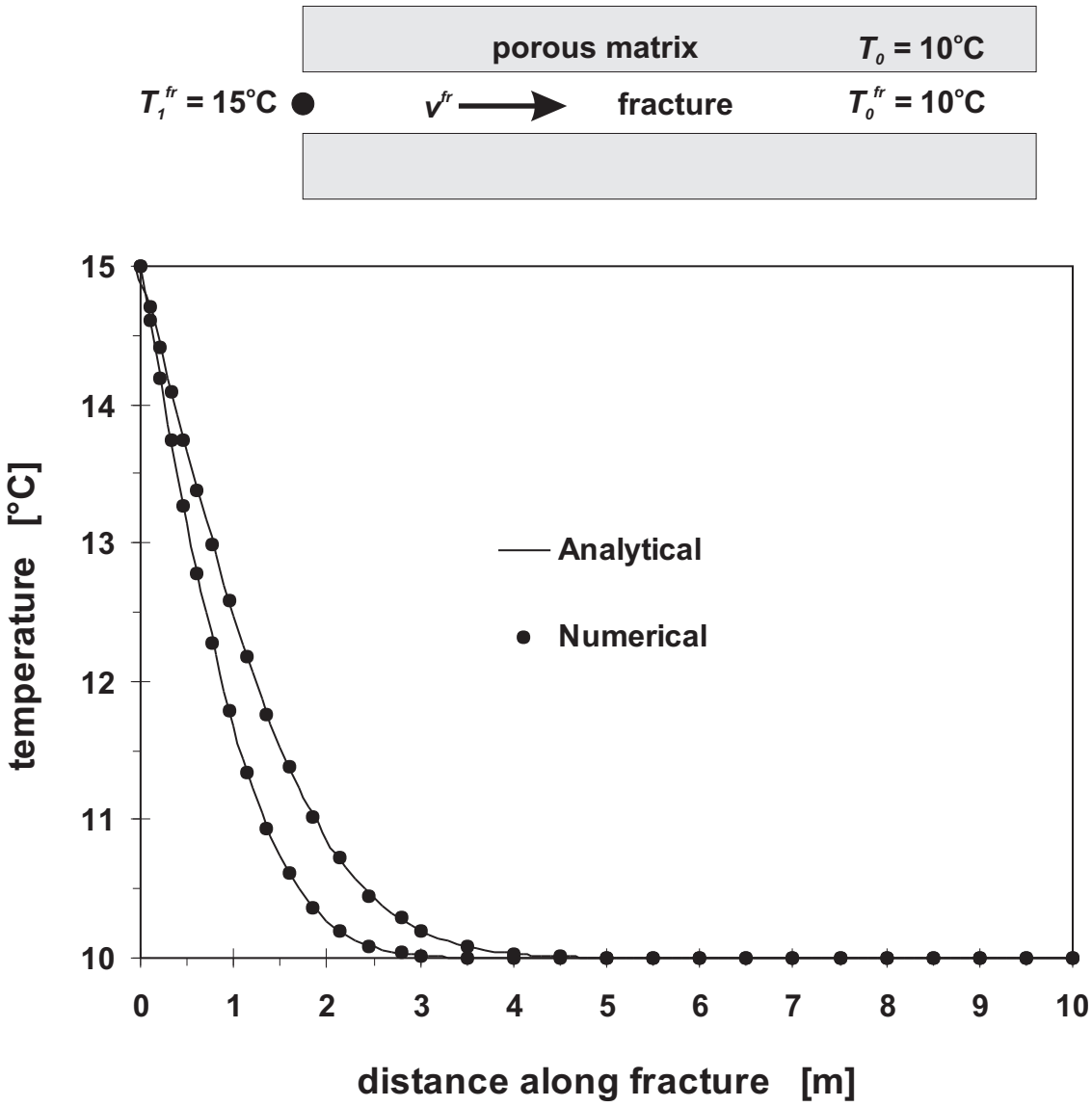

Figure 5.20: Temperature profiles of 2D heat transfer in discretely-fractured porous media (*heat3*). Shown are the temperatures in the fracture at 5,000 (left) and 10,000 (right) seconds.

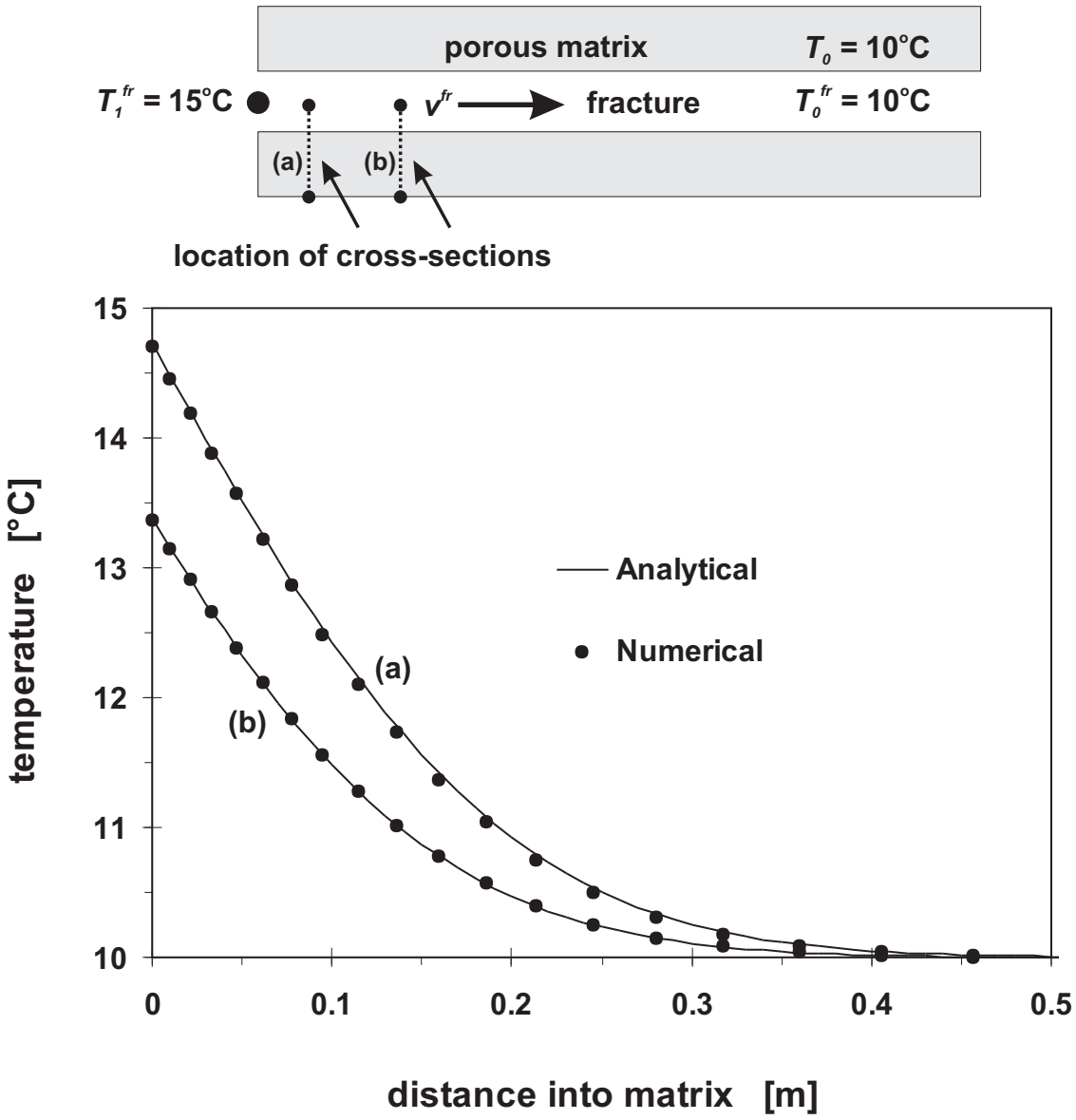

Figure 5.21: Temperature profiles of 2D heat transfer in discretely-fractured porous media (*heat3*). Shown are the temperatures in the matrix at 10,000 seconds simulation time at the distances (a) 0.1 m and (b) 0.61 m from the fracture.

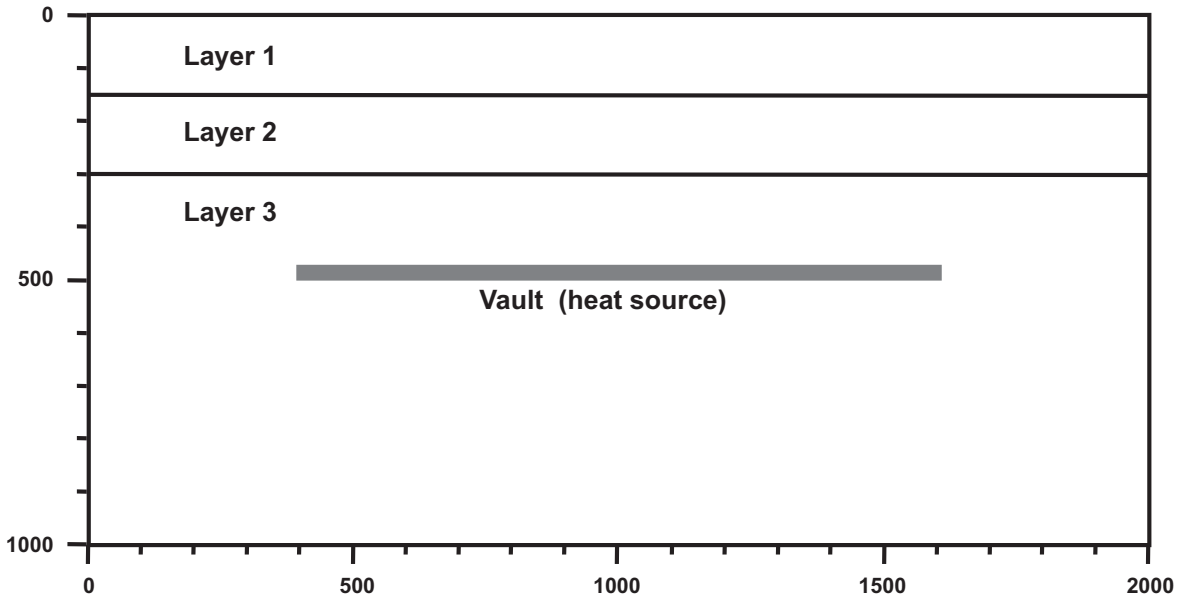

Figure 5.22: The conceptual model for variable-density heat transfer in anisotropic porous media (*heat4*; Yang and Edwards, 2000). The heat source in the vault is due to the remaining radioactivity of the stored waste. Top and bottom boundaries are assigned the constant temperatures 6°C and 17.5°C, respectively, with the corresponding geothermal gradient 11.5 K km^{-1}.

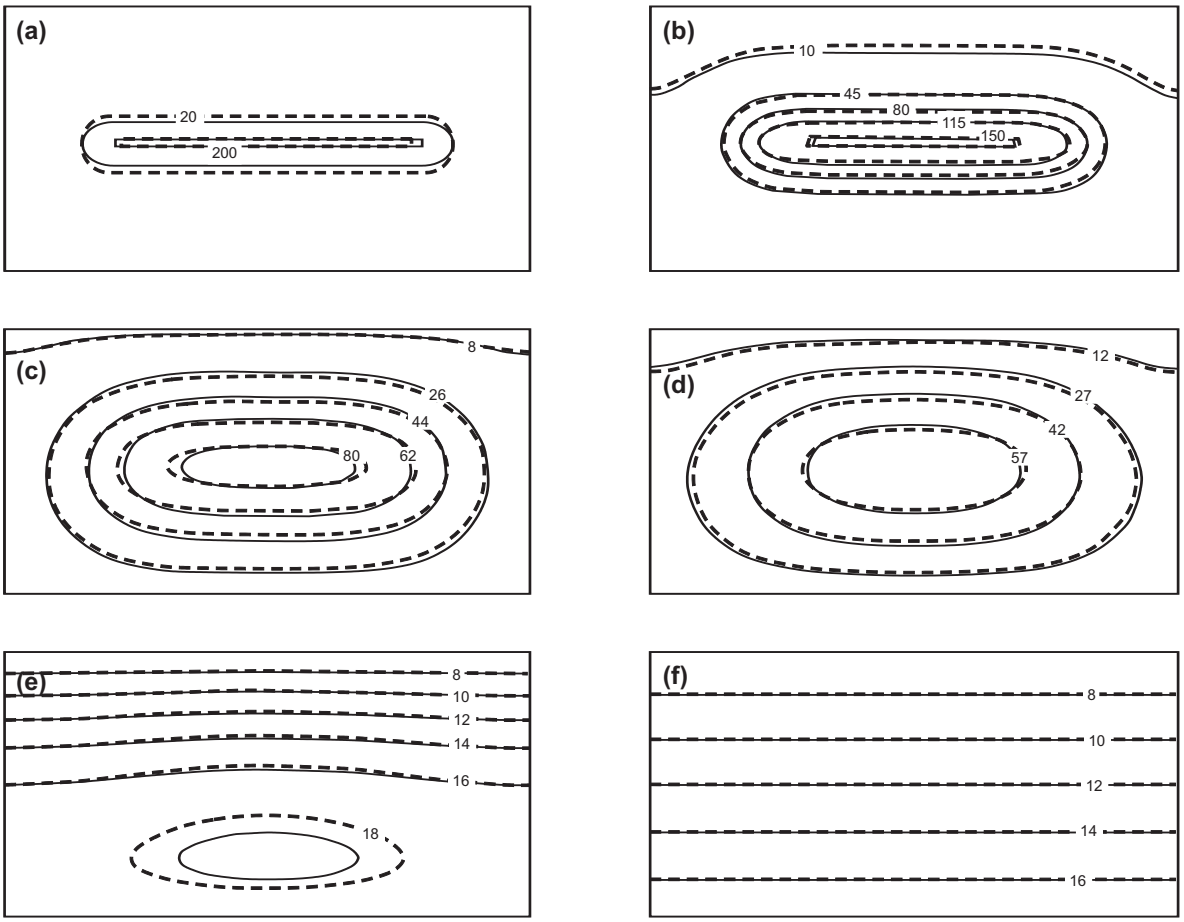

Figure 5.23: Evolution of temperature in anisotropic porous media with an exponentially decreasing heat source (*heat4*). Simulation times are (a) 10^4 days, (b) 10^5 days, (c) 3×10^5 days, (d) 5×10^5 days, (e) 3×10^6 days, (f) 7×10^6 days. Shown are isotherms in Celsius, obtained from Yang and Edwards (2000) [—] and from the developed model [- -].

Chapter 6

Illustrative Examples

This chapter presents examples to demonstrate the capacities of the new model. The first three examples account for density differences due to salinity variations. These examples simulate variable-density flow and nonreactive transport in a fractured system of increasing complexity. Starting with a single variably inclined fracture (Section 6.1), moving to an orthogonal fracture network, interspersed by small fractures (Section 6.2), and finally, modeling using irregular random fracture networks, where fracture trace, orientation and aperture are nonuniform (Section 6.3). The final two problems simulate thermohaline flow, coupled with heat transfer and reactive transport. These two examples illustrate reactive transport of a hot plume in porous (Section 6.4) and fractured porous media (Section 6.5). The last two examples also underline the efficiency of the adaptive time stepping scheme.

6.1 Variable-Density Flow in a Single Inclined Fracture

Variable-density flow simulations in a single fracture were conducted. The domain geometry, as well as initial and boundary conditions are identical to those used in the model verification example given in Section 5.1 and Figure 5.5. All model parame-

ters correspond to those used by Shikaze et al. (1998), shown in Table 6.3. Similar to the model verification examples, constant time step sizes of 0.2 years were used. Simulations were first run for a 45°-inclined fracture, embedded in a porous matrix. Then, simulations were carried out demonstrating different buoyancy effects in a single fracture of variable inclines. Remember (from Section 2.3) that spatial dimensionality affects convective flow patterns in finite element grids. The 1D representation of the discrete fracture in the following examples does not allow convection within the fracture but within the entire 2D domain.

Variable-Density Flow in a 45° - Inclined Fracture

For the 45°-inclined fracture case, concentration distributions as well as velocity fields at 2, 4 and 10 years simulation time are shown in Figure 6.1. The simulated concentrations versus time for this problem are given as tabular data in Appendix C. After 2 years, a convection cell ("eddy") has formed on the left of the fracture near the source. Flow along the fracture-matrix interface is mostly away from the fracture. Thus, solutes are transported from the fracture into the adjoining matrix not only by molecular diffusion but also by advection. At 4 years, a second eddy has formed to the right of the fracture near the solute source. Both eddies migrate downwards into the aquifer. However, the left eddy has already moved further downwards because it has been formed earlier.

Consider again Figure 5.8 shown in Section 5.1. Figure 6.1 demonstrates that the more effective left eddy forces the flow direction very close to the fracture at the top of the domain to change directions. As a consequence, the advective transport through the upper boundary of the domain increases after about 4 years, resulting in a rise of the Sherwood number as shown in Figure 5.8a. Both convection cells are separated by the high-permeability fracture, which, therefore, acts as a barrier to convection. After 10 years, several flow vectors near the solute source have changed direction, thus, advectively transporting tracer from the matrix into the fracture, and enhancing the buoyancy-induced flow within the fracture. Therefore, convection in the porous matrix appears to control the transport rate in an inclined fracture.

Figure 6.2 shows a closeup of Figure 5.8. The closeup, along with Figure 6.1,

explains the seemingly strange behavior of the maximum matrix velocity at early times. Before 2.4 years, the matrix velocity has its maximum near the downwards advancing front of the 20% concentration contour. Until this time, no eddy has formed and the maximum in velocity is due to purely density-driven, non-convective flow. At 2.4 years, however, the left convection cell is fully generated and its rotation velocity larger than in the previous non-convection case. Thus, the maximum velocity is now due to the strong convection of the left eddy.

Variable-Density Flow in a Variably Inclined Fracture

Several simulations were run where the incline, φ, varies between 0^o (vertical) and 70^o (nearly horizontal) to investigate the transport behavior at the limits of the fracture slope (0^o and 90^o). For all simulations, the grid had to be locally refined to ensure that the fracture consists of only inclined faces. A value of 70^o was the maximum incline used. The breakthrough curves within the fracture at $z = 6$ m were monitored and are shown in Figure 6.3. The figure illustrates that, for decreasing inclines, the observed buoyancy effect approaches the solution for a vertical fracture. Analogously, the effect becomes less and less pronounced for increasing inclines, finally being the solution for a horizontal fracture. Clearly, the two breakthrough curves for the vertical and (almost) horizontal fracture cases are the envelope functions for the family of curves, which can be described by $c = c_\varphi(t)$.

Interestingly, the difference in concentration between two scenarios at a given time is large for inclines which exceed 45^o (close to horizontal). Conversely, the concentration difference is much smaller for almost vertical fractures. In Figure 6.3, this phenomenon is indicated at 9 years by two double-arrows. In both cases, two scenarios are compared where the difference of the fracture incline is 10^o. This phenomenon can be understood by remembering that the buoyancy term in the Darcy equation (3.9) is weighted with the cosine of the slope. The cosine function changes weakly for small arguments because its derivative, the negative sine, almost vanishes. On the contrary, the change of the cosine function is relatively large for arguments close to 90^o. Thus, the weight of the buoyancy term in the Darcy equation changes weakly for almost vertical fractures and changes greatly for almost horizontal ones.

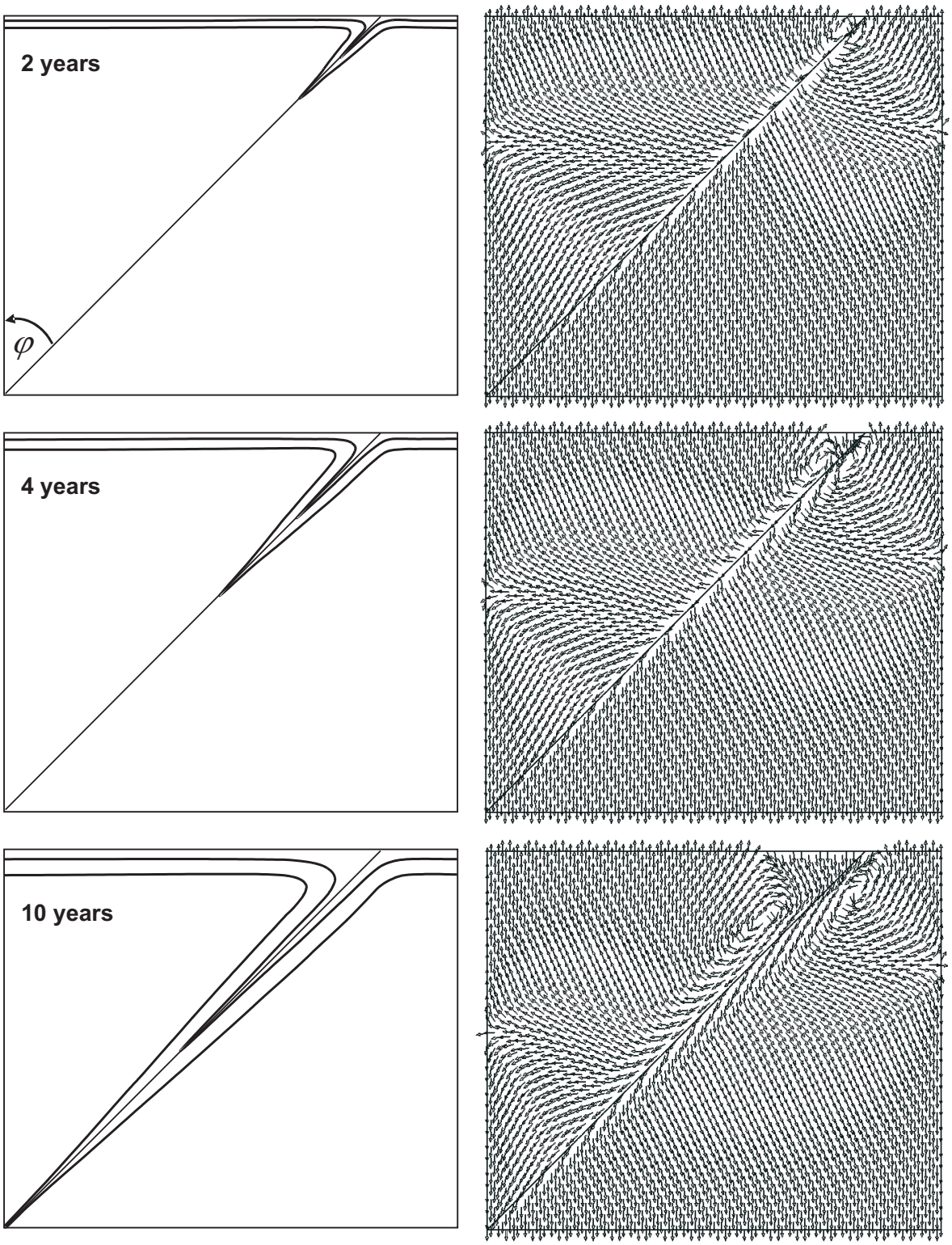

Figure 6.1: Results of variable-density flow simulations after 2, 4 and 10 years simulation time. Shown are the concentration contours 20% and 60% (left) and the velocity field (right). The domain size is 12 m × 10 m.

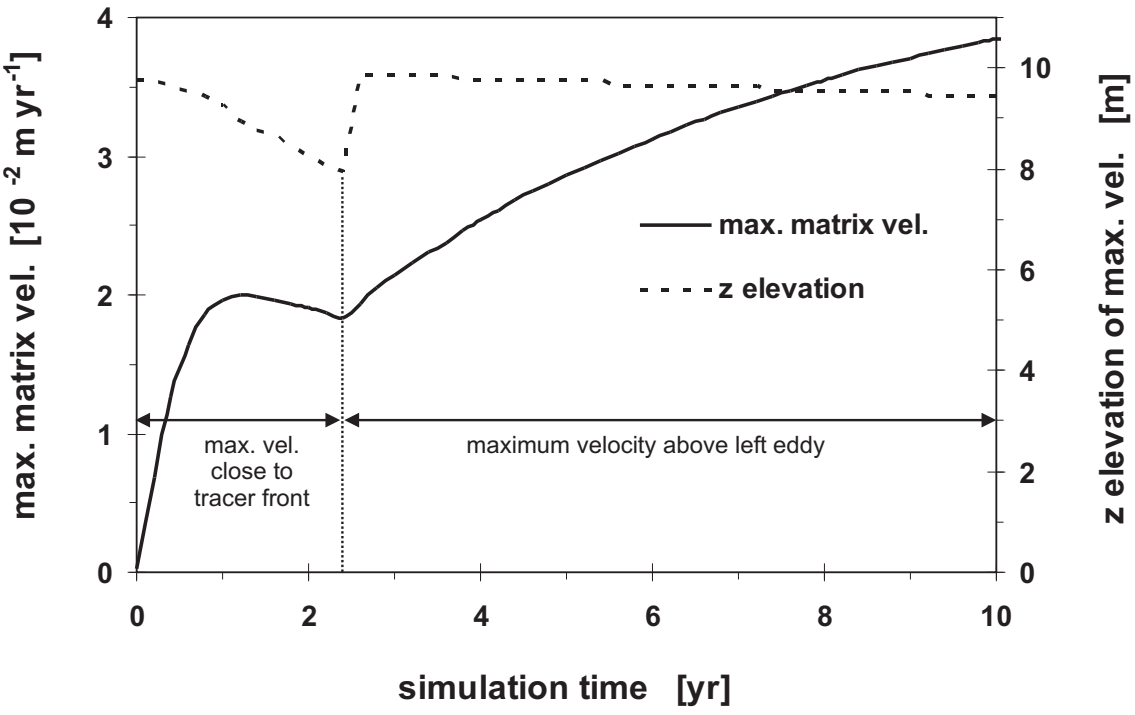

Figure 6.2: Maximum matrix velocity versus time curve. The dashed line shows the z elevation of the maximum velocity. It is located near the downwards advancing tracer front at early times and above the left eddy at later times.

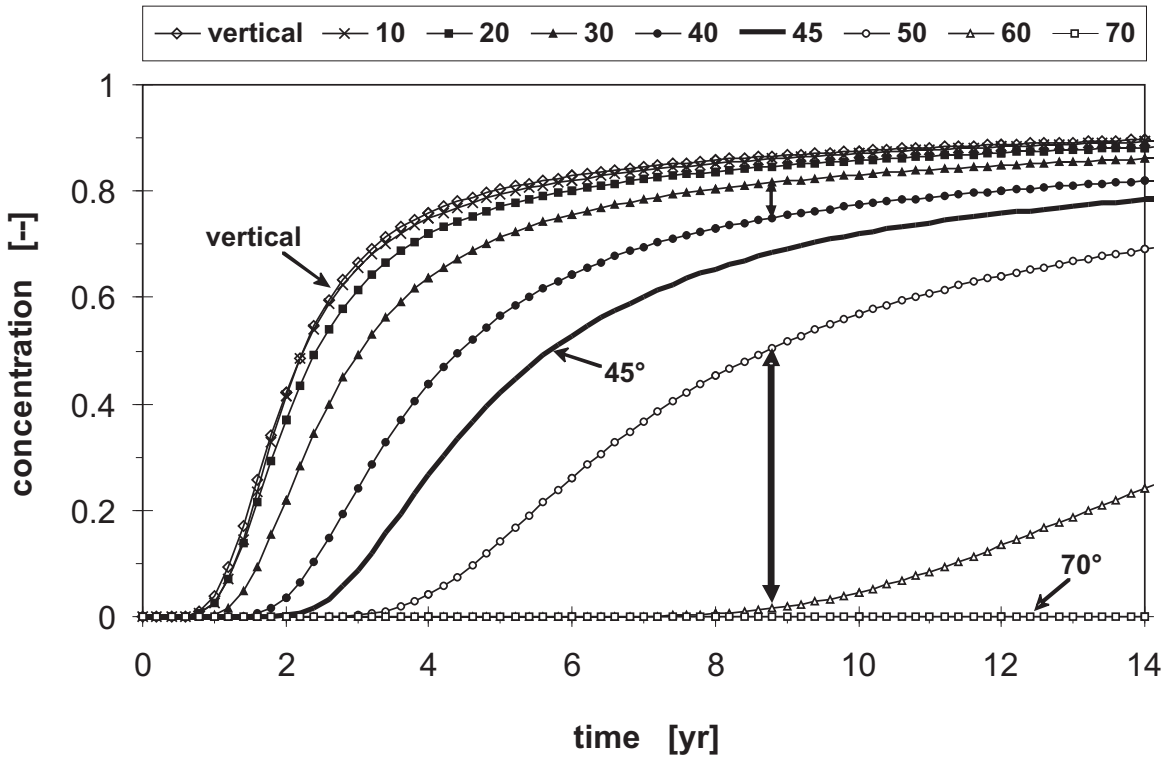

Figure 6.3: Results of variable-density flow simulations with a single variably inclined fracture: breakthrough curves at $z = 6$ m in the fracture.

6.2 Variable-Density Flow in an Orthogonal Fracture Network

This section focuses on the role of small fractures within an orthogonal network of large fractures. At present, it is unknown if small fractures enhance mixing and, thus, diminish plume instabilities that grow in large fractures. A similar phenomenon occurs in heterogeneous porous media, where low-permeability lenses can effectively dampen instability growth (Schincariol et al., 1997; Schincariol, 1998; Simmons et al., 2001). These authors have shown that the more anisotropic or heterogeneous a permeability field, the greater the dampening of instability growth. Thus, it remains unclear if especially horizontally oriented small fractures reduce vertical plume migration in fractured media.

A vertical slice of dimension 15 m $\times$ 10 m with a unit thickness was assumed (Figure 6.4). The domain consists of 30,000 square elements of size $\Delta x = \Delta z = 0.05$ m. The constant time step sizes were 1 month and the output was observed at 3 years. Initial and boundary conditions are the same as used in the model verification example given in Section 5.1. All model parameters are identical to those assumed by Shikaze et al. (1998), summarized in Table 5.1. The major fractures have a uniform aperture ($2b$) = 50 μm and the constant fracture spacing ($2B$) = 1.25 m. A set of four model setups was assumed where the aperture of the small fractures, $(2b)^*$, is 1 μm, 5 μm, 10 μm and 25 μm, respectively. For each of these four setups, four simulation trials were run (thus a total of 16 trials), where the spacing of the small fractures, $(2B)^*$, was chosen such that the ratio, $(2B)/(2B)^*$ was 2, 3, 4 and 5, respectively.

Figure 6.5 shows the result if small fractures are not considered. Four fingers form in different vertical fractures, counterbalanced by upwards flow in other vertical fractures. This base case will be the reference for comparison with further simulations.

First, the described set of 16 simulations was run assuming only horizontal small fractures. In a second step, the 16 experiments were done again assuming horizontal and vertical small fractures. In both cases, the results with small fractures of size 10 μm and smaller were identical to the base case (Figure 6.5). This outcome shows

that, in the present example, small fractures of aperture smaller than 10 μm do not impact vertical plume migration. Apparently, dispersion in small fractures does not disturb the established convective pattern with downwelling in some large fractures and upwelling in others. Even the scenario where $(2b)^* = 10$ μm and $(2B)/(2B)^* = 5$ and where the equivalent hydraulic conductivity of the system is 1.438×10^{-7} m sec^{-1}, hence more than 3% higher than that of the base case (1.391×10^{-7} m sec^{-1}) does not show any influence of small fractures. This result is important because it illustrates that mapping tiny fissures is insignificant for reliably simulating density-driven flow in fractured materials.

If the aperture of the small fractures reaches 25 μm, the results are different from the base case and depend on the $(2B)/(2B)^*$ ratio. The influence of only horizontal fractures on vertical plume migration is discussed first. Figure 6.6 exhibits the results using small horizontal fractures of aperture $(2b)^* = 25$ μm and different spacing ratios. Spacing ratios of 4 and smaller do not impact total vertical transport rates, number of instabilities and the shape of each finger. For ratios 3 and 4, only the locations of the two central fingers are different. It is remarkable that an increase of equivalent conductivity by about 20% (ratio 4), relative to the base case, does not increase vertical plume migration. This was evaluated with the penetration depth of the 0.3 concentration contour at 3 years, quantified as 9.15 m for the base case as well as for ratios 2, 3 and 4.

In all results shown in Figure 6.6, the presence of horizontal small fractures was not found to stabilize vertical plume transport by enhanced dispersive mixing. The contrary was discovered for ratio 5 (Figure 6.6d) where additional fractures enable rapid fluid exchange between adjacent vertical fractures. This leads to alternating flow directions in those fractures and allows more fingers to grow.

In a second step, horizontal and vertical fractures were included in the simulations with results shown in Figure 6.7. All simulations with ratios 3, 4 and 5 (Figures 6.7b, c and d) have a major impact on the number of fingers. This is because the rate of downwards transport in fingers always depends on the balancing upwards flow in other vertical fractures or the porous matrix. Thus, adding small vertical fractures to the system increases the upwards flow and, therefore, enables more instabilities to develop.

In the extreme case of ratio 5 (Figure 6.7d), where 4 small fractures are situated between two large ones, the upwards flow in the small fractures is large enough to counterbalance fingering in all 11 large vertical fractures.

All simulations presented here demonstrated that small fractures do not stabilize vertical plume migration. Dispersive mixing in small fractures was not found to play a key role. Variable-density flow in a network consisting of fractures of different aperture is merely dominated by the convective pattern that establishes in the large fractures. The examples also showed that fractures smaller than 10 μm have no impact on density-driven flow in large fractures of aperture equal to 50 μm.

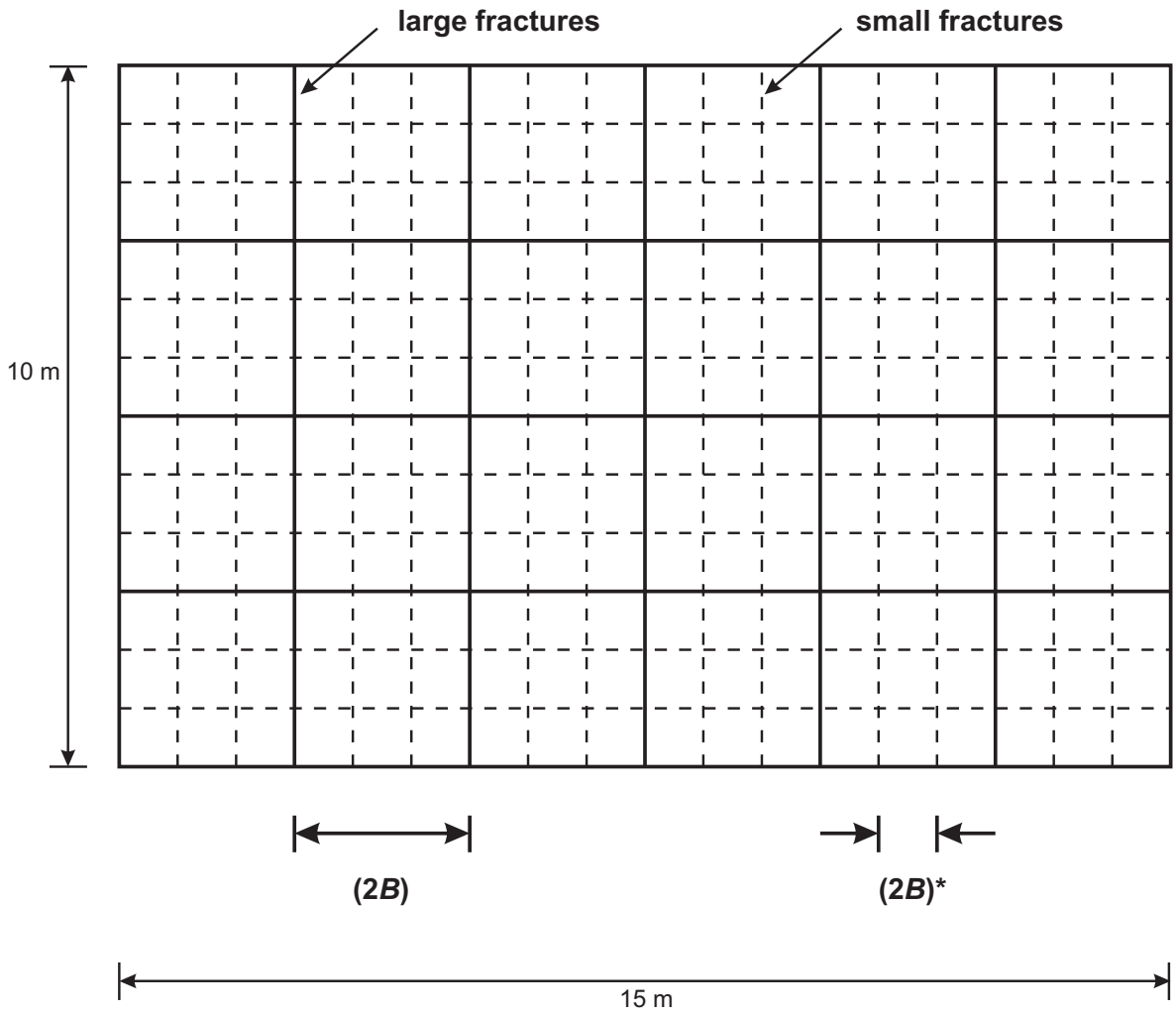

Figure 6.4: Geometry of the orthogonal fracture network consisting of large fractures (—) and small fractures (- -).

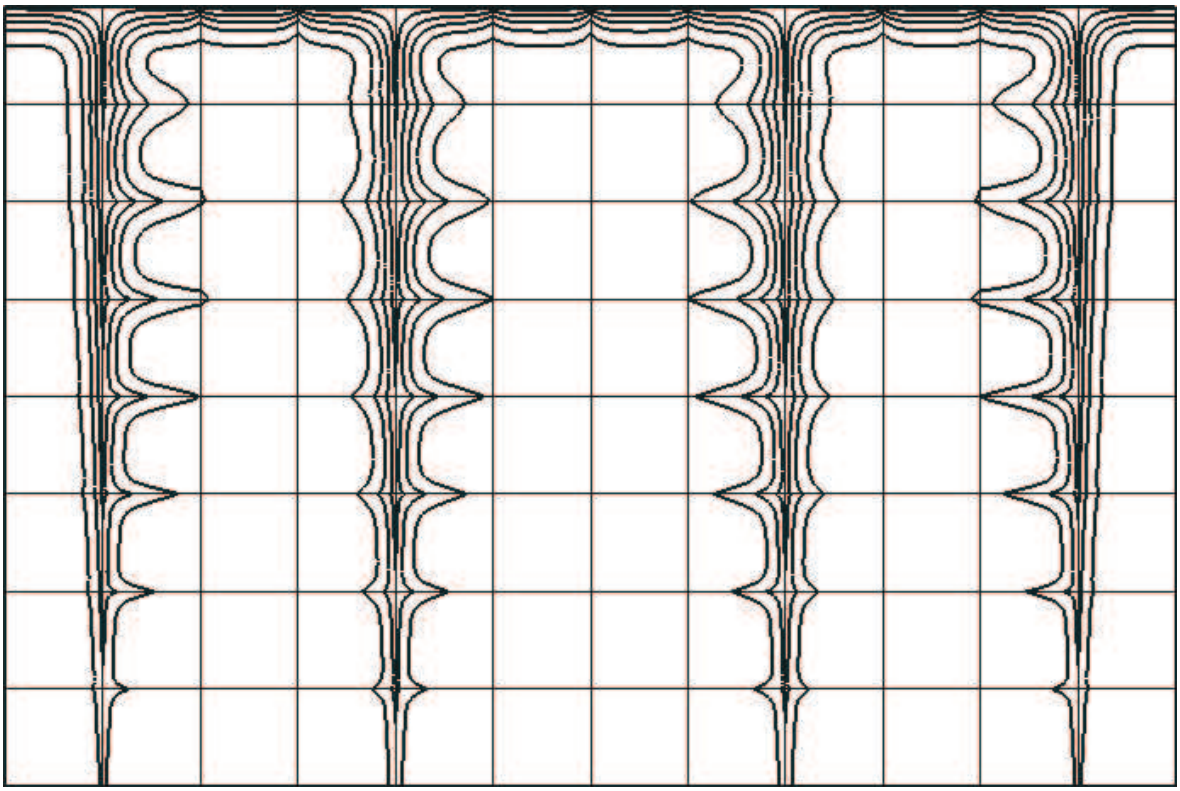

Figure 6.5: Concentration distribution at 3 years in a network of only large fractures of aperture $(2b) = 50$ μm. Concentration contours are 0.1 to 0.9 with a contour interval of 0.2.

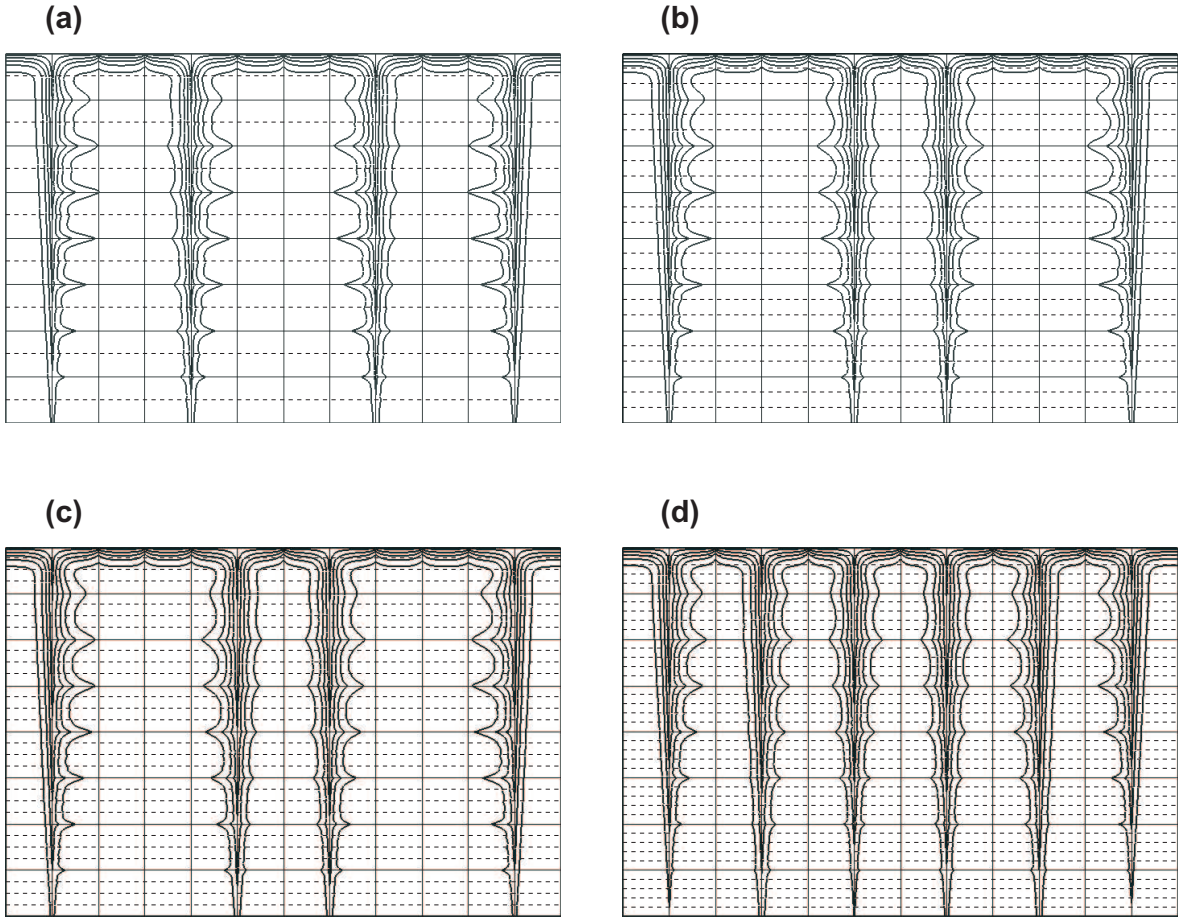

Figure 6.6: Concentration distribution at 3 years in a network of large fractures (—) disturbed by horizontal small fractures (- -) of aperture $(2b)^* = 25$ μm. The $(2B)/(2B)^*$ ratio is (a) 2, (b) 3, (c) 4 and (d) 5. Concentration contours are 0.1 to 0.9 with a contour interval of 0.2.

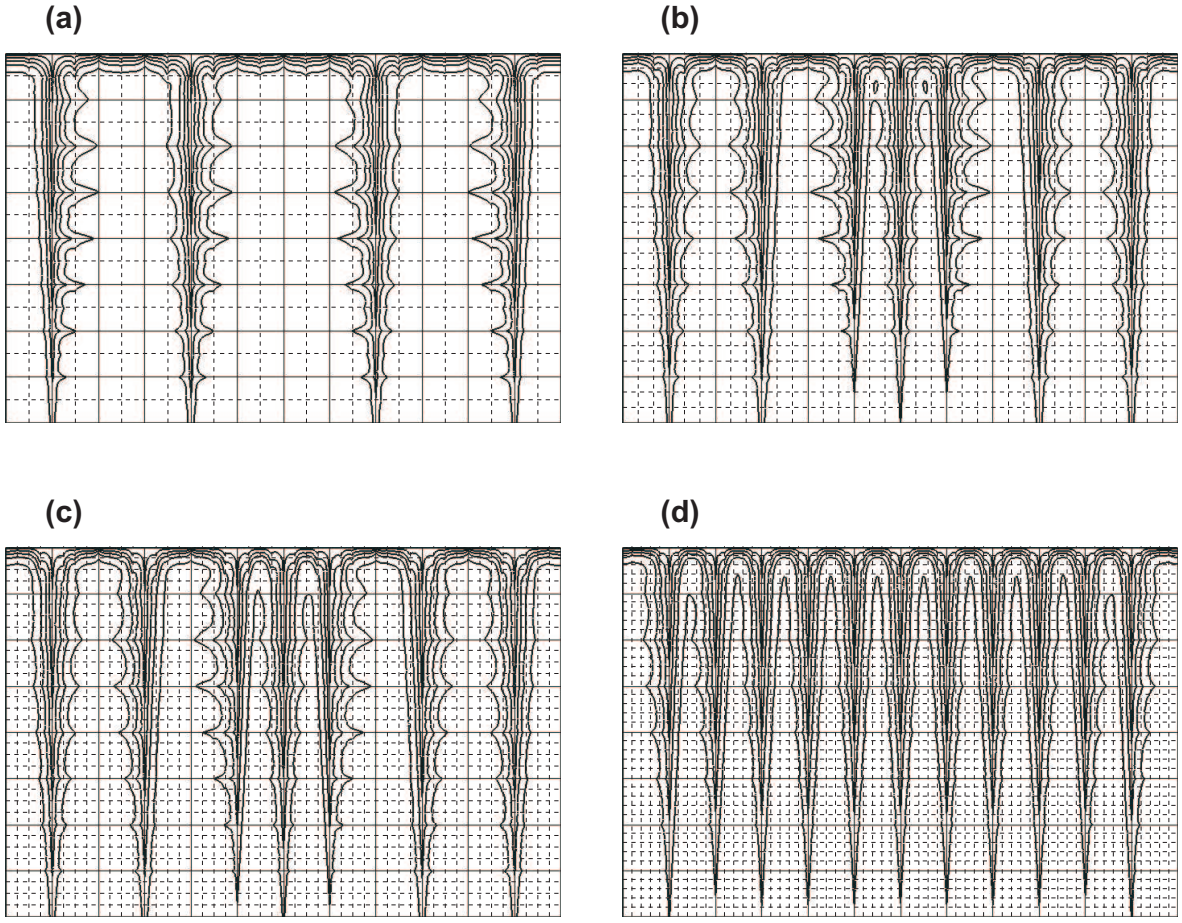

Figure 6.7: Concentration distribution at 3 years in a network of large fractures (—) disturbed by horizontal and vertical small fractures (- -) of aperture $(2b)^* = 25$ μm. The $(2B)/(2B)^*$ ratio is (a) 2, (b) 3, (c) 4 and (d) 5. Concentration contours are 0.1 to 0.9 with a contour interval of 0.2.

6.3 Variable-Density Flow in a Complex Fracture Network

The developed model was used to study plume migration in irregular fracture networks. The model design was the same as in the previous example where the parameters are given in Table 5.1. A set of 25 random fracture networks was generated, each consisting of 50 fully connected fractures. Each of these networks are based on geostatistical distributions of fracture trace, aperture and orientation. Fracture traces are assumed to be distributed log-normally (Mathab et al., 1995) between 2 and 10 m with mean = 1.4 m and sigma = 0.4 m. Fracture apertures obey an exponential distribution between 150 and 250 μm with lambda = 9000 μm^{-1}. The aperture is assumed to be constant for a single fracture. Furthermore, the fractures are assumed to be of tectonic origin, leading to a conjugated system of two fracture families (Figure 2.1). Therefore, fracture orientations (φ) follow a two-peak Gaussian distribution with the peaks at -30^o and +30^o and with the assumed standard deviation, sigma = 15^o. All networks are statistically equivalent; three of them are exhibited in Figure 6.8.

Several transient simulations were run using the systems shown in Figure 6.8. Constant time step sizes of 1 month were used and the output was observed at 3 years where the differences between the scenarios was greatest. For the three statistically equivalent fracture networks, completely different behavior was observed depending on the spatial location of the high-permeability fracture zones. Results range from virtually stable in Figure 6.9a to entirely erratic and unstable in Figure 6.9c. The different level of instability can be judged both subjectively by visual inspection (Figure 6.9) and objectively using measurable characteristics. These can be the penetration depth of some isohaline or the total stored mass as proposed by Prasad and Simmons (2004). The temporal evolution of the penetration depth and total mass (Figure 6.10) objectively confirms the subjective assessment of the degree of instability of the three examples. The 60% contour migrates faster into the aquifer in the unstable case (c) than in the relatively stable case (a). Correspondingly, system (a) stores much less solutes at any time than system (c). Thus, the two quantities shown in Figure 6.10 reflect the different stability behavior of the three network systems compared.

The formation of instabilities is restricted to the highly permeable fracture zones. The fracture network dictates the number of fingers, which is 6, 3 and 1 in the cases (a), (b) and (c), respectively. The number of fingers coincides with the number of equidistantly distributed fractures, that are connected with the source. Clearly, systems with numerous equidistantly distributed fractures are more stable, whereas systems with few fractures at the salt lake are unstable. In contrast to density-driven transport in porous media, the number of instabilities in fractured media does not change with time. Simmons et al. (1999) demonstrated that in a sandy aquifer, the number of fingers decreases with time because large fingers increase, decreasing the number of small fingers. In fractured media, however, this is not the case because the location of the fingers is strongly controlled by the geometry of the fracture network.

Furthermore, plume development in irregular fractured media is influenced by the formation of convection cells. Figures 6.11 and 6.12 display the highly nonuniform velocity field after 0.5 years. The flow system is characterized by complicated convection, where many convection cells form. Two selected streamlines of the velocity field are shown in Figure 6.12. As a result of the convective nature of the system, the flow direction in the dominant fracture at the top right corner is downward and upward in other fractures. Thus, only one instability develops, because the two fractures close to the surface that seem to be contaminated by the source, located on top of the system, are actually contaminated from below.

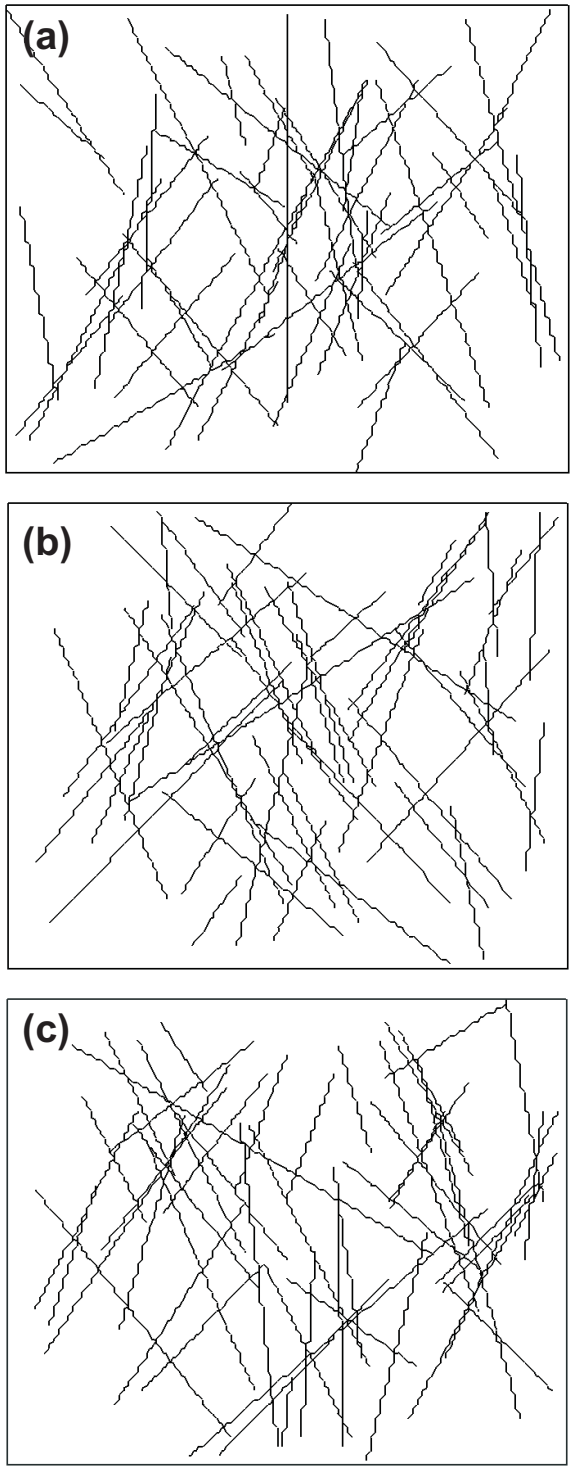

Figure 6.8: Three stochastic fracture networks, defined by an exponential aperture distribution, a log-normal trace distribution and a double-peak Gaussian orientation distribution.

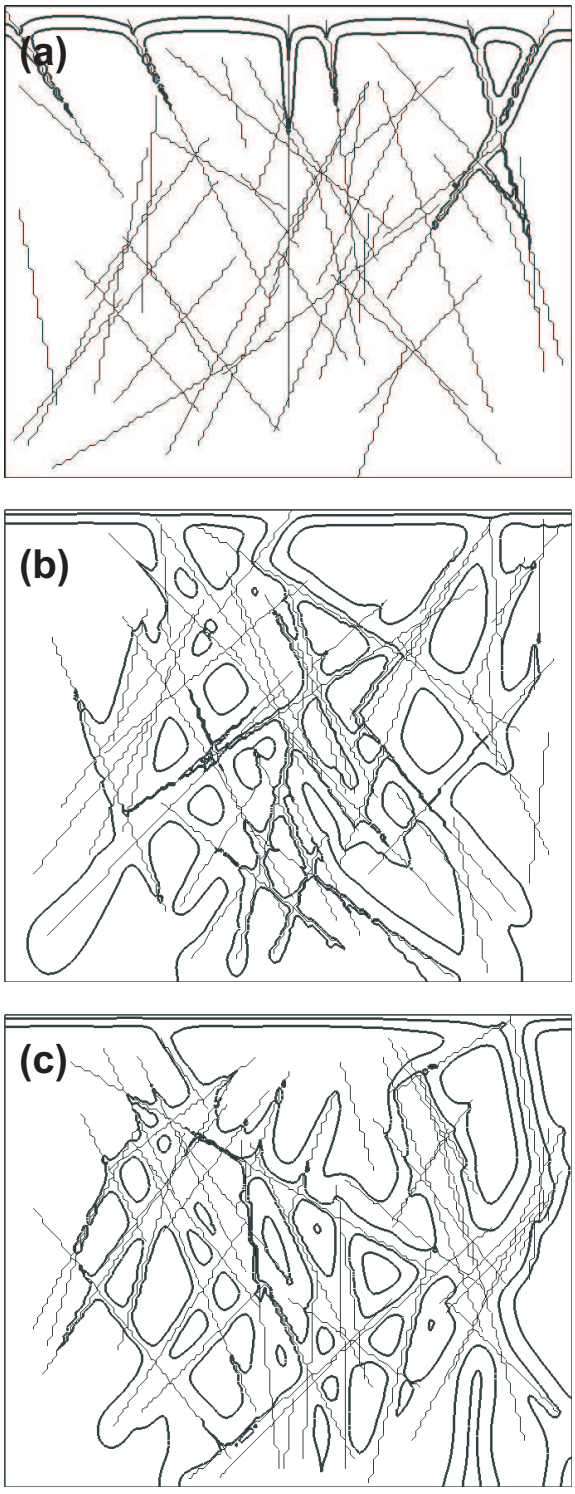

Figure 6.9: Simulated concentration at 3 years for 3 different fracture networks. Shown are the concentration contours 20% and 60%. The number of equidistantly distributed fractures connected to the source is 6, 3 and 1 for figures (a), (b) and (c), respectively.

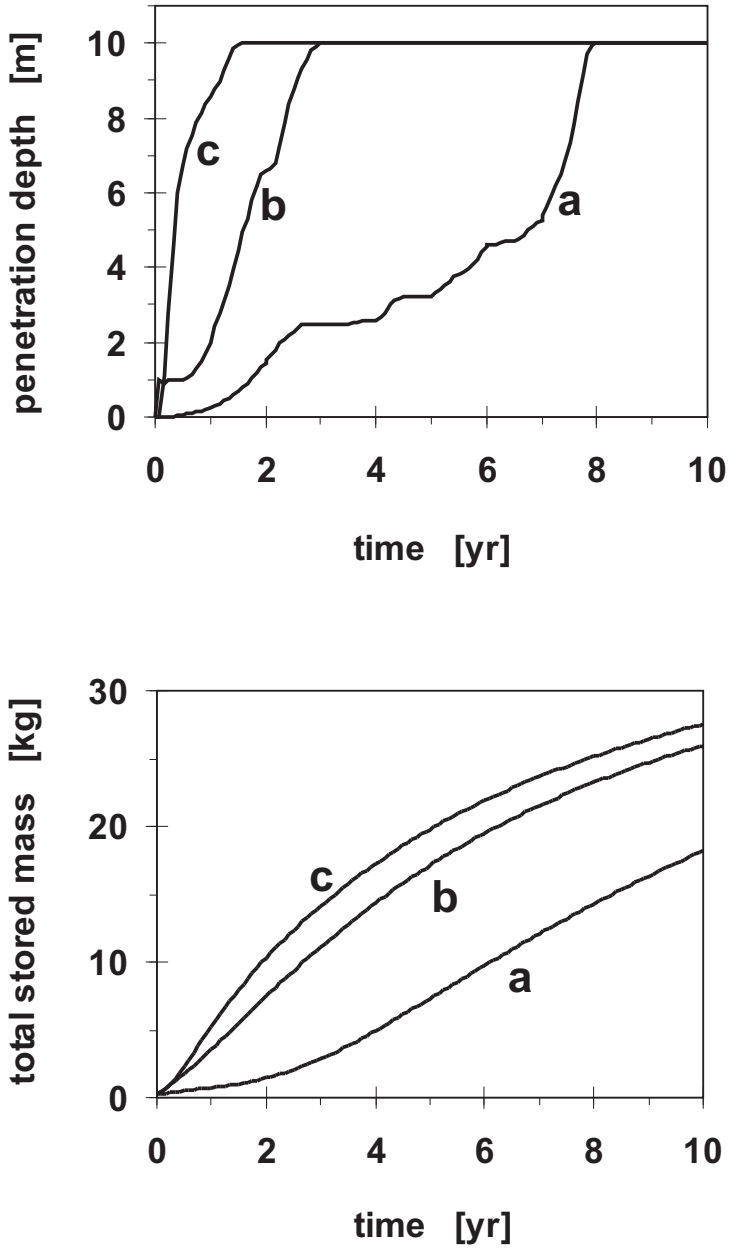

Figure 6.10: Penetration depth of the 60% isochlor and total stored mass for the three simulation results presented in Figure 6.9.

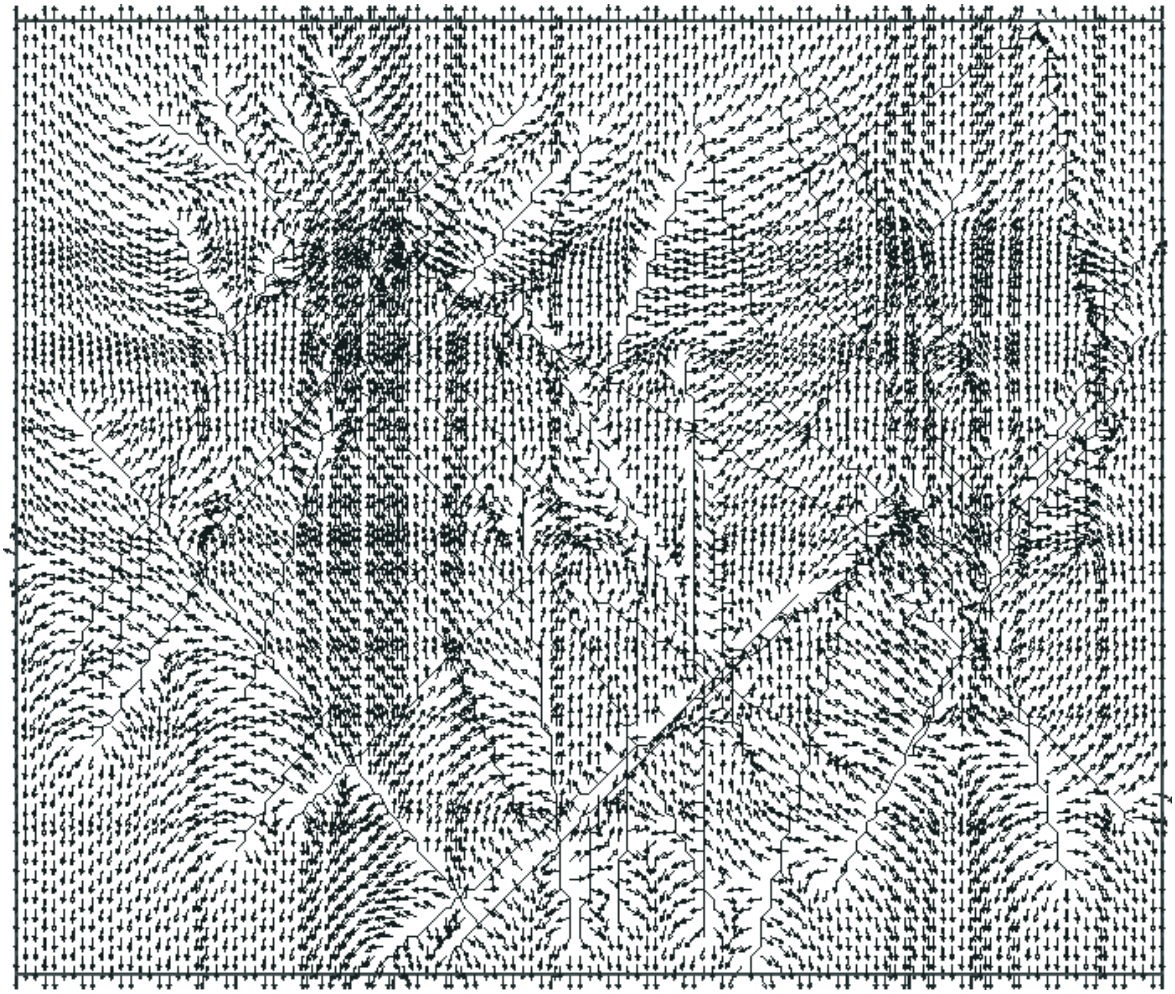

Figure 6.11: Matrix velocity vectors for the network shown in Figure 6.8c after 0.5 years. The velocity field is highly irregular and complex convection cells form.

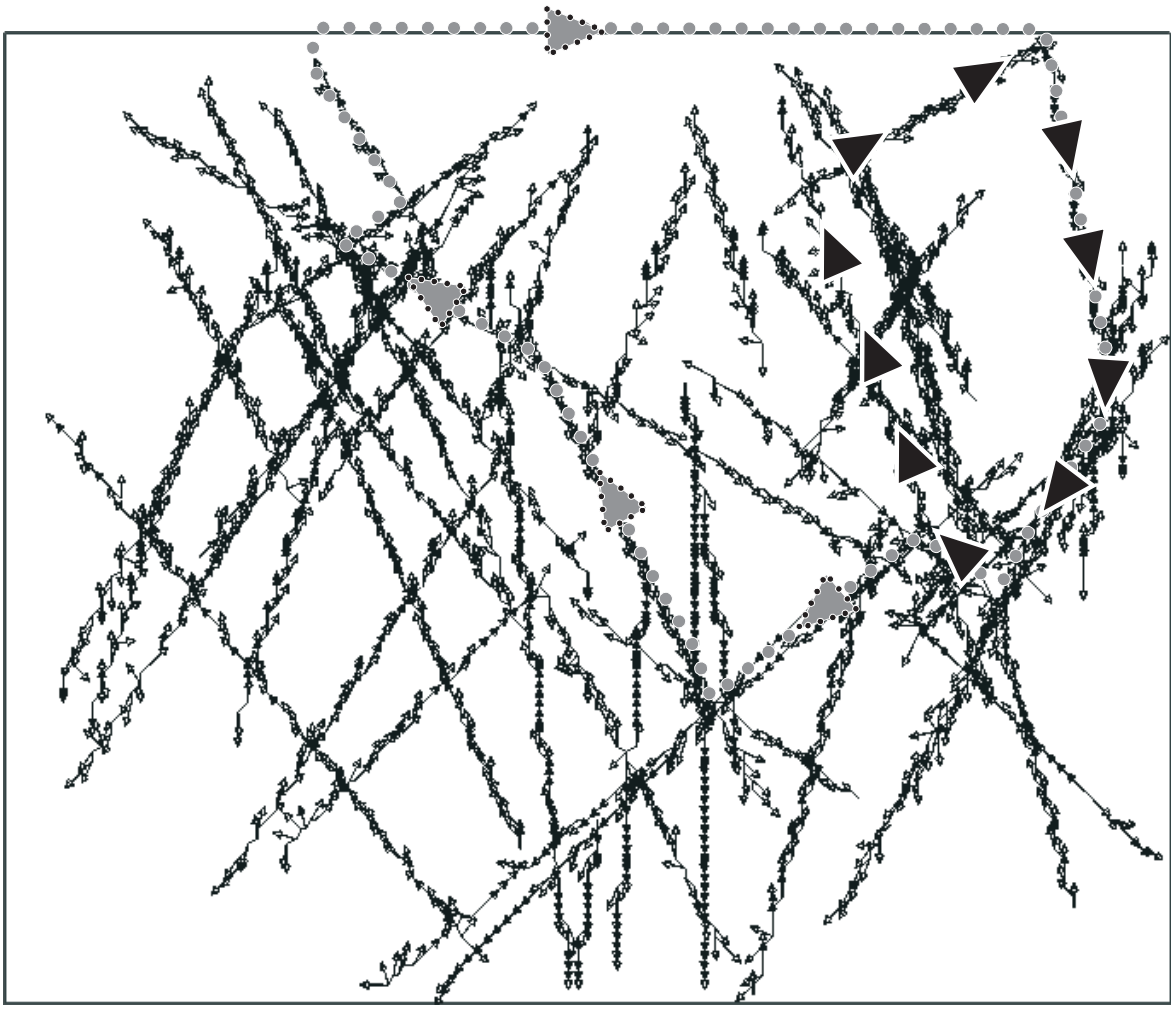

Figure 6.12: Fracture velocity vectors for the network shown in Figure 6.8c after 0.5 years. Two convection cells are highlighted. Some fractures that are close to the salt lake are contaminated from below.

6.4 Thermohaline Flow and Reactive Solute Transport in Porous Media

In order to consider heat transfer and chemical reactions in a fracture network, existing studies on reactive transport in porous media must first be expanded to include heat transfer. In successive steps, this section first focuses on reactive transport, then thermohaline variable-density, variable-viscosity flow and finally couples the two. These processes will in turn be considered for a fracture network in the next section.

This section involves a series of three numerical simulations within a vertical sand tank as shown in Figure 6.13. Such simulations have been carried out in a similar way by Schincariol et al. (1994), Ibaraki (1998) and Freedman and Ibaraki (2002). The vertical tank was chosen to highlight the coupling between variable-density flow and reactive solute transport as done previously by Freedman and Ibaraki (2002).

The 2D simulation domain is of dimension 1.0 m $\times$ 0.25 m with a unit thickness. Because the simulations are for a porous medium, the domain does not contain the discrete fractures shown in Figure 6.13. The domain has been spatially discretized by 63,000 rectangular finite elements, which are smaller at the left boundary (Δx = 0.5 mm, Δz = 2.0 mm), and which increase towards the right (Δx = 2.0 mm, Δz = 2.0 mm).

A horizontal flow field is imposed by assigning constant fluxes ($q = 1.045\times10^{-6}$ m sec^{-1}) along the left and right boundaries. Both top and bottom are impermeable to fluid flow. The Figure 6.13 also shows the location of a source of constant concentration and temperature. The four common ions Na^+, Ca^{2+}, Mg^{2+} and Cl^- are used and assigned the uniform concentration 1000 mg l^{-1} at the source. The source also corresponds to the prescribed temperature boundary condition, T_C = 247°C. Zero concentrations and a constant temperature equal to 239°C have been assigned along the remaining left boundary to make sure that the only solute input is the source. Both top and bottom as well as the right side are zero-conductive heat transfer and zero-dispersive solute flux boundaries. Thus, thermal energy and contaminants can not penetrate the top and bottom walls of the slice. However, heat and solutes are able

to penetrate the right side by convection and advection, respectively. Aqueous silica is the fifth mobile species. Unlike salt concentrations and temperature, the silica molality at the source is not constant but recalculated at each time step. All boundaries are zero-dispersive flux boundaries for silica.

Initially, the entire system is solute-free and the uniform initial temperature is 239°C (Johnson et al., 1998), lower than that at the source. The system is initially in thermodynamic equilibrium ($r_{net} = 0$), where $m_{\mathrm{H_4SiO_4}} = K_{eq}/\gamma_{\mathrm{H_4SiO_4}} = 6.4996$ mmol kg^{-1} is the initial silica molality at $C_\sigma = 0.0$ mg l^{-1} and $T_C = 239$°C. At the source, the corresponding equilibrium silica molality is $m_{\mathrm{H_4SiO_4}} = K_{eq}/\gamma_{\mathrm{H_4SiO_4}} = 6.9361$ mmol kg^{-1} at $C_\sigma = 1000.0$ mg l^{-1} and $T_C = 247$°C. The choice of initial thermodynamic equilibrium makes it easy to identify every deviation from the silica equilibrium as the result of a chemical reaction (dissolution or precipitation).

The three simulations cover a time of 3 days with increasing time step sizes. Thermal deformations of the rock are not considered. The spatiotemporal discretization as well as all simulation parameters are summarized in Table 6.1.

The first trial, entitled *pm_reac*, simulates reactive transport but does not consider density and viscosity variations. Both fluid properties are assumed to be identical to those of the ambient groundwater. In *pm_reac*, the time step sizes change dynamically, based on porosity changes. The maximum permitted change in porosity per time step, ϕ^*, was set to 10^{-3} (0.1%). The initial and maximum time step sizes chosen were 1 minute and 2 hours, respectively. Figure 6.14 shows the results of *pm_reac* after 3 days. Thermal energy is predominantly transferred by conduction in both the longitudinal and the transverse direction (Figure 6.14a). Because buoyancy forces are not considered in *pm_reac*, the plume is mainly transported by advection and migrates laterally across the domain. Molecular diffusion and transverse dispersion slightly increase the plume extension in the vertical direction. The chloride concentration (Figure 6.14b; no retardation) and the magnesium concentration (Figure 6.14c; highest retardation) illustrate this transport behavior. The non-reactive and non-sorptive chloride indicates the position of the advective front.

Figure 6.14d shows the molal concentration of silica and reveals an interesting

Table 6.1: Model parameters used in reactive transport studies.

Parameter	Value
Domain size[a] (ℓ_x, ℓ_z)	1.0 m, 0.25 m
Spatial discretization[d] $(\Delta x, \Delta z)$	0.5 mm ... 2.0 mm, 2.0 mm
Temporal discretization[e] (Δt)	1 min ... 2 h
Longitudinal dispersivity[a,b,c] (α_l)	3.0×10^{-4} m
Transverse dispersivity[a,b,c] (α_t)	0.0 m
Tortuosity[b,c] (τ)	0.35
Average Darcy flux[a,b,c] (q)	1.045×10^{-6} m sec^{-1}
Free-solution diffusion coefficient[b,c] (D_d)	1.6×10^{-9} m^2 sec^{-1}
Distribution coefficient (K_d)	[Na^+] 3.0×10^{-6} kg^{-1} m^3
	[Ca^{2+}] 5.0×10^{-5} kg^{-1} m^3
	[Mg^{2+}] 1.0×10^{-4} kg^{-1} m^3
	[Cl^-] 0.0 kg^{-1} m^3
	[H_4SiO_4][f] 0.0 kg^{-1} m^3
Reference fluid density[g] (ρ_0)	815.969 kg m^{-3}
Reference fluid dynamic viscosity[g] (μ_0)	1.1184×10^{-4} kg m^{-1} sec^{-1}
Fluid compressibility[h] (α_{fl})	4.4×10^{-10} kg^{-1} m sec^2
Matrix compressibility[h] (α_m)	1.0×10^{-8} kg^{-1} m sec^2
Initial porosity[b,c] (ϕ^{init})	0.38
Initial hydraulic freshwater conductivity[b] $(K_{ij}^{0,init})$	5.6×10^{-4} m sec^{-1}
Initial specific surface area in the matrix[i] (A_{qz}^{init})	54.2 m^2 kg^{-1}
Solid phase density[j] (ρ_s)	2650 kg m^{-3}
Specific heat of solid[j] $(\tilde{c}_s)$	738 J kg^{-1} K^{-1}
Specific heat of liquid[j] $(\tilde{c}_l)$	4186 J kg^{-1} K^{-1}
Thermal conductivity of solid[j] (k_s)	5.0 W m^{-1} K^{-1}
Thermal conductivity of liquid[j] (k_l)	0.6 W m^{-1} K^{-1}

[a] Freedman and Ibaraki (2002)

[b] Schincariol et al. (1994)

[c] Ibaraki (1998)

[d] To fulfill the Péclet criterion, $Pe < 2.3$, used by b and c

[e] To fulfill the Courant criterion, $Cr \leq 1.0$, used by b

[f] Yeh and Tripathi (1989)

[g] Computed by this model for deionized water at $T_C = 239$°C

[h] Shikaze et al. (1998)

[i] Johnson et al. (1998)

[j] Bolton et al. (1996)

result of the *pm_reac* simulation. In the near field of the source, temperatures are relatively high, such that quartz dissolves. However, further away from the source, the temperatures are close to the background temperature, 239°C. In this far field of the source, solute concentrations are high, decreasing the solubility of silica. Therefore, the salinity controls the silica concentration in the far field. Conversely, the silica concentration follows the isotherms in both the near field as well as in regions of low salinity above and below the plume. Figure 6.15 is a vertical cross-section at $x = 0.12$ m from the source. The figure shows that the silica concentration is proportional to temperature in low-salinity zones and inversely proportional to salinity in high-salinity zones. Clearly, these observations demonstrate the solubility-lowering effect of salt and the solubility-increasing effect of temperature as discussed in Section 2.2 and shown in Figure D.1 (Appendix D). Figure 6.14e finally shows the distribution of the hydraulic freshwater conductivity. As expected, the area around the source became more conductive because of quartz dissolution. However, the elongated blueish fields, situated on the right of the source, indicate a conductivity value smaller than the initial one. Apparently, dissolved silica was transported by advection to the right. Silica is assumed to be non-sorptive and its transport rate is, therefore, comparable to the chloride transport rate. If silica molecules are transported laterally to regions of lower temperature and high salinity, the system becomes locally supersaturated and some of the previously dissolved silica precipitates, resulting in lower hydraulic conductivity.

The second simulation trial, called *pm_dens*, models variable-density flow in the porous medium but ignores chemical reactions. Fluid density and viscosity are calculated with Equations (2.29) and (2.32) and as shown in Figure D.1 (Appendix D). Unlike the previous simulation, time step sizes are prescribed and gradually increase from 1 minute to 2 hours.

Figure 6.16 demonstrates that density effects cause vertical flow movement. The figure shows concentration profiles of Cl^- at different times, highlighting the mixed convective flow character: Forced convection (advection) remains the main lateral transport mechanism whereas buoyancy-induced free convection controls the shape of the plume in the vertical direction. The magnitude of buoyancy is controlled by the fluid density, being a function of both temperature (Figure 6.17a) and salinity (Figures 6.17b and 6.17c). Different diffusivities are the reason for completely different transport behavior

of thermal energy and solutes, which is known as double diffusive transport (Stern, 1960; Turner, 1979; Tyvand, 1980; Evans and Nunn, 1989; Brandt and Fernando, 1995; Oldenburg and Pruess, 1998). In the *pm_dens* simulation, heat transfer is practically independent of groundwater flow, while water flow dominates solute transport. This difference results in an interesting density distribution (Figure 6.17d). In the near field of the source, temperature appears to control the fluid density, while in the far field, the salt concentration is crucial. The inflowing hot saline fluid has a density of 808.443 kg m^{-3}, lower than the reference density (815.969 kg m^{-3}). In this case, the inflowing fluid is less dense than the ambient fluid. As a consequence, the relative density, ρ_r, is negative (-9.223×10^{-3}), resulting in a positive buoyancy effect near the source. However, further away from the source, the influence of the solutes on density dominates because advective solute transport is more efficient than conductive heat transfer. Therefore, the fluid density exceeds its reference value and the density contrast is positive (in the range of 10^{-3}), which results in a noticeable sinking of the plume.

The last simulation, *pm_reac_dens*, couples the effect of density with chemical reactions. As in *pm_reac*, time step sizes adapt to porosity changes with the maximum permitted porosity change, ϕ^*, set to 10^{-3} (0.1%). Figure 6.18 shows that dissolved silica travels with the solute plume laterally across the domain. As before, the temperature is the important factor in the near field of the source, where it controls quartz solubility and fluid density. In the far field, however, the salt content dictates variable-density flow and chemical reactions.

In *pm_reac_dens*, the hydraulic conductivity and the matrix porosity change with time as a result of the reactions. This contrasts with *pm_dens*, where conductivity and porosity remain constant over time. However, the results of the two simulations are not significantly different. This observation is in agreement with findings by Freedman and Ibaraki (2002), who simulated the chemistry of calcite, coupled with density-driven flow. The regarded time scale of some days is too short to perceive a major impact of the reactions. Nevertheless, the three simulations presented here illustrate the coupling between variable-density flow, heat transfer and reactive transport in porous media. They also show that adaptive time stepping is a useful tool and certainly competitive compared with the conventional use of predefined time step sizes (Table 6.2).

Table 6.2: Simulations and CPU times in porous media (*pm*).

Simulation	Chemical reactions	Density variations	Time stepping	CPU time*
pm_reac	√	–	adaptive	31 min
pm_dens	–	√	prescribed	1 h 24 min
pm_reac_dens	√	√	adaptive	1 h 34 min

* Computed on a Pentium 4, 2.6 GHz, 500 MB RAM.

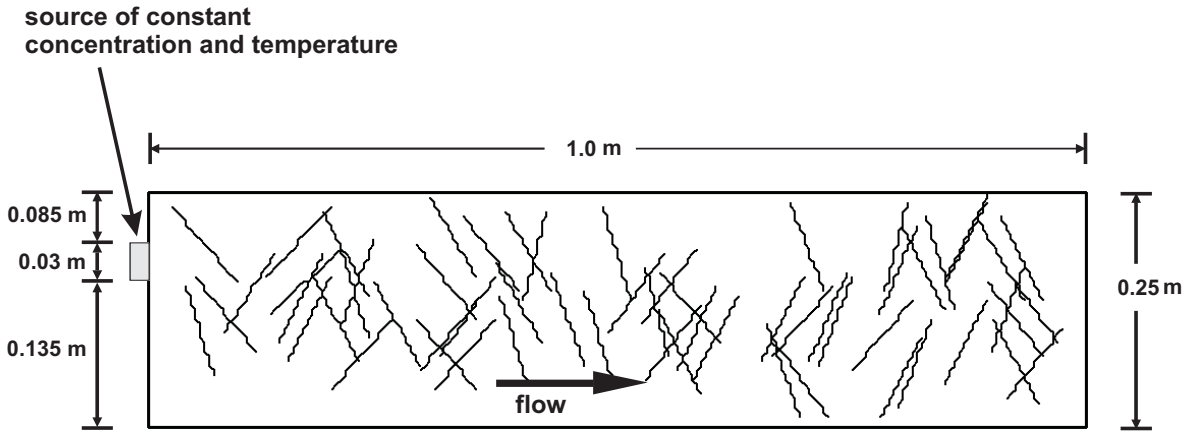

Figure 6.13: Model domain and location of the solute source for numerical simulations of reactive silica transport and variable-density thermohaline flow in porous and fractured media. The parameters are the same for studies in porous media, except no discrete fractures are used.

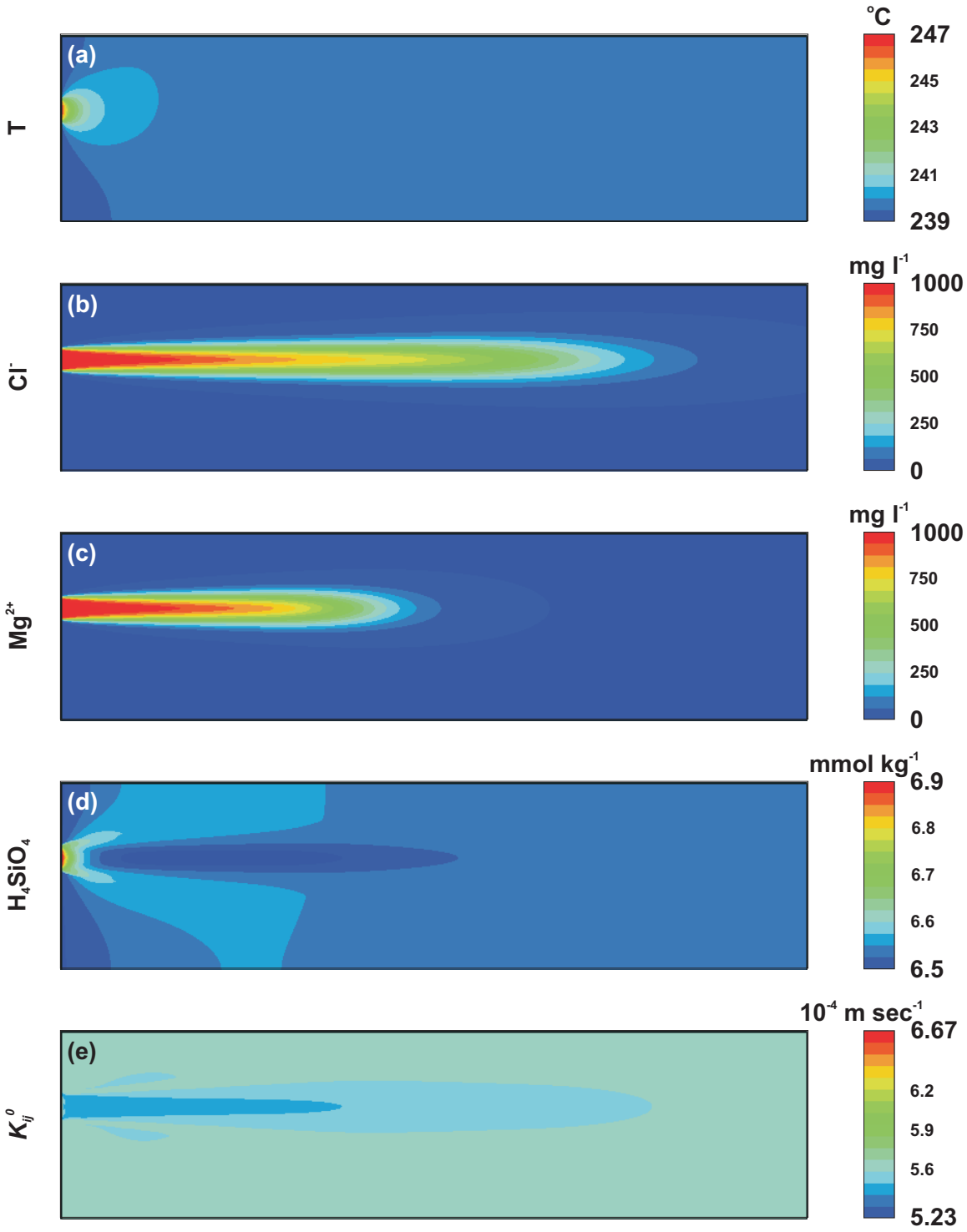

Figure 6.14: Results of non-density dependent reactive transport simulations in porous media (*pm_reac*) at 3 days. Shown are (a) temperature, (b) chloride and (c) magnesium ion concentration, (d) molal concentration of aqueous silica and (e) freshwater hydraulic conductivity.

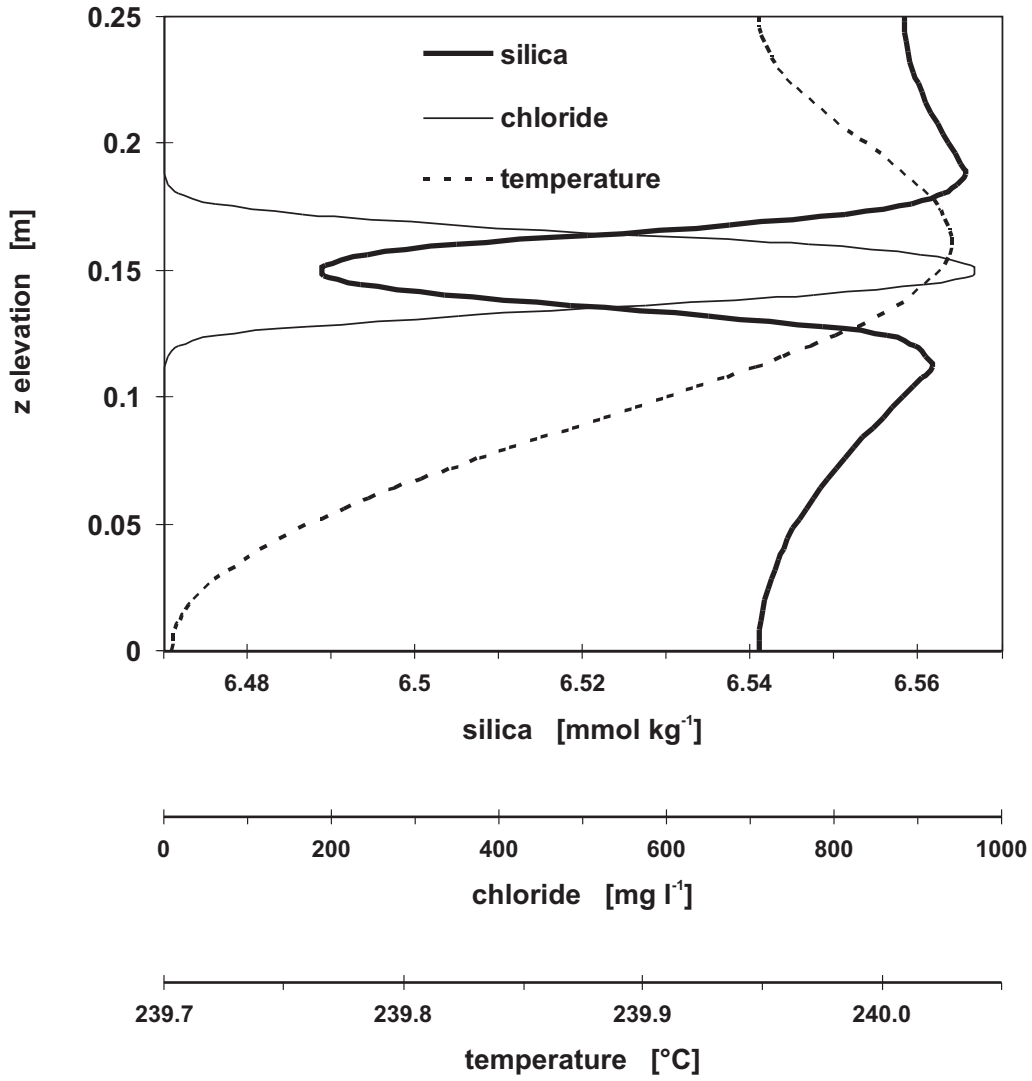

Figure 6.15: Vertical cross-section at $x = 0.12$ m from the source for the simulation *pm_reac*.

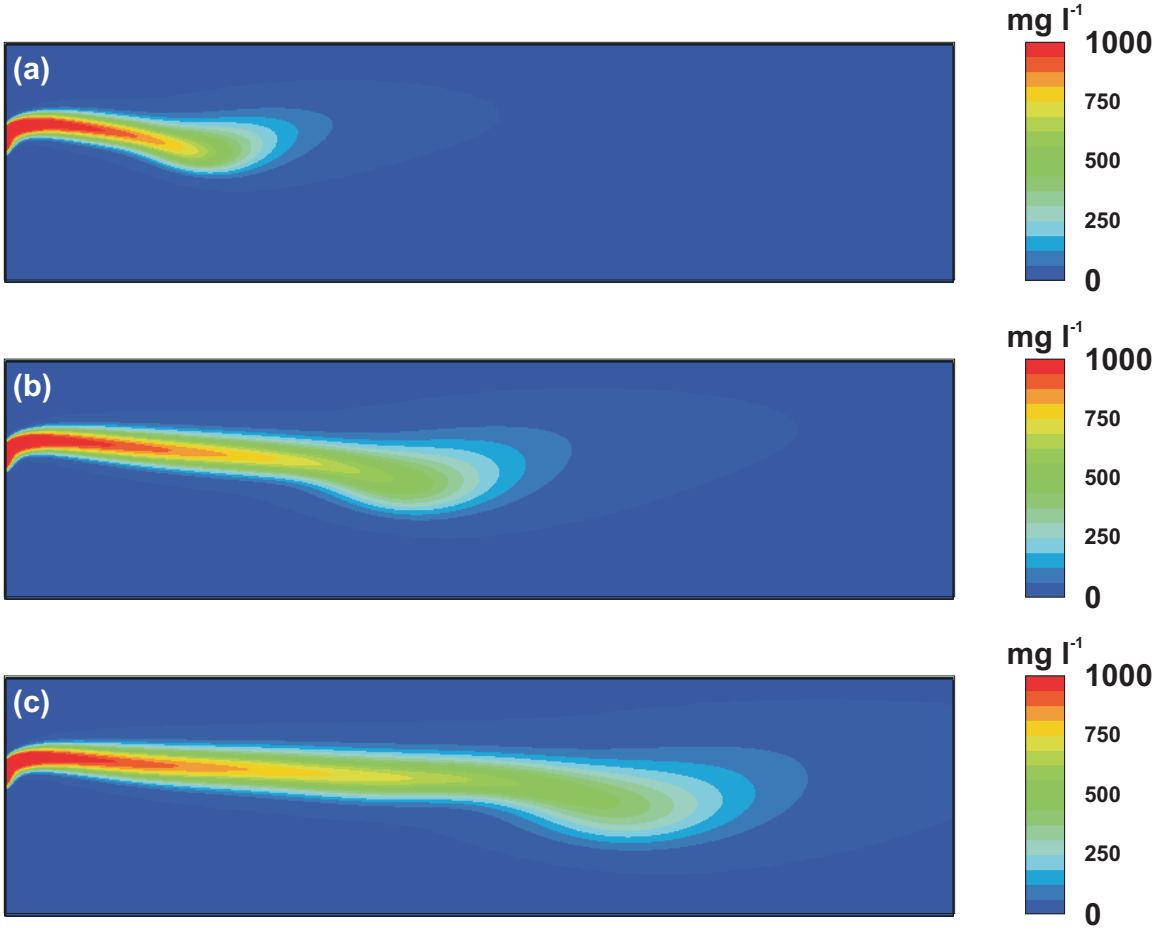

Figure 6.16: Results of density dependent non-reactive transport simulations in porous media (*pm_dens*). Shown is the chloride ion concentration at different simulation times: (a) 1 day, (b) 2 days and (c) 3 days.

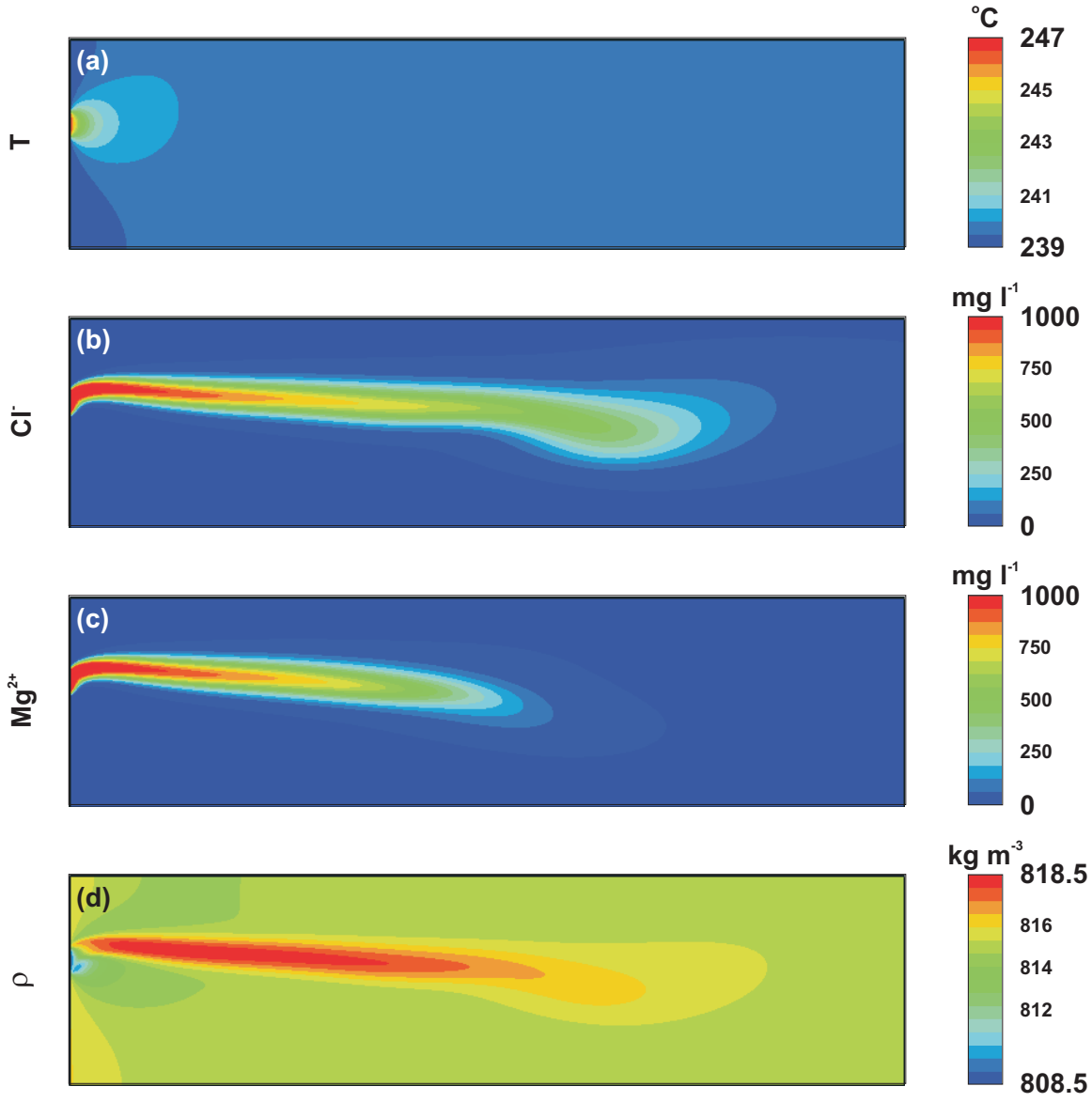

Figure 6.17: Results of density dependent non-reactive transport simulations in porous media (*pm_dens*) at 3 days. Shown are (a) temperature, (b) chloride and (c) magnesium ion concentration and (d) fluid density.

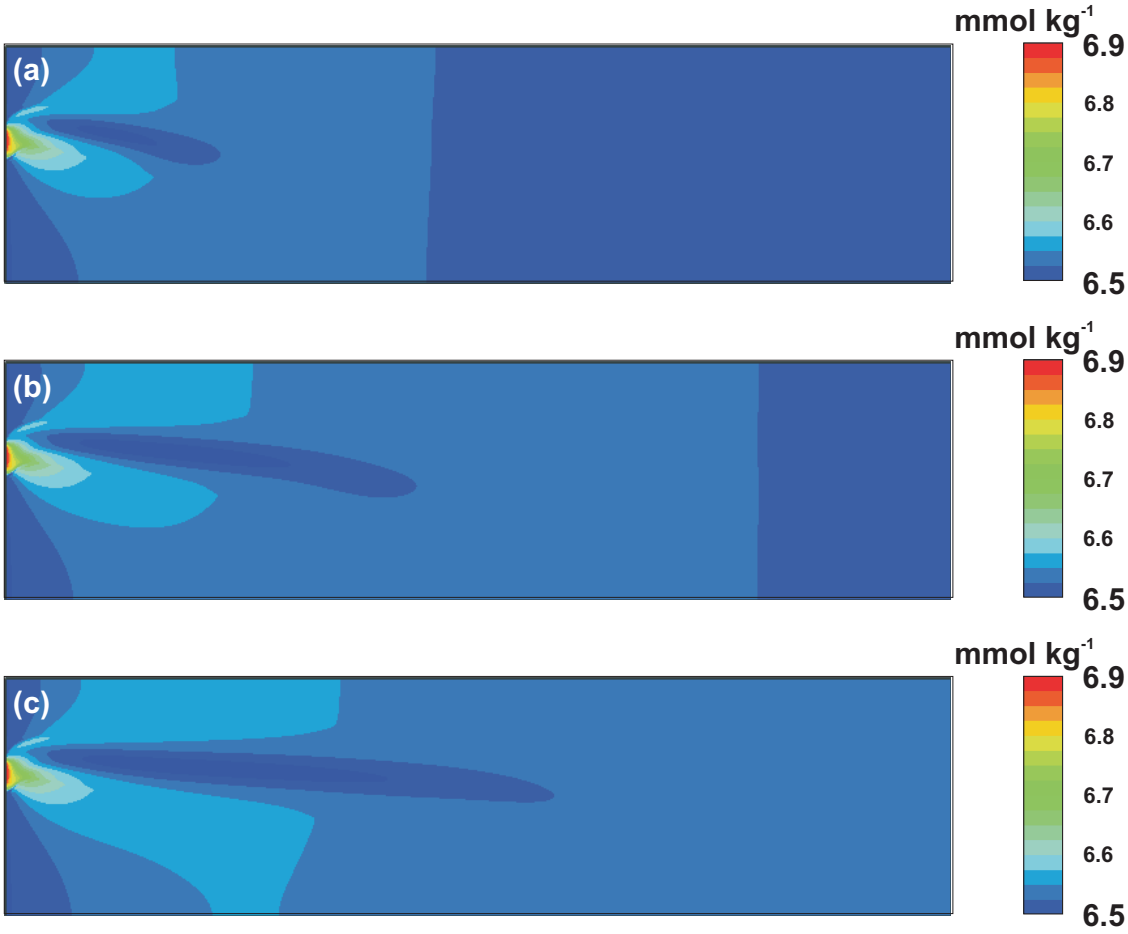

Figure 6.18: Results of density dependent reactive transport simulations in porous media (*pm_reac_dens*). Shown is the molal concentration of aqueous silica at different simulation times: (a) 1 day, (b) 2 days and (c) 3 days.

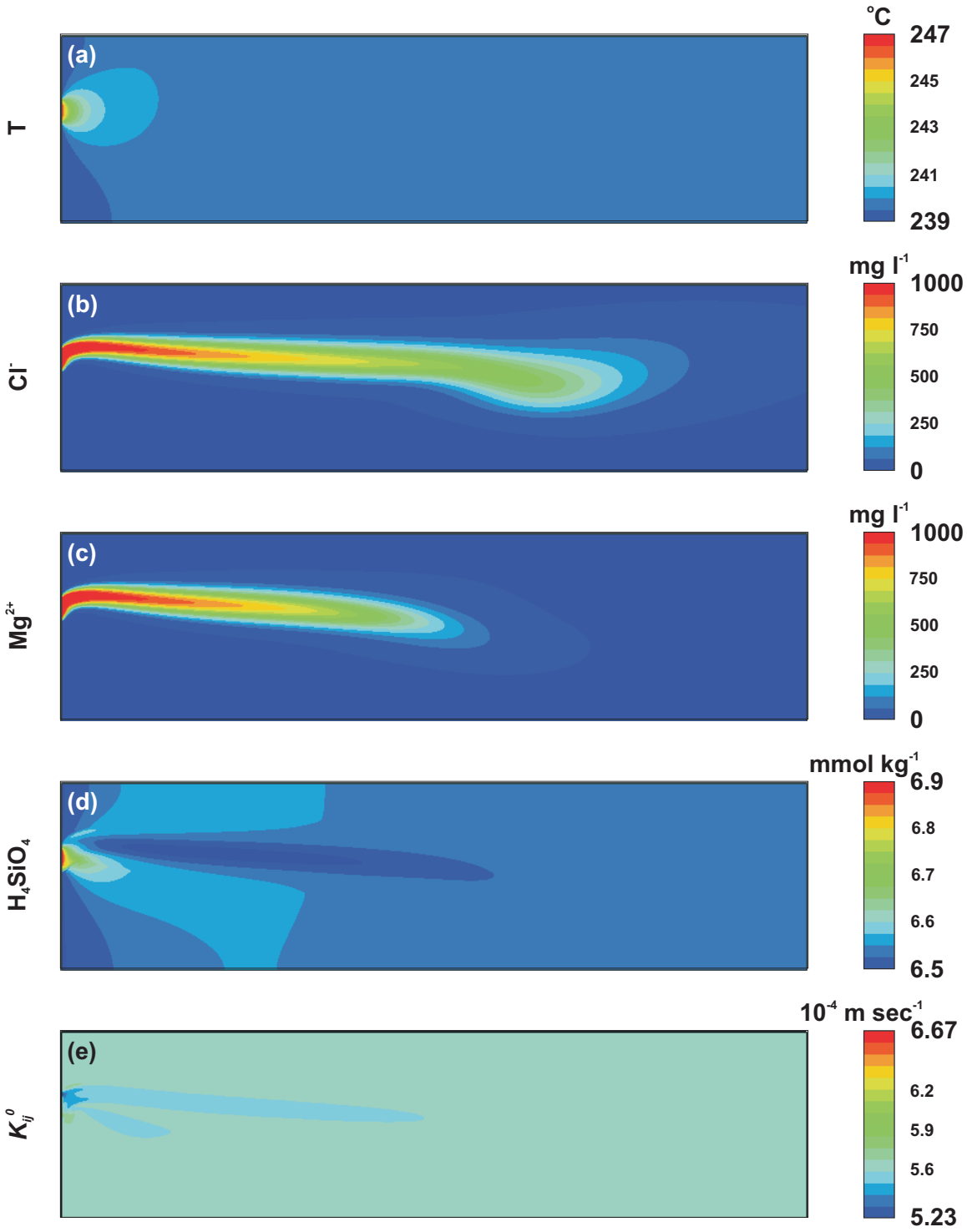

Figure 6.19: Results of density dependent reactive transport simulations in porous media (*pm_reac_dens*) at 3 days. Shown are (a) temperature, (b) chloride and (c) magnesium ion concentration, (d) molal concentration of aqueous silica and (e) freshwater hydraulic conductivity.

6.5 Thermohaline Flow and Reactive Solute Transport in Fractured Porous Media

A second series of three simulations assumes the presence of fractures (*fm*) oriented transversely to the ambient flow direction as shown in Figure 6.13. The developed random fracture generator produced 60 random fractures, which follow the two main orientations 60° and 120° with the standard deviation of the Gaussian distribution, sigma = 1°. All fractures are 0.1 m in length and have the uniform aperture of 100 μm. Initial and boundary conditions of the *fm* simulations are identical to those used in the previous example in porous media. Table 6.1 presents the simulation parameters while Table 6.3 shows additional parameters for the studies including fractures.

Table 6.3: Additional model parameters used in reactive transport studies in fractured media.

Parameter	Value
Fracture dispersivity[a,b] (α^{fr})	0.1 m
Initial fracture aperture[b,c] $(2b)^{init}$	100 μm
Initial specific surface area in the fracture[d] ($A_{qz}^{fr,init}$)	49.021 m^2 kg^{-1}
Fracture roughness coefficient[e] (ω)	1.0

[a] Therrien and Sudicky (1996)
[b] Tang et al. (1981)
[c] Sudicky and Frind (1982)
[d] From relation (2.40)
[e] Steefel and Lasaga (1994)

The first experiment, *fm_reac*, ignores density effects but simulates chemical transport. The time step sizes adapt to changes in matrix porosity and/or fracture aperture. Maximum permitted changes of porosity and aperture are chosen as $\phi^* = 10^{-3}$ (0.1%) and $(2b)^* = 0.1$ μm, respectively. Figure 6.20 shows the results after 3 days. The fractures have a substantial impact on the result because their hydraulic conductivity is more than 100 times greater than that of the porous matrix. The high-permeability fractures increase the transverse dispersion of the plume. This results in a larger vertical extension of the plume and reduced lateral migration (Figures 6.20b and 6.20c), compared with results in porous media (Figures 6.14b and 6.14c). Figure 6.20d exemplifies

the thermohaline influence on silica solubility. The plume is now more dispersed and solute concentrations in the far field are low, causing less silica precipitation. Therefore, silica precipitation only insignificantly lowers hydraulic conductivity (Figure 6.20e).

The second trial, *fm_dens*, simulates variable-density flow but ignores chemical reactions. Time step sizes are prescribed and gradually increase from 1 minute to 2 hours. Figure 6.21 shows the concentration profile of the non-reactive, non-sorptive chloride ion at 1, 2 and 3 days. Figure 6.22d suggests that the fluid density in the far field of the source is smaller than in the previous example in porous media (Section 6.4) due to the more dispersed plume. As a consequence, density contrasts in the far field are generally small and in the range of 10^{-4}. Therefore, the buoyancy effect in the fractures (Equation 3.9) is minor and does not significantly change fracture velocities. Figure 6.21 demonstrates that, in this case, the fractures do not act like preferential pathways as was shown in the examples presented in Sections 6.1, 6.2 and 6.3. In those examples and in the studies done by Shikaze et al. (1998), the relative density has values up to 0.2, more than three orders of magnitude greater than those encountered here.

The last *fm_reac_dens* experiment simulates variable-density flow in combination with chemical reactions using adaptive time stepping as in *fm_reac*. Figure 6.23 shows that silica concentrations in the far field are smaller than in the *pm_reac_dens* example in porous media. This corresponds to the silica solubility-lowering effect of dissolved salt. The dissolved ions are now distributed over a larger cross-sectional area with smaller salt concentrations (Figures 6.24a and 6.24b) than before (Figures 6.19a and 6.19b). Aperture changes are insignificant on the temporal scale regarded in this example, and are not shown.

The CPU times are typically greater than in the *pm* simulations because fractures are present (Table 6.4). It is again shown that adaptive time stepping is a helpful means to accelerate and control the simulation process.

The simulations run in porous and fracture media show that the developed model is a reliable and stable model to numerically simulate variable-density flow and reactive transport in fractured porous media.

Table 6.4: Simulations and CPU times in fractured porous media (fm).

Simulation	Chemical reactions	Density variations	Time stepping	CPU time*
fm_reac	$\surd$	–	adaptive	36 min
fm_dens	–	$\surd$	prescribed	1 h 32 min
fm_reac_dens	$\surd$	$\surd$	adaptive	1 h 48 min

* Computed on a Pentium 4, 2.6 GHz, 500 MB RAM.

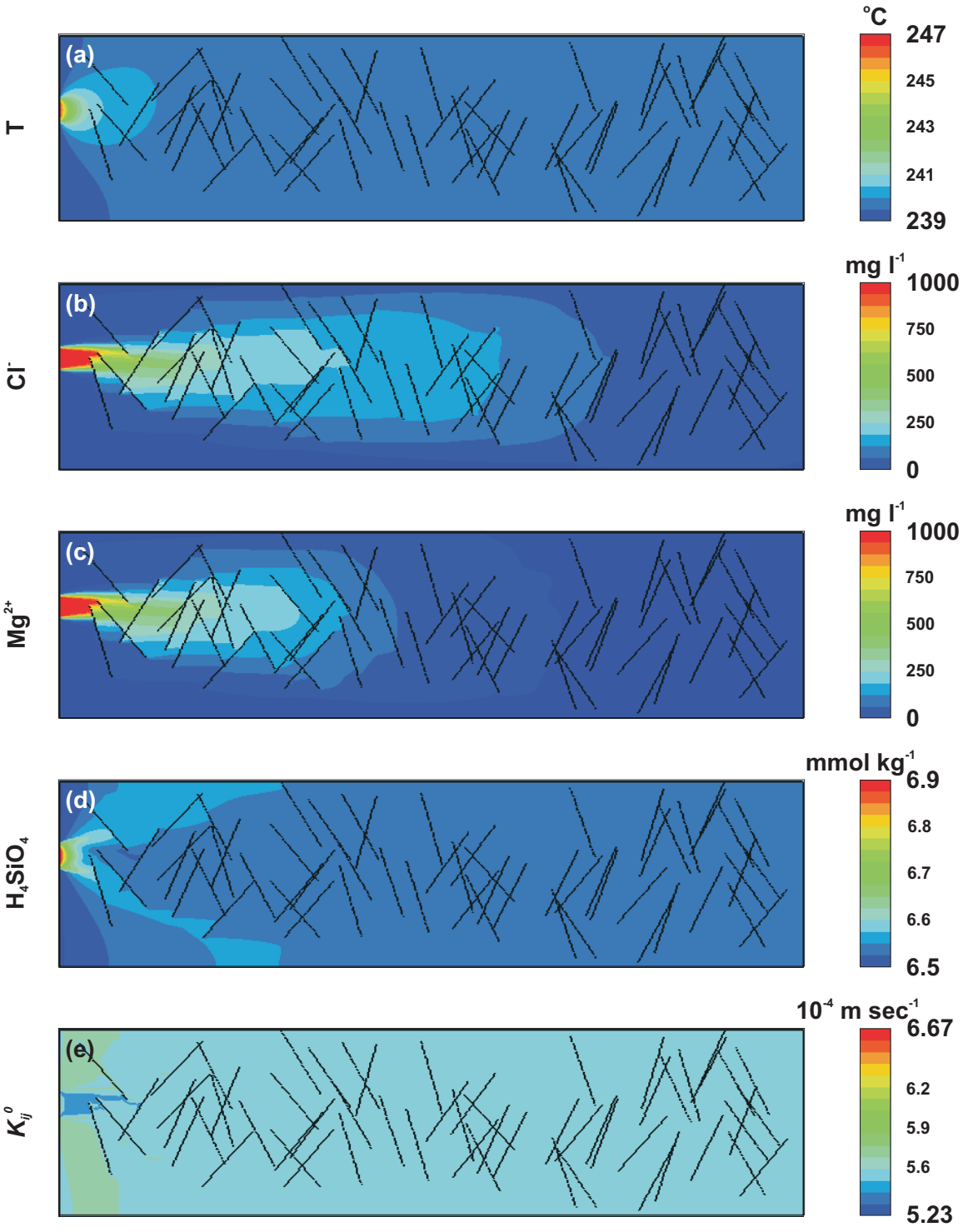

Figure 6.20: Results of non-density dependent reactive transport simulations in fractured media (*fm_reac*) at 3 days. Shown are (a) temperature, (b) chloride and (c) magnesium ion concentration, (d) molal concentration of aqueous silica and (e) freshwater hydraulic conductivity.

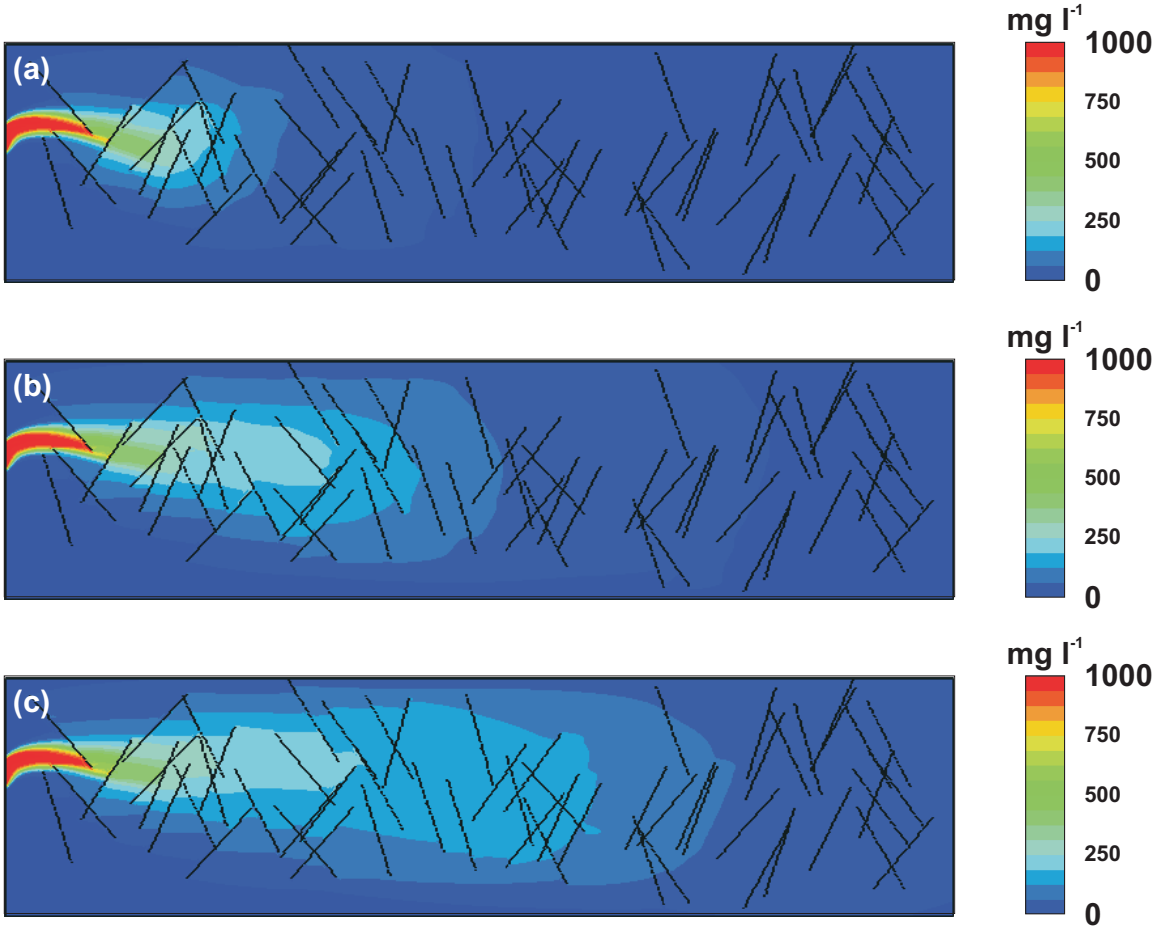

Figure 6.21: Results of density dependent non-reactive transport simulations in fractured media (*fm_dens*). Shown is the chloride ion concentration at different simulation times: (a) 1 day, (b) 2 days and (c) 3 days.

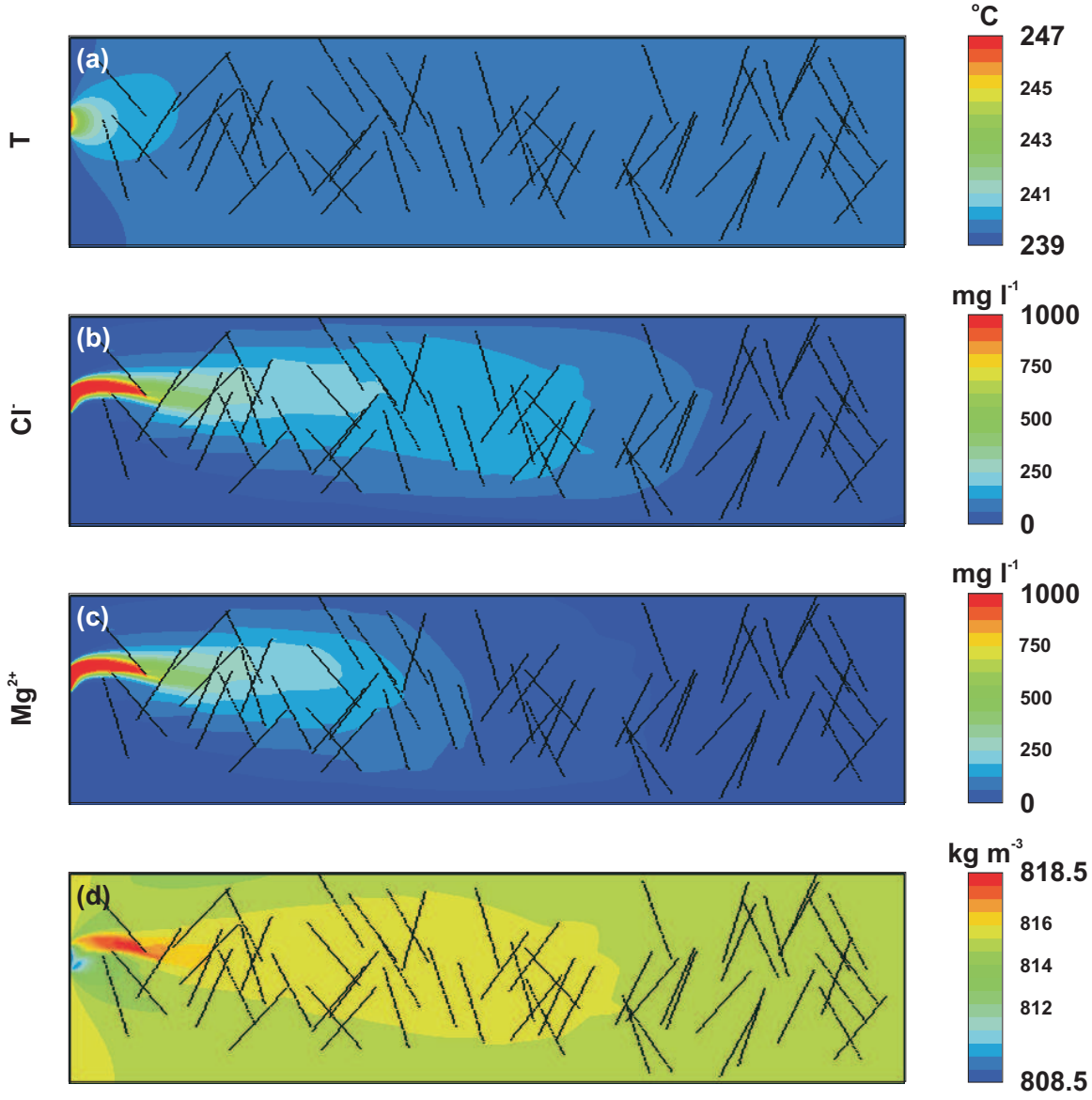

Figure 6.22: Results of density dependent non-reactive transport simulations in fractured media (*fm_dens*) at 3 days. Shown are (a) temperature, (b) chloride and (c) magnesium ion concentration and (d) fluid density.

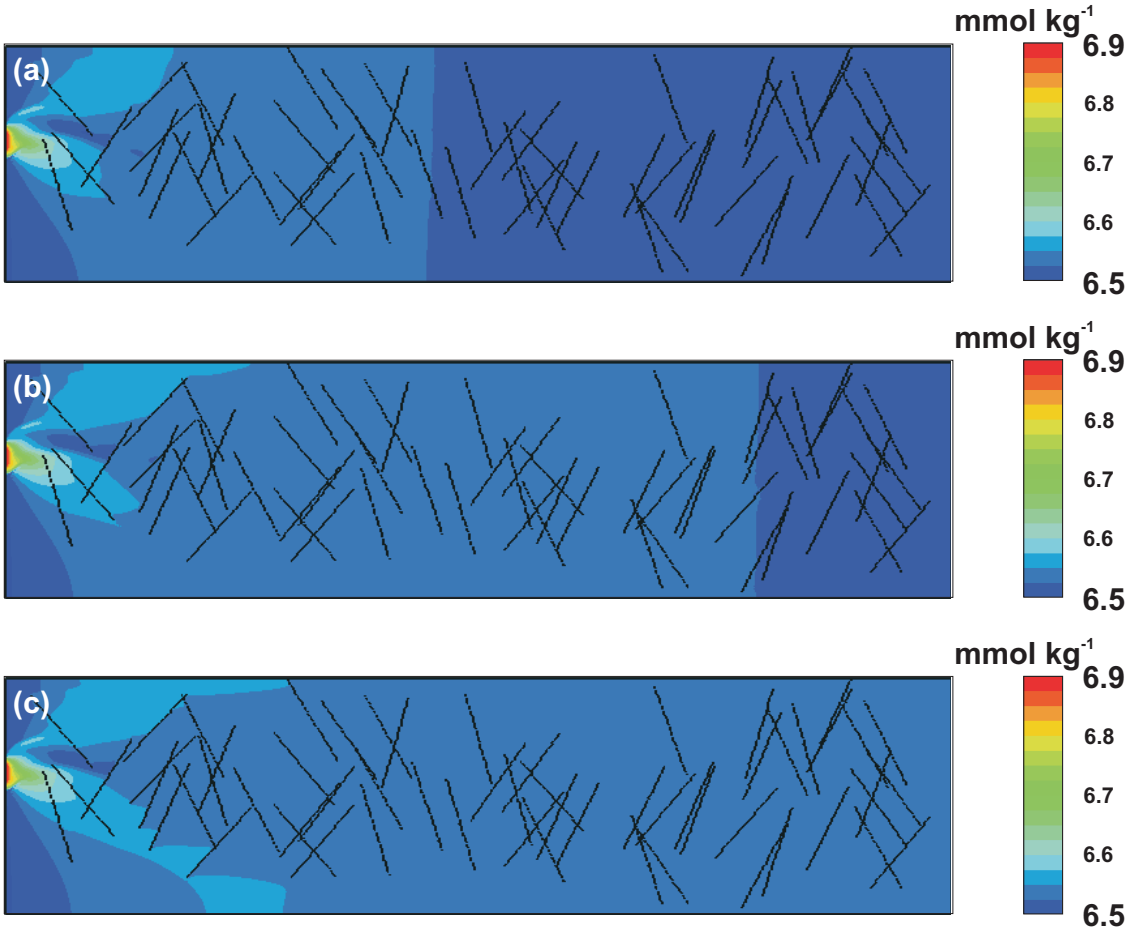

Figure 6.23: Results of density dependent reactive transport simulations in fractured media (*fm_reac_dens*). Shown is the molal concentration of aqueous silica at different simulation times: (a) 1 day, (b) 2 days and (c) 3 days.

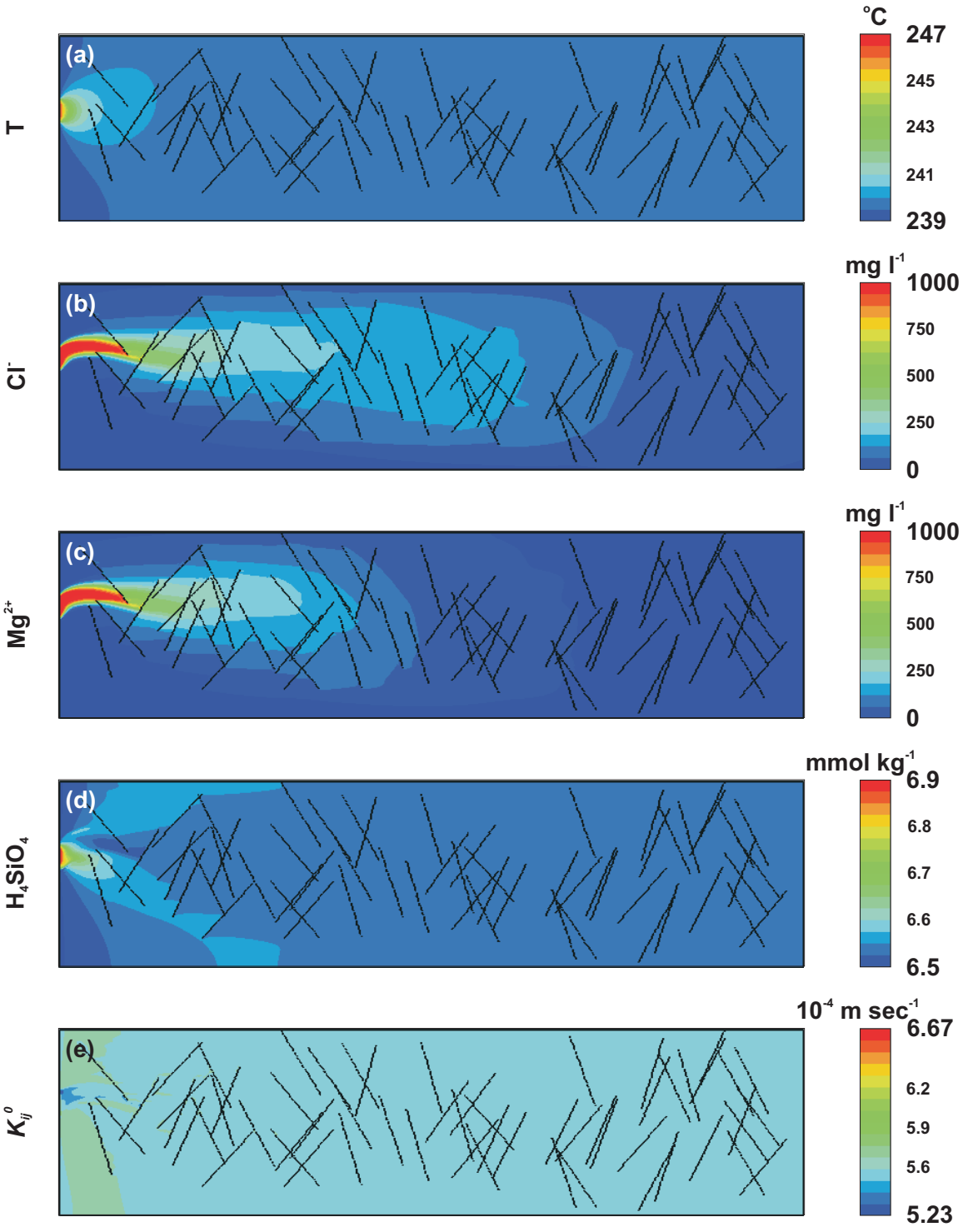

Figure 6.24: Results of density dependent reactive transport simulations in fractured media (*fm_reac_dens*) at 3 days. Shown are (a) temperature, (b) chloride and (c) magnesium ion concentration, (d) molal concentration of aqueous silica and (e) freshwater hydraulic conductivity.

Chapter 7

Sensitivity Analysis

The developed model was applied to assess the impact of parameter uncertainties on variable-density flow (Section 7.1) and reactive solute transport (Section 7.2). In both cases, a base case simulation was defined, where unmodified parameter values were used. Starting with the base case, two simulations were run for every parameter tested, using a lower and a higher parameter value.

All simulations were characterized with a dependent variable that appropriately represents the simulation. If this quantity is named ξ, the terms ξ^{low}, ξ^{org} and ξ^{high} denote the results obtained when simulating with a low, unmodified and high value of parameter π: π^{low}, π^{org} and π^{high}, respectively. A dimensionless sensitivity of the model parameter π, X_π, is evaluated using an equation presented by Zheng and Bennett (2002):

$$X_\pi = \frac{\partial \xi / \xi^{org}}{\partial \pi / \pi^{org}} \tag{7.1}$$

According to Zheng and Bennett (2002), the partial derivative of the dependent variable, ξ, with respect to the input parameter, π, can be normalized by the original value of the variable, ξ^{org}, and the parameter, π^{org}.

The choice of the range over which the input parameter is varied, is subjective. However, if parameter changes (i.e. perturbations) are too small, computer round-off errors may conceal differences of the dependent variable. On the other hand, pertur-

bations which are too large may yield inaccurate sensitivities, especially if the relation between dependent variable and parameter is nonlinear. In the present mathematical sensitivity analysis, a uniform perturbation size of 5% is applied as suggested by Zheng and Bennett (2002). In order to visualize parameter sensitivity, further simulations were carried out with much wider ranges of the input parameters. These second perturbations are not identical for all parameters and are not used in a mathematical sense but only for visualization purpose.

7.1 Variable-Density Flow

A first series of eight simulations of variable-density flow in a complex fracture network was carried out. The fracture network shown in Figure 6.8a was chosen because it allows the behavior of the network as a whole to be examined, rather than the behavior of few individual fractures that dominate the system as shown in Figure 6.8c. Figure 6.9a shows the base case scenario. It is assumed that the penetration depth of the 30% contour at 4 years adequately characterizes this simulation and is used as the dependent variable, ξ. The sensitivity of the matrix permeability, matrix porosity, fracture aperture and free-solution diffusion coefficient was analyzed by lowering and increasing original values given in Table 7.1 by uniform 5%. Figure 7.1 shows the calculated sensitivities for each input parameter

Table 7.1: Model parameter modifications used for visualization only in the sensitivity analysis of variable-density flow.

Parameter	Low value	Original value	High value
Free-solution diffusion coefficient (D_d)	5×10^{-10} m^2 sec^{-1}	5×10^{-9} m^2 sec^{-1}	5×10^{-8} m^2 sec^{-1}
Fracture aperture[a] ($2b$)	50 ... 150 μm	150 ... 250 μm	250 ... 350 μm
Matrix permeability (κ_{ij})	5×10^{-16} m^2	1×10^{-15} m^2	2×10^{-15} m^2
Matrix porosity (ϕ)	0.25	0.35	0.45

[a] Exponentially distributed

A second series of eight simulations was run for visualization purpose, where much larger parameter perturbations were used as shown in Table 7.1. The fracture apertures are distributed exponentially as described in Section 2.1. The result of this visual

sensitivity test of variable-density flow in a complex fracture network is shown in Figure 7.2. Note that the output time is now 3 years.

The free-solution diffusion coefficient explicitly impacts diffusion rate. Diffusion only implicitly affects flow velocities and convection rates by mixing. If diffusion is high, enhanced diffusive mixing reduces plume instability. However, diffusion has no explicit influence on velocities and convection. Therefore, its sensitivity was found to be relatively minor. The simulations further indicate that a high diffusion coefficient leads to high diffusion from the fractures into the adjacent porous matrix, often termed "loss of tracer". Therefore, the fractures are depleted in solutes resulting in less efficient buoyancy within the fractures. Conversely, a low diffusion coefficient leads to less matrix diffusion and, thus, the concentration gradients as well as the concentrations in the fractures remain high, resulting in high diffusive as well as buoyancy-driven transport within the fractures. Thus, solutes migrate further into the porous matrix in the high diffusion case but deeper into the aquifer in the low diffusion case (Figure 7.2a).

Convection is an important mechanism controlling variable-density flow in fractured porous media. Therefore, the system is sensitive to fracture aperture and matrix permeability, both affecting the flow velocity in convection cells. The dependency of fracture flow velocity on aperture is quadratic and, thus, stronger than the linear relationship between matrix flow velocity and matrix permeability. In the example, however, the volume fraction of the fractures is much smaller than that of the porous matrix. Consequently, inaccuracies of the fracture aperture (sensitivity of 0.98) are less severe than erroneous matrix permeability (sensitivity of 2.13).

According to the Cubic Law, the discharge in fractures changes with the cube of the fracture aperture. Therefore, uncertainties in aperture size have a major impact on the result, with large apertures promoting instability because of higher convection rates (Figure 7.2b).

Increased matrix permeability destabilizes the system because of higher computed Darcy fluxes in the matrix (Equations (3.6) and (3.7)). Section 6.1 illustrates that variable-density flow rates in fractures are controlled by convection in the porous matrix. It was also shown in Figure 6.1 that such a convection cell includes both the fracture

and the porous matrix with fluid moving upwards in the matrix and downwards in the fracture. As a consequence, rapid upwards flow in the matrix enables rapid downwards flow in the fracture. Thus, the magnitude of the groundwater velocities in the porous matrix controls the transport rate in fractures with greater matrix permeability leading to higher transport rates in fractures (Figure 7.2c).

The impact of matrix porosity changes on variable-density transport was found to be similar to the case where the fluid density is constant. The latter has been investigated by Sudicky and McLaren (1992), who showed that in discretely-fractured porous formations, the bulk travel distance is inversely proportional to porosity. This trend could be confirmed with the presented variable-density flow simulations. In the base case scenario, the 30% penetration depth after 4 years is 6.1 m. If porosity is increased by 5%, this depth is 5.5 m, giving a ratio of 1.11. This value is close to the inverse porosity ratio, $0.3675/0.35 = 1.05$. Thus, decreasing the porosity results in more rapid solute migration within fractures. This last statement holds for both the constant-density case (Sudicky and McLaren, 1992) as well as for variable-density flow (Figure 7.2d). Matrix porosity affects both transport mechanisms, hydrodynamic dispersion and advective transport. The average flow velocity is calculated as $v_i = q_i/\phi$, thus, a smaller porosity results not only in less attenuation of the plume (Sudicky and McLaren, 1992), but also in greater advective transport. The high sensitivity of the matrix porosity, evaluated as -3.28, expresses its twofold control on dense plume transport.

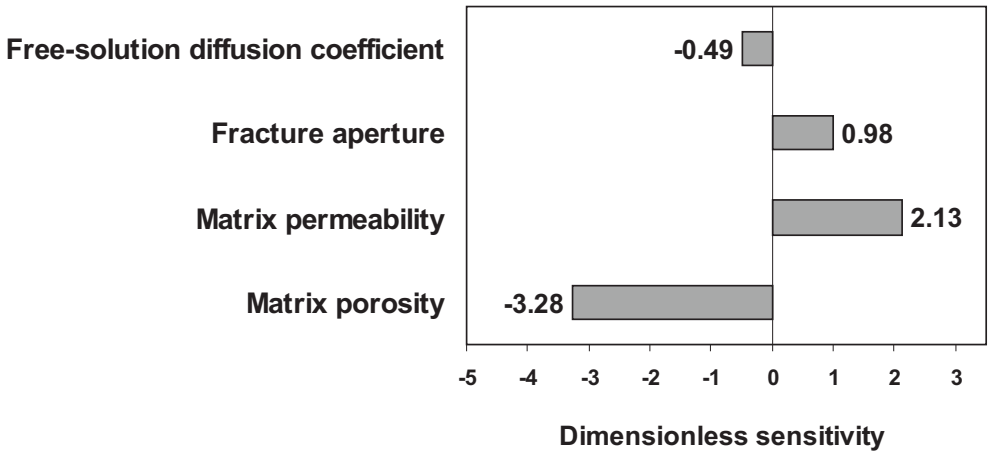

Figure 7.1: Dimensionless sensitivity of model parameters in variable-density flow simulations in order from least (top) to most (bottom) sensitive.

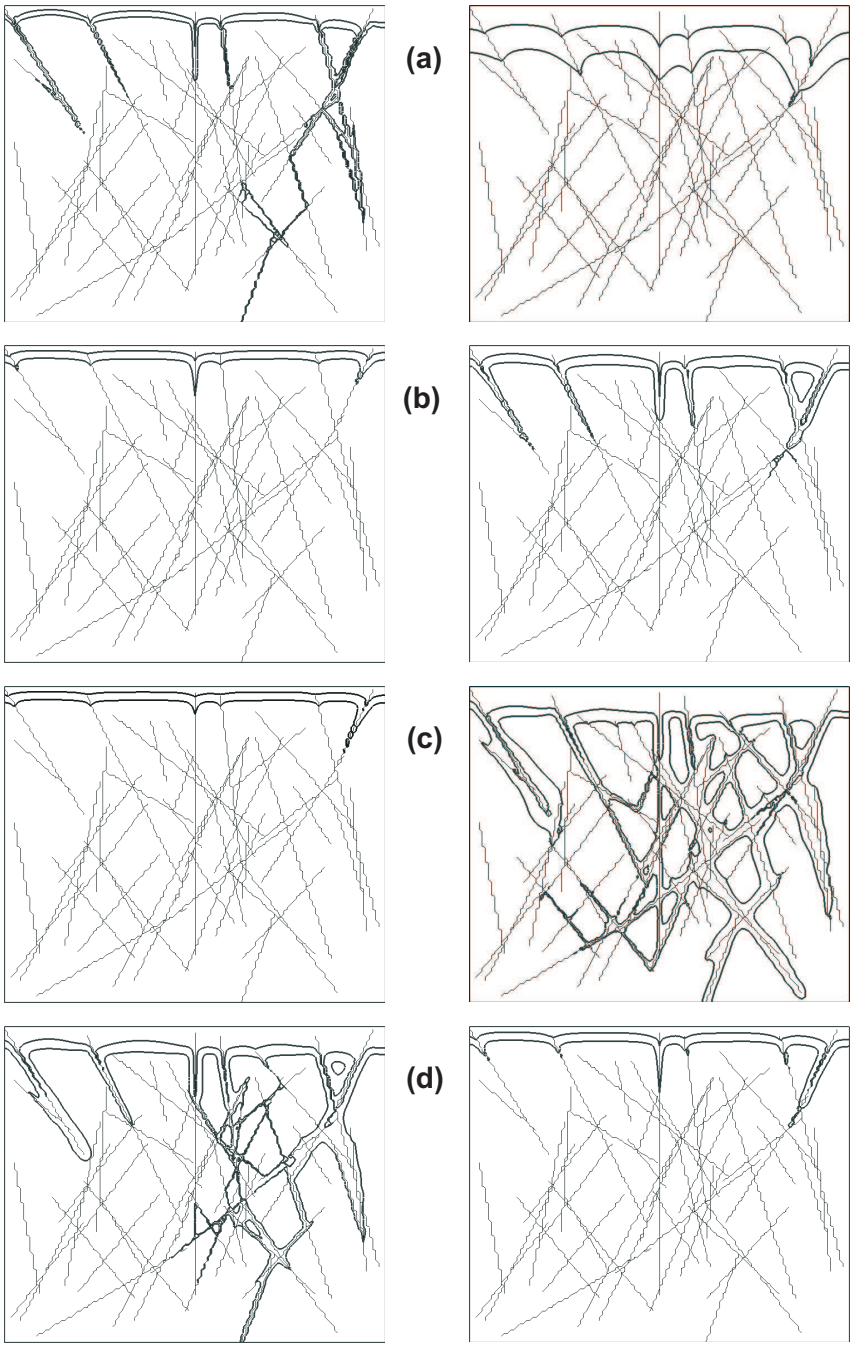

Figure 7.2: Visual sensitivity of input parameters at 3 years. Shown are the concentration contours 20% and 60% for lower (left) and higher (right) values of the following parameters: (a) free-solution diffusion coefficient, (b) fracture aperture, (c) matrix permeability and (d) matrix porosity.

7.2 Reactive Solute Transport

The base case scenario simulates reactive transport in a single fracture embedded in a porous matrix as presented by Steefel and Lichtner (1998a). This simulation has been described before in Section 5.2 and was used as a verification example (Figure 5.16).

The steady state silica concentration at the fracture outlet ($z = 3.1$ cm) was chosen as the dependent variable, ξ. The simulation of the base case scenario with unmodified parameter values yields the characteristic number $\xi^{org} = 3.5887\times10^{-3}$ mol kg^{-1}. The reactive transport simulation was run with modified values of the specific quartz surface area in the fracture and matrix, quartz volume fraction and temperature. The original value of each input parameter, shown in Table 7.2, was lowered and increased by uniform 5%. Figure 7.3 presents the calculated dimensionless sensitivity for each input parameter.

Table 7.2: Model parameter modifications used for visualization only in the sensitivity analysis of reactive solute transport.

Parameter	Low value	Original value	High value
Specific quartz surface area in the fracture (A_{qz}^{fr})	1.15 m^2 kg^{-1}	6.15 m^2 kg^{-1}	11.15 m^2 kg^{-1}
Specific quartz surface area in the matrix (A_{qz})	34.2 m^2 kg^{-1}	54.2 m^2 kg^{-1}	74.2 m^2 kg^{-1}
Quartz volume fraction (ϕ_{qz})	0.6	1.0	1.0
Temperature (T_C)	209°C	239°C	269°C

A second set of simulations was run for visualization purpose, where much larger parameter perturbations were used as indicated in Table 7.2. The result of this visual sensitivity analysis is shown in Figure 7.4.

The simulations show that the uncertainties of the fracture surface area have a negligible impact on the results (Figure 7.4a), expressed by the low sensitivity of 0.01. However, the fracture surface area is about one order of magnitude smaller than in the matrix. Consequently, the fracture reaction rate is also one order of magnitude slower. Therefore, the fast reaction in the matrix is dominant and suppresses unprecise fracture reaction rates.

Both the surface area in the matrix and the quartz volume fraction are directly proportional to the reaction rate (Equations (2.8) and (2.9)). Thus, the sensitivity of the two parameters is similar (Figure 7.4b and c). However, uncertainties of the quartz volume fraction also impact the fracture reaction rate, which may cause the slightly higher sensitivity (0.34) than that of the matrix surface area (0.32).

Temperature variations have the most significant influence on the results (Figure 7.4d). If, for example, the ambient temperature increases, the dissolution reactions proceed faster (relation (2.10)) and, in addition, more quartz dissolves (relation (2.20)). Both geochemical processes considerably increase the net reaction rate (Figure D.1), resulting in the high sensitivity of temperature with a value of 4.28.

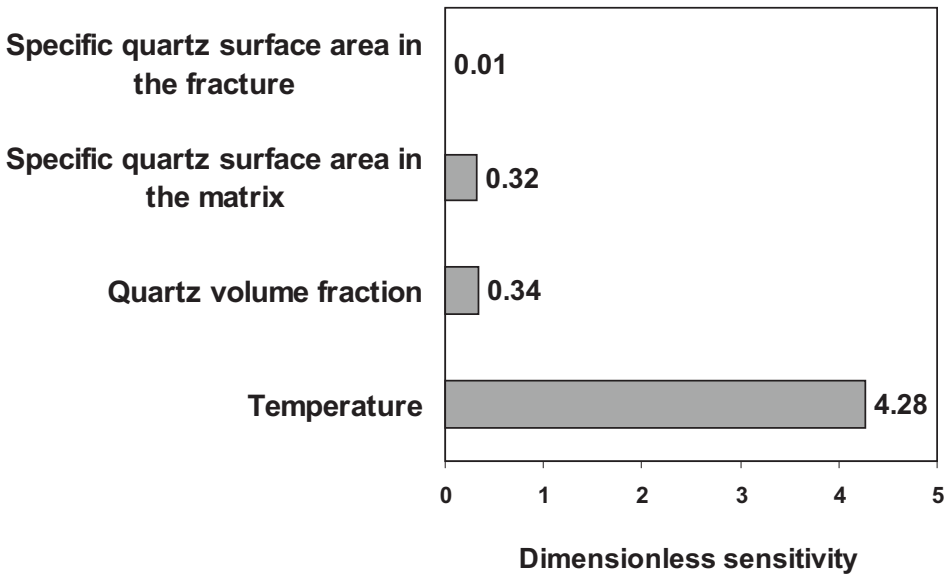

Figure 7.3: Dimensionless sensitivity of model parameters in reactive solute transport simulations in order from least (top) to most (bottom) sensitive.

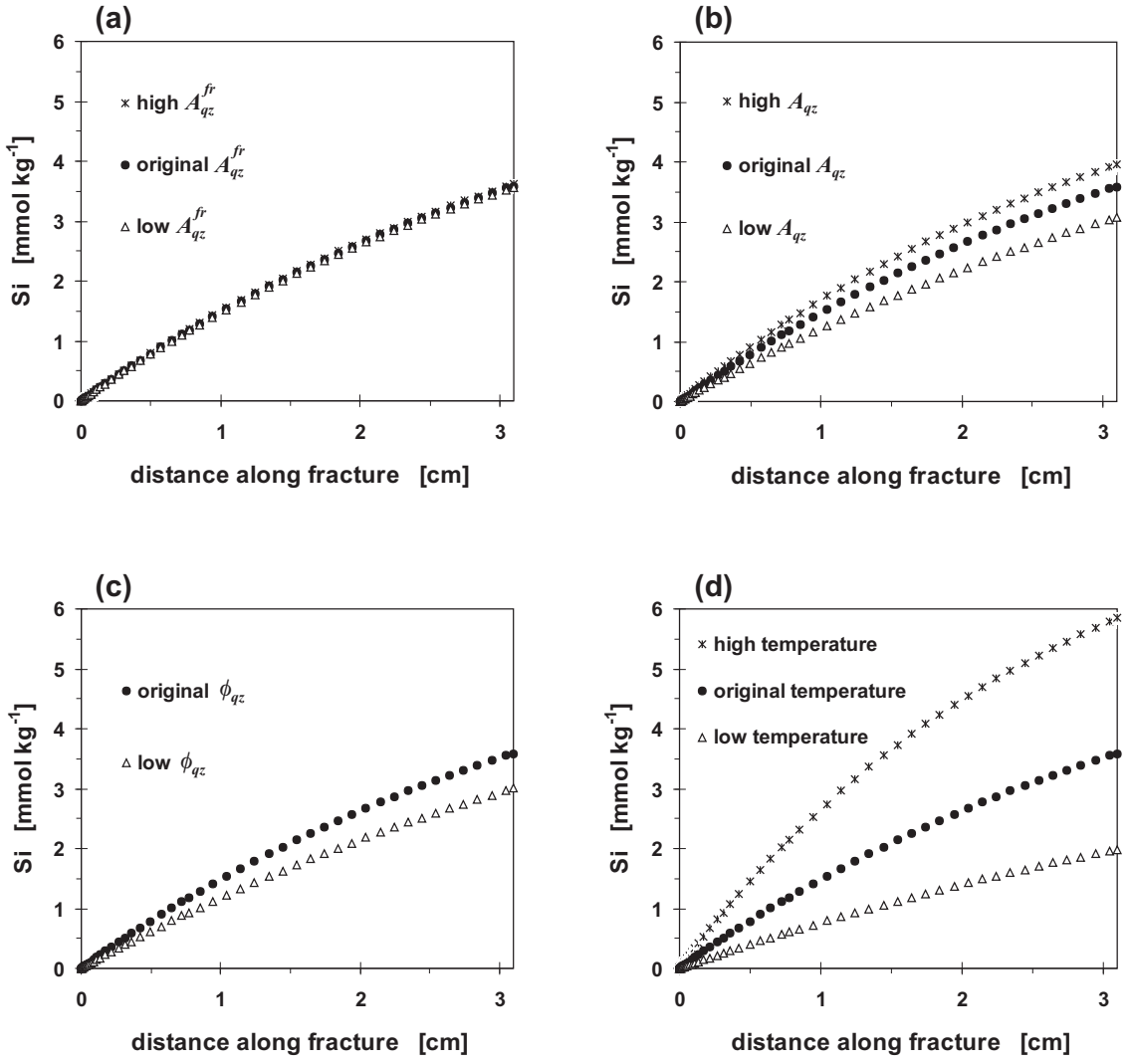

Figure 7.4: Visual sensitivity input parameters at steady state. Shown is the steady state quartz concentration in the fracture if the following parameters are uncertain: (a) specific quartz surface area in the fracture and (b) in the matrix, (c) quartz volume fraction and (d) temperature.

Chapter 8

Conclusions

The primary goal of this work was to develop a numerical model, capable of simulating coupled variable-density, variable-viscosity flow and kinetically controlled reactive transport in fractured porous media.

The newly developed model is unique in its formulation. Unlike previous models, this model allows variable-density flow to be simulated in realistic fracture networks. In addition, it is the first model that couples thermohaline groundwater flow with reactive transport and with changes of flow/transport parameters in fractured porous media with the exception of specific storage. The model focuses on the chemistry of the common quartz-water system with aqueous silica as the only mobile reactive species. Flow is linked with heat transfer and solute transport through an iterative Picard approach. After each iteration, the fluid properties density and viscosity are updated using the primary variables ion concentration and temperature. Chemical reactions are calculated outside the Picard Iteration because the reactive species silica does not significantly impact the fluid properties. According to the quasi-stationary state approximation (Lichtner, 1988), flow and reactive transport parameters are also updated at the end of a time step. An adaptive time stepping is used to further enhance the efficiency of the model. New time increments depend on maximum changes in matrix porosity and/or fracture aperture. This robust, dynamic time marching scheme is very useful to accelerate and slow down the simulation to prevent physically unrealistic changes of porosity and/or aperture.

New Insights from Model Applications

Although the main objective of the research was to increase modeling capabilities, the model was also used to simulate a number of illustrative examples, demonstrating the capacities of the new model. All examples were run in a vertical two-dimensional domain consisting of one layer of 3D porous matrix blocks. In this vertical slice, fractures are described by 2D faces, which is essentially a 1D representation of fractures. This constraint in spatial dimensionality implies that all following statements (except item [2]) neglect convection within fractures. In summary, the simulations indicate that

[1] In addition to previous variable-density flow studies including vertical fractures (Murphy, 1979; Malkovsky and Pek, 1997; 2004; Shikaze et al., 1998), inclined fractures were shown to trigger unstable variable-density flow.

[2] The analytically derived critical Rayleigh number for different aspect rations (Caltagirone, 1982) was shown to be a useful test case for the onset of convection in vertical and inclined discrete fractures.

[3] Variable-density flow in an inclined fracture causes free convective flow in the surrounding porous matrix.

[4] In an orthogonal network of large and small fractures, fractures smaller than 10 μm have no impact on the established convective pattern in large fractures of aperture equal to 50 μm. Small fractures do not stabilize vertical plume migration by enhanced dispersive mixing.

[5] Convective flow in irregular, yet statistically equivalent networks proved to be highly sensitive to the geometry of the network. Thus, unknown fracture interconnectivity can be a limiting factor of reliable numerical simulations.

[6] If fractures of a random network are connected equidistantly to the contaminant source, few equidistantly distributed fractures enable rapid downward transport of contaminants. On the other hand, numerous fractures have a stabilizing effect.

[7] Convection cells in complex fracture networks include both the porous matrix and fractures. Their transport rates, thus, depend on matrix and fracture flow properties.

[8] Variable-density flow tends to be unstable for high matrix permeability, low matrix porosity and large fracture apertures. In all three cases, flow velocities become large, leading to strong convection. This finding supports the previous statement.

[9] Large diffusion rates even out plume migration in complex fracture networks by matrix diffusion.

[10] Double-diffusive reactive transport in fractured media impacts both buoyancy-driven flow and chemical reactions.

[11] The silica concentration is inversely proportional to salinity in high-salinity regions and directly proportional to temperature in low-salinity regions.

[12] The reactive system studied is the most sensitive to temperature inaccuracy. This is because temperature impacts both the dissolution kinetics (Arrhenius equation) and the quartz solubility.

New Research Capacities

This new model lays the foundation for further numerical studies of a variety of topics that could not be simulated before.

Prior studies of convection in discretely fractured media have represented the fractures by one-dimensional segments (Shikaze et al., 1998), inhibiting convection within the fracture. The developed model can be used to extend studies into the second and third dimension. With little effort, 2D convection with a rotation axis normal to the fracture can be examined. Such simulations can help understand the fracture-matrix interaction and how matrix diffusion will dissipate or enhance convection in the fracture. To date, these processes are not at all clear. However, numerically speaking, a 2D representation of fractures does not allow convection cells to form parallel to the fracture plane. Studying convection where the rotation axis is parallel to the fracture could prove challenging. It must first be clarified how several node layers represent a single discrete fracture, followed by a thorough 3D analysis. Other questions that the new model can answer are: What is the role of spatial discretization on plume migration in a single fracture? How does spatial discretization influence matrix diffusion

and, thus, convection in a fracture? Can analytically derived onset criteria for convection be applied to fractured porous media, where matrix permeability and porosity are nonzero?

The model can also be used to study the onset as well as the subsequent development of instabilities in a fracture network, without being limited to only vertical and horizontal fractures. To date, the role of network characteristics, such as fracture density and interconnectivity, as trigger mechanisms is still unclear. Past studies of density-driven flow in fractured materials (Shikaze et al., 1998) were mostly descriptive; a quantitative interpretation of convection must follow. One future challenge is definitely to quantify the onset of convection in regular and complex fracture networks and to eventually derive a modified Rayleigh number that includes network features.

Double diffusive convection (DDC) in fractured media is yet another process that is barely understood. In the past, this was mostly due to the lack of a model that simulates thermohaline effects in fractures. Especially in deep waste repositories where groundwater is a hot brine, the typical layering of fluid convection may form in a complicated fashion. To date, it is completely unknown if these layers are stable in space and time as is the case in porous media and how the fracture network controls the shape and thickness of convection layers. Similar to fractures, DDC in open wells is commonly ignored. However, this assumption has not yet been justified with the help of numerical simulation techniques.

This study shows that free convection in fractured porous media is a fast process, relative to kinetic chemical reactions. In the examples presented in Sections 6.4 and 6.5, unstable flow develops first, creating local thermodynamic disequilibriums that trigger reactions. However, at Rayleigh numbers that are only slightly larger than the required critical Rayleigh number, unstable flow may be slow enough to proceed at the same time scale as the chemical reaction. Such a scenario of simultaneously occurring convection and reaction has the potential for fascinating and worthwhile studies.

Similar to prior reactive transport models, this model applies to a specific chemical system. Additional model modifications will certainly enable studying other chemistries and, thus, broaden the spectrum of possible applications. With some further model

development, any reversible reaction of the form

$$X_{(s)} + H_2O_{(aq)} \rightleftharpoons H_2XO_{(aq)} \tag{8.1}$$

could be simulated where $X_{(s)}$ is any solid mineral with its aqueous form $H_2XO_{(aq)}$. Furthermore, it would easily be possible to model any irreversible reaction (e.g. only dissolution) of the form

$$X_{(s)} + H_2O_{(aq)} \rightarrow H_2XO_{(aq)} \tag{8.2}$$

or only precipitation described by

$$X_{(s)} + H_2O_{(aq)} \leftarrow H_2XO_{(aq)} \tag{8.3}$$

From Conceptual 2D Results to Reliable 3D Predictions

The presented results of thermohaline flow and reactive transport simulations are numerically stable and obtained from the developed and fully verified model. However, the model has not been validated because appropriate field data are currently lacking. The used model input is mostly fictive and contains some uncertainties. For example, exact fracture locations and fracture interconnectivity are hard to measure in the field but were shown to have a crucial impact on plume migration. Another classical uncertainty is the mineral surface area in the matrix and especially in the fracture. The fracture roughness is difficult to determine, such that prior studies have commonly assumed perfectly smooth fracture surfaces for simplicity. As a consequence of highly uncertain model input, the presented 2D results thus far only allow an analysis and interpretation in a conceptual way.

The necessary step from obtaining conceptual 2D results to making reliable 3D long-term predictions will involve an iterative cycle of further model development - sensitivity analysis - data gathering - numerical modeling - model development as proposed by Glynn and Plummer (2005). Realizing this cycle, however, is highly challenging because "there are relatively few studies that have used 3-D geochemical transport codes" (Glynn and Plummer, 2005). Prior research that would help complete the cycle described above is rare and it remains greatly demanding to simulate a complex 3D thermohaline flow - reactive transport feedback scenario in a numerically stable fashion.

The complexity of nature and the need to find secure deep repositories for hazardous waste are the reasons why exploring the coupled system of thermohaline flow and reactive transport "will be an area of ongoing research" (Post, 2005). The model developed here was shown to be a very useful tool that can advance this future research.

References

[1] Bear J, 1988. Dynamics of fluids in porous media. New York, NY, USA: *Elsevier*; 764 pp.

[2] Bear J and Verruijt A, 1987. Modeling groundwater flow and pollution. Dordrecht, Netherlands: *Reidel Publishing Company*; 414 pp.

[3] Beck JL, 1972. Convection in a box of porous material saturated with fluid. *Physics of Fluids* **15**: 1377-1383.

[4] Bénard H, 1900. Les tourbillons cellulaires dans une nappe liquide. *Revue Générale des Sciences Pures et Appliquées* **11**: 1261-1271, 1309-1328.

[5] Bennett PC, 1991. Quartz dissolution in organic-rich aqueous systems. *Geochimica et Cosmochimica Acta* **55**: 1781-1797.

[6] Bennett PC, Melcer ME, Siegel DI and Hassett JP, 1988. The dissolution of quartz in dilute aqueous solutions of organic acids at 25°C. *Geochimica et Cosmochimica Acta* **52**: 1521-1530.

[7] Berkowitz B, Bear J and Braester C, 1988. Continuum models for contaminant transport in fractured porous formations. *Water Resources Research* **24** (8): 1225-1236.

[8] Blum A and Lasaga AC, 1988. Role of surface speciation in the low-temperature dissolution of minerals. *Nature* **331**: 431-433.

[9] Bolton EW, Lasaga AC and Rye DM, 1996. A model for the kinetic control of quartz dissolution and precipitation in porous media flow with spatially vari-

able permeability: Formulation and examples of thermal convection. *Journal of Geophysical Research* **101** (B10): 22157-22187.

[10] Bories SA and Combarnous MA, 1973. Natural free convection in a sloping porous layer. *Journal of Fluid Mechanics* **57**, part 1: 63-79.

[11] Boussinesq VJ, 1903. Théorie analytique de la chaleur. Paris, France: *Gauthier-Villars* vol. 2. [2.3].

[12] Brady PV and Walther JV, 1989. Controls on silicate dissolution rates in neutral and basic pH solutions at 25°C. *Geochimica et Cosmochimica Acta* **53**: 2823-2830.

[13] Brandt A and Fernando HJS, 1995. Double-diffusive convection. Washington, DC, USA: *American Geophysical Union*, Geophysical Monograph 94; 334 pp.

[14] Caltagirone JP, 1975. Thermoconvective instabilities in a horizontal porous layer. *Journal of Fluid Mechanics* **72**: 269-287.

[15] Caltagirone JP, 1982. Convection in a porous medium. In: Zierep J and Oertel H (editors). Convective transport and instability phenomena. Karlsruhe, Germany: *Braunsche Hofbuchdruckerei und Verlag*; 199-232 [chapter 1.3.2].

[16] Clift SS, D'Azevedo F, Forsyth PA and Knightly JR, 1996. WATSIT-1 and WATSIT-B Waterloo sparse iterative matrix solvers. User's guide with developer notes for version 2.0.0, (8): 40 pp.

[17] Cody WJ, 1964. Double-precision square root for the CDC-3600. Argonne, Il, USA: *Argonne National Laboratory* **7** (12): 715-718.

[18] Davis SH, 1967. Convection in a box: linear theory. *Journal of Fluid Mechanics* **30** (3): 465-478.

[19] Davison CC, Chan T and Brown A, 1994a. The disposal of Canada's nuclear fuel waste: site screening and site evaluation technology. Atomic Energy of Canada Limited research (AECL-10719). Pinawa, MB, Canada: *Whiteshell Laboratories*; 255 pp.

[20] Davison CC, Chan T and Brown A, 1994b. The disposal of Canada's nuclear fuel waste: the geosphere model for postclosure assessment. Atomic Energy of Canada

Limited research (AECL-10713). Pinawa, MB, Canada: *Whiteshell Laboratories*; 497 pp.

[21] Diersch H-JG and Kolditz O, 1998. Coupled groundwater flow and transport: 2. Thermohaline and 3D convection systems. *Advances in Water Resources* **21** (5): 401425.

[22] Diersch H-JG and Kolditz O, 2002. Variable-density flow and transport in porous media: approaches and challenges. *Advances in Water Resources* **25** (8-12): 899-944.

[23] Domenico PA and Schwartz FW, 1998. Physical and chemical hydrogeology. New York, NY, USA: *John Wiley & Sons, Inc.*; 506 pp.

[24] Dove PM, 1999. The dissolution kinetics of quartz in aqueous mixed cation solutions. *Geochimica et Cosmochimica Acta* **63** (22): 3715-3727.

[25] Dove PM and Crerar DA, 1990. Kinetics of quartz dissolution in electrolyte solutions using a hydrothermal mixed flow reactor. *Geochimica et Cosmochimica Acta* **54**: 955-969.

[26] Dove PM and Nix CJ, 1997. The influence of the alkaline earth cations, magnesium, calcium, and barium on the dissolution kinetics of quartz. *Geochimica et Cosmochimica Acta* **61** (16): 3329-3340.

[27] Elder JW, 1965. Laminar free convection in a vertical slot. *Journal of Fluid Mechanics* **23**: 77-98.

[28] Elder JW, 1966. Numerical experiments with free convection in a vertical slot. *Journal of Fluid Mechanics* **24** (4): 823-843.

[29] Elder JW, 1967. Transient convection in a porous medium. *Journal of Fluid Mechanics* **27** (3): 609-623.

[30] Evans GE and Nunn JA, 1989. Free thermohaline convection in sediments surrounding a salt column. *Journal of Geophysical Research* **94**: 2707-2716.

[31] Farvolden RN, Pfannkuch O, Pearson R and Fritz P, 1988. The Precambrian Shield. In: The Geological Society of America (editor). The Geology of North

America, Vol O-2, *Hydrogeology*, Chapter 15: 101-114.

[32] Fournier RO, 1983. A method of calculating quartz solubilities in aqueous sodium chloride solutions. *Geochimica et Cosmochimica Acta* **47**: 579-586.

[33] Freedman V and Ibaraki M, 2002. Effects of chemical reactions on density-dependent fluid flow: on the numerical formulation and the development of instabilities. *Advances in Water Resources* **25** (4): 439-453.

[34] Freedman V and Ibaraki M, 2003. Coupled reactive mass transport and fluid flow: Issues in model verification. *Advances in Water Resources* **26** (1): 117-127.

[35] Freeze RA and Cherry JA, 1979. Groundwater. Englewood Cliffs, NJ, USA: *Prentice Hall*; 604 pp.

[36] Frind EO, 1982. Simulation of long-term transient density-dependent transport in groundwater. *Advances in Water Resources* **5** (2): 73-88.

[37] Frolkovič P and De Schepper H, 2000. Numerical modeling of convection dominated transport coupled with density driven flow in porous media. *Advances in Water Resources* **24** (10): 63-72.

[38] Ganor J, Huston TJ and Walter LM, 2005. Quartz precipitation kinetics at 180°C in NaCl solutions implications for the usability of the principle of detailed balancing. *Geochimica et Cosmochimica Acta* **69** (8): 2043-2056.

[39] Geiger S, Haggerty R, Dilles JH, Reed MH and Matthäi SK, 2002. New insights from reactive transport modelling: the formation of the sericitic vein envelopes during early hydrothermal alteration at Butte, Montana. *Geofluids* **2**: 185-201.

[40] Ghogomu NF and Therrien R, 2000. Reactive mass transport modeling in discretely-fractured porous media. In: Bentley et al. (editors). Computational Methods in Water Resources XIII, Rotterdam, Netherlands; ISBN 90-5809-123-6; 285-292.

[41] Glynn PD and Plummer LN, 2005. Geochemistry and the understanding of ground-water systems. *Hydrogeology Journal* **13**: 263-287.

[42] Heisenberg W, 1927. Über den anschaulichen Inhalt der quantentheoretischen Kinematik und Mechanik. *Zeitschrift für Physik* **43**: 172-198.

[43] Holzbecher EO, 1998. Modeling density-driven flow in porous media. Berlin, Germany: *Springer Verlag*; 286 pp.

[44] Horton CW and Rogers Jr. FT, 1945. Convective currents in a porous medium. *Journal of Applied Physics* **16**: 367-370.

[45] Huyakorn PS, Andersen PF, Mercer JW and White Jr. HO, 1987. Saltwater intrusion in aquifers: development and testing of a three-dimensional finite element model. *Water Resources Research* **23** (2): 293-312.

[46] Ibaraki M, 1998. A robust and efficient numerical model for analyses of density-dependent flow in porous media. *Journal of Contaminant Hydrology* **34** (10): 235-246.

[47] Istok J, 1989. Groundwater modeling by the finite element method. Washington, DC, USA: *American Geophysical Union*; 495 pp.

[48] Johannsen K, Kinzelbach W, Oswald SE and Wittum G, 2002. The saltpool benchmark problem - numerical simulation of saltwater upconing in a porous medium. *Advances in Water Resources* **25** (3): 335-348.

[49] Johnson JW, Knauss KG, Glassley WE, DeLoach LD and Tompson AFB, 1998. Reactive transport modeling of plug-flow reactor experiments: quartz and tuff dissolution at 240°C. *Journal of Hydrology* **209** (10): 81-111.

[50] Kolditz O, Ratke R, Diersch H-JG and Zielke W, 1998. Coupled groundwater flow and transport: 1. Verification of variable-density flow and transport models. *Advances in Water Resources* **21** (1): 27-46.

[51] Krauskopf KB and Bird DK, 1995. Introduction to geochemistry. New York, NY, USA: *McGraw-Hill*; 647 pp.

[52] Kreith F, 1965. Principles of heat transfer. Scranton, PA, USA: *International Textbook Company*; 620 pp.

[53] Langmuir D, 1997. Aqueous environmental geochemistry. Upper Saddle River, NJ, USA: *Prentice Hall*; 600 pp.

[54] Lapwood ER, 1948. Convection of a fluid in a porous medium. *Proceedings of the Cambridge Philosophical Society* **48**: 508-521.

[55] Lasaga AC, 1984. Chemical kinetics of water-rock interactions. *Journal of Geophysical Research* **89** (B6): 4009-4025.

[56] Leijnse A and Oostrom M, 1994. The onset of instabilities in the numerical simulation of density-driven flow in porous media. In: Peters A et al. (editors). Computational Methods in Water Resources, **IX** (2), *Mathematical Modeling in Water Resources*. London, *Elsevier*: 273-280.

[57] Lichtner PC, 1988. The quasi-stationary state aproximation to coupled mass transport and fluid-rock interaction in a porous medium. *Geochimica et Cosmochimica Acta* **52**: 143-165.

[58] Malkovsky VI and Pek AA, 1997. Conditions for the onset of thermal convection of a homogeneous fluid in a vertical fault. *Petrology* **5** (4): 381-387.

[59] Malkovsky VI and Pek AA, 2004. Onset of thermal convection of a single-phase fluid in an open vertical fault. *Physics of the Solid Earth* **40** (8): 672-679.

[60] Marcus Y, 1985. Ion solvation. Chichester, Great Britain: *John Wiley & Sons, Ltd.*; 306 pp.

[61] Marshall WL and Chen TAC, 1982. Amorphous silica solubilities V. Predictions of solubility behavior in aqueous mixed electrolyte solutions to 300°C. *Geochimica et Cosmochimica Acta* **46** (2): 289-291.

[62] Mathab A, Xu S, Grasso P and Kendorski FS, 1995. Use of alternative distributions for characterizing joint extent and spacing. In: Myer, Cook, Goodman and Tsang (editors). Fractured and jointed rock masses, 199-204.

[63] Mayer KU, Frind EO and Blowes DW, 2002. Multicomponent reactive transport modeling in variably saturated porous media using a generalized formulation for kinetically controlled reactions. *Water Resources Research* **38** (9), 1174, DOI: 10.1029/2001WR000862.

[64] Meyer JR, 2004. Development of a heat transport analytical model for a single

fracture in a porous media. Unpublished project report of the course *Earth 661, Analytical Solutions in Hydrogeology* submitted to EA Sudicky and CJ Neville. *Waterloo Center for Groundwater Research*; 46 pp.

[65] Molson JWH, Frind EO and Palmer C, 1992. Thermal energy storage in an unconfined aquifer 2: Model development, validation and application. *Water Resources Research* **28** (10): 2857-2867.

[66] Monnin C, 1989. An ion interaction model for the volumetric properties of natural waters: Density of the solution and partial molal volumes of electrolytes to high concentrations at 25°C. *Geochimica et Cosmochimica Acta* **53**: 1177-1188.

[67] Monnin C, 1994. Density calculation and concentration scale conversions for natural waters. *Computers and Geosciences* **20** (10): 1435-1445.

[68] Mroczek EK and Christenson B, 2000. Solubility of quartz in hypersaline brine - implication for fracture permeability at the brittle-ductile transition. *Proceedings World Geothermal Congress*, Kyushu-Tohoku, Japan: 1459-1462.

[69] Murphy HD, 1979. Convective instabilities in vertical fractures and faults. *Journal of Geophysical Research* **84** (B11): 6121-6130.

[70] Nield DA and Bejan A, 1999. Convection in porous media. New York, NY, USA: *Springer Verlag*; 546 pp.

[71] Nusselt W, 1944. Technische Thermodynamik II (Theorie der Wärmekraftmaschinen). *Sammlung Göschen* **1151**: 144 pp.

[72] Oberbeck A, 1879. Ueber die Wärmeleitung der Flüssigkeiten bei Berücksichtigung der Strömung infolge von Temperaturdifferenzen. *Annalen der Physik und Chemie* **7**: 271-292.

[73] Ogata A and Banks RB, 1961. A solution of the differential equation of longitudinal dispersion in porous media. *US Geological Survey*, Technical Report **411-A**, Professional Paper.

[74] Oldenburg CM and Pruess K, 1998. Layered thermohaline convection in hypersaline geothermal systems. *Transport in Porous Media* **33**: 29-63.

[75] Oswald SE, 1999. Dichteströmungen in porösen Medien: Dreidimensionale Experimente und Modellierung. Ph.D. Thesis, Institut für Hydromechanik und Wasserwirtschaft, ETH Zürich, Switzerland; 112 pp.

[76] Oswald SE and Kinzelbach W, 2004. Three-dimensional physical benchmark experiments to test variable-density flow models. *Journal of Hydrology* **290** (5): 22-42.

[77] Planck M, 1906. Vorlesungen über die Theorie der Wärmestrahlungen. Leipzig, Germany: *Verlag von Johann Ambrosius Barth*; 222 pp.

[78] Post VEA, 2005. Fresh and saline groundwater interaction in coastal aquifers: Is our technology ready for the problems ahead? *Hydrogeology Journal* **13**: 120-123.

[79] Prasad A and Simmons CT, 2003. Unstable density-driven flow in heterogeneous porous media: A stochastic study of the *Elder* [1967b] "short heater" problem. *Water Resources Research* **39** (1), 1007, DOI: 10.1029/2002WR001290.

[80] Prasad A and Simmons CT, 2004. Using quantitative indicators to evaluate results from variable-density groundwater flow models. *Hydrogeology Journal*, eFIRST, DOI: 10.1007/s10040-004-0338-0

[81] Rausch R, Schäfer W, Therrien R and Wagner C, 2005. Introduction to Solute Transport Modelling. Berlin, Germany: *Gebrüder Borntraeger*; for publication.

[82] Rayleigh JWS, 1916. On convection currents in a horizontal layer of fluid when the higher temperature is on the under side. *Philosophical Magazine* Series 6, **32** (192): 529-546.

[83] Rimstidt JD, 1997. Quartz solubility at low temperatures. *Geochimica et Cosmochimica Acta* **61** (13): 2553-2558.

[84] Rimstidt JD and Barnes HL, 1980. The kinetics of silica-water reactions. *Geochimica et Cosmochimica Acta* **44**: 1683-1699.

[85] Rimstidt JD and Dove JD, 1986. Mineral/solution reaction rates in a mixed flow reactor: Wollastonite hydrolysis. *Geochimica et Cosmochimica Acta* **50**: 2509-2516.

[86] Saaltink MW, Carrera J and Ayora C, 2001. On the behavior of approaches to simulate reactive transport. *Journal of Contaminant Hydrology* **48** (4): 213-235.

[87] Sanford WE and Konikow LF, 1989. Simulation of calcite dissolution and porosity changes in saltwater mixing zones in coastal aquifers. *Water Resources Research* **25** (4): 655-667.

[88] Schäfer W and Therrien R, 1995. Simulating transport and removal of xylene during remediation of a sandy aquifer. *Journal of Contaminant Hydrology* **19** (9): 205-236.

[89] Schäfer D, Schäfer W and Kinzelbach W, 1998. Simulating of reactive processes related to beodegradation in aquifers 1. Structure of the three-dimensional reactive transport model. *Journal of Contaminant Hydrology* **31** (5): 167-186.

[90] Schincariol RA and Schwartz FW, 1990. An experimental investigation of variable-density flow and mixing in homogeneous and heterogeneous media. *Water Resources Research* **26** (10): 2317-2329.

[91] Schincariol RA, Schwartz FW and Mendoza CA, 1994. On the generation of instabilities in variable-density flows. *Water Resources Research* **30** (4): 913-927.

[92] Shi M, 2005. Characterizing heterogeneity in low-permeability strata and its control on fluid flow and solute transport by thermalhaline free convection. Unpublished Ph.D. thesis, *University of Texas at Austin*; 229 pp.

[93] Shibue Y, 1994. An empirical equation for quartz solubility in NaCl solution. *Journal of Mineralogy, Petrology and Economic Geology* **89**: 203-212.

[94] Shikaze SG, Sudicky EA and Mendoza CA, 1994. Simulations of dense vapour migration in discretely-fractured geologic media. *Water Resources Research* **30** (7): 1993-2009.

[95] Shikaze SG, Sudicky EA and Schwartz FW, 1998. Density-dependent solute transport in discretely-fractured geologic media: is prediction possible? *Journal of Contaminant Hydrology* **34** (10): 273-291.

[96] Simmons CT and Narayan KA, 1997. Mixed convection processes below a saline

disposal basin. *Journal of Hydrology* **194** (7): 263-285.

[97] Simmons CT, Narayan KA and Wooding RA, 1999. On a test case for density-dependent groundwater flow and solute transport models: The salt lake problem. *Water Resources Research* **35** (12): 3607-3620.

[98] Simmons CT, Fenstemaker TR and Sharp Jr. JM, 2001. Variable-density groundwater flow and solute transport in heterogeneous porous media: approaches, resolutions and future challenges. *Journal of Contaminant Hydrology* **52** (11): 245-275.

[99] Simmons CT, 2005. Variable density groundwater flow: From current challenges to future possibilities. *Hydrogeology Journal* **13**: 116-119.

[100] Spycher NF, Sonnenthal EL and Apps JA, 2003. Fluid flow and reactive transport around potential nuclear waste emplacement tunnels at Yucca Mountain, Nevada. *Journal of Contaminant Hydrology* **62-63**: 653-673.

[101] Steefel CI and Lasaga AC, 1994. A coupled model for transport of multiple chemical species and kinetic precipitation/dissolution reactions with application to reactive flow in single phase hydrothermal systems. *American Journal of Science* **294** (5): 529-592.

[102] Steefel CI and Lichtner PC, 1998a. Multicomponent reactive transport in discrete fractures: I. Controls on reaction front geometry. *Journal of Hydrology* **209**: 186-199.

[103] Steefel CI and Lichtner PC, 1998b. Multicomponent reactive transport in discrete fractures: II. Infiltration of hyperalkaline groundwater at Maqarin, Jordan, a natural analogue site. *Journal of Hydrology* **209**: 200-224.

[104] Steefel CI and MacQuarrie KTB, 1996. Approaches to modeling of reactive transport in porous media. In: Lichtner PC, Steefel CI, Oelkers EH (editors). Reviews in Mineralogy, **34**. Washington, DC, USA: *Mineralogical Society of America*; 83-129 [chapter 2].

[105] Steefel CI and Yabusaki SB, 1996. OS3D/GIMRT: Software for modeling multicomponent-multidimensional reactive transport; user manual and programmer's

guide. Technical Report PNL-1116, Pacific Northwest National Laboratory, Richland, WA, USA; 56 pp.

[106] Stern ME, 1960. The "salt-fountain" and thermohaline convection. *Tellus* **12** (1): 172-175.

[107] Stober I and Bucher K, 2005. Deep fluids: Neptune meets Pluto. *Hydrogeology Journal* **13**: 112-115.

[108] Sudicky EA and Frind EO, 1982. Contaminant transport in fractured porous media: Analytical solution for a system of parallel fractures. *Water Resources Research* **18** (6): 1634-1642.

[109] Sudicky EA and McLaren RG, 1992. The Laplace transform Galerkin technique for large-scale simulation of mass transport in discretely-fractured porous formations. *Water Resources Research* **28** (2): 499-514.

[110] Tang DH, Frind EO and Sudicky EA, 1981. Contaminant transport in fractured porous media: Analytical solution for a single fracture. *Water Resources Research* **17** (3): 555-564.

[111] Taylor GI, 1954. Diffusion and mass transport in tubes. *Proceedings of the Physical Society, Section B* **67** (12): 857-869.

[112] Tester JW, Worley WG, Robinson BA, Grigsbay CO and Feerer JL, 1994. Correlating quartz dissolution kinetics in pure water from 25 to 625°C. *Geochimica et Cosmochimica Acta* **58** (11): 2407-2420.

[113] Therrien R and Sudicky EA, 1996. Three-dimensional analysis of variably saturated flow and solute transport in discretely-fractured porous media. *Journal of Contaminant Hydrology* **23** (6): 1-44.

[114] Therrien R, McLaren RG, Sudicky EA and Panday SM, 2004. HYDROSPHERE - A three-dimensional numerical model describing fully-integrated subsurface and surface flow and solute transport. *Université Laval, University of Waterloo*; 275 pp.

[115] Thomas GB Jr. and Finney RL, 1988. Calculus and analytic geometry, 7th edition. Reading, MA, USA: *Addison-Wesley Publishing Company*; 1136 pp.

[116] Turner JS, 1979. Buoyancy effects in fluids. Cambridge, UK: *Cambridge University Press*; 368 pp.

[117] Tyvand PA, 1980. Thermohaline instability in anisotropic porous media. *Water Resources Research* **16**: 325-330.

[118] von Damm KL, Bischoff JL and Rosenbauer RJ, 1991. Quartz solubility in hydrothermal seawater: an experimental study and equation describing quartz solubility for up to $0.5m$ NaCl solutions. *American Journal of Science* **291** (12): 977-1007.

[119] von Hippel FN, 2001. Plutonium and reprocessing of spent nuclear fuel. *Science* **293** (5539): 2397-2398.

[120] Voss CI, 1984. SUTRA: A Finite-Element Simulation Model for Saturated-Unsaturated Fluid Density-Dependent Groundwater Flow with Energy Transport or Chemically Reactive Single-Species Solute Transport. *US Geological Survey* Water Resour. Invest. Rep. 84-4369, 409 pp.

[121] Walter AL, Frind EO, Blowes, DW, Ptacek CJ and Molson JWH, 1994. Modelling of multicomponent reactive transport in groundwater, 2,Metal mobility in aquifers impacted by acidic mine tailings discharge. *Water Resources Research* **30**: 3149-3158.

[122] Ward DS, Reeves M and Duda LE, 1984. Verification and field comparison of the Sandia waste-isolation flow and transport (SWIFT) model. *NUREG/CR- 3316, SAND83-1154*, Sandia National Laboratories, Albuquerque, NM, USA.

[123] Weatherill D, Simmons CT, Voss CI, and Robinson NI, 2004. Testing density-dependent groundwater models: two-dimensional steady state unstable convection in infinite, finite and inclined porous layers. *Advances in Water Resources* **27**: 547-562.

[124] Weir GJ, 2003. http://www.irl.cri.nz/applied-maths/history.html

[125] Weir GJ and White SP, 1996. Surface deposition from fluid flow in a porous medium. *Transport in Porous Media* **25**: 79-96.

[126] White SP and Mroczek EK, 1998. Permeability changes during the evolution of a geothermal field due to the dissolution and precipitation of quartz. *Transport in Porous Media* **33**: 81-101.

[127] Wooding RA, 1957. Steady state free thermal convection of liquid in a saturated permeable medium. *Journal of Fluid Mechanics* **2**: 273-285.

[128] Wooding RA, 1962. Free convection of fluid in a vertical tube filled with porous material. *Journal of Fluid Mechanics* **13**: 129-144.

[129] Wooding RA, Tyler SW, White I and Anderson PA, 1997a. Convection in groundwater below an evaporating salt lake: 1. Onset of instability. *Water Resources Research* **33** (6): 1199-1217.

[130] Wooding RA, Tyler SW and White I, 1997b. Convection in groundwater below an evaporating salt lake: 2. Evolution of fingers and plumes. *Water Resources Research* **33** (6): 1219-1228.

[131] Xue Y, Xie C, Wu J, Liu P, Wang J and Jiang Q, 1995. A three-dimensional miscible transport model for seawater intrusion in China. *Water Resources Research* **31** (4): 903-912.

[132] Yang J and Edwards RN, 2000. Predicted groundwater circulation in fractured and unfractured anisotropic porous media driven by nuclear fuel waste heat generation. *Canadian Journal of Earth Sciences* **37**: 1301-1308.

[133] Yeh GT and Tripathi VS, 1989. A critical evaluation of recent developments in hydrogeochemical transport models of reactive multichemical components. *Water Resources Research* **25** (1): 93-108.

[134] Yoshida J, Nagashima H and Nagasaka M, 1995. Numerical experiment on double diffusive currents. In: Brandt A and Fernando HJS (editors). Double-diffusive convection, *American Geophysical Union*. Washington, DC, USA; 69-79.

[135] Zheng C and Bennett GD, 2002. Applied contaminant transport modeling. New York, NY, USA: *John Wiley & Sons, Inc.*; 621 pp.

[136] Zysset A, Stauffer F and Dracos T, 1994. Modeling of chemically reactive ground-

water transport. *Water Resources Research* **30** (7): 2217-2228.

Appendix A

Transport Matrices and Vectors

In this appendix, the matrices and vectors used in the semi-discrete form (4.42) of the reactive transport equation are defined. All terms contain two parts, where the first and the second part are contributions of the discretized reactive transport equation in the matrix and the fracture zone, respectively. The second fracture part of the terms presented below is, therefore, comparable to the coefficients given by Frind (1982).

The fracture part of the advective-dispersive-reactive transport matrix, $\mathbf{R}$, is identical to the definition in Frind (1982) except the last term representing the quartz precipitation rate. The fracture terms of the matrix $\mathbf{T}$ and the vector $\mathbf{b}$ are essentially identical to those presented by Frind (1982). Similar to the storage term in the flow equation, all off-diagonal entries of $\mathbf{T}$ are nought. The additional vector $\mathbf{u}$ represents the quartz dissolution reaction rate, which is independent of the quartz molality.

In the developed model, only regularly shaped finite elements, such as blocks in 3D and rectangles in 2D, are used. This allows the integral in (A.1) to be solved analytically using influence coefficient matrices. Details on the influence coefficient matrices required are given by Therrien and Sudicky (1996) and Frind (1982).

$$R_{IJ} = \sum_e \int_{V^e} \left(\phi D_{ij} \, \frac{\partial w_I}{\partial x_i} \, \frac{\partial w_J}{\partial x_j} \; + q_i \, w_I \, \frac{\partial w_J}{\partial x_i} + \frac{\varepsilon \, \gamma_{\mathrm{H_4SiO_4}}}{K_{eq}} \, w_I \, w_J \right) \, \mathrm{d}V^e +$$

$$\sum_{fe} (2b) \int_{A^{fe}} \left(D^{fr}_{i'j'} \, \frac{\partial w^{fr}_I}{\partial x_{i'}} \, \frac{\partial w^{fr}_J}{\partial x_{j'}} \; + q^{fr}_{i'} \, w^{fr}_I \, \frac{\partial w^{fr}_J}{\partial x_{i'}} + \frac{\varepsilon^{fr} \, \gamma^{fr}_{\mathrm{H_4SiO_4}}}{K_{eq}} \, w^{fr}_I \, w^{fr}_J \right) \, \mathrm{d}A^{fe}$$

$$i, j = 1, 2, 3 \qquad i', j' = 1, 2 \qquad I, J = 1...Nn \tag{A.1}$$

$$T_{IJ} = \sum_e \int_{V^e} (\phi R \, w_I \delta_{IJ}) \, \mathrm{d}V^e + \sum_{fe} (2b) \int_{A^{fe}} \left(R^{fr} \, w^{fr}_I \delta_{IJ} \right) \, \mathrm{d}A^{fe}$$

$$I, J = 1...Nn \tag{A.2}$$

$$u_I = - \sum_e \int_{V^e} (\varepsilon \, w_I) \, \mathrm{d}V^e - \sum_{fe} (2b) \int_{A^{fe}} \left(\varepsilon^{fr} \, w^{fr}_I \right) \, \mathrm{d}A^{fe}$$

$$I = 1...Nn \tag{A.3}$$

$$b_I = \sum_e \oint_{\Gamma^e} \left(\phi D_{ij} \, w_I \, \frac{\partial \hat{m}}{\partial n} \right) \, \mathrm{d}\Gamma^e + \sum_{fe} (2b) \oint_{\Gamma^{fe}} \left(D^{fr}_{i'j'} \, w^{fr}_I \, \frac{\partial \hat{m}}{\partial n} \right) \, \mathrm{d}\Gamma^{fe}$$

$$i, j = 1, 2, 3 \qquad i', j' = 1, 2 \qquad I = 1...Nn \tag{A.4}$$

Appendix B

Fluid Pressure Formulation

In order to reproduce the Elder (1967) results given by Frolkovič and De Schepper (2000), the FRAC3DVS model had to be modified such that the same flow variable, the fluid pressure P, can be used to simulate variable-density flow and solute transport in porous media.

The governing equation for variable-saturated variable-density flow in porous media is given by Voss (1984) and has under fully saturated flow conditions the three-dimensional form

$$\frac{\partial}{\partial x_i}\left[\beta K_{ij}^0\left(\frac{1}{g}\frac{\partial P}{\partial x_j}+\rho\eta_j\right)\right]=\rho S_{op}\,\frac{\partial P}{\partial t}+\phi\frac{\partial \rho}{\partial c}\,\frac{\partial c}{\partial t} \qquad i,j=1,2,3 \quad \text{(B.1)}$$

where $\beta=\rho/\rho_{max}$ [–] and S_{op} [M^{-1} L T^2] is the specific pressure storativity, given in Voss (1984) as

$$S_{op}=(1-\phi)\alpha_m+\phi\;\alpha_{fl} \qquad \text{(B.2)}$$

All other parameters have been defined in the text. Moreover, the pressure gradient form of Darcy's law is

$$q_i=-\frac{\kappa_{ij}}{\mu}\left(\frac{\partial P}{\partial x_j}+\rho g\eta_j\right) \qquad i,j=1,2,3 \qquad \text{(B.3)}$$

Lacking externally applied solute mass sources, which is the case in the Elder (1967) problem, the governing equation for solute transport in porous media does not need to be adapted to the new flow variable, P, and is given by Equation (3.17).

Appendix C

Tabular Simulation Results

Table C.1 presents tabulated concentration versus time data of the variable-density flow simulation in a single inclined fracture from Section 6.1. The availability of tabular results enables an objective model verification of further groundwater models and, thus, goes beyond pure isochlor comparison.

Table C.1: Simulation results of scenario 1: concentration breakthrough at $z = 6$ m in the fracture.

t [yr]	c [–]	t [yr]	c [–]	t [yr]	c [–]	t [yr]	c [–]	t [yr]	c [–]
0.0	0.00000								
0.2	0.00000	4.2	0.30192	8.2	0.66246	12.2	0.76073	16.2	0.803484
0.4	0.00000	4.4	0.33476	8.4	0.67039	12.4	0.76362	16.4	0.805039
0.6	0.00000	4.6	0.36559	8.6	0.67783	12.6	0.76640	16.6	0.806557
0.8	0.00000	4.8	0.39437	8.8	0.68482	12.8	0.76908	16.8	0.808038
1	0.00000	5	0.42114	9	0.69141	13	0.77166	17	0.809485
1.2	0.00000	5.2	0.44599	9.2	0.69762	13.2	0.77415	17.2	0.810899
1.4	0.00002	5.4	0.46903	9.4	0.70349	13.4	0.77656	17.4	0.812281
1.6	0.00014	5.6	0.49037	9.6	0.70903	13.6	0.77888	17.6	0.813633
1.8	0.00071	5.8	0.51015	9.8	0.71428	13.8	0.78113	17.8	0.814955
2	0.00264	6	0.52847	10	0.71925	14	0.78331	18	0.816250

2.2	0.00749	6.2	0.54547	10.2	0.72398	14.2	0.78542	18.2	0.817518
2.4	0.01724	6.4	0.56124	10.4	0.72847	14.4	0.78747	18.4	0.818759
2.6	0.03342	6.6	0.57590	10.6	0.73274	14.6	0.78946	18.6	0.819976
2.8	0.05652	6.8	0.58953	10.8	0.73681	14.8	0.79139	18.8	0.821169
3	0.08578	7	0.60222	11	0.74069	15	0.79326	19	0.822339
3.2	0.11961	7.2	0.61404	11.2	0.74440	15.2	0.79508	19.2	0.823487
3.4	0.15615	7.4	0.62507	11.4	0.74795	15.4	0.79685	19.4	0.824614
3.6	0.19362	7.6	0.63537	11.6	0.75135	15.6	0.79858	19.6	0.825719
3.8	0.23092	7.8	0.64500	11.8	0.75461	15.8	0.80025	19.8	0.826805
4	0.26720	8	0.65402	12	0.75773	16	0.80189	20	0.827872

Appendix D

Parameter Dependency on Temperature and Salinity

The developed model computes every physicochemical system parameter over the low-temperature range 0°C to 300°C and a wide range of salinity, shown in Table D.1. Figure D.1 graphically illustrates the corresponding model parameters.

Table D.1: Water chemistry at different depths in the Canadian Shield; all concentrations are in mg l^{-1} (Farvolden et al., 1988).

solute	freshwater	brackish water	saltwater	dense brine
	0 m	-500 m	-1,000 m	-1,500 m
Na^{+}	9	360	3,550	34,000
Mg^{2+}	2	90	95	25
Ca^{2+}	15	630	7,600	60,000
Cl^{-}	30	730	24,000	150,000

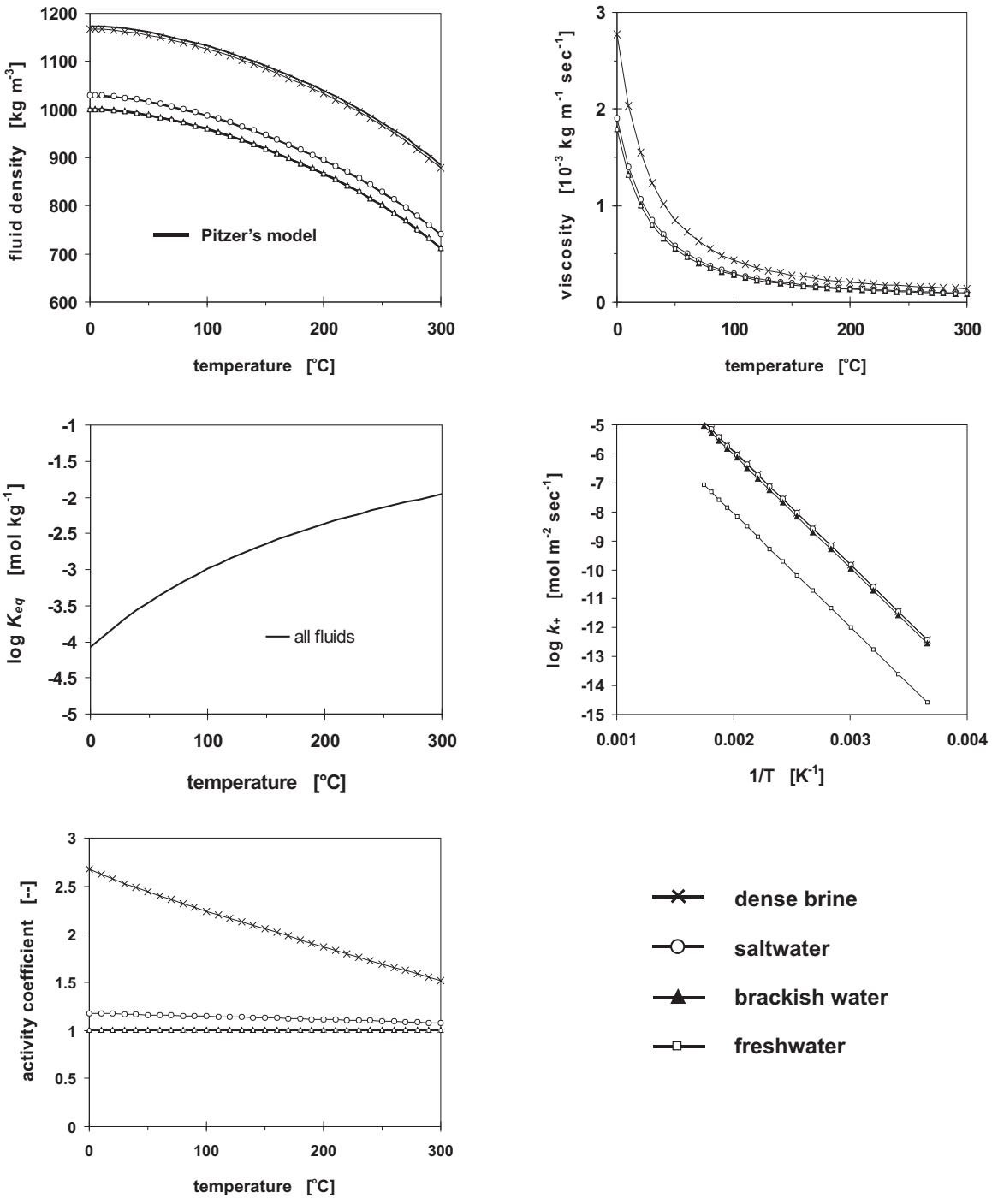

Figure D.1: All physicochemical parameters calculated by FRAC3DVS are functions of temperature and salinity.

Appendix E

Mathematical Notation

The use of symbols for main variables is consistent throughout the entire text. The print mode for symbols is applied as follows:

- scalar variables are denoted in normal italic letters
- vector variables are denoted in bold small letters
- matrix variables are denoted in bold capital letters

Latin letters

$(2b)$	[L]	Fracture aperture
$(2B)$	[L]	Fracture spacing
a	[MOL M^{-1}]	Activity
A	[–]	Aspect ratio between domain length and height
A_{qz}	[M^{-1} L^2]	Specific surface area in the matrix
A_{qz}^{fr}	[M^{-1} L^2]	Specific surface area in the fracture
A_s	[L^2]	Active surface area
B	[–]	Aspect ratio between domain length and width
B	[MOL^{-1} L^3]	Coefficient in the Jones-Dole equation
c	[–]	Solute concentration, expressed as relative concentration

c_{max}	[–]	Maximum relative solute concentration
$\tilde{c}$	[L^2 T^{-2} ϑ^{-1}]	Specific heat
C	[M L^{-3}]	Solute concentration, expressed as volumetric mass
D	[–]	Marshall-Chen coefficient
D_d	[L^2 T^{-1}]	Free-solution diffusion coefficient
D_{ij}	[L^2 T^{-1}]	Hydrodynamic matrix dispersion tensor
D_{ij}^{fr}	[L^2 T^{-1}]	Hydrodynamic fracture dispersion coefficient
D_{th}	[L^2 T^{-1}]	Thermal dispersion coefficient
e	[–]	Euler's constant; $e = 2.718281828$
E_a	[MOL^{-1} M L^2 T^{-2}]	Activation energy
g	[L T^{-2}]	Acceleration due to gravity
$\mathbf{g}$	[L^2 T^{-1}]	Buoyancy vector
h_0	[L]	Equivalent freshwater head
$\mathbf{i}$	[–]	Unit vector in x-direction
I^+, I^-	[–]	Fracture-matrix interface
$\hat{j}$	[M T^{-1}]	Mass flux rate
$\mathbf{j}$	[–]	Unit vector in y-direction
J	[M L^{-2} T^{-1}]	Flow rate of solute mass
$\mathbf{J}$	[–]	Jacobian matrix
k	[M L T^{-3} ϑ^{-1}]	Thermal conductivity
$\mathbf{k}$	[–]	Unit vector in z-direction
k_+	[MOL L^{-2} T^{-1}]	Dissolution (forward) reaction constant
k_+^0	[MOL L^{-2} T^{-1}]	Dissolution reaction constant in deionized water
k_+^{corr}	[MOL L^{-2} T^{-1}]	Dissolution reaction constant in saltwater
k_-	[M L^{-2} T^{-1}]	Precipitation (backward) reaction constant
K_{ad}	[MOL^{-1} M]	Equilibrium adsorption coefficient
K_d	[M^{-1} L^3]	Equilibrium distribution coefficient
K_d^{fr}	[L]	Fracture-surface distribution coefficient
K_{eq}	[MOL M^{-1}]	Equilibrium constant
K_{ij}^0	[L T^{-1}]	Coefficients of hydraulic conductivity tensor of freshwater
K_0^{fr}	[L T^{-1}]	Hydraulic freshwater conductivity of the fracture
ℓ_χ	[L]	Geometry of the model domain; $\chi = x, y, z$
L_χ	[L]	Geometry of a block element; $\chi = x, y, z$
L^{TG}	[L]	Characteristic length scale

m	[MOL M^{-1}]	Molal concentration
M	[MOL L^{-3}]	Molar concentration
M_w	[M]	Mass of water
Nn	[–]	Total number of nodes in a finite element grid
Nfe	[–]	Total number of fracture elements in a finite element grid
Nu	[–]	Nusselt number
P	[M L^{-1} T^{-2}]	Dynamic pressure of the fluid
Pe_g	[–]	Grid Peclet number
PPM	[–]	Mass parts per million
q_i	[L T^{-1}]	Darcy flux
Q	[M L^{-2} T^{-1}]	Flow rate of fluid mass
r_+	[MOL M^{-1} T^{-1}]	Dissolution (forward) reaction rate
r_-	[MOL M^{-1} T^{-1}]	Precipitation (backward) reaction rate
r_M	[MOL L^{-3} T^{-1}]	Net molar production rate
r_{net}	[MOL M^{-1} T^{-1}]	Net molal production rate
R	[–]	Retardation factor
R^*	[MOL^{-1} M L^2 T^{-2} ϑ^{-1}]	Universal gas constant R = 8.3144 mol^{-1} kg m^2 sec^{-2} K^{-1}
R^{fr}	[–]	Fracture retardation factor
R^{th}	[–]	Thermal retardation coefficient
Ra	[–]	Rayleigh number of a vertical layer
Ra^*	[–]	Rayleigh number of an inclined layer
Ra_c	[–]	Critical Rayleigh number of a horizontal layer
Ra_c^*	[–]	Critical Rayleigh number of an inclined layer
Re	[–]	Reynolds number
REV	[L^3]	Representative elementary volume
Sh	[–]	Sherwood number
S_{op}	[M^{-1} L T^2]	Specific pressure storativity
S_S	[L^{-1}]	Specific storage of the porous matrix
S_S^{fr}	[L^{-1}]	Specific storage of an open fracture
t	[T]	Time
T	[ϑ]	Absolute temperature in Kelvin
T_C	[ϑ]	Relative temperature in Celsius
v_i	[L T^{-1}]	Linear flow velocity

v_{th}	[L T^{-1}]	Retarded flow velocity
V_{qz}	[MOL^{-1} L^3]	Molar volume of quartz
w_i	[–]	Approximation function
X_π	[–]	Dimensionless sensitivity of parameter π

Greek letters

α	[1^o]	Bond angle
α_{fl}	[M^{-1} L T^2]	Coefficient of the compressibility of the fluid due to fluid pressure or hydraulic head variations
α_l	[L]	Matrix longitudinal dispersivity
α_l^{fr}	[L]	Longitudinal fracture dispersivity
α_m	[M^{-1} L T^2]	Coefficient of the compressibility of the porous medium due to fluid pressure or hydraulic head variations
α_t	[L]	Matrix transverse dispersivity
α_t^{fr}	[L]	Transverse fracture dispersivity
α^{salt}	[M^{-1} L^3]	Solutal expansion coefficient
β	[–]	Ratio of saltwater density to freshwater density
γ	[–]	Maximum relative density
γ_σ	[–]	Activity coefficient of species σ
Γ_m	[M L^{-3} T^{-1}]	Mass sources and sinks
δ_{ij}	[–]	Kronecker delta function
Δt	[T]	Temporal discretization
$\Delta\chi$	[L]	Spatial discretization; $\chi = x, y, z$
η_j	[–]	Indicator for flow direction
θ_σ	[–]	Fraction of sites occupied by cation σ
κ_{ij}	[L^2]	Coefficients of the intrinsic permeability tensor
λ	[T^{-1}]	Decay constant
Λ	[M T^{-3}]	Convective-conductive-dispersive loss or gain of heat
μ	[M L^{-1} T^{-1}]	Dynamic viscosity of the fluid
ν	[L^2 T^{-1}]	Kinematic viscosity of the fluid
ν_i	[–]	Weighting function
ξ	[problem dependent]	Unknown variable or function
ρ	[M L^{-3}]	Density

ρ_r	[–]	Relative fluid density
$\rho\tilde{c}$	[M L^{-1} T^{-2} ϑ^{-1}]	Heat capacity
σ_i	[M L^{-1} T^{-2}]	Normal stress component in direction i
τ	[–]	Factor of tortuosity
ϕ	[–]	Porosity of the rock matrix
ϕ_{qz}	[–]	Quartz volume fraction
φ	[1°]	Fracture incline
χ	[L]	Global coordinates; $\chi = x, y, z$
$\overline{\chi}$	[L]	Local coordinates; $\overline{\chi} = \overline{x}, \overline{y}, \overline{z}$
ω	[–]	Fracture roughness coefficient
Ω	[M M^{-1} T^{-1}]	Advective-dispersive loss or gain of solute mass

Sub- and superscripts

0	[–]	Reference fluid
b	[–]	Bulk
e	[–]	Matrix element
fe	[–]	Fracture element
fr	[–]	Fracture
i, j	[–]	Spatial indices
I, J	[–]	Nodal indices
$init$	[–]	Initial time level
l	[–]	Liquid phase
L	[–]	Time level
n	[–]	Normal direction
s	[–]	Solid phase
σ	[–]	Species

Special symbols

∂	[–]	Partial differential operator
Δ	[–]	Difference
∇	[L^{-1}]	Nabla or divergence operator; $\nabla() = \frac{\partial()}{\partial x} + \frac{\partial()}{\partial y} + \frac{\partial()}{\partial z}$
$\overline{\xi}$	[problem dependent]	Average value of the variable ξ